



UNIVERSITÀ  
DEGLI STUDI  
FIRENZE

DOTTORATO DI RICERCA IN  
SCIENZE FISICHE E ASTROFISICHE

CICLO XXXI

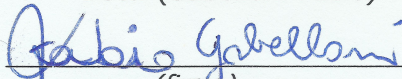
COORDINATORE Prof. D'Alessandro Raffaello

**Optical spectroscopy of advanced materials for  
energy harvesting**

Settore Scientifico Disciplinare FIS/03

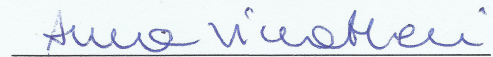
**Dottorando**

Dott. (Gabelloni Fabio)


  
\_\_\_\_\_  
(firma)

**Tutori**

Prof. (Vinattieri Anna)

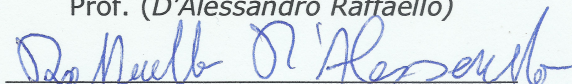
  
\_\_\_\_\_  
(firma)

Dott. (Biccari Francesco)

  
\_\_\_\_\_  
(firma)

**Coordinatore**

Prof. (D'Alessandro Raffaello)

  
\_\_\_\_\_  
(firma)

Anni 2015/2018

# Contents

<b>Introduction</b>	<b>iii</b>
<b>1 Perovskites: a review</b>	<b>1</b>
1.1 Crystal structure and phase transition . . . . .	1
1.2 Electronic properties . . . . .	3
1.2.1 Electronic structure . . . . .	3
1.2.2 Band gap tunability . . . . .	6
1.2.3 Electrical properties . . . . .	9
1.3 Optical properties . . . . .	11
1.3.1 Absorption . . . . .	11
1.3.2 Emission properties . . . . .	12
1.4 Defects . . . . .	17
<b>2 Synthesis techniques and material stability</b>	<b>20</b>
2.1 Synthesis of MAPI . . . . .	20
2.2 Synthesis of CsPbX <sub>3</sub> . . . . .	22
2.3 Stability of perovskite materials . . . . .	25
2.3.1 Stability of MAPI . . . . .	25
2.3.2 Stability of inorganic perovskites . . . . .	31
<b>3 Perovskites applications</b>	<b>35</b>
3.1 Perovskite solar cells . . . . .	35
3.1.1 Stability of PSCs . . . . .	38
3.1.2 Graphene in perovskites solar cell . . . . .	44
3.2 Applications beyond photovoltaics . . . . .	47
3.2.1 Perovskite LEDs . . . . .	47
3.2.2 Lasing in perovskites . . . . .	49
<b>4 Experimental techniques and setup</b>	<b>51</b>
4.1 Photoluminescence . . . . .	51
4.1.1 Recombination processes . . . . .	51
4.2 Experimental setups . . . . .	52
4.2.1 Macro-PL . . . . .	53
4.2.2 Micro-PL . . . . .	54
4.2.3 Polarization resolved measurements . . . . .	55
4.2.4 Time correlated single photon counting . . . . .	56
4.2.5 Streak camera . . . . .	57



<b>5</b>	<b>Graphene-based ETL: a step-up for an efficient carrier collection</b>	<b>59</b>
5.1	Description of the samples . . . . .	59
5.2	PL at room temperature . . . . .	60
5.3	PL measurements at low temperature . . . . .	63
5.4	Temperature dependent PL measurements . . . . .	65
5.5	PL measurements versus excitation energy . . . . .	66
5.6	J-V characterization . . . . .	67
<b>6</b>	<b>Superlinear emission in MAPI perovskites</b>	<b>69</b>
6.1	Description of the samples . . . . .	69
6.2	Power dependent PL measurements . . . . .	70
6.3	Spatial PL maps . . . . .	70
6.4	Polarization resolved measurements . . . . .	72
6.5	Conclusions . . . . .	72
<b>7</b>	<b>Surface states in CsPbBr<sub>3</sub> nanocrystals</b>	<b>74</b>
7.1	Description of the sample . . . . .	74
7.2	PL measurements at low temperature . . . . .	75
7.3	PL measurements as a function of temperature . . . . .	77
<b>8</b>	<b>Cooling dynamics in CsPbBr<sub>3</sub> perovskites</b>	<b>80</b>
8.1	Description of the samples . . . . .	80
8.2	Main PL features . . . . .	80
8.2.1	Single-crystal . . . . .	81
8.2.2	Spin-coated film . . . . .	82
8.3	Thermalization . . . . .	83
8.3.1	Single-crystal . . . . .	83
8.3.2	Spin-coated film . . . . .	86
8.4	Measurements with CW bias . . . . .	87
<b>9</b>	<b>Conclusions and perspectives</b>	<b>93</b>
	<b>List of abbreviations</b>	<b>96</b>
	<b>List of publications</b>	<b>97</b>
	<b>Partecipation to conferences</b>	<b>97</b>
	<b>References</b>	<b>97</b>

# Introduction

Nowadays, one of the most important research field regards the development of environmentally sustainable and commercially viable sources of energy due to the continuous growth in energy demand. The global energy consumption is of about 14 thousand of Mtoe<sup>1</sup> [1] and is expected to further increase in the future. Since fossil fuels are finite energy resources and their burning causes environmental air pollution, the research of green and sustainable energy sources is mandatory.

The sun is an inexhaustible renewable energy source enough to provides an energy amount much larger than the total world consumption. However, actually, solar energy contributes of merely 2% of the total electricity production [1] and less than 1 % of the total energy consumption [2] due to the high cost of photovoltaic technology. For this reason, the research of novel materials to advance solar energy harvesting is necessary.

In this context, a new class of low-cost semiconductor materials, called “perovskites”, attracted a lot of attention from the scientific community in the last decade given their very good electrical and optical properties [3–5]. Indeed, these materials have a high absorption in the visible spectral region ( $10^4 \div 10^5 \text{ cm}^{-1}$  [6–8]), long carrier diffusion lengths [9–12], low effective masses of electrons and holes [13, 14], high carrier mobilities ( $\geq 100 \text{ cm}^2 \text{ V}^{-1} \text{ s}^{-1}$  [12, 15]), tolerance towards defects [16, 17]; in addition, their emission is easily tunable from near-infrared to near-ultraviolet by varying the composition [18].

Since 2009 hybrid organic-inorganic perovskites, in particular methylammonium lead iodide ( $\text{CH}_3\text{NH}_3\text{PbI}_3$ , see also MAPI), have gained attention in photovoltaics for the development of a new generation of low-cost solar cells [5, 19, 20]: perovskite is used as absorbing layer and embedded between two transporting layers, that separately collect electrons and holes. The first perovskite solar cell (PSC), with a structure similar to a dye-sensitized solar cell (DSSC), was reported by Kojima et al. [21] in 2009: MAPI was used as light absorber and the power conversion efficiency (PCE), i.e. the ratio between the output electrical power and the incident sunlight power, was of merely 3.8%. Remarkably, after just seven years of active research, the PCE of perovskite solar cells (PSCs) has increased to above 22% [22, 23], reaching value comparable to that of other thin-film photovoltaics [19, 20], with the major advantages that PSCs are realized through low-cost fabrication techniques.

However, despite such rapid progress, the commercialization of PSCs is hindered by several factors [24], in particular the material instability and the toxicity of lead. Indeed, hybrid organic-inorganic lead halide perovskites easily degrade in presence of moisture [25, 26], light [27, 28] and heat [29] due to the organic part of the compound. In addition, also other components of the cell (transporting layers, electrodes) can introduce further degradation mechanisms [30–33]. The stability in PSCs was enhanced, maintaining the performance, by replacing methylammonium ( $\text{CH}_3\text{NH}_3^+$ ) cation with caesium [34–36] and/or formamidinium ( $\text{HC}(\text{NH}_2)_2^+$ ) [37–39], or partially replacing iodine anion with bromide [27, 40]. The lifetime of PSCs was increased from few hours in 2009 [21] to about one year in 2017 [41]. However, this value is not sufficient for the

---

<sup>1</sup>1 Mtoe (Million of toils equivalent) corresponds to about 4.4 TWh.



commercialization: silicon panels are guaranteed to work for at least 20 years.

Concerning the toxicity problem, other metal cations were recently investigated as substitute of lead, both in inorganic and in hybrid organic-inorganic perovskites [42]. Among them, Sn-based halide perovskites are particularly promising alternatives to Pb-based counterparts given their narrow band gap ( $\sim 1.3$  eV for  $\text{MASnI}_3$  [43]), close to the Shockley-Queisser limit (1.34 eV [44]). However, tin-based PSCs are unstable when exposed to air for the oxidation of  $\text{Sn}^{2+}$  to  $\text{Sn}^{4+}$ . This process leads to the easy formation of tin vacancies, causing large p-doping concentrations [45–47]. In order to passivate these defects,  $\text{SnF}_2$  or other excess divalent Sn compounds are used as additives during the synthesis [48, 49].

Another key point for the commercialization is the possibility to replicate small cells in large area modules and panels without loss in efficiency. Unfortunately, PSCs used in fundamental studies are typically small in area ( $\leq 1 \text{ cm}^2$ ) and only few reports have recently appeared on the preparation of large area modules ( $\geq 10 \text{ cm}^2$ ) with good efficiency ( $> 10\%$ ) [50–53].

Besides photovoltaics, perovskites are promising materials also for the realization of efficient light sources [54, 55] in the whole visible range due to the high photoluminescence quantum efficiency, being a direct band gap semiconductor, and the easy tunability of their emission spectra. In this context, a key work of Protesescu et al. [18] in 2015 reported, for the first time, the synthesis of highly-luminescent all-inorganic colloidal caesium lead halide ( $\text{CsPbX}_3$ ,  $X = \text{Cl}$ ,  $\text{Br}$ , and  $\text{I}$ ) nanocrystals (NCs). After this report, inorganic perovskite NCs have attracted intense research interest because their superior optical properties also with respect to inorganic quantum dots (QDs). First of all, halide perovskite NCs show narrow linewidths ( $\sim 20 \text{ nm}$  [18, 56, 57]) irrespective on their size, while inorganic QDs shows size-sensitive emission spectra [54]. Moreover, perovskite NCs exhibit a high photoluminescence quantum efficiency even without any surface passivation [18, 56, 58], that is related to the direct band gap and to the tolerance towards defects [17]. These properties make perovskite NCs suitable for electrically driven LEDs; the efficiency of perovskite LEDs reaches value of 8.7% [59], 14.1% [60] and 1.9% [61] for green, red and blue regions, respectively, but, at present, remains below the efficiency ( $> 20\%$ ) demonstrated for organic LEDs and QD LEDs operating in the visible [62, 63]. Moreover, due to the narrow emission and the continuous spectral tunability, halide perovskite NCs exhibit a wide colour gamut, that covers a greater area ( $> 140\%$ ) than the National Television System Committee (NTSC) colour standard [18], making them promising candidate as light converters in back-light display applications.

Finally, perovskites are interesting materials for multicolour lasing devices. Indeed, room temperature amplified spontaneous emission (ASE) [64, 65] and lasing [66–70] were demonstrated in hybrid and all-inorganic perovskites films and nanostructures with low threshold values (from  $\text{nJ cm}^{-2}$  to  $\mu\text{J cm}^{-2}$ ). In addition, very recently [71], lasing in perovskites was also demonstrated under continuous-wave optical pumping at room temperature.

Despite the impressive technological advancement of perovskite materials for light sources and energy harvesting applications, a deep knowledge and understanding of the physical processes that rule the carriers recombination and transport in these materials is still necessary in order to improve the performance of the devices.

In this thesis I present an experimental study of the optical properties of hybrid organic-inorganic MAPI perovskites and all-inorganic caesium lead bromide ( $\text{CsPbBr}_3$ ) perovskites by means of high-resolution photoluminescence (PL) spectroscopy. MAPI perovskites are mainly studied for photovoltaic applications, given the band gap of  $\sim 1.6$  eV at room temperature, and for near-infrared light sources. On the contrary,  $\text{CsPbBr}_3$  perovskites are mainly investigated for the realization of efficient green light sources. This work comes from the scientific collaboration with several groups that provided us the different samples:

- Prof. Aldo di Carlo group's of the Centre for Hybrid and Organic Solar Energy (CHOSE) of University of Rome Tor Vergata. This group provided us samples to study the charge recombination dynamics in MAPI PSCs with different graphene-based electron transporting layers (ETLs);
- Dr. Alexander Weber Bargioni's group of the Molecular Foundry National Laboratory of Berkeley, who provided us MAPI perovskites with different morphology (thin films and microstructures) to investigate the physical origin of the superlinear emission in these materials;
- Dr. Stefano Caporali's group at the Department of Industrial Engineering and the Department of Chemistry at the University of Florence, who provided us several  $\text{CsPbBr}_3$  perovskite samples (nanocrystalline film, single crystals, ...) that allowed us to study different aspects of the radiative emission (recombination dynamics, relaxation processes, ...) in these materials.

In summary, this PhD thesis is organized as follows:

- ▶ in Chap. 1 I discuss the structural, optical and electrical properties of perovskite materials, focusing on MAPI and  $\text{CsPbBr}_3$  perovskites;
- ▶ in Chap. 2 I describe the main synthesis techniques used to obtain perovskite films, single crystals, microstructures and nanostructures. Moreover, I present the main factors that cause instability in perovskite materials;
- ▶ in Chap. 3 I briefly review the possible applications of perovskites;
- ▶ in Chap. 4 I describe the experimental setups used to perform time-integrated and time-resolved PL measurements;
- ▶ in Chap. 5 I present results concerning the improvement of the performance of MAPI PSCs using graphene-based ETLs;
- ▶ in Chap. 6 I discuss the origin of the superlinear emission in MAPI perovskite film and microstructures;
- ▶ in Chap. 7 I show the relevant role of the surface states in the recombination dynamics of  $\text{CsPbBr}_3$  nanocrystals;
- ▶ in Chap. 8 I discuss the relaxation process in  $\text{CsPbBr}_3$  single crystals and spin-coated films;
- ▶ Finally, in the conclusions, I resume the most relevant results obtained in this work.





# §1§ Perovskites: a review

In this chapter are summarized the main structural, electrical and optical properties of perovskite semiconductors, mainly focusing on methylammonium lead iodide ( $\text{CH}_3\text{NH}_3\text{PbI}_3$ , hereafter called MAPI) and caesium lead bromide ( $\text{CsPbBr}_3$ ) perovskites.

## 1.1 Crystal structure and phase transition

Perovskites are a class of materials with the same crystal structure of calcium titanium oxide ( $\text{CaTiO}_3$ ), discovered by the mineralogist Gustav Rose in 1839 in the Ural Mountains [72]. He named this structure *perovskite* in honour of Russian mineralogist Lev Aleksevich von Perovski, that firstly classified this crystalline structure.

Perovskites are described by the chemical formula  $\text{ABX}_3$ , where A is a monovalent cation, B is a divalent cation and X is an anion. Perovskites are classified as *hybrid* and *inorganic* depending on the nature of A cation. In *hybrid* perovskites A is an organic cation, such as *methylammonium* ( $\text{CH}_3\text{NH}_3^+$ , MA) or *formamidinium* ( $\text{HC}(\text{NH}_2)_2^+$ , FA), while the most common *inorganic* ion employed is caesium ( $\text{Cs}^+$ ). B cation is generally a divalent metal ( $\text{Pb}^{2+}$ ,  $\text{Sn}^{2+}$ ,  $\text{Ge}^{2+}$ ) and X is a halogen ( $\text{I}^-$ ,  $\text{Br}^-$ ,  $\text{Cl}^-$ ).

The ideal perovskite crystal structure (Fig. 1.1) has a cubic symmetry: A ions occupy the cube-corner positions, B ion the body-centered position and X ions the face-centered positions; B and X ions are coordinated in a  $\text{BX}_6$  octahedron. To predict the stability of perovskite structure two geometrical parameters are typically used: the tolerance factor ( $t$ ), developed by Goldschmidt [73], and the octahedral factor ( $\mu$ ), developed by Li and coworkers [74]. The tolerance factor is the ratio between the A-X distance and the B-X distance in a cubic structure and it is given by

$$t = \frac{R_A + R_X}{\sqrt{2}(R_B + R_X)}, \quad (1.1)$$

where  $R_A$ ,  $R_B$  and  $R_X$  are the ionic radii for A, B and X respectively.

In the case of hybrid organic-inorganic perovskites, A ions are organic molecular cations, where the variation of the bond lengths due to hydrogen-bonding interactions make difficult to define an ionic radius. To address this point, Kieslich et al. [75, 76] proposed a rigid sphere model to obtain an effective ionic radius for the molecular cation ( $r_{A,eff}$ ), defined as

$$r_{A,eff} = r_{mass} + r_{ion}. \quad (1.2)$$

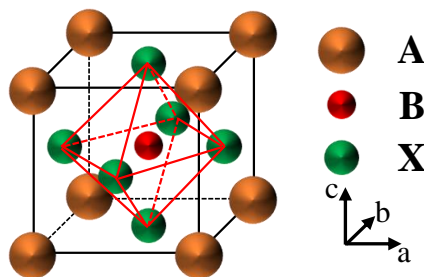


**Figure 1.1:** The perovskite cubic crystal structure. The  $\text{BX}_6$  octahedra are evidenced.



**Table 1.1:** Ionic radii (in Å) of the ions most common employed in perovskites [4, 76]. The effective ionic radii are reported for organic A cations (MA, FA).

	A	B	X
MA	2.17	Sn 1.1	I 2.2
FA	2.53	Pb 1.19	Br 1.96
Cs	1.67		Cl 1.81

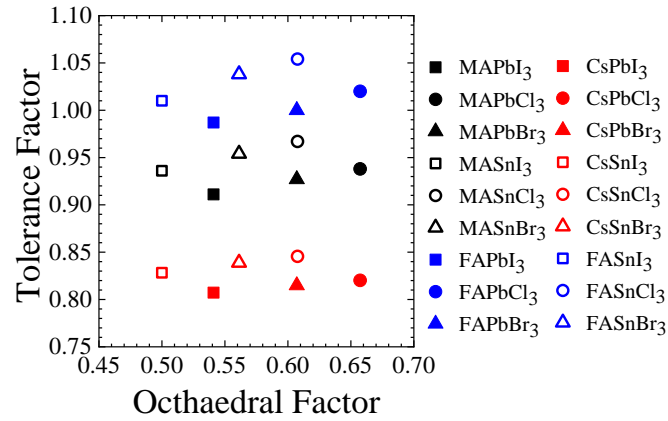


**Figure 1.2:** Calculated tolerance and octahedral factor for various organic and inorganic perovskite compounds.

In Eqn. 1.2  $r_{mass}$  is the distance between the centre of mass of the molecule and the non-hydrogen atom with the largest distance to the centre of mass, while  $r_{ion}$  is the corresponding ionic radius of this atom. The ionic radii of the ions most common employed in perovskites are reported in Tab. 1.1. The effective molecular cation radii are reported for the organic A cations (MA, FA).

Instead, the octahedral factor provides a measure of the octahedral stability and it is defined as

$$\mu = \frac{R_B}{R_X}. \quad (1.3)$$

In Fig. 1.2 the tolerance and the octahedral factors for various perovskites are reported. These values were calculated through Eqn. 1.1 and Eqn. 1.3, using the ionic radii values of Tab. 1.1.

Studies of formability in halide perovskites [74] showed that the perovskite crystal structure is stable when  $0.8 \leq t \leq 1$  and  $0.44 \leq \mu \leq 0.9$ . For  $t$  values in the range of 0.9–1.0, mostly cubic perovskites are found [75]. Instead, lower tolerance factors give a less symmetrical perovskite structure due to deformation and/or tilting of  $BX_6$  octahedra; the most common are the orthorhombic and tetragonal phases (see Fig. 1.3). On the contrary, if  $t > 1$  the hexagonal structure is more stable due to a large A cation radius [77].

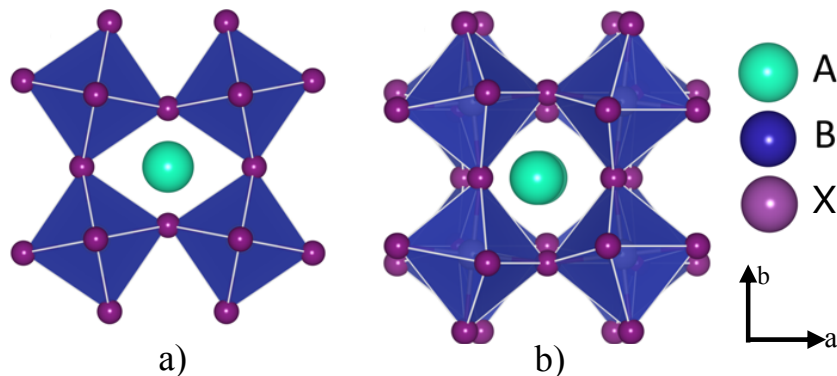


**Figure 1.3:** Tetragonal (a) and orthorhombic (b) perovskite crystalline phases [78].

**Table 1.2:** Phase transition temperatures for MAPbX<sub>3</sub> (left) and CsPbX<sub>3</sub> (right) perovskites [79–82].

Composition	Crystal Structure	Temperature (K)	Composition	Crystal Structure	Temperature (K)
MAPbCl <sub>3</sub>	Cubic	> 179	CsPbCl <sub>3</sub>	Cubic	> 320
	Tetragonal	173-179		Tetragonal	315-320
	Orthorhombic	< 173		Orthorhombic	310-315
		Monoclinic		< 310	
MAPbBr <sub>3</sub>	Cubic	> 237	CsPbBr <sub>3</sub>	Cubic	> 403
	Tetragonal	147-237		Tetragonal	361-403
	Orthorhombic	< 147		Orthorhombic	< 361
MAPbI <sub>3</sub>	Cubic	> 327	CsPbI <sub>3</sub>	Cubic	> 602
	Tetragonal	162-327		Orthorhombic	< 602
	Orthorhombic	< 162			

Moreover, perovskites crystal structure depends also from temperature. In fact perovskites undergo structural phase transitions, with a reduction of symmetry decreasing the temperature, with the orthorhombic phase at lower temperature than the tetragonal one. In Tab. 1.2 the phase transition temperatures for MA and Cs lead halide perovskites are summarized. For MAPI, the phase transition from the orthorhombic to the tetragonal phase occurs at about 162 K, while the cubic phase is stable only at temperature higher than 327 K. On the contrary, MAPbBr<sub>3</sub> and MAPbCl<sub>3</sub> are stable in the cubic phase at room temperature due to the higher tolerance factor (see Fig. 1.2). Finally, CsPbBr<sub>3</sub> is stable in the orthorhombic phase up to 361 K. We can see that, decreasing the halogen radius (Cl → Br → I), the phase transitions occur at lower temperatures. This can be due to an increase of the stability of the perovskite structure since the tolerance factor increases with a reduction of  $R_X$ <sup>1</sup>.

## 1.2 Electronic properties

### 1.2.1 Electronic structure

Both theoretical electronic band structure calculation [83–85] and absorption measurements [6, 7, 86] show that perovskite materials are direct band gap semiconductors. Thus, the valence band maximum (VBM) and the conduction band minimum (CBM) lie at the same k-point in the reciprocal space.

The electronic band structure of perovskite semiconductor near the band edge is primarily defined by the BX<sub>6</sub> octahedra [87–90]. As shown in Fig. 1.4(a), for lead halide perovskites the VBM is composed of an antibonding coupling of the halide  $np^6$  orbitals ( $n$  is the principal quantum number,  $n=3, 4$  and  $5$  for Cl, Br, and I, respectively) and the metal  $6s^2$  orbitals. Due to the antibonding nature, the VBM is above the halogen  $p$  atomic orbital level. Instead, the CBM arises from an antibonding mixing of the metal  $np^6$  orbitals and the halide  $np^6$  orbitals, with a prevalent contribution of the metal  $np^6$  orbitals. Due to the ionic character of lead halide perovskites, the antibonding coupling between Pb( $6p$ ) and X( $6p$ ) is not strong [16]. Therefore,

<sup>1</sup>The Eqn. 1.1 can be also written as  $t = \frac{1}{\sqrt{2}} + \frac{R_A - R_B}{\sqrt{2}(R_B + R_X)}$ . Since  $R_A$  is typically greater than  $R_B$  (see Tab. 1.1),  $t$  increases if  $R_X$  decreases.

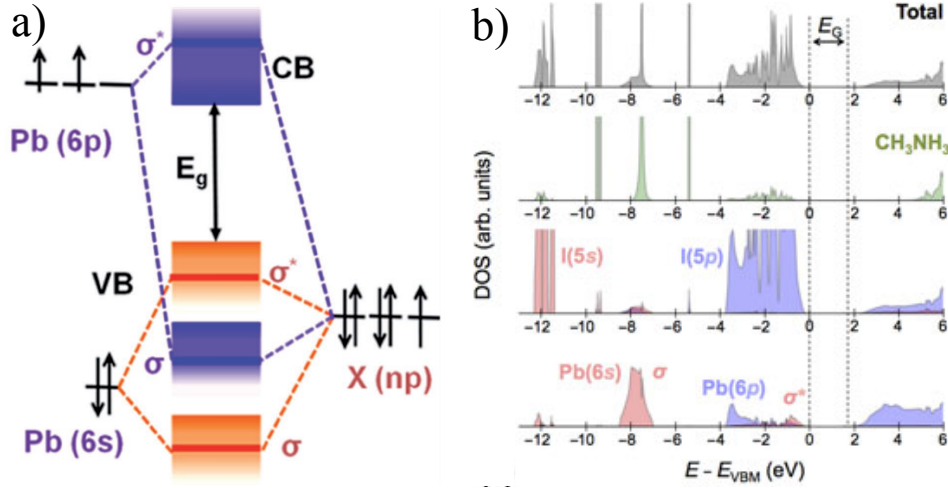


**Figure 1.4:** a) Schematic representation of bonding ( $\sigma$ ) and antibonding ( $\sigma^*$ ) orbitals in lead halide ( $\text{APbX}_3$ ,  $X = \text{Cl, Br, I}$ ) perovskites showing the formation of the valence and conduction bands [92]. b) Density of states (DOS) of MAPI perovskites separated into cation and anion contributions. The MA cation does not introduce states at the band edge [89].

the energy difference between the CBM and the  $\text{Pb}(6p)$  atomic orbital level is not large. The electronic states of the A cation lie far away from VBM and CBM (see Fig. 1.4(b)), thus do not provide any direct electronic contribution near the band edge [89, 91]. We can note that the electronic structure of metal halide perovskites is inverted with respect to conventional covalent semiconductors such as GaAs, where the CBM primarily has  $s$  orbital character, whereas the VBM primarily has  $p$  orbital character. This peculiar electronic structure gives rise to the anomalous band gap behaviour (the band gap energy increases with temperature), the high absorption coefficient and the tolerance towards defects.

In Fig. 1.5 the calculated electronic structures for the cubic phase of MAPI and  $\text{CsPbX}_3$  ( $X = \text{Cl, Br, I}$ ) are shown, taking into account relativistic corrections and spin-orbit interactions. All perovskites show a direct band gap, that, in the cubic phase, is located at the R-point in the first Brillouin zone. Instead, in the low symmetric phases the band gap lies on  $\Gamma$  point [93]. Another feature of the band structure is the parabolic trend of the valence (VB) and the conduction (CB) bands near the band-edge, as shown in Fig. 1.5, with similar dispersion for both the bands. Thus, the band dispersion near the band-edge can be expressed according to the effective mass approximation [94],

$$E(k) = \frac{\hbar^2 k^2}{2m^*} \quad (1.4)$$

where  $\hbar$  is the reduced Planck constant and  $m^*$  is the effective mass of electrons (holes) in the CB (VB) respectively. Calculated and measured effective masses for electrons and holes in MAPI and  $\text{CsPbBr}_3$  perovskites are reported in Tab. 1.3.

We can see that perovskite materials have similar and low values of effective masses for both electrons and holes. As a consequence, the transport is similar in these materials for both carriers. On the contrary, in III-V semiconductors the electron effective mass is much smaller than the hole effective mass due to the different band dispersion; consequently, the mobility is higher for electrons than holes.

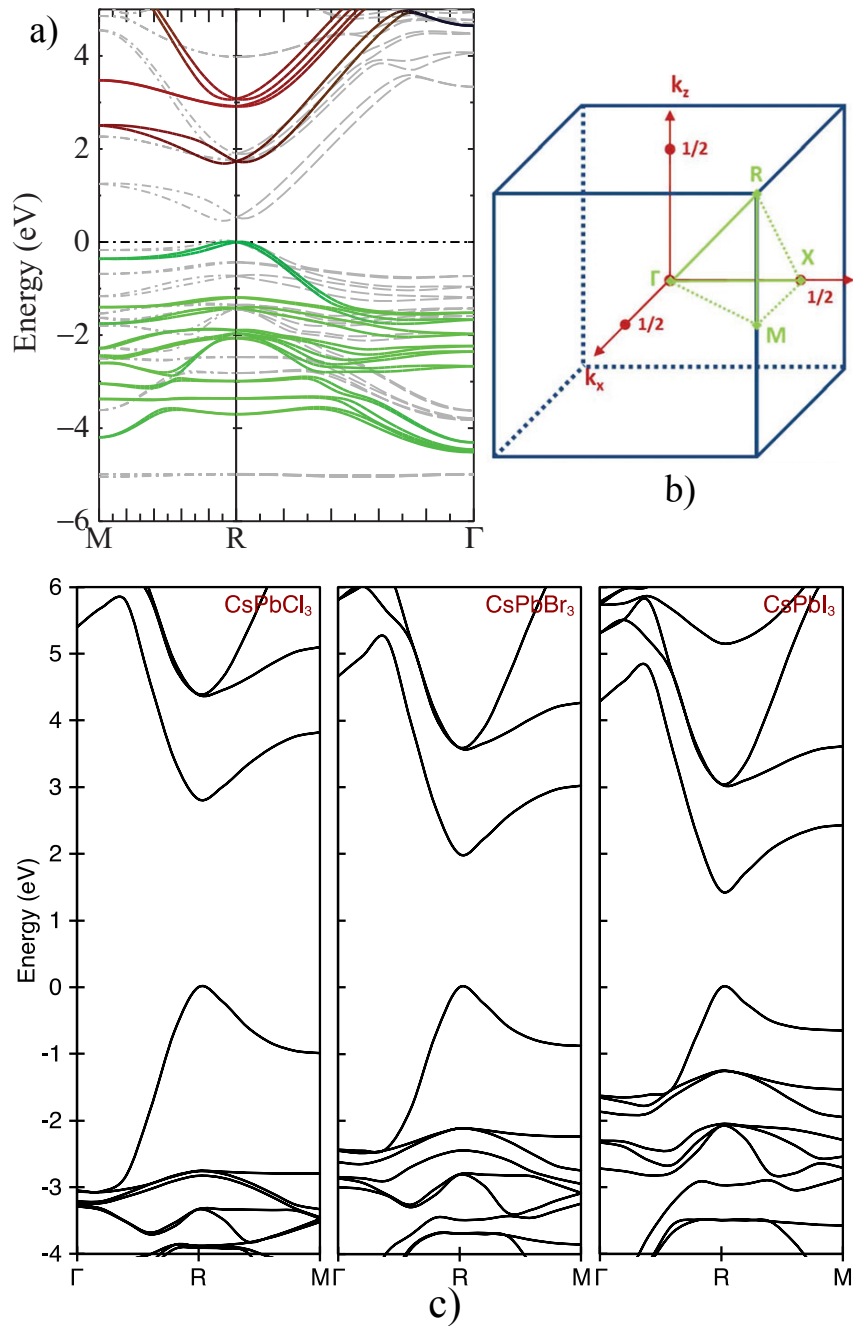


**Figure 1.5:** a) Quasiparticle self-consistent GW (QSGW) electronic band structure calculation for MAPbI<sub>3</sub> perovskites in the cubic phase [91]. b) Schematic representation of the first Brillouin zone (BZ) showing the position of the high symmetry points.  $\Gamma$  denotes the origin of the BZ, X is the center of a square face, M is a center of a cube edge and R are vertices of the cube [95]. c) Density functional theory (DFT) electronic band structure calculation for CsPbX<sub>3</sub> (X = Cl, Br, I) perovskites in the cubic phase [18]. In all graphs the VBM is set to 0 eV.

**Table 1.3:** Calculated and experimentally measured effective mass for electrons ( $m_e^*$ ) and holes ( $m_h^*$ ) in MAPbI<sub>3</sub> and CsPbBr<sub>3</sub> perovskites. The quantities are expressed in unit of the free electron mass  $m_0$ .

Composition	$m_e^*$	$m_h^*$	Technique	Ref.
MAPbI <sub>3</sub>	0.19	0.25	Theo	[83]
	0.12	0.15	Theo	[91]
	0.23	0.29	Theo	[13]
	0.104 <sup>a</sup>		Exp	[14]
CsPbBr <sub>3</sub>	0.15	0.14	Theo	[18]
	0.23	0.23	Theo	[96]
	0.22	0.24	Exp	[12]

Notes: Theo=theoretically calculated, Exp=experimentally measured.

<sup>a</sup> Exciton reduced mass  $1/\mu^* = 1/m_e^* + 1/m_h^*$ .

## 1.2.2 Band gap tunability

### Influence of the composition

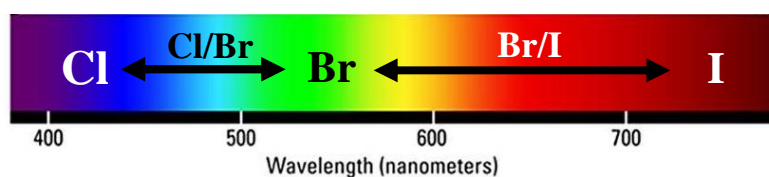
An interesting property of perovskite semiconductors is the easy tunability of the band gap energy by varying the composition and, therefore, it comes the relevance of this materials for tunable light emitter devices. In Tab. 1.4 the band gap values at room temperature for the most common lead halide (APbX<sub>3</sub>, A = FA, MA, Cs ; X = Cl, Br, I) perovskites at room temperature are reported. We can see that the emission energy ranges from the near ultraviolet (NUV) to the near infrared (NIR) depending on the composition.

**Table 1.4:** Band gap values at room temperature for the most common lead halide (APbX<sub>3</sub>) perovskites.

MAPbX <sub>3</sub>		CsPbX <sub>3</sub>		APbI <sub>3</sub>	
I	1.57 eV [37]	I	1.73 eV [37]	Cs	1.73 eV [37]
Br	2.24 eV [95]	Br	2.28 eV [97]	MA	1.57 eV [37]
Cl	2.97 eV [95]	Cl	2.88 eV [97]	FA	1.48 eV [37]

The tunability of the emission is obtained mostly varying the halogen in the X site [18, 85], as shown in Fig. 1.6. Indeed, moving down in the halogen group (Cl → Br → I) the energy of the X(np) orbital increases, with a reduction of the band gap, that is ascribed to the shift of the VBM to higher energy [90] and of the CBM to lower energy [98]. As seen before, also the orbitals of the metal cation determine the electronic band structure; however, the band gap variation that is obtained by varying the metal cation is lower compared to those obtained by changing the halogen. For example, tin (Sn) perovskites have a lower band gap with respect to lead perovskites [43, 98, 99] due to the difference in energy between the Sn(5s) and the Pb(6s) orbitals [83].

Finally, the band gap can be also modified with the choice of A cation, although it has not a direct contribution towards the electronic band structure. Indeed, A cations influence indirectly

**Figure 1.6:** Wavelength tunability of perovskite emission by changing the halogen composition.

the band edge structure via the modification of the bonding strength and the angle between B and X atoms in the  $BX_6$  octahedra depending on their size and/or chemical nature [100, 101]. Larger cations expand the lattice and, mostly, lead to a reduction of the B-X-B angle (equals to  $\theta=180^\circ$  in the cubic structure), lowering the symmetry [101]. Theoretical calculations show that, if  $\theta$  decreases, there is an increment of the antibonding overlap between the B(*ns*) and X(*mp*) atomic orbitals, that produces a shift of the VBM to higher energy [101]. At the same time, there is also a decrease of the energy of the CBM with the overlap, mainly due to the electron transfer from the halogen to the metal cation induced by the change of the chemical composition and crystal structure. Thus, larger A cation cause a reduction of the band gap, as shown in Tab. 1.4 for lead iodide perovskites [37].

Moreover, also the chemical nature of A cation can alter the bonding strength between B and X cations [100]. For example, FAPbI<sub>3</sub> has a smaller band gap [37] with respect to MAPbI<sub>3</sub>, despite the small difference in the cations size (see Tab. 1.1). This behaviour is ascribed to a different interaction between the organic A cation with the inorganic framework. Indeed, the interaction of FA cation with PbI<sub>6</sub> octahedra is stronger than that of MA cation due to a high tendency to form hydrogen bonding (higher number of protons in FA cation) with the iodide anion [100], altering the ionic character of Pb-I bonds. As a consequence, there is a reduction of the B-X-B angle, lowering the symmetry and the band gap. In addition, FAPI has a different crystalline structure at room temperature with respect to MAPbI<sub>3</sub>, although the exact nature is still controversial: hexagonal (yellow phase [99]) or trigonal (black phase [102]).

### Influence of temperature

A peculiar feature of perovskite materials is the increase of the band gap with temperature [103–109], that is opposite to the common behaviour observed in semiconductors [110]. In a semiconductor, the variation of the band gap with temperature is due to two different contributions: the thermal expansion of the lattice, that produces a variation of the electronic levels, and the renormalization of band energies due to electron-phonon interaction [111]. Thus, the temperature dependence of the band gap (at constant pressure) can be written as [111]

$$\left(\frac{\partial E_g}{\partial T}\right)_P = \left(\frac{\partial E_g}{\partial T}\right)_V + \left(\frac{\partial E_g}{\partial \ln V}\right)_P \left(\frac{\partial \ln V}{\partial T}\right)_P, \quad (1.5)$$

where the first term represents the electron-phonon interaction and the second term the thermal expansion;  $\left(\frac{\partial \ln V}{\partial T}\right)_P$  is the volume thermal expansion coefficient. In most semiconductors the contribution of the thermal expansion is negligible with respect to the phonon-interaction and a red-shift of the band gap occurs increasing temperature [112]. On the contrary, in perovskite materials the second term of Eqn. 1.5, that can be either positive or negative depending on the electronic band structure, plays a fundamental role, since the thermal expansion coefficient ( $\approx 10^{-4} \text{ K}^{-1}$  for MAPbI<sub>3</sub> [104]) is much higher compared to other semiconductors, such as silicon ( $7 \cdot 10^{-6} \text{ K}^{-1}$  [113]) or GaAs ( $< 10^{-5} \text{ K}^{-1}$  [114]). Due to the nature of VBM, that, as seen before, is formed by an antibonding mixing between the *s* atomic orbitals of the metal cation and the *p* orbitals of the halogen, in perovskites the term  $\left(\frac{\partial E_g}{\partial \ln V}\right)_P$  is positive [115]. Indeed, as the lattice expands, there is a reduction of the antibonding overlap between the B(*s*) and X(*p*) atomic orbitals, that, as seen before, produces a shift of the VBM to lower energy [101], leading to a



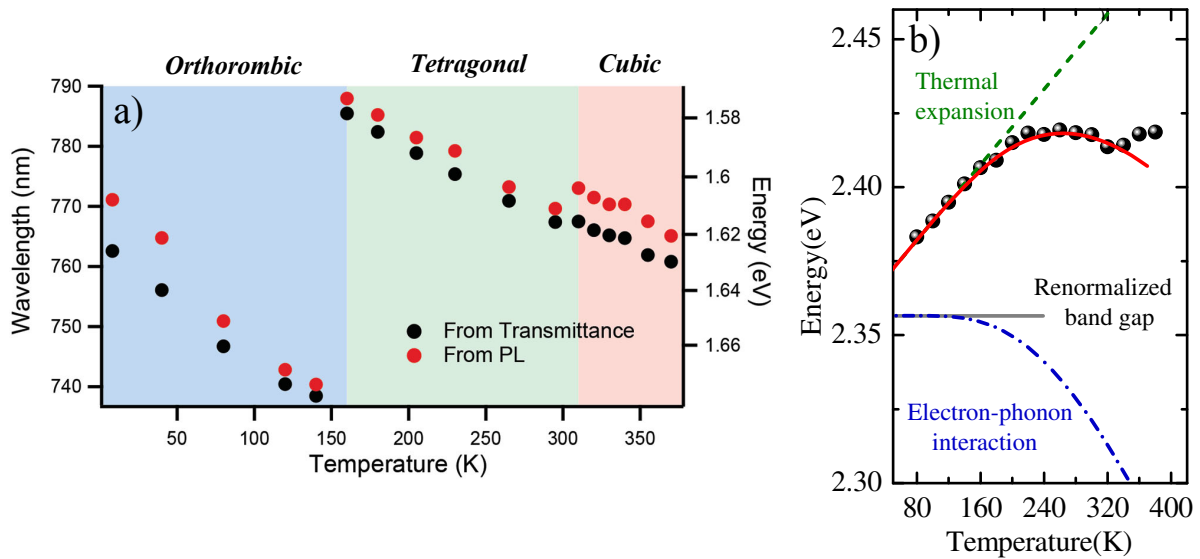


**Figure 1.7:** a) Absorption band-edge wavelength (energy) and PL peak wavelength (energy) of MAPI as a function of temperature, extracted from the transmittance and the PL spectra, respectively [106]. b) PL peak energy as a function of temperature for CsPbBr<sub>3</sub> [109]. Data are fitted with a model that includes a linear thermal expansion term and an harmonic approximation of the electron-phonon interaction. See Ref. [109] for details.

blue shift of the band gap [103].

Increasing temperature, if no transition phases occur (we discuss the influence of the phase transitions in the following paragraph) the electron-phonon term becomes also important, due to the population of optical phonon modes, leading to an increasingly negative contribution. For example in CsPbBr<sub>3</sub> Wei et al. [109] showed a linear blue shift ( $\sim 0.3 \text{ meV K}^{-1}$ ) of the photoluminescence (PL) emission below 220 K, where the thermal expansion contribution dominates, and, at higher temperature, PL peak approaches to a constant value, due to a much higher contribution of the negative electron-phonon term (see Fig. 1.7(b)).

### Influence of phase transitions

In addition to the composition and the temperature, the band gap of perovskites is strongly dependent on the crystalline phase [103, 105, 108, 116, 117]. For example, in MAPI the band gap is higher for the orthorhombic phase with respect to the tetragonal one (Fig. 1.7(a)), that is stable above 160 K (see Tab. 1.2). In both the phases of MAPI the band gap increases with temperature ( $dE_g/dT \approx 0.3 \div 0.5 \text{ meV K}^{-1}$  [105]) and near the transition temperature there is a significant red shift of the band-edge (about 100 meV) in the transmission spectra, that marks the phase change from the orthorhombic to the tetragonal structure. In sec. 1.3 we discuss the behaviour of the PL spectra in MAPI near the phase transition.

### Influence of size

Perovskite materials can be synthesized as thin films or low dimensional structures (nanocrystals (NCs), quantum dots (QDs), nanowires (NWRs), nanoplates (NPs)). In case of nanostructures, the band gap is closely related to the size/shape of the structure, as shown in Fig. 1.8. Decreasing the size of the structure, the emission peak shifts to higher energies due to quantum confinement effects. For example, decreasing the size of CsPbBr<sub>3</sub> NCs from 11.8 nm to 3.8 nm the emission energy increases of about 300 meV [18]. Similar results are found in CsPbBr<sub>3</sub> NWRs [122]. Moreover, also the thickness of the structure strongly influences the optical band gap [118, 119, 123]: decreasing the thickness of CsPbBr<sub>3</sub> NPs from several nanometers to few monolayers

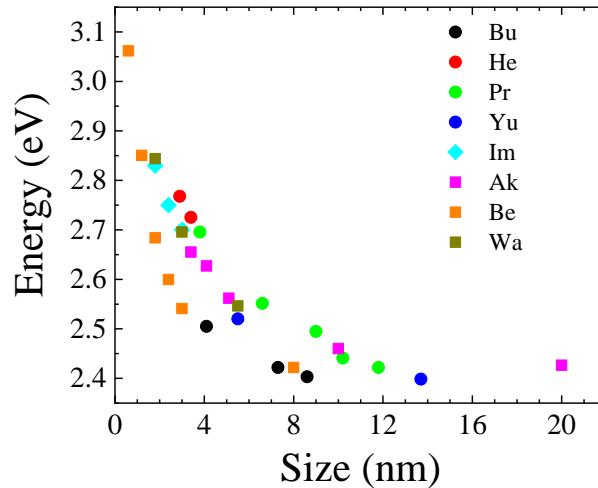


**Figure 1.8:** Emission energy of CsPbBr<sub>3</sub> nanostructures as a function of size. We consider as "size" the diameter for the NCs (○), the width for the NWRs (◇) and the thickness for the NPs (□). The values are obtained from the following references: Ak [118], Be [119], Bu [120], He [121], Im [122], Pr [18], Wa [123] and Yu [124].

(1 ML  $\sim$  0.6 nm) the emission can be tuned from green to near ultraviolet ( $\sim$  400 nm).

### 1.2.3 Electrical properties

In this section we discuss the exceptional electrical properties of perovskite materials, that make them extremely attracting for photovoltaic and optoelectronic applications. The main parameters used to describe the transport of charge carriers in a semiconductor are the diffusion length, the mobility and the lifetime [94].

Diffusion length ( $L$ ), i.e. the average distance that a charge can travel by diffusion before recombination, is used to describe the transport when a gradient of carrier population is present in a semiconductor, for example after light excitation. A long diffusion length is important especially for photovoltaic applications since it affects the photo-carriers collection efficiency. Diffusion length can be calculated from the diffusion coefficient  $D$  and the charge carrier lifetime  $\tau$  via the relation

$$L = (D\tau)^{1/2}. \quad (1.6)$$

Diffusion length is also related to the mobility  $\mu$ , that describes the transport of carriers under the effect of an electric field, via the Einstein relation

$$\mu = \frac{eD}{k_B T} \quad (1.7)$$

Snaith and Grätzel groups [11,125] determined for the first time the diffusion length of electrons and holes in MAPI films with selective quenching layers to collect one type of carriers; they used photoluminescence-quenching (PLQ) and transient absorption (TA) measurements, modelling the charge carrier dynamics by using a diffusion equation. Diffusion lengths exceeding 100 nm were found for both electron and holes, that indicate the ambipolar nature of transport in perovskites, as a consequence of the similar and low effective masses for electrons and holes (see Tab. 1.3). Moreover, Snaith et al. [11] showed that chlorine doping in MAPI perovskites lead to longer diffusion lengths (of about one order of magnitude) compared to pure MAPI, due to an increased PL lifetime, predominantly arising from an inhibition of non-radiative charge recombination centres. Indeed Stewart et al. [126] demonstrated that chlorine inclusion in MAPI

films suppressed the formation of tetraiodoplumbate ( $\text{PbI}_4^{2-}$ ), that is correlated with the density of non-radiative charge recombination centres in the perovskite film.

Thanks to the progress in the synthesis techniques, diffusion lengths above 1  $\mu\text{m}$  are achieved in MAPI perovskite films [127, 128] and up to 175  $\mu\text{m}$  in MAPI single crystals [9]. For  $\text{CsPbBr}_3$ , diffusion length values were obtained mainly from the mobility, through Eqn. 1.7: values of about 10  $\mu\text{m}$  are reported for both NCs and single crystals (see Tab. 1.5).

The electrical mobility in perovskites has been measured using several techniques: time-of-flight [9, 136], Hall effect [9, 10, 99] and photoconductivity [96, 134] measurements, time resolved Terahertz (THz) spectroscopy [12, 106, 129, 131], space-charge-limited current [9, 10, 15, 133, 135]. As shown in Tab. 1.5, the electrical mobility is of about  $10 \div 100 \text{ cm}^2 \text{ V s}^{-1}$  in MAPI films for both electrons and holes, that is comparable to those of crystalline inorganic semiconductors [137]. Temperature dependent THz spectroscopy measurements [106] in MAPI films showed that the electrical mobility follows a  $T^{-3/2}$  dependence, which implies that the charge transport is limited by the scattering with phonons [94]. The mobility can be improved by A-site substitution: for example Cs-based perovskites show an higher mobility compare to MA perovskites (see Tab. 1.5).

**Table 1.5:** Measured values for the electrical parameters of MAPI and  $\text{CsPbBr}_3$  perovskites.

Composition	Type	$\mu_e$ ( $\text{cm}^2/\text{Vs}$ )	$\mu_h$ ( $\text{cm}^2/\text{Vs}$ )	$L_e$ ( $\mu\text{m}$ )	$L_h$ ( $\mu\text{m}$ )	Technique(s)	Ref.
MAPI	Film	–	–	$\sim 0.13^d$	$0.09^d$	PLQ	[125]
	Film	–	–	$\sim 0.13^d$	$0.11^d$	PLQ,TA	[11]
	Film	–	–	$1^d$	$\sim 1^d$	TRTS	[128]
	Film	–	–	$1.2^d$	$\sim 1.2^d$	TA	[127]
	Film	$8.1^\Sigma$	$8.1^\Sigma$	–	–	TRTS	[129]
	Film	12.5 (2)	7.5 (1)	–	–	TRTS (TRMC)	[130]
	Film	$27^\Sigma$	$27^\Sigma$	–	–	TRTS	[131]
	Film	$35^\Sigma$	$35^\Sigma$	–	–	TRTS	[106]
	Film	66	–	–	–	HALL	[99]
	SC	$2.5^\Sigma$	$2.5^\Sigma$	–	–	SCLC	[15]
	SC	3	17	–	–	TRMC	[132]
	SC	24	$67^\Sigma$	$9.7^m$	$9.7^m$	SCLC	[133]
	SC	$67^\Sigma$	164 (105)	–	$175^m$	ToF,SCLC,IS,(HALL)	[9]
$\text{CsPbBr}_3$	SC	–	143	–	–	PHC, PL	[134]
	SC	1000	–	–	–	PHC,PL	[96]
	SC	–	–	$5.5^m$	$2.5^m$	SCLC, PL	[135]
	SC	2300	2060	$10.9^m$	$9.5^m$	HALL,ToF, SCLC, PL	[10]
	NCs	$4500^\Sigma$	$4500^\Sigma$	$9.2^m$	$9.2^m$	TRTS, PL	[12]

**Techniques:**

HALL=Hall effect measurements, TRTS=time-resolved terahertz spectroscopy, ToF=time-of-flight,

TRMC=time-resolved microwave conductivity, SCLC=Space-charge-limited current, PHC=photoconductivity,

PLQ=photoluminescence quenching, TA=transient absorption, IS=impedance spectroscopy.

**Notes:**

SC=single crystal, NCs=Nanocrystals.

<sup>m</sup> Diffusion length extracted from mobility via the Eqn. 1.7.

<sup>d</sup> Diffusion length calculated through the Eqn. 1.6.

<sup>Σ</sup> Electron–hole sum mobility.

## 1.3 Optical properties

### 1.3.1 Absorption

Another important property of perovskites is the very high optical absorption coefficient: for MAPI is of about  $10^4 \div 10^5 \text{ cm}^{-1}$  in the visible range [6, 7]. In Fig. 1.9(a) the absorption coefficient of MAPI is compared with other photovoltaic materials. We can see that the absorption of crystalline silicon (*c*-Si) is lower and less steeper around the band edge with respect to MAPI and GaAs because of the indirect band gap nature of Si. MAPI has a comparable and even higher absorption coefficient with respect to GaAs [8] in the visible spectral range.

The optical absorption of a semiconductor at an energy  $\hbar\omega$  depends to the transition matrix from states in the VB to states in the CB and to the joint density of states (JDOS) [94]. The transition matrix measures the probability of each transition, the JDOS the number of possible transition at a the energy  $\hbar\omega$ . The transition matrix near the absorption edge are similar for MAPI and GaAs [8], but the joint density of states (JDOS) is remarkably different for the two semiconductors since they have different electronic structures, as discussed in sec. 1.2.1. As seen before, the lower part of the MAPI CB is mainly composed by the Pb(6*p*) states, whereas the lower part of the GaAs CB is composed by *s* orbitals. Since the atomic *p* states have more orbitals than the *s* states and exhibit less dispersion, the JDOS in the lower part of the CBM is significantly higher for MAPI perovskites [8]. Therefore, the high absorption coefficient of perovskites is due to the direct halide-*p*  $\rightarrow$  metal-*p* transition at the band edge. The very high absorption coefficient made possible to achieve photovoltaic conversion efficiency (PCE) above 20% [22] by using thin perovskites absorbers ( $\sim 500 \text{ nm}$ ) in solar cells. For comparison, the typical thicknesses of silicon and thin film solar cells are of about tens of microns and  $2 \mu\text{m}$ , respectively [20].

Another important features of the optical absorption is the exponential tail (Urbach tail) below the band gap ( $\alpha(E) \propto e^{-E/E_U}$ ,  $E_U$  Urbach tail energy), as shown in Fig. 1.9(a). This tail arises from disorder and/or impurities, producing exponentially decaying subgap states [138].

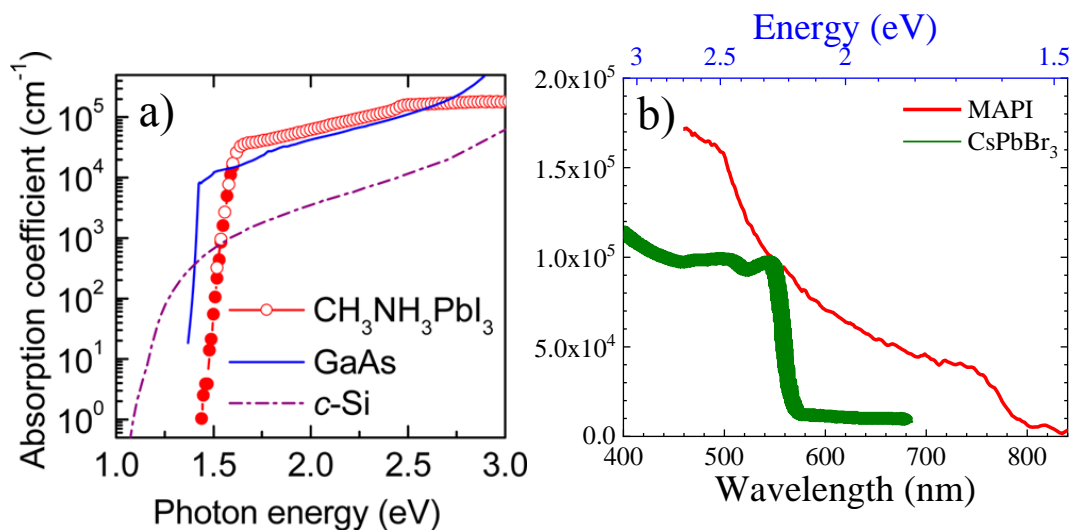


**Figure 1.9:** a) Absorption coefficient of a MAPI thin film compared with other typical photovoltaic materials, all measured at room temperature [6]. b) Absorption spectra at room temperature of a MAPI film [6] and of a CsPbBr<sub>3</sub> bulk crystal [10].

In MAPI film the Urbach tail energy reaches a low values of about 15 meV [6] at room temperature, which is close to the values of GaAs and *c*-Si. To conclude this paragraph, in Fig. 1.9(b) absorption spectra of MAPI and CsPbBr<sub>3</sub> perovskites at room temperature are compared.

### 1.3.2 Emission properties

In this section we discuss the emission properties of MAPI and CsPbBr<sub>3</sub>.

#### Interplay between excitons and free carriers

In a semiconductor, the Coulomb interaction between an electron and an hole can produce a bound state called exciton. Excitons can easily dissociate into free carriers when their binding energy is smaller than the thermal energy; otherwise, the emission and transport properties of the material are driven by bound electron-hole pairs. Given the analogy of the exciton with an hydrogen atom, the exciton binding energy ( $E_x$ ) of a bulk semiconductor is given by

$$E_x = \frac{\mu^*/m_0}{\epsilon^2} R_y, \quad 1/\mu^* = 1/m_e^* + 1/m_h^*, \quad (1.8)$$

where  $\mu^*$  is the exciton effective mass,  $m_0$  the free electron mass,  $\epsilon$  the dielectric constant of the material and  $R_y$  the hydrogen Rydberg constant ( $R_y = 13.6$  eV).

A knowledge of the elementary photoexcited species is crucial for the material applications. A solar cell needs free photoexcited carriers, since electrons and holes must be separated and collected to generate a photo-current. On the contrary, materials with high exciton binding energy are more suitable for light sources, given the fast recombination rates and high emission quantum yields. In hybrid organic-inorganic perovskites, it is still debated if the emission properties arise from excitons or free carriers. For MAPI, a wide range of values for  $E_x$  are reported (2 ÷ 50 meV) at room temperature using magnetoabsorption [14], optical absorption [139–142] and PL measurements [143, 144], as shown in Tab. 1.6.

Absorption spectra at room temperature show the influence of the excitonic states at the band-edge; conversely, power dependent PL measurements in a wide range of excitation den-

**Table 1.6:** Calculated and experimentally measured values for exciton binding energy in MAPI and CsPbBr<sub>3</sub> perovskites.

Composition	$E_x$ (meV)	Technique(s)	Ref.
MAPI	12	Magnetoabsorption	[14]
	2 <sup>a</sup>	CELIV	[145]
	6	Absorption	[139]
	9	Absorption	[146]
	29	Absorption	[140]
	25	Absorption	[141]
	5	Absorption	[142]
	45	PL	[143]
	19	PL	[144]
CsPbBr <sub>3</sub>	37	Reflectivity	[147]
	38	Absorption	[18]
	40	Theor.	[145]

**Notes:**

CELIV = Charge carrier extraction by linearly increasing voltage.

<sup>a</sup>Value calculated using  $\epsilon_s$ . Theor. = Theoretically calculated.

sity suggest that the radiative recombination occurs mainly from free electrons and holes [148]. Moreover, the exciton binding energy in MAPI is dependent on the temperature and the crystalline phase [139] due to a variation of the dielectric constant [79, 142]. Indeed the dielectric constant of MAPI is frequency dependent and different values are reported for the two phases, especially in the low frequency range. The high-frequency (or optical) dielectric constant ( $\epsilon_\infty$ ) is comparable for the two phases ( $\epsilon_\infty \sim 6.5$  [88, 142, 149]). On the contrary, the static ( $\epsilon_s$ ) dielectric constant value is about 36 in the orthorhombic phase [150] and about 60-70 at room temperature [145, 150]. The increase of the low-frequency dielectric constant at room temperature is attributed to the dynamic disorder of MA ion dipole [79, 142, 150]. In the high temperature phase, MA cations undergo rotations around the C-N axis, that contribute to the dielectric response.

For all-inorganic CsPbBr<sub>3</sub> perovskites, there is an agreement between theory [18] and experimental results [68, 147] about the exciton binding energy and values of about 35-40 meV are reported. Most of the works that investigate the emission properties in CsPbBr<sub>3</sub> perovskites attribute the recombination to excitons [58, 151–153], especially in NCs, given the greater overlap between electron and hole wavefunction due to the charge carriers quantum confinement.

### Recombination processes

In perovskites, charge-carrier recombination can be described with the following rate equation [106, 141]

$$\frac{dn}{dt} = -k_1n - k_2n^2 - k_3n^3, \quad (1.9)$$

where  $n$  is the carrier concentration and the three terms on the right side account for monomolecular ( $k_1n$ ), bimolecular ( $k_2n^2$ ) and three-body Auger ( $k_3n^3$ ) recombination processes, respectively. In this equation we consider an intrinsic semiconductor ( $n = p$ ), where  $n$  and  $p$  are the electrons and holes concentrations, respectively. Monomolecular term, that involves one charge at a time, is associated with trap-mediated charge recombination or exciton recombination. Bimolecular term is associated with the radiative recombination of electron-hole pair or exciton-exciton annihilation. Finally, Auger recombination is a three non-radiative particles process that becomes important at high excitation density. In this process, an electron-hole pair recombines non radiatively and the energy released during the recombination is transferred to a third particle.

In MAPI, recombination dynamics have been investigated in a broad range of photo-carrier density in order to explore the different processes [106, 129, 141, 154]. At low excitation density ( $n < 10^{17} \text{ cm}^{-3}$  [141, 154]), where trap states are not filled, trap-assisted recombination dominates. Monomolecular rate constant ( $k_1$ ) is of about  $10^7 \text{ s}^{-1}$  at room temperature [106, 129] and decreases with temperature, suggesting a charge recombination process assisted by ionized impurities [106]. In this regime, the intensity grows with a power law  $P_{exc}^{1.5}$  if only one carrier is trapped and with a power law  $P_{exc}^2$  if both carriers are trapped [154]. When the bimolecular recombination becomes important, in absence of non-radiative channels, the intensity grows linearly with the excitation power since  $I_{em} \propto n^2 \propto P$  [141]. Bimolecular rate constant is of about  $10^{10} \text{ cm}^{-3} \text{ s}^{-1}$  for MAPI at room temperature [106, 129] and increases decreasing the temperature. Finally, Auger recombination becomes important at excitation density



above  $10^{18} \text{ cm}^{-3}$  [141]; in this regime the PL intensity increases sublinearly with the excitation power [141]. Auger recombination constant is of about  $10^{28}$ - $10^{29} \text{ cm}^6 \text{ s}^{-1}$  at room temperature and is strongly dependent to the crystalline phase [106].

For  $\text{CsPbBr}_3$ , whose excited-state populations are primarily excitons, when defect trapping is negligible, at low power ( $< \mu\text{J}/\text{cm}^2$ ) dominates single-exciton radiative recombination, as evidenced by the monoexponential decay and the linear dependence of the PL intensity on the excitation power [151–153]. At higher density, multiexcitonic recombination processes can take place also in  $\text{CsPbBr}_3$ . Wei et al. [152], under high carrier density ( $> 10^{15} \text{ cm}^{-3}$ ), showed that reciprocal of the carrier density had a linear dependence on time in the first  $\sim 60 \text{ ps}$  after the excitation, that indicates a two-body recombination process<sup>2</sup>. Wei et al. ascribed this trend to the exciton-exciton annihilation, that is a two excitons interaction process where one exciton recombines and the other either dissociates into a free electron-hole pair or is promoted into a higher energy level. An exciton-exciton annihilation rate of  $7.0 \cdot 10^{-7} \text{ cm}^3 \text{ s}^{-1}$  was reported by Wei et al. Other groups [151, 153] attributed the multi-exponential decay under high excitation density to the biexciton non-radiative Auger recombination, with a rate constant  $k_3$  of about  $10^{-29}$ - $10^{-30} \text{ cm}^6 \text{ s}^{-1}$ .

Finally, if the contribution of traps is not negligible, also at low power multiexponential decays are observed and the slow component is related to the trap dynamics [155]. In particular, given the large ratio between surface states and volume states, in  $\text{CsPbBr}_3$  NCs surface states strongly influence the recombination dynamics since can efficiently capture charge carriers, that can be released by thermal activation. We will discuss in Chap. 7 how surface states affect the recombination dynamic in  $\text{CsPbBr}_3$  NCs.

### PL emission from MAPI

As seen previously, MAPI undergoes two phase transitions: from the orthorhombic to the tetragonal phase ( $T \sim 160 \text{ K}$ ) and from the tetragonal to the cubic phase ( $T \sim 330 \text{ K}$ ). The crystalline phase strongly influences the PL emission properties in these materials.

At low-temperature, PL spectra in MAPI typically show two emission bands (Fig. 1.10(a)), whose weight depends to the excitation conditions. The high energy band, at about  $1.65 \text{ eV}$ , is ascribed to the radiative recombination from the orthorhombic phase of MAPI.

Instead, the origin of the low energy band is debated in the literature and it is ascribed to different contributions:

- the radiative emission from residual tetragonal inclusions in the orthorhombic phase of MAPI, that are maintained below the phase transition [108, 156, 157]. Given the smaller band gap with respect to the orthorhombic phase, tetragonal domains can trap carriers, that eventually recombine within these inclusions [156, 157];
- the radiative recombination from localized states, that are ascribed to radiative traps [105, 116, 158] or, very recently, to methylammonium-disordered domains in orthorhombic phase of MAPI [103].

We want to remark that, in both interpretations of the low energy side emission as radiative traps or disordered domains, a carrier localization is present. More relevant is the fact that the

---

<sup>2</sup>If  $n \propto 1/t \rightarrow dn/dt \propto -n^2$ .

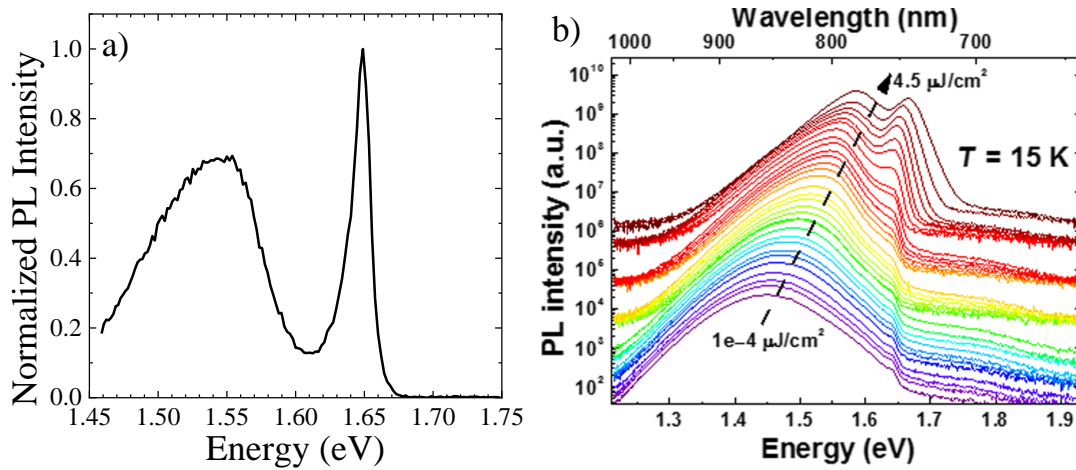


**Figure 1.10:** a) Normalized PL spectra of a MAPI film at 10 K under pulsed excitation at 600 nm, with an average intensity of 10 W/cm<sup>2</sup>. b) Power dependent PL spectra of a MAPI film at 15 K under pulsed excitation at 425 nm [103].

low energy states are radiative and do not produce a loss of photogenerated carriers. Increasing the excitation power (see Fig. 1.10(b)), the low energy band blue shifts and its weight becomes less important with respect to the orthorhombic phase emission: this trend is due to the filling of the localized states and/or the tetragonal domains [103,105,116].

Increasing the temperature (Fig. 1.11(a)), the orthorhombic phase emission blue shifts, as expected, due to the increase of the band gap with the temperature in perovskites (see sec. 1.2.2). This emission disappears above 150 K, where the phase transition of MAPI from the orthorhombic to the tetragonal phase occurs. Concerning the low energy band, a complex behaviour is observed, especially near the phase transition. First of all, a reduction of the full width at half maximum (FWHM) is observed increasing temperature up to 150 K (Fig. 1.11(b)) due to a lower contribution of the emission from radiative traps as the temperature raises. Moreover, the low energy band shows an S shape in the peak emission energy (Fig. 1.11(a)). Finally, the spectrally integrated PL intensity has an enhancement around the phase transition (Fig. 1.11(c)). The complex behaviour of the peak energy of the low energy band and of the PL intensity near the phase transition was explained recently by Dobrovolsky et al. [108]. They assumed that the transition into the tetragonal phase develops starting from MAPI regions with lower concentra-

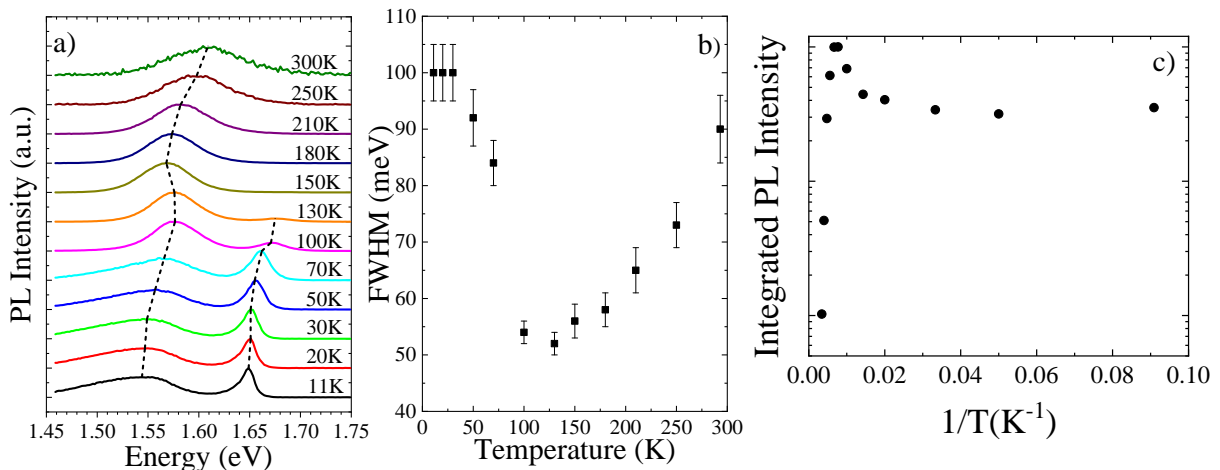


**Figure 1.11:** a) Normalized PL spectra of a MAPI film as a function of temperature. b) FWHM of the low energy band as a function of temperature. c) Spectrally integrated PL intensity as a function of temperature.

tion of defects, while the regions with more defects remain in the orthorhombic phase. Because the tetragonal phase has a lower energy gap, charge carriers can migrate into the tetragonal domains. Therefore, the PL enhancement is due to an increase of the PL intensity from the tetragonal phase domains, that have lower defects (so the radiative emission is expected to be higher). On the contrary, the red shift is related to an increase of the tetragonal domains sizes, that emit at lower energies.

Above 160 K, PL spectra show a single band, that arises from the radiative recombination in the tetragonal phase of MAPI. The emission energy of this band monotonically blue shifts rising the temperature, with the same trend of the absorption spectra. At about 327 K, well within the operative temperature range of a solar cell, the tetragonal-to-cubic phase transition occurs. However, across the tetragonal-to-cubic phase transition, Quarti et al. [159] did not observe any abrupt change of the band-gap, that rather monotonically blue shifts following the same temperature evolution observed in the tetragonal phase. In addition, Zhang et al. [160] showed that the photovoltaic parameters of MAPI-based solar cells do not change dramatically across the tetragonal-to-cubic phase transition.

### PL emission from CsPbBr<sub>3</sub>

Given the tolerance towards defects (see sec. 1.4) and the direct band gap, CsPbX<sub>3</sub> NCs exhibit very bright emission at room temperature, even without any surface passivation: PL quantum yield (PLQY), i.e. the number of photons emitted for photon absorbed, reaches value of 90 % for CsPbBr<sub>3</sub> NCs [18,56,58]. Through post synthesis surface passivation, the PLQY in CsPbBr<sub>3</sub> NCs approaches unity [155, 161]. In addition, all-inorganic CsPbX<sub>3</sub> NCs show narrow PL emission (FWHM  $\sim 10 \div 40$  nm, see Fig. 1.12(d)) at room temperature irrespective of their size [18,56,57]. These features make CsPbX<sub>3</sub> perovskites attractive for light-emitting applications. By comparison, traditional organic and inorganic QD emitters show broader spectra (FWHM  $> 30$  nm) and as-grown QDs without surface passivation typically exhibit low PLQY ( $< 20\%$ ) due to the high concentration of defects, that act as non-radiative recombination centres.

At low temperature, several groups showed the exciton fine structure in CsPbBr<sub>3</sub> NCs, that cannot be resolved at room temperature due to the homogeneous broadening [162, 163]. Three narrow PL lines (FWHM  $< 1$  meV) with well-defined polarization, whose separation is less than 1 meV, was observed in CsPbBr<sub>3</sub> NCs (Fig. 1.12(a-b)): these three peaks were ascribed to three bright excitonic states. We can see that the higher and the lower energy lines have linear and orthogonal polarizations in zero field (Fig. 1.12(a)) and they become circularly polarized with opposite helicities under applied magnetic field (Fig. 1.12(b)). The central line has no clear polarization. A scheme of the exciton fine structure is shown in Fig. 1.12(c); the polarization of each line is also reported. The exciton fine structure in the orthorhombic phase of CsPbBr<sub>3</sub> was also calculated theoretically [164], confirming the presence of a bright triplet state as lower exciton state. This fine structure is remarkably different of what happens in the most common inorganic semiconductors, where the lower exciton state is a “dark exciton”, meaning that optical transitions to the ground state are dipole-forbidden. The consequence of the bright character of the lowest exciton is the faster emission rate of CsPbBr<sub>3</sub> NCs with respect to other semiconductors, both at room than at cryogenic temperature.

Increasing the temperature, PL spectra in CsPbBr<sub>3</sub> show a broadening and a blue shift

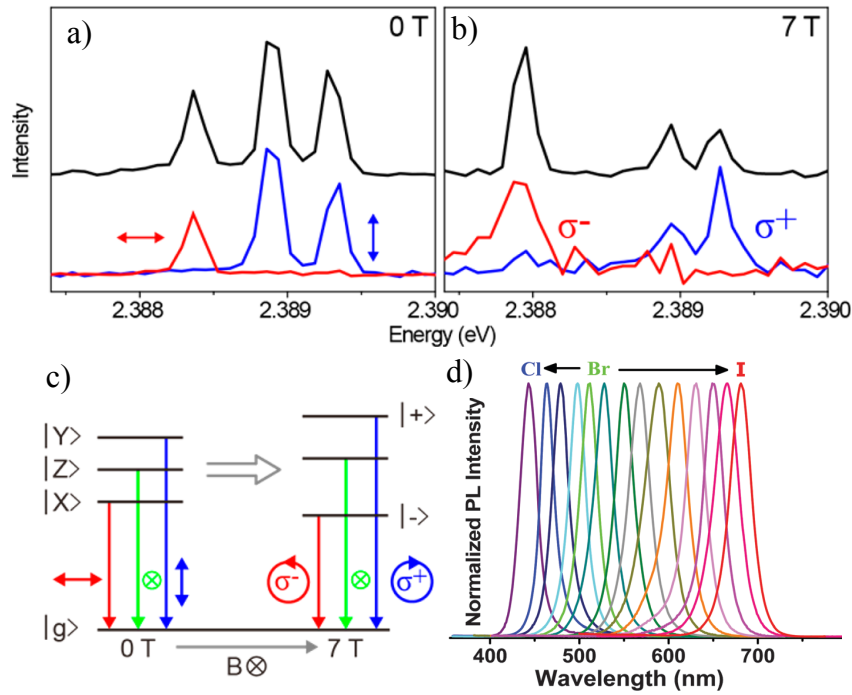


**Figure 1.12:** a-b) Polarization analysis of the exciton fine structure of a CsPbBr<sub>3</sub> NCs at 10 K [162]. The black lines correspond to the PL spectra at zero magnetic field (a) and at 7 T (b), respectively. At 0 T,  $\leftrightarrow$  and  $\updownarrow$  indicate the horizontal and vertical linear polarizations, respectively. At 7 T,  $\sigma^-$  and  $\sigma^+$  indicate the anticlockwise and clockwise circular polarizations, respectively. c) Scheme of Zeeman splitting and polarization properties of the bright exciton triplet in CsPbBr<sub>3</sub>. The symbol  $\otimes$  indicates absence of polarization. d) PL spectra at room temperature of CsPbX<sub>3</sub> NCs. The linewidths of these spectra range from 12 nm to 34 nm.

of the emission due to the increase of the band gap with the temperature [107, 109]. The blue shift occurs until the thermal expansion term dominates with respect to the electron-phonon term (see Eqn. 1.5). After that, due to the population of optical phonon, the PL peak approaches to a constant value, as discussed in sec. 1.2.2. Furthermore, CsPbBr<sub>3</sub> NCs show temperature-independent optical band gap at temperatures higher than room temperature, due to the combination of several effects (thermal expansion, electron-photon interaction, phase transition between the orthorhombic and the tetragonal phase). More precisely, Wei et al. [109] showed that the PL emission energy slightly decrease between room temperature and 340 K (electron-photon interaction) and then increases from 340 to 380 K (phase transition), but the variation of the PL peak in this range of temperature is less than 1 nm (see Fig. 1.7(b)). The temperature-independent chromaticity is very important for the application of CsPbBr<sub>3</sub> in light-emitting sources, since LEDs often heat up during prolonged operation.

## 1.4 Defects

In this section we discuss the main kind of defects present in MAPI and CsPbBr<sub>3</sub> perovskites, that are crucial to determine the performance of optoelectronic devices since defects affect the electrical and optical properties of the material. Impurities and defects in semiconductors create localized states that can be located either in the band gap or in the continuum of the valence/conduction band. If a localized state lies in the middle of the band gap the defect is deep, otherwise, if it is close to the band edge, the defect is shallow. Shallow levels may donate carriers into the CB or VB; on the contrary, deep defects usually act as non-radiative

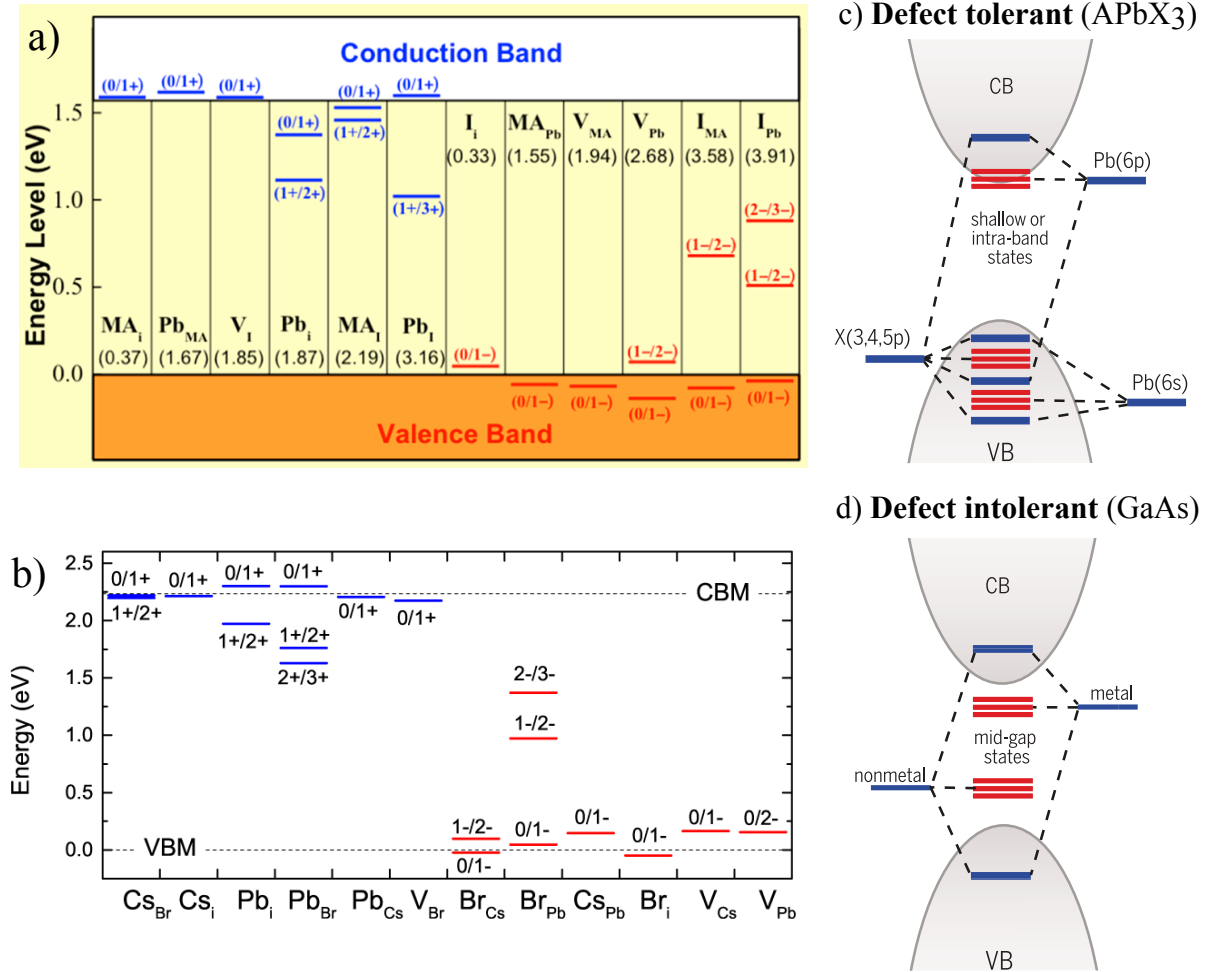


**Figure 1.13:** On the left: energy levels of the intrinsic point defects in MAPI (a) and CsPbBr<sub>3</sub> (b) perovskites: V<sub>α</sub> indicates a vacancy of the ion α, I<sub>α</sub> an interstitial defect of the ion α, Y<sub>Z</sub> an antisite substitution of the ion Y with the ion Z. Zero in energy is referred to the VBM [16, 165]. On the right: electronic structure of defect-tolerant (c) and defect-intolerant (d) semiconductors [166].

recombination centres.

Defects in perovskites are mainly investigated with theoretical calculations [16, 17, 165]. In Fig. 1.13(a) and Fig. 1.13(b) the calculated transition energy levels of the intrinsic point defects (vacancies, interstitial, antisite substitution) in MAPI and CsPbBr<sub>3</sub> perovskites are reported.

We can see that all cation/anion vacancies form shallow or intra-band defects and that only few interstitial defects (Pb<sub>i</sub>) and antisite substitution (Pb<sub>X</sub>, X<sub>Pb</sub>, MA<sub>I</sub>, I<sub>MA</sub>) produce deep transition levels. Wang [17] and Yang [16] groups also calculated the formation energy of these defects, i.e. the difference in the total crystal energy before and after the defect arises. They showed that all deep defects in MAPI and CsPbBr<sub>3</sub> have high formation energies, thus their concentration is expected to be very low. Beside that, Kim et al. [165] calculated the energy level of neutral defects in MAPI perovskites: Schottky (equal number of positive and negative vacancies) and Frenkel (equal number of vacancies and interstitial of the same ion). They showed that those defect pairs do not create any deep gap state.

As regards the surface states, Haruyama et al. [167] investigated the structural electronic properties of PbI<sub>2</sub> and MAI surface termination in MAPI perovskites: calculations showed that no deep levels are formed. Moreover, Infante et al. investigated how the surface termination

affects the electronic structure in CsPbX<sub>3</sub> NCs, including the ligands typically employed during their synthesis (see sec.2.2). They showed that deep states are still absent and the electronic structure remains substantially unchanged.

In polycrystalline semiconductors, also grain boundaries (GBs) can create deep gap levels and are detrimental for solar cells. Instead, in MAPI perovskites, GBs contain mainly Pb and I dangling bonds, Pb-I-Pb wrong bond and PbI<sub>2</sub> extra bond, that do not generate any mid gap states [16]. Therefore, in perovskites GBs are intrinsically electrically benign.

This “defect tolerant” behaviour of halide perovskite materials is closely related to their electronic structure (Fig. 1.13(c)), that originate from the high ionicity and the strong Pb(6*p*)-X(*ns*) antibonding coupling [16,17], as discussed in sec.1.2.1. We consider for example a cation/anion vacancy in MAPI perovskites (the same explanation is also valid for CsPbBr<sub>3</sub>). When an I<sup>-</sup> vacancy is formed in MAPI, the defect state is composed by the Pb<sup>2+</sup> anion dangling bond surrounding the I<sup>-</sup> vacancy. Therefore, a donor defect state is formed, that lie between the Pb(6*p*) orbital and the CBM. Since the difference between the Pb(6*p*) orbital and the CBM is small due to the ionicity of halide perovskites (see sec.1.2.1), this vacancy produces a shallow donor state close to the CBM. Instead, in case of a Pb<sup>2+</sup> vacancy, a shallow acceptor vacancy level is formed below the VBM, since the I(5*p*) atomic orbital level is below the VBM. On the contrary, in the most common covalent semiconductors (GaAs, GaN, CdSe), that are “defect intolerant”, the atomic orbitals lie within the band gap, thus mostly defects create mid gap states (see Fig. 1.13(d)). The consequences of this tolerance towards defects are the low non-radiative recombination of perovskites and the high performance of perovskite-based devices, even without any defects passivation.



## §2§ Synthesis techniques and material stability

In this chapter we describe the main techniques used to synthesize MAPI and CsPbBr<sub>3</sub>. Moreover, we discuss the problem of the chemical stability of these materials.

### 2.1 Synthesis of MAPI

Hybrid organic-inorganic perovskites, such as MAPI, can be synthesized using different techniques depending on the type of structure (thin film or nanostructures) that we are interested to realize. In Fig. 2.1 a photograph of a MAPI film and a scanning electron microscopy (SEM) image of MAPI nanostructures are reported.

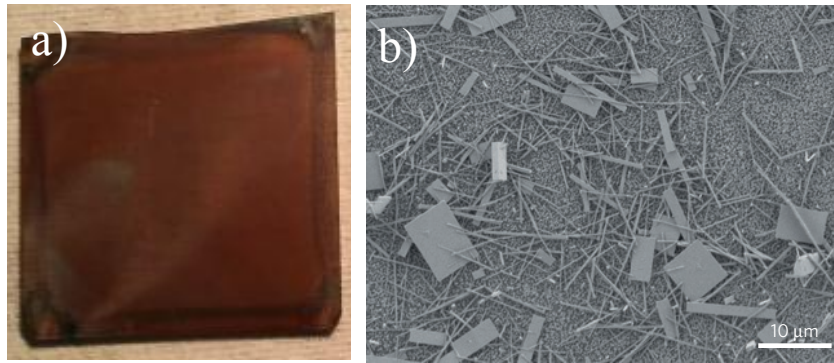


**Figure 2.1:** a) Photograph of a MAPI film [38]. b) SEM image of MAPI nanostructures [66].

#### Film

Hybrid perovskite films can be fabricated by either solution or vapour deposition methods, as shown in Fig. 2.2. In vapour deposition process, perovskite films are synthesized under vacuum condition ( $10^{-5}$  mbar) [168–171]. The two precursors (MAI and PbI<sub>2</sub>) can be co-evaporated simultaneously from two separate sources (Fig. 2.2(a)) on the substrate or deposited in a two step sequence (Fig. 2.2(b)). In the second case, inorganic PbI<sub>2</sub> film is deposited by spin-coating and subsequently exposed to organic vapours of MAI [169–171]. In both cases, after the deposition, the film is annealed at about 100 °C to enable the full crystallization of the perovskite. We will discuss in sec. 2.3.1 how the annealing temperature influences the quality of the perovskite film.

Solution deposition methods are more extensively used to produce perovskite films due to the lower cost with respect to vapour-deposition processes [172–177]. Again, the deposition of a perovskite film can occur in a single-step (Fig. 2.2(c)) or in two steps (Fig. 2.2(d)). In the first case, a solution of the two precursors is prepared by dissolving them in a highly polar solvent (*N,N*-dimethylformamide (DMF), Dimethylacetamide (DMA), dimethyl sulfoxide (DMSO)). The as prepared solution is then spin-coated onto the substrate. In the double-step method, PbI<sub>2</sub> dissolved in DMF is firstly spin-coated onto the substrate and subsequently transformed into the perovskite by exposing it to a solution of MAI in isopropanol (IPA). In both cases, the film is annealed after the deposition.

In the one-step method, the main problem comes from the poor solubility of PbI<sub>2</sub> in DMF solvent that leads to a non-uniform perovskite layer, whereas after the two-step deposition

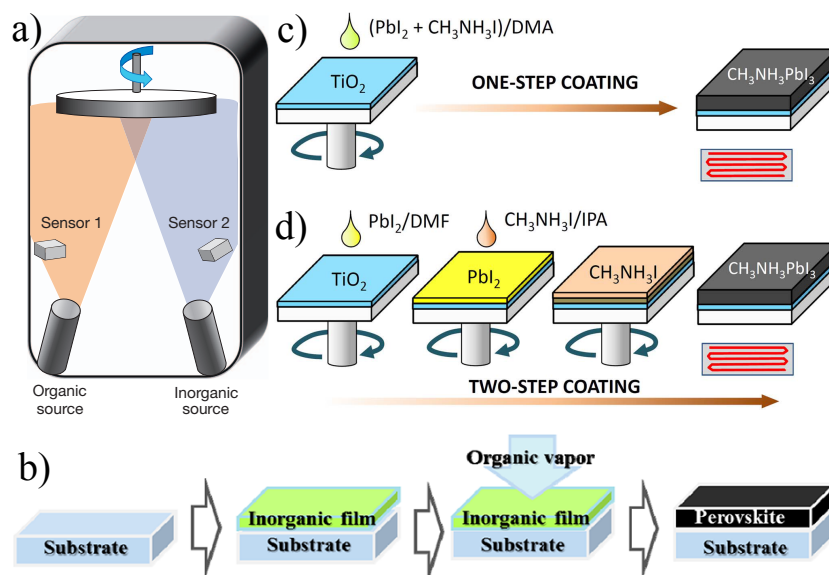


**Figure 2.2:** Schematic illustration of the most common deposition methods of hybrid perovskites films: a) Dual-source vapour deposition. b) Vapour-assisted deposition. c) One-step solution deposition. d) Two-step solution deposition. [168, 171, 172]

a more uniform film is obtained. Moreover, perovskite solar cells (PSCs) with MAPI layer synthesized by two-step deposition exhibit better photovoltaic performances. In order to improve the crystallization, Xiao et al. [174] proposed a one-step deposition method followed immediately by exposure of the wet film to a second solvent (chlorobenzene) to induce crystallization during the spin-coating (fast crystallization process). They obtained a highly uniform perovskite film with respect to the conventional one-step deposition. Alternatively, other groups report a slow crystallization process [175–177] that, however, increases the deposition times.

For the synthesis of MAPI film, also the substrate plays a fundamental role. Indeed, the properties of the substrate (wettability, roughness) strongly influence the morphology, the structural and the interfacial properties of MAPI films [178–182]. Bi et al. [181] investigated the morphology of MAPI film grew on a wide range of substrates. They showed that, as the wettability of the substrate decreases, the grain size of the perovskite film increases. Active materials with larger grains are preferable in solar cells to have a faster carrier transport. Moreover, the type of substrate (p-type, n-type, insulating) affects the energy position of MAPI bands at the interface [178, 182]. Miller et al. [178] showed that the Fermi level of MAPI is shifted closer to the VB using a p-type substrate as opposed to an insulating or n-type substrate. Instead, Olthof et al. [182] observed a variation of the band alignment of MAPI film depending on the work function of the substrate. The possibility to control the energy level at the interfaces with the substrate is relevant in PSCs, where the band alignment is crucial for an efficient carrier collection (see sec. 3.1).

### Crystals and nanostructures

Besides polycrystalline films, also perovskite single crystals and nanostructures can be prepared. Typically, a  $\text{PbI}_2$  (or lead acetate ( $\text{PbAc}_2$ )) film is deposited on a substrate and then immersed in a MAI/IPA solution. Depending on the MAI concentration, crystal formation occurs through two different processes [66, 183, 184]: in-situ phase transformation (Fig. 2.3(a)), also called interfacial reaction, or dissolution-recrystallization (Fig. 2.3(b)).

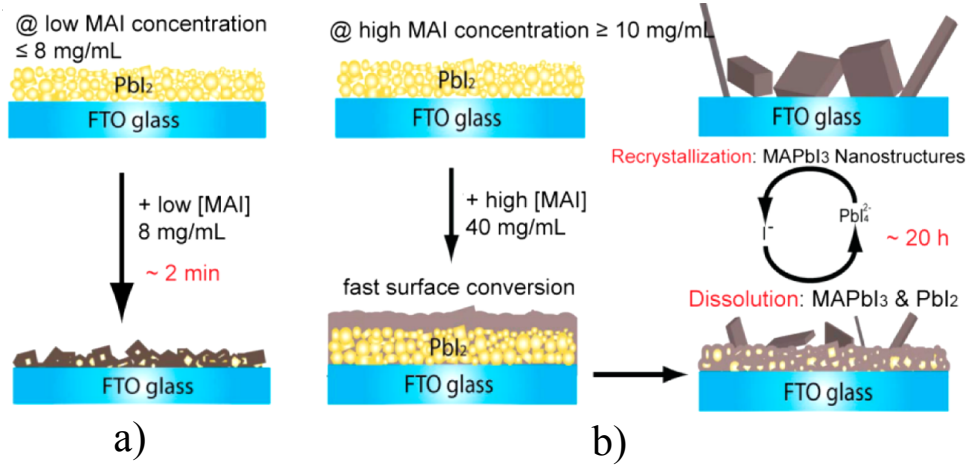
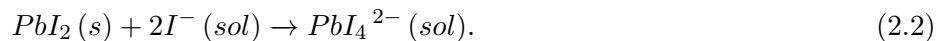
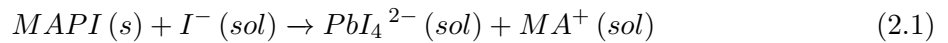


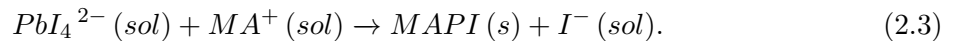
**Figure 2.3:** Schematic illustration of the growth mechanisms of crystalline MAPI nanostructures: a) Interfacial reaction at low MAI concentration. b) Dissolution-recrystallization at high MAI concentration. [184]

At low concentration of MAI precursor ( $< 10 \text{ mg ml}^{-1}$ ), the crystallization occurs through in-situ transformation (Fig. 2.3(a)): diffusion of MAI into the layered structured  $\text{PbI}_2$  results in the direct formation of MAPI.  $\text{MA}^+$  and  $\text{I}^-$  ions are prone to be directly intercalated into the inorganic lead frameworks, which gives rise to MAPI crystals with the same shapes of the original  $\text{PbI}_2$  crystals [183].

On the contrary, when the concentration of MAI is much higher ( $> 30 \text{ mg ml}^{-1}$ ), the crystal growth occurs through dissolution-recrystallization process (Fig. 2.3(b)). In this condition, a MAPI thin film immediately forms on the  $\text{PbI}_2$  surface after the exposure to MAI solution. Because of the excess of  $\text{I}^-$  ions, the formation of  $\text{PbI}_4^{2-}$  complex becomes thermodynamically favourable. Indeed,  $\text{I}^-$  ions can dissolve the initially formed MAPI and react with the unconverted  $\text{PbI}_2$  to form  $\text{PbI}_4^{2-}$  through the following reactions:



When the MAI solution is oversaturate with  $\text{PbI}_4^{2-}$  complexes,  $\text{PbI}_4^{2-}$  ions react with  $\text{MA}^+$  ions to recrystallize into MAPI nanostructure



## 2.2 Synthesis of $\text{CsPbX}_3$

### Film and NCs

To obtain homogeneous and uniform  $\text{CsPbX}_3$  perovskite film, single [120, 185, 186] or double-step [35, 187, 188] solution deposition methods are used, as for hybrid perovskites. In this case,  $\text{CsX}$  is used as precursor instead of MAI. DMSO, DMF and toluene (for  $\text{PbX}_2$ ) are the solvent more extensively used.

On the other hand,  $\text{CsPbX}_3$  NCs in solution can be obtained with different methods (see Fig. 2.4): hot injection method [18, 119, 189–191] or room temperature methods [56, 192]. In Fig. 2.4(a) a schematic illustration of the hot injection method is shown. Firstly, a powder of

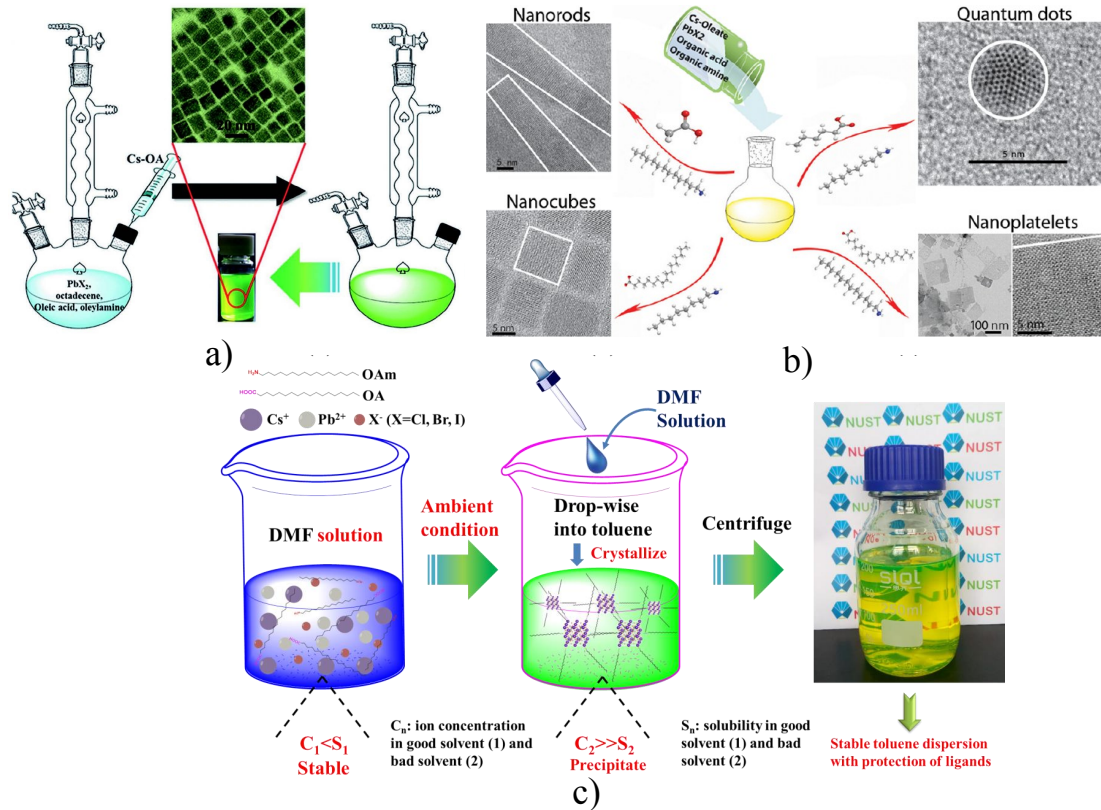
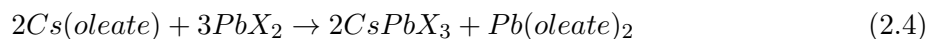


**Figure 2.4:** Schematic illustration of the most common methods to synthesize CsPbX<sub>3</sub> NCs: a) Hot injection method. The inset shows a corresponding TEM image of the as-produced NCs. b) Room temperature ligand-mediated reprecipitation. By varying the surfactants different structures can be obtained. c) Room temperature supersaturated recrystallization. [56, 92, 192]

lead halide salt (PbX<sub>2</sub>) is dissolved in a hot solvent (octadecene (ODE)) with the surfactants (oleylamine(OAm), oleic acid (OA)), that act as ligands for stabilizing the resulting NCs. After that, a preheated Cs(oleate) (caesium carbonate Cs<sub>2</sub>CO<sub>3</sub> with ODE) is injected into the previous solution. The formation reaction of CsPbX<sub>3</sub> NCs can be expressed as [191]

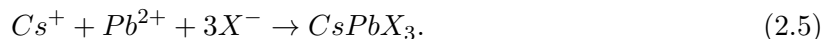


In the hot-injection method, the size of CsPbX<sub>3</sub> NCs can be varied by changing the reaction temperature (typically 140-200 °C), the reaction time, the precursor concentration and the surfactants [119, 189]. Pan et al. [189] investigated how the length of acid and amine chain and the injection temperature influence the size and the shape of the NCs. Low reaction temperatures and shorter chain amine lead to the formation of thin NPs. On the other hand, high reaction temperature leads to thick NPs or nanocubes.

Apart from the hot-injection synthesis, room temperature methods are proposed to synthesize CsPbX<sub>3</sub> NCs: ligand-mediated reprecipitation (Fig. 2.4(b)) and supersaturated recrystallization (Fig. 2.4(c)). In the first method, a solution of precursors (PbX<sub>2</sub>, Cs-oleate and surfactants) in a polar solvent (DMF or DMSO) is mixed with a nonpolar solvent, such as toluene. The polar solvent acts as a good solvent to dissolve the inorganic salts and molecule ligands, while the nonpolar solvent acts as a bad solvent to promote the reprecipitation process.

In the supersaturated recrystallization (Fig. 2.4(c)), perovskite precursors (CsX and PbX<sub>2</sub>) are dissolved together with the surfactants in a polar solvent (DMF or DMSO). An important

point is that the concentrations of such ions are smaller than their solubility limit in the polar solvent; as a consequence, they can be well dissolved in DMF/DMSO without crystallization. After that, the above solution is transferred into toluene, that is a poor solvent. After such transfer, the drop in solubility produces an highly supersaturated state and then induces a very rapid recrystallization according to the following equation:



Eventually, the NCs solution can be deposited on a substrate by either drop-cast or spin-coating to obtain nanocrystalline films.

### Single crystals

In this section we discuss the main techniques used to synthesize all-inorganic  $CsPbX_3$  perovskite single crystals. Most of the techniques here presented are also used to growth hybrid perovskite single crystals.

At the beginning,  $CsPbX_3$  single crystals were obtained via the Bridgmann method [96,193], that requires high temperature and highly pure starting reagent. In this technique (Fig. 2.5(a)), perovskite precursors are put in a quartz flask, sealed under high vacuum ( $10^{-4}$  mbar pressure) and are melted above  $600^\circ\text{C}$ . The flask is then slowly passed through a vertical tube furnace having a temperature gradient, that decreases from top to bottom. The melt cools slowly and the crystallization of the melt begins from the tip of the flask. Using this technique, large single crystals (several millimetres) of  $CsPbBr_3$  [96] and  $CsPbCl_3$  [193] were obtained.

Afterwards, low-temperature methods were developed to growth single crystals from the precursor solution: antisolvent vapour-assisted crystallization (AVC) and inverse temperature crystallization (ITC). In the first method, the precursor solution ( $CsX$  and  $PbX_2$  in DMSO [194]) is placed in a clean crystallization flask and covered with a filter paper to limit antisolvent vapour diffusion (Fig. 2.5(b)). The covered crystallization flask is then put inside a deeper glass dish, that contain the antisolvent (acetonitrile or methanol) and is placed on a hot plate. In the AVC method, the antisolvent vapour slowly diffuse into the crystal precursor solution, resulting in the formation of the perovskite crystals on the bottom of the crystallization flask.

The ITC method is based to the decrease of the perovskite solubility in some organic solvents with increasing temperature (inverse temperature solubility) [133,194–197]. For example MAPI,

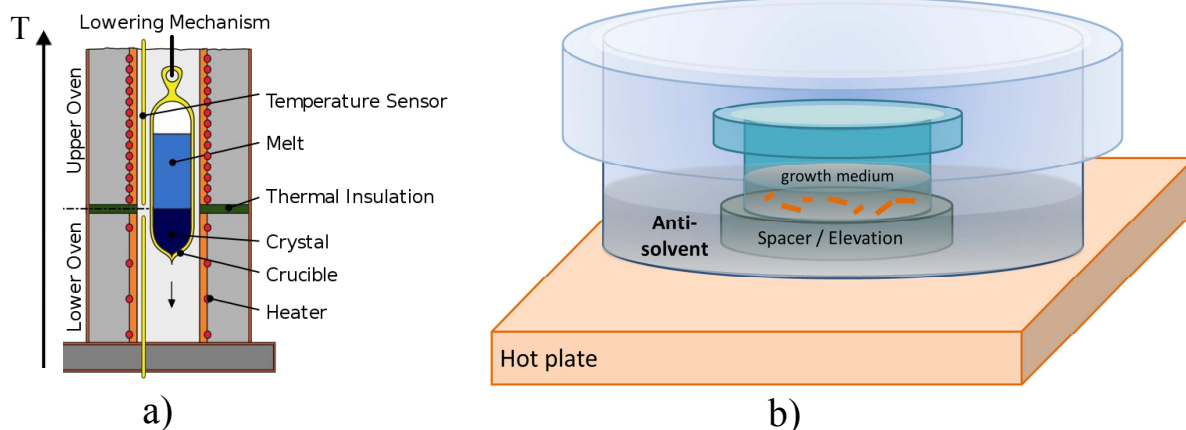


**Figure 2.5:** Synthesis techniques to growth perovskite single crystals: a) Bridgmann method. b) AVC method. [194]



MAPbBr<sub>3</sub> and MAPbCl<sub>3</sub> show inverse temperature solubility in  $\gamma$ -butyrolactone (GBL) [195], DMF [133] and DMSO [196], respectively. The precursors solution dissolved in the suitable solvent is placed in a vial and heated. Crystal growth occurs relatively fast, within several hours. The temperature to which the crystallization occurs depends to the perovskite composition and to the solvent used during the growth. For CsPbBr<sub>3</sub> perovskites, Dirin et al. [197] showed that the optimal solvent for the growth of this perovskite using the ITC method was DMSO. More in details, they used a solution of CsBr and PbBr<sub>2</sub> (1:2 molar ratio), dissolved in a mixture of DMSO with cyclohexanol (CyOH) and DMF; heating this solution at about 90 °C, CsPbBr<sub>3</sub> single crystals of about 8 mm in length were obtained. Instead, Rakita et al. [194] used a solution of CsBr and PbBr<sub>2</sub> with (1:1 molar ratio) in DMSO to growth CsPbBr<sub>3</sub> single crystals. Heating the solution, other products were formed, especially Cs<sub>4</sub>PbBr<sub>6</sub> [197]. To eliminate the undesired products and grown pure CsPbBr<sub>3</sub> single crystals they developed a two-step heating cycle.

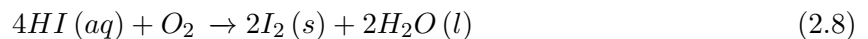
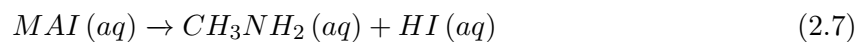
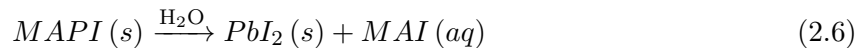
## 2.3 Stability of perovskite materials

In this section we discuss the problem of stability in perovskite materials, that arises from several factors and in particular from moisture, light, heat. It is worth noting that the stability of perovskite is related to its composition.

### 2.3.1 Stability of MAPI

#### Degradation in ambient air

First of all, hybrid organic-inorganic perovskites, such as MAPI, easily decompose in presence of moisture and oxygen due to the hygroscopic amine component in the compound [25, 26]. For MAPI, the main degradation steps in presence of moisture and oxygen can be summarized by the following chemical reactions [198, 199]:



Firstly, MAPI decomposes into MAI solution and PbI<sub>2</sub> (reaction 2.6) reacting with water. Then, MAI continues to decompose into CH<sub>3</sub>NH<sub>2</sub> and HI (reaction 2.7). This degradation process can be further accelerated by the oxidation of HI in presence of oxygen (reaction 2.8) and under UV irradiation (see the paragraph “Photo-induced degradation”).

The degradation of MAPI in presence of water was investigated in detail by Leguy et al. [25] through time-resolved X-ray diffraction (XRD) and ellipsometry. They demonstrated that, when MAPI is exposed to water vapor, hydrated crystal phases were formed, as shown in XRD spectra (Fig. 2.6). MAPI single crystals exposed to 70 % relative humidity (RH) for 60 h convert into monohydrate phase (MAPI·H<sub>2</sub>O), as shown in Fig. 2.6(a). Moreover, longer exposure (above 2 h) to 80 % RH leads to a formation of the dihydrate crystal phases (MA<sub>4</sub>PbI<sub>6</sub>·2H<sub>2</sub>O) in the perovskite film (Fig. 2.6(b)). This hydration process is reversible: indeed the hydrated film could return back into the initial MAPI structure if it is subsequently exposed to a dry atmosphere (Fig. 2.6(c)). On the contrary, when the whole film changes to dihydrate crystal phase, an excess



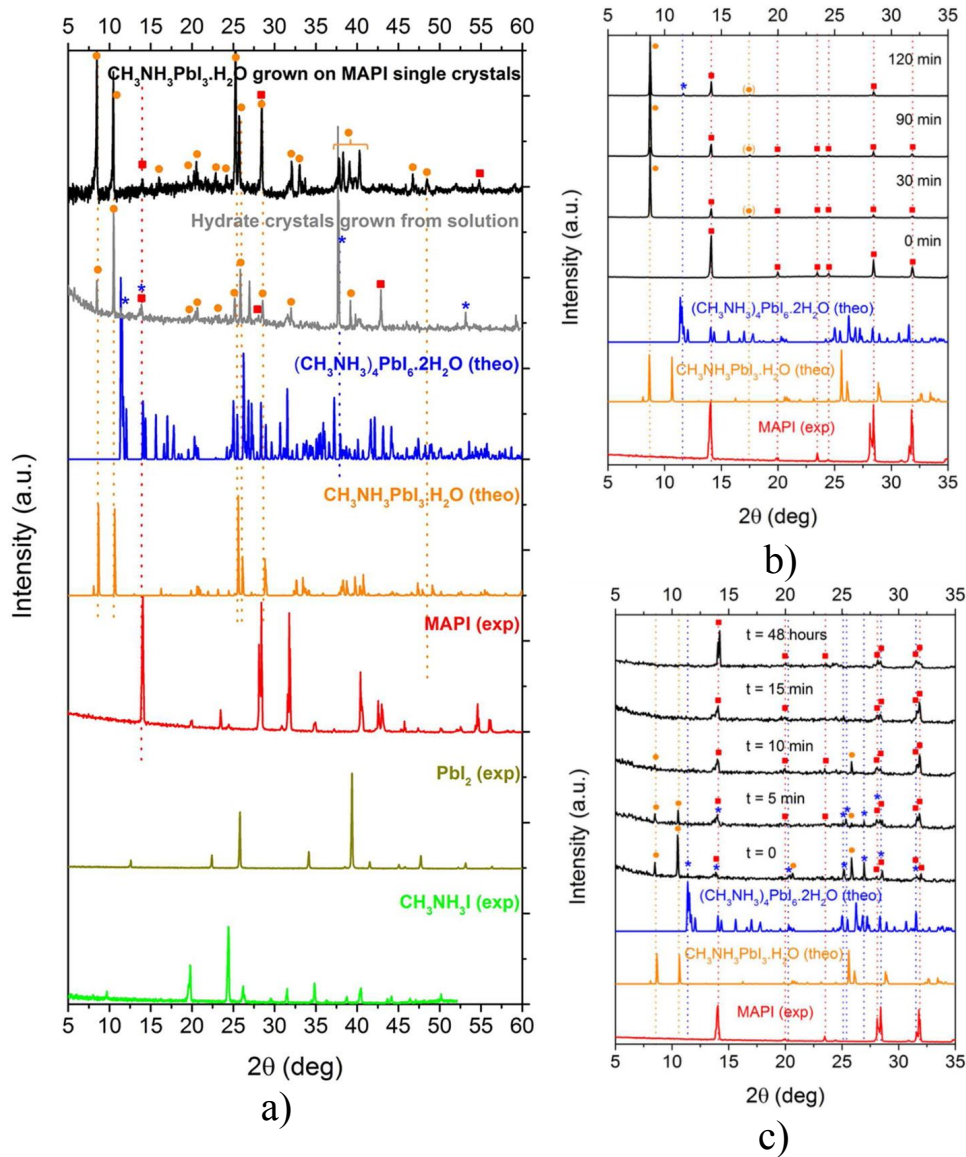
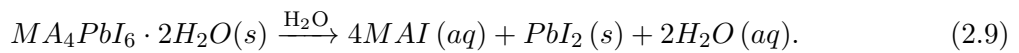


**Figure 2.6:** a) XRD spectra of MAPI single crystals after exposure to water vapors and of MAPI hydrated crystals obtained from solution. Below these, XRD patterns of the species that hydrated crystals is likely to contain are reported. Symbols are used to tag the main features, according to the color of their respective spectra. b) Time-resolved XRD patterns of polycrystalline MAPI during exposure to 80% RH. c) Time-resolved XRD patterns of the hydrate MAPI film during the dehydration in dry air [25].

of water can produce an irreversible degradation of MAPI into MAI and  $\text{PbI}_2$ :



Christians et al. [26] investigated the degradation of MAPI upon humidity exposure in the dark by monitoring the evolution of the optical absorption spectra and of the film morphology. They showed that, after humidity exposure in the dark, MAPI does not convert entirely into  $\text{PbI}_2$ , as the decrease in absorbance occurs across the entire visible spectrum and not only at wavelength greater than 500 nm (Fig. 2.7(a)). Humidity exposure also modifies the film morphology [26], as shown in SEM images (Fig. 2.7(b)). Before humidity exposure, the perovskite film have a rough surface. On the contrary, after 90% RH exposure for 14 days, the perovskite undergoes a recrystallization process, becoming smooth and highly ordered. Christians et al. investigated

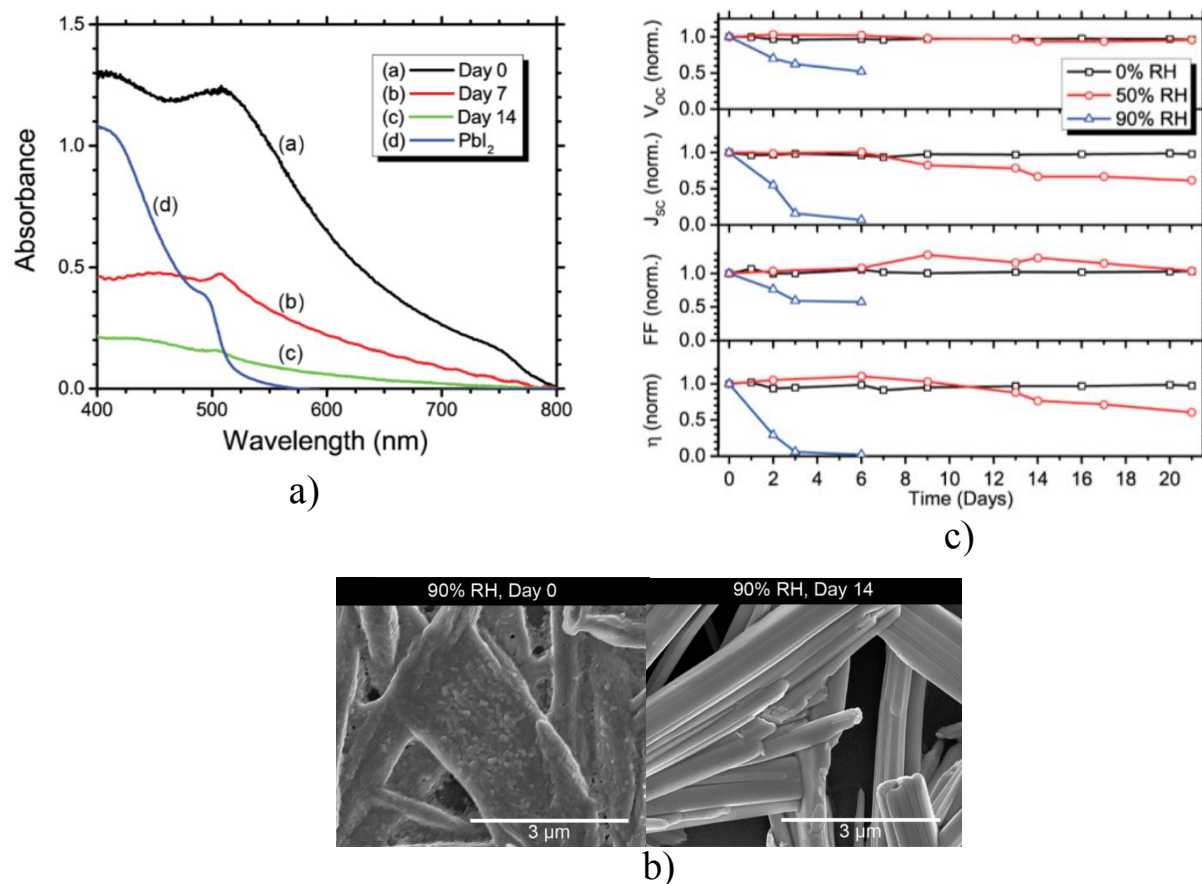


**Figure 2.7:** a) Evolution of the absorption spectra of MAPI film stored in the dark, at room temperature, to 90 % RH. Absorption spectra of pristine Pbl<sub>2</sub> film are also reported. b) SEM images of MAPI film before (Day 0) and after 14 days exposure in the dark to 90 % RH. c) Temporal evolution of the photovoltaic parameters for MAPI PSCs stored to different RH conditions [26].

also the evolution of the performance of MAPI solar cells stored in dark under different RH conditions (Fig. 2.7(c)). Solar cells exposed to 90 % RH underwent a drop in PCE of about 95 % in only three days, while solar cells stored to 0 % and 50 % RH were more stable, with a PCE reduction of about 5 % in the same period.

### Thermal degradation

As discussed in sec.2.1, for most of the synthesis techniques where perovskite materials are deposited from solution, a subsequent heat treatment of the film is required in order to remove any excess solvent in the film and to facilitate the crystallization. The annealing temperature strongly influences the morphology of perovskite film, the stability and the photovoltaic performance of the device. Dualeh et al. [29] found that an annealing temperature higher than 60 °C is necessary for a complete formation of MAPI and that the ideal annealing temperature is 100 °C. Indeed samples annealed at 100 °C showed the higher absorbance (Fig. 2.8(a)) and the better morphology (Fig. 2.8(c)). Annealing temperatures higher than 100 °C lead to a decrease in absorbance and the appearance of an additional feature at about 500 nm, that is a marker of Pbl<sub>2</sub> formation (Fig. 2.8(a)), together with the change in colour of the film from brown to yellow. MAPI degradation into Pbl<sub>2</sub> at high annealing temperature was also observed by other groups [200, 201].

It has to be noted that the morphology of the perovskite film is influenced by the annealing

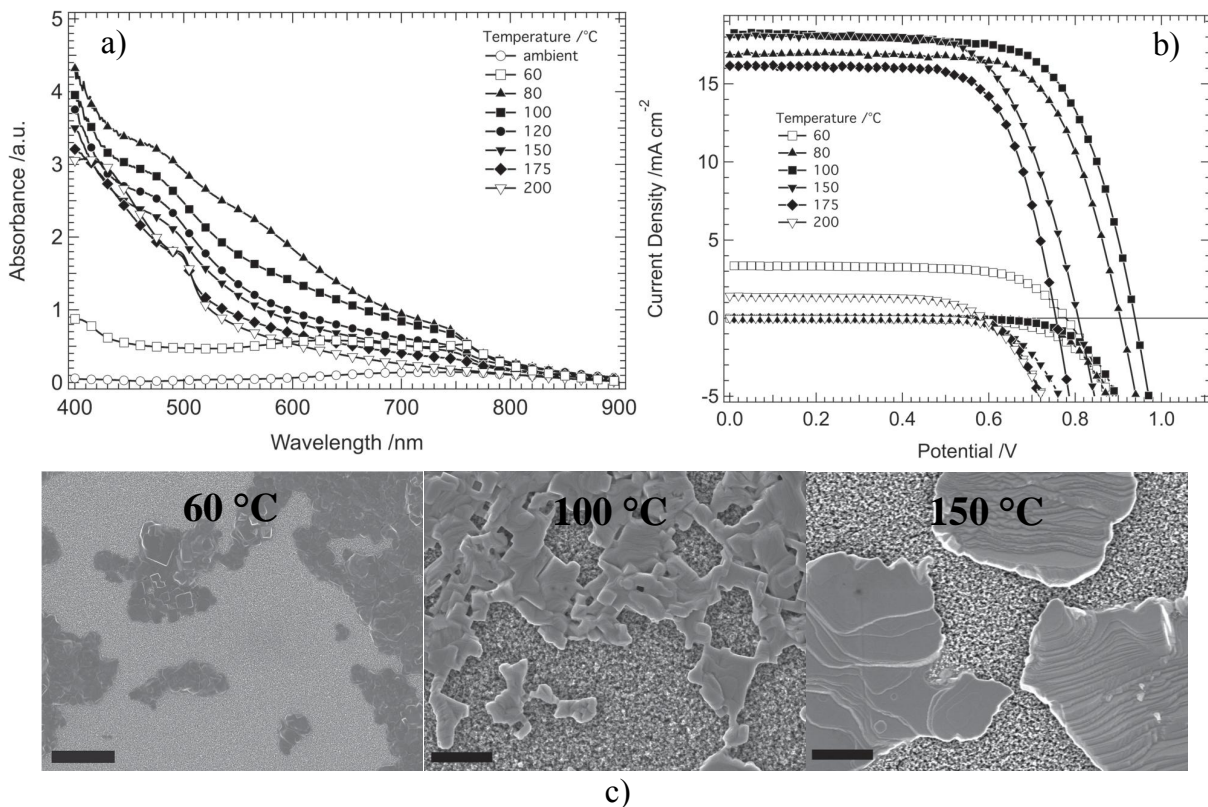


**Figure 2.8:** a) Absorption spectra for  $m\text{TiO}_2/\text{MAPI}$  films, with perovskite annealed at different temperatures. b) J-V characteristics under illumination and in the dark for solar cells with MAPI layer annealed at different temperatures. c) SEM images of MAPI films  $m\text{TiO}_2/\text{MAPI}$  films, with perovskite annealed at different temperatures. Black scale bars correspond to  $5\ \mu\text{m}$  ( $60\ ^\circ\text{C}$ ) and  $1\ \mu\text{m}$  ( $100\ ^\circ\text{C}$  and  $150\ ^\circ\text{C}$ ), respectively [29].

temperature too, as shown in SEM images of perovskite films on mesoporous  $\text{TiO}_2$  ( $m\text{TiO}_2$ ) (Fig. 2.8(c)). For samples annealed at  $60\ ^\circ\text{C}$ , only large island of the precursors are seen and no homogeneous film is formed. The film annealed at  $100\ ^\circ\text{C}$  shows the typical structure of perovskite, with individual crystallites much better defined. On the contrary, a further increase of the annealing temperature leads to the formation of larger perovskite crystalline particles and the surface coverage of  $m\text{TiO}_2$  is lower.

Finally, Dualeh et al. correlated the photovoltaic performance of the device with the annealing temperature of the perovskite film. PSCs composed by perovskite films annealed at  $100\ ^\circ\text{C}$  showed the highest PCE (Fig. 2.8(b)). On the contrary, when the annealing temperature is lower ( $60\ ^\circ\text{C}$ ) or higher than  $100\ ^\circ\text{C}$  the PCE decreases as a consequence of perovskite degradation or incomplete crystallization of the perovskite film.

### Photo-induced degradation

A key problem that limit the application of MAPI for solar cells is its instability towards light irradiation. Indeed the exposure of MAPI films to light irradiation lead to the conversion of perovskite into  $\text{PbI}_2$ , as clearly shown by optical absorption spectra [27, 202], XRD patterns [27, 28, 202–205] and the yellow colour of the film (see Fig. 2.9(a)). Moreover, also PL spectra (Fig. 2.9(c)) and PL images (Fig. 2.9(b)) of degraded MAPI films bring evidence the  $\text{PbI}_2$  emission.

Photo-induced degradation of MAPI perovskites is strongly influenced by the temperature, limiting the light exposition. Indeed Misra et al. [27] showed that, after the exposure to concen-

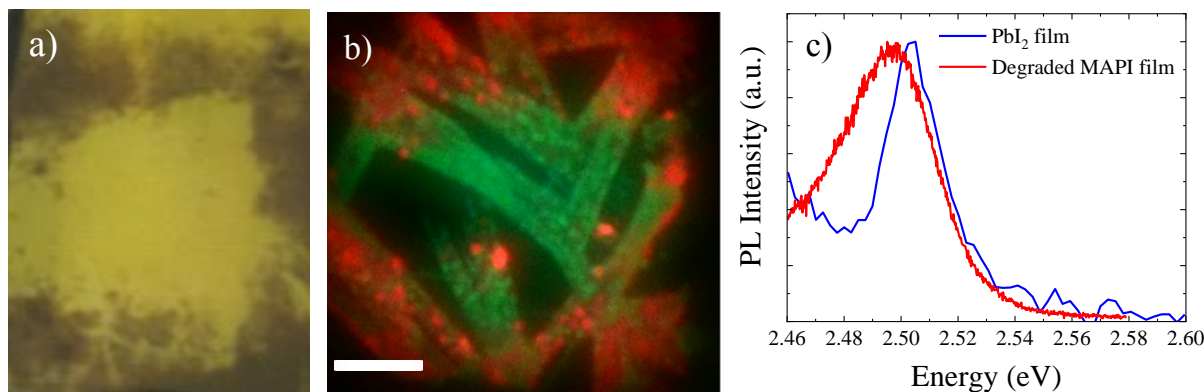


**Figure 2.9:** a) Photograph of a degraded MAPI film. Degraded regions are yellow due to the perovskite decomposition into PbI<sub>2</sub>. b) PL image of a degraded MAPI film after prolonged excitation at 458 nm [206]. We can see the MAPI emission (red) and the PbI<sub>2</sub> emission from the degraded regions (green). Scale bar corresponds to 10  $\mu\text{m}$ . c) Comparison between a PL spectra of a PbI<sub>2</sub> film and a PL spectra of a degraded MAPI film, showing the presence of the PbI<sub>2</sub> band. These spectra were acquired from our samples.

trated sunlight of 100 SUNs ( $10 \text{ W/cm}^2$ ) for 1 h at about  $50^\circ\text{C}$ , MAPI films decomposed into PbI<sub>2</sub>, as clearly evidenced by the increase of the absorption at about 500 nm (Fig. 2.10(a)) and the appearance of PbI<sub>2</sub> reflection peaks in XRD spectra. On the contrary, no degradation is observed after exposure of MAPI films to the same sunlight intensity, but at room temperature ( $25^\circ\text{C}$ ). Moreover, Misra et al. excluded that the degradation process was due to the sample heating: MAPI film annealed in the dark from 25 to  $75^\circ\text{C}$  showed an increase of absorbance, in agreement with the results of Dualeh et al. [29].

In the photo-decomposition of MAPI, oxygen plays a fundamental role [28,202], as shown in Fig. 2.10(b). After light irradiation of MAPI, excited free carriers are generated in the perovskite film. The photo-excited electrons can react with O<sub>2</sub> molecules, leading to the formation of superoxide (O<sub>2</sub><sup>-</sup>), as recently demonstrated by fluorescent molecular probe studies [202]. Superoxide species chemically react with the organic component of MAPI (i.e. MA cation), leading to the deprotonation of its ammonium group to form methylamine (CH<sub>3</sub>NH<sub>2</sub>), PbI<sub>2</sub>, I<sub>2</sub> and water. Because of the low boiling point ( $-6.7^\circ\text{C}$  [207]), methylamine molecule evaporates, leaving pure PbI<sub>2</sub> behind. We can see that MAPI degrades in presence of both oxygen and light, because

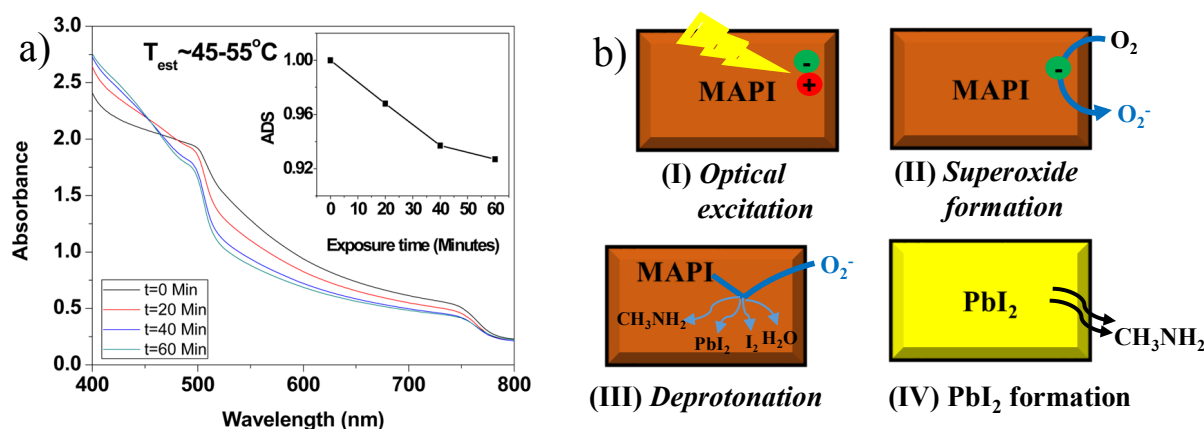


**Figure 2.10:** Photoinduced degradation of MAPI perovskite films: a) Absorption spectra of an encapsulated MAPI film exposed to 100 suns for various times. The estimated temperature of perovskite film is of about  $45\text{--}55^\circ\text{C}$ . The inset shows the time evolution of the absorption degradation state (ADS), that is the ratio of the number of absorbed solar photons for the exposed film with respect to the as-produced film [27]. b) Photo-decomposition process of MAPI in presence of oxygen.



the photo-decomposition process is triggered by the superoxide species. Indeed, Abdelmageed et al. [28] showed that MAPI films are insensitive to oxygen in the dark and stable under intense light (at room temperature) with absence of oxygen. However, this is not true for MAPI films implemented in PSCs, because other components of the device can induce degradation, as discussed in sec. 3.1.1.

### Influence of the composition

The stability of perovskites is strongly influenced by their chemical composition [27, 34, 35, 40, 208]. Firstly, the stability of perovskite film can be improved by halide mixing or exchanging. Lee et al. [209] reported that iodide-chloride mixed halide perovskites ( $\text{MAPbI}_{3-x}\text{Cl}_x$ ) is remarkably stable during processing in air. Noh et al. [40] showed that PSCs fabricated with bromide-iodide mixed halide perovskites ( $\text{MAPbI}_{3-x}\text{Br}_x$ ) as light absorber are more stable if compared with MAPI PSCs (Fig. 2.11(a)). After exposure to 55% RH for 1 day,  $\text{MAPbI}_{3-x}\text{Br}_x$  PSCs with low Br content ( $x=0, 0.06$ ) exhibited serious degradation of PCE, whereas the other  $\text{MAPbI}_{3-x}\text{Br}_x$  cells

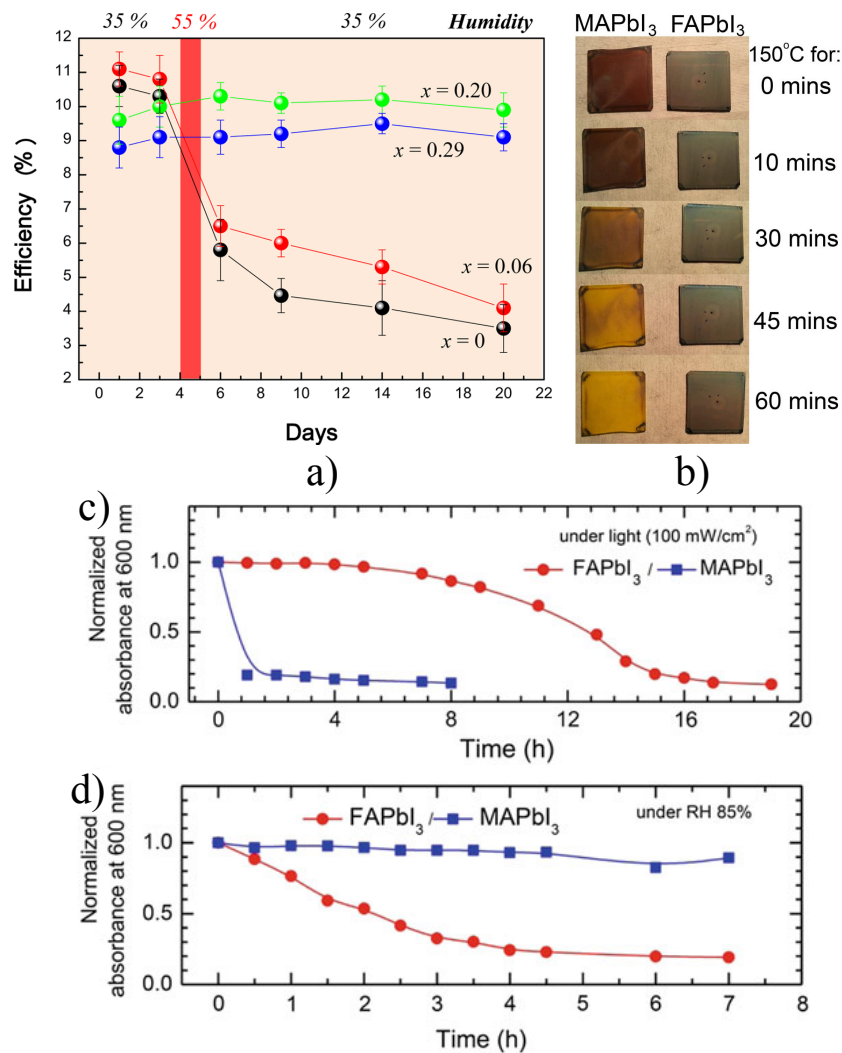


**Figure 2.11:** a) PCE evolution with time for  $\text{MAPbI}_{3-x}\text{Br}_x$  PSCs with different Br content ( $x = 0, 0.06, 0.2, 0.29$ ). The devices were stored in air at room temperature without encapsulation [40]. b) Photograph of MAPI and  $\text{FAPbI}_3$  films heated in air at  $150^\circ\text{C}$  for the times indicated. c) Normalized absorbance at 600 nm as a function of time for  $\text{FAPbI}_3$  and MAPI films exposed to a continuous  $1 \text{ SUN} = 100 \text{ mW/cm}^2$  illumination [38, 210]. d) Normalized absorbance at 600 nm as a function of time for  $\text{FAPbI}_3$  and MAPI films stored in the dark to a RH of about 85% [38, 210].

( $x=0.2, 0.29$ ) maintained their PCE. Moreover, MAPbBr<sub>3</sub> is more stable with respect to MAPI after light exposure at elevated temperature ( $\sim 55^\circ\text{C}$ ) [27]. The higher stability of MAPbBr<sub>3</sub> films compared with their iodide counterpart can be attributed to the different bond strength and crystalline phases at room temperature (see Tab. 1.2) between these two perovskites [27,40].

Apart from halogen modification, also cation substitution was proposed in order to further improve the stability. For example, FAPbI<sub>3</sub> was recently introduced to replace MAPI in PSCs due to its lower band gap [37–39,100,201]. Moreover, theoretical calculation [100,211] showed that the interaction of FA cations with the inorganic cage is stronger with respect to MA cation due to the higher probability to form hydrogen bonding. As a consequence, FAPbI<sub>3</sub> stability should be better than MAPI due to the reduced tendency to form and release volatile species. As a matter of fact, the thermal stability [37,201,208] and the photo-stability [38] of FAPbI<sub>3</sub> perovskites are better with respect to MAPI (see Fig. 2.11(b-c)). However, moisture stability of FAPb<sub>3</sub> is found to be poor if compared to MAPI [38] (Fig. 2.11(d)). Black perovskite phase of FAPbI<sub>3</sub> ( $\alpha$ -phase) converts into yellow non-perovskite phase in presence of solvent [99]. Moreover, FA cation dissociates into ammonia and sym-triazine in presence of water [99]. In order to stabilize the black perovskite phase of FAPbI<sub>3</sub>, Cs<sup>+</sup> cations were incorporated into the alloy with FA [38]. Upon Cs<sup>+</sup> doping, photo- and moisture stability of the perovskite film were significantly improved, together with the film morphology and the device performance.

### 2.3.2 Stability of inorganic perovskites

All-inorganic caesium lead halide perovskites exhibit a better stability compared to the hybrid counterpart due to the absence of the organic cation. [34–36]. For example, Kulbak et al. [35] showed that CsPbBr<sub>3</sub>-based solar cells are more stable with respect to MAPbBr<sub>3</sub> after ageing (Fig. 2.12). However, stability problems under light illumination, heat and moisture are still present in CsPbBr<sub>3</sub> perovskites.

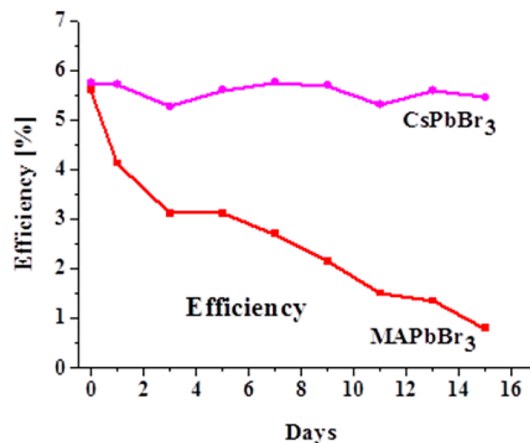


Figure 2.12: PCE evolution with time for MAPbBr<sub>3</sub> and CsPbBr<sub>3</sub> based PSCs [35].

#### Moisture, oxygen and light degradation

Under UV illumination, a decrease of the PL intensity and morphology changes are observed in CsPbBr<sub>3</sub> perovskites [123,212–215]. Wang et al. [123] showed that, under UV illumination at high intensity ( $\sim 20\text{ mW cm}^{-2}$ ), PL emission spectra of CsPbBr<sub>3</sub> NPs decrease in intensity and red shift with time. Monitoring the evolution of the PL and absorption spectra, they suggest that

a photon driven transformation (PDT) process occurs in  $\text{CsPbBr}_3$  NPs: under laser irradiation  $\text{CsPbBr}_3$  NPs coalesce into larger crystals. The absorption of photons tends to remove the surface bonding ligands between the NPs, given their small binding energy [216], facilitating the ion migration and the coalescence between the nearest NPs. PDT is directly demonstrated by the morphology change in the SEM images of the film: crystals with micrometre size are formed upon the laser exposure. The PL loss was attributed to the formation of carrier traps due to the photo-induced desorption of surface ligands.

Huang et al. [212] investigated in details the degradation of  $\text{CsPbBr}_3$  NCs in presence of light, moisture and oxygen.  $\text{CsPbBr}_3$  NCs film stored to 60% RH showed a sharp reduction in the PL intensity under blue illumination at  $\sim 175 \text{ mW cm}^{-2}$ : the residual PL was of about 10.6% after 8 h of illumination. In addition, the PL emission red shifts, due to the formation of larger crystals during illumination, as already observed by Wang et al. [123]. The degradation was slowed down if the film was isolated from moisture and oxygen and no PL loss was observed with the film stored in the dark, even at high RH (> 60%). Oxygen plays a crucial role for the degradation of  $\text{CsPbBr}_3$  NCs: film stored in pure oxygen showed a PL reduction of 73.4% after 1 h of illumination. Huang et al. [212] proposed a possible degradation pathway for  $\text{CsPbBr}_3$  NCs, showed in Fig. 2.13. Despite the presence of surface bonding ligands, moisture and oxygen

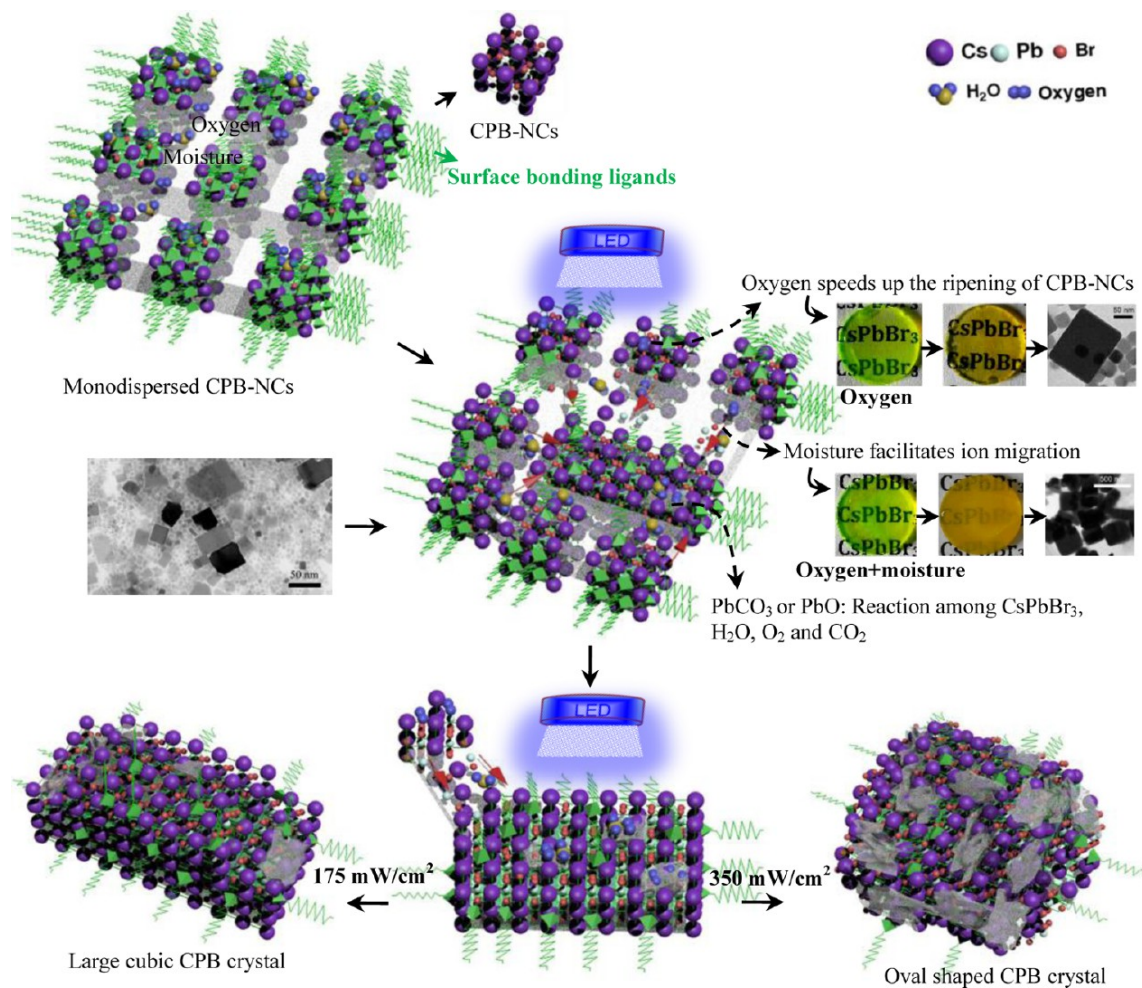
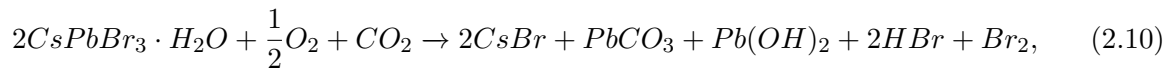


**Figure 2.13:** Scheme of the possible degradation pathways of  $\text{CsPbBr}_3$  (CPB) film under illumination at different power density in presence of moisture and oxygen [212].



can reach the NCs surface and some hydrated  $\text{CsPbBr}_3$  species ( $\text{CsPbBr}_3 \cdot 2\text{H}_2\text{O}$ ) may be formed, as for MAPI. Under illumination, surface bonding ligands are easily removed by the absorption of photons and the NCs tend to be aggregated due to the strong Van der Waals attraction forces. Obviously, the amount of hydration reaction increases due to removal of surface ligands. The unstable  $\text{CsPbBr}_3$  NCs may be eroded by oxygen and the dissociated ions migrate to the large  $\text{CsPbBr}_3$  crystals, contributing to the crystal growth (Ostwald ripening process). Moreover, also hydrated  $\text{CsPbBr}_3$  species may support the ion transport and facilitate the crystal growth. On the other hand, hydrated  $\text{CsPbBr}_3$  species can react with  $\text{O}_2$  and  $\text{CO}_2$ , leading to the surface decomposition:



Indeed, Huang et al. observed Pb clusters at the surface edge of the crystals in high-angle annular dark field scanning TEM images due to the formation of  $\text{PbCO}_3$  and  $\text{PbO}$  phases. Surface decomposition and the photo-induced desorption of surface ligands are the main factors that produce the PL loss.

### Thermal degradation

Besides moisture, oxygen and light, also thermal annealing has been regarded as another factor for the degradation of  $\text{CsPbX}_3$  perovskites.

Yuan et al. investigated the structural and optical properties of  $\text{CsPbBr}_3$  NCs annealed at different temperatures [124, 217]. They showed a red shift of the PL emission at room temperature after the annealing process, that became more evident increasing the annealing temperature. The red shift of the emission was ascribed to the coalescence of the NCs during the thermal annealing process due to the removal of surface ligands (see TEM images of Fig. 2.14). Moreover, a reduction of the PL intensity occurred for NCs annealed above 340 K and temperature-dependent PL measurements bring evidence of a more rapid drop of the PL intensity for NCs annealed at higher temperature. This reduction was ascribed to the formation of non-radiative recombination centres due to the removal of surface ligands [124, 217].

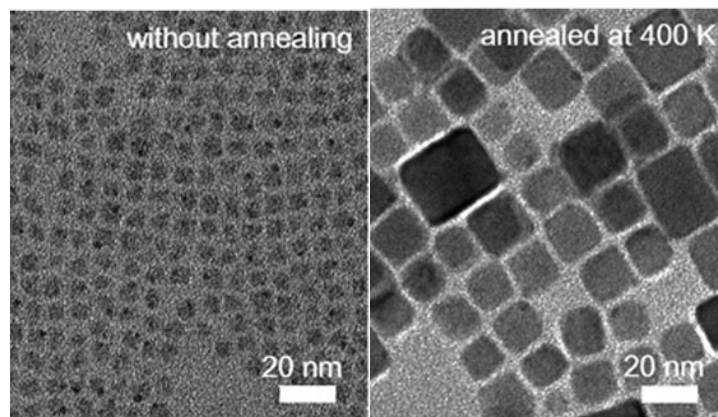


**Figure 2.14:** TEM images of  $\text{CsPbBr}_3$  NCs at room temperature without thermal annealing and with thermal annealing at 400 K for 20 min, respectively [124].

### Improvement stability

In order to improve the stability of the NCs, surface passivation [155, 215, 218, 219] and encapsulation methods [213, 220, 221] were carried out.

**Passivation methods** Jing et al. [214] proposed an acetone-etching selecting method to form a passivation layer on mixed  $\text{CsPb}(\text{Br}_x\text{I}_{1-x})_3$  NCs: acetone wash partially etches iodine away on the iodine-rich NCs surface, forming a Br-rich self-passivation layer. After the treatment, the stability of the NCs was significantly enhanced. Woo et al. developed an inorganic passivation method that made  $\text{CsPbBr}_3$  NCs more stable, introducing a metal bromide ( $\text{ZnBr}_3$ ) in the precursor solution. Koscher et al. [155] demonstrated a post synthetic treatment of  $\text{CsPbBr}_3$  nanocrystals with thiocyanate salt to passivate the NCs surfaces. After the treatment, the PLQY approaches unit and the stability was significantly enhanced.

**Encapsulation methods** In order to improve the stability,  $\text{CsPbBr}_3$  were embedded into alumina and/or silica ( $\text{SiO}_2$ ) templates [213, 220]. For example, Loudice et al. [213] proposed an amorphous alumina ( $\text{AlO}_x$ ) encapsulation method to prepare  $\text{CsPbBr}_3$  NCs/ $\text{AlO}_x$  inorganic nanocomposites. These nanocomposites exhibited exceptional stability towards exposure to air (for 45 day), irradiation (for 8 h) and heat (up to  $\sim 200^\circ\text{C}$ ). On the contrary, pristine sample degraded in few days. However, these encapsulation matrix are carried out with insulating templates (Al,  $\text{SiO}_2$ ). Alternatively, Li et al. [221] synthesize  $\text{CsPbBr}_3/\text{TiO}_2$  NCs, that exhibit exceptional stability in water (only 15% PL loss after 3 month).

To conclude this paragraph, we report in Tab. 2.1 the improvement in the stability of  $\text{CsPbBr}_3$  NCs obtained with passivation and/or encapsulation methods. We can see that, up to now, a stability of about 300 h under light exposure and of few month under moisture has been reached.

**Table 2.1:** Some representative results concerning the stability improvement in  $\text{CsPbBr}_3$  NCs with passivation and/or encapsulation methods.

Passivation	Encapsulation	Stability test		Ref.
		Description	PL loss	
–	$\text{AlO}_x$	Thermal (heating at $200^\circ\text{C}$ ) Moisture (RH=30% at $25^\circ\text{C}$ )	5 % No PL loss after 45 days	[213]
DDAB, DBATES	$\text{SiO}_2/\text{Al}_2\text{O}_3$	Photostability (470 nm LED at $21\text{ mW}/\text{cm}^2$ )	10% in 300 h.	[220]
$\text{S}^{2-}$ -DDA and $\text{In}(\text{Ac}_3)$	–	Photostability (450 nm LED at $175\text{ mW}/\text{cm}^2$ )	No PL loss for 188 h	[219]
$\text{TiO}_2$	$\text{TiO}_2$	Water	15% in 3 month	[221]

Notes: DDAB = dymethyl ammonium bromide, DBATES = Di-sec-butoxyaluminiumxytriethoxysilane,  
 $\text{S}^{2+}$ -DDA = didodecyl dimethylammonium sulfide

## §3§ Perovskites applications

In this chapter we discuss the possible applications of perovskite materials for photovoltaics and for light sources. In sec. 3.1 we describe the structure, the operating principle and the history of perovskite solar cells (PSCs); in addition we discuss the problem of stability in these devices. In sec. 3.2 we present applications of perovskite materials for light emission.

### 3.1 Perovskite solar cells

In the field of photovoltaics, it is common to distinguish between different generations of solar cells. First generation solar cells are based on a p-n junction of crystalline silicon wafers. Silicon solar cells have a good stability [222] and a high conversion efficiency (record 26.7% [223]), but are rigid and the manufacturing cost is very high. Second generation solar cells [224] are based on low cost thin-film semiconductors alternative to silicon wafers, such as amorphous silicon (a-Si), GaAs, CdTe, copper indium gallium diselenide ( $\text{Cu(In,Ga)(Se,S)}_2$ , CIGS) and InP. However, the production of these devices is still expensive due to the synthesis techniques, such as sputtering, physical vapour-deposition, and plasma-enhanced chemical vapour deposition. Third generation of solar cells are recently emerged as alternative to thin-films solar cells given their low-cost synthesis techniques. This class of solar cells includes dye-sensitized solar cells (DSSC) [225], organic solar cells [226], quantum dot solar cells [227] and, finally, perovskite solar cells (PSCs) [19].

As widely discussed in Chap. 1, perovskites have unique properties, such as a very high absorption coefficient in the visible, long and balanced carriers diffusion length and tolerance towards defects, that make them suitable for light absorbers in solar cells. In addition, as shown in Fig. 3.1, the band gap of MAPI ( $\sim 1.6$  eV at room temperature), the perovskite most commonly used in PSCs, is close to the Shockley-Queisser limit [44, 228–230], i.e. the radiative limit for the photovoltaic conversion efficiency (PCE) of a solar cells with a single semiconductor as light absorber ( $\text{PCE}_{max} \sim 33\%$ ,  $E_{g,max} \sim 1.34$  eV).

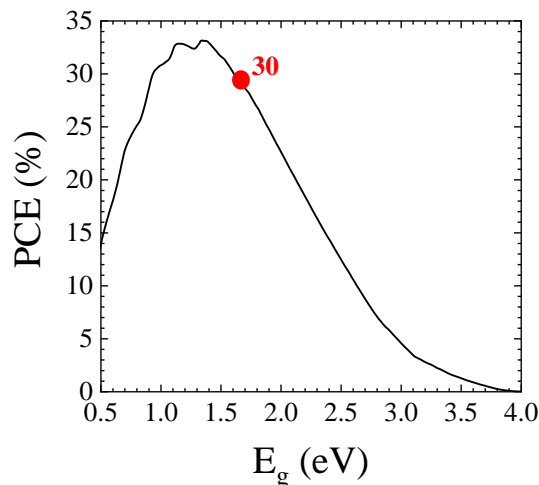


**Figure 3.1:** PCE as a function of the absorber band gap energy for a single-junction solar cell in the radiative limit (Shockley-Queisser limit). The curve is calculated under standard conditions: air mass (AM) 1.5 illumination at 1 SUN, cell temperature 25 °C. The value obtained for MAPI as light absorber ( $E_g = 1.6$  eV) is reported in red.

The schematic structure of a PSC is shown in Fig. 3.2(a). On a transparent conductive oxide (TCO) glass, an electron transporting layer (ETL), in case of direct configuration (n-i-p), or an hole transporting layer (HTL), in case of inverted configuration (p-i-n), is deposited. On top of the transporting layer a thin perovskite absorbing layer is synthesized, followed by the deposition of the HTL (or the ETL for p-i-n PSCs) and the top metal electrode. In case of mesoporous ETL, a compact hole blocking layer is used before the ETL [231] to prevent holes to reach the cathode (see Fig. 3.4(b)). Given the high absorption coefficient of MAPI in the visible, thin films ( $\lesssim 500$  nm) are used as light absorber in PSCs.

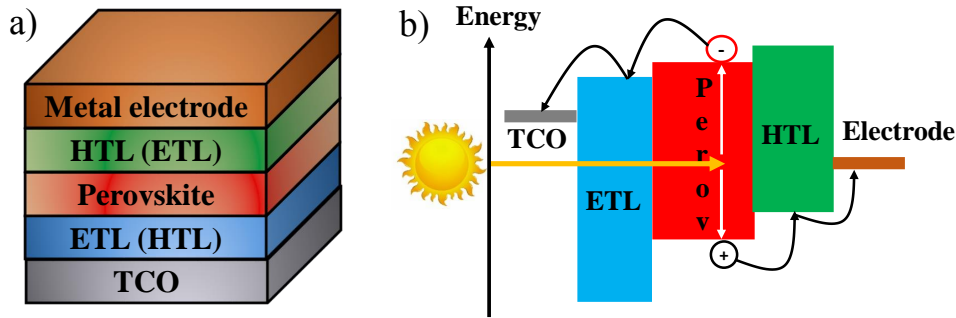


**Figure 3.2:** a) Schematic structure of a PSC. The transporting layers indicated in brackets refer to the inverted planar configuration. b) Energy level diagram and operating principle of a PSC. The solar cell is illuminated from the TCO side.

The general operating principle of a PSC is illustrated in Fig. 3.2(b). In this kind of solar cell, the perovskite layer absorbs the sun light and electron-hole pairs are generated. The photo-generated carriers are separated by the injection of electrons and holes from the perovskite into the ETL and HTL, respectively. Finally, electrons and holes are collected by the respective electrodes. In PSCs, the band alignment between the perovskite and the carrier transporting layers (i.e. ETL and HTL) is fundamental for charge separation. In particular, the conduction band minimum of the perovskite must be higher respect to the ETL and its valence band maximum must be lower respect to the HTL. A scheme of the energy levels for the materials most commonly used in PSCs is shown Fig. 3.3.

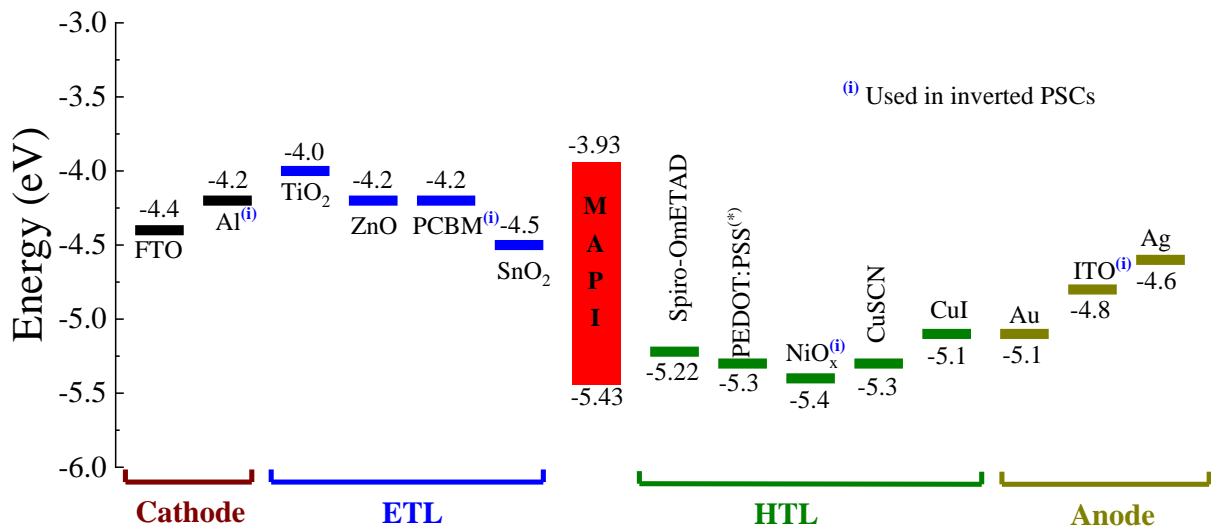


**Figure 3.3:** Scheme of the energy levels with respect to vacuum of the materials most commonly used in PSCs [136, 232, 233]. Only the values of the LUMO/conduction band for the ETLs and the HOMO/valence band for the HTLs are reported. Variations from the values of this graph are reported in the literature.

Now we discuss the characteristics of the materials most commonly used for each layer.

### ■ TCO

The transparent electrode collects electrons in PSCs with direct configuration and holes in inverted PSCs. It is usually a doped metal oxide, such as fluorine-doped tin oxide (FTO) and indium tin oxide (ITO). FTO and ITO have a high conductivity and high transmittance in the visible range [234–236].

### ■ ETL

The ETL extracts electrons from the absorbing layer, that are then collected by the cathode. Until now, mesoporous titanium oxide  $\text{TiO}_2$  ( $\text{mTiO}_2$ ) is the ETL most commonly used in PSCs. However, the synthesis of  $\text{mTiO}_2$  requires high temperature ( $> 450^\circ\text{C}$ ) [237], which is incompatible with flexible substrates. Direct planar structure based on compact  $\text{TiO}_2$  ( $\text{cTiO}_2$ ) can be synthesized at low temperature, but suffers of large J-V hysteresis [238]. Moreover, PSCs with  $\text{TiO}_2$  are unstable under UV light irradiation (see sec. 3.1.1).

In addition to  $\text{TiO}_2$ , other metal oxide, such as  $\text{ZnO}$  [239,240] and  $\text{SnO}_2$  [218,241–243], have been demonstrated as alternative ETLs for high-efficiency PSCs.  $\text{ZnO}$  and  $\text{SnO}_2$  exhibit similar or even better electrical and optical properties as compared to  $\text{TiO}_2$ , in particular an higher electron mobility [244]. The synthesis of  $\text{SnO}_2$  films requires low temperature ( $150^\circ\text{C}$ ) with respect to  $\text{TiO}_2$ , that will allow fabrication of the photovoltaic device on flexible substrates.

For inverted planar PSCs, fullerenes, such as [6,6]-phenyl- $\text{C}_{61}$ -butyric acid methyl ester (PCBM) and [60]fullerene ( $\text{C}_{60}$ ) are the ETLs most commonly used [245–247].

### ■ Perovskite active layer

In the perovskite layer, carriers are generated and transported to the selective transport layers (ETL and HTL). Thus, the active layer must have strong absorption in the visible, a suitable band gap and good transport properties. MAPI, with a band gap of about 1.6 eV at room temperature, high absorption coefficient and diffusion length exceeding 100 nm (see Chap. 1), is the material most extensively used in PSCs. However, MAPI suffers of moisture, light and thermal instability, as discussed in sec. 2.3.1. PSCs with the best efficiencies [22, 248] were obtained using  $\text{FAPbI}_3$  as active layer instead of MAPI, given the smaller  $E_g$  (see Tab. 1.4), that allowed a broader absorption of the solar spectrum. A small amount of  $\text{MAPbBr}_3$  was also introduced to stabilize the perovskite crystalline structure of  $\text{FAPbI}_3$  at room temperature.

### ■ HTL

HTL extracts holes from the absorbing layer, that are then collected by the anode.

2,2',7,7'-tetrakis(*N,N*-di-*p*-methoxyphenylamine)-9,9'-spirobifluorene (Spiro-OMeTAD) is the HTL most commonly used, especially in mesoporous and direct planar PSCs. This molecule was already used in solid state DSSCs [249]. Spiro-OMeTAD is chosen as HTL since its synthesis does not require high temperature; as a consequence, it can be deposited without damaging the perovskite layer. Spiro-OMeTAD is usually doped in order to increase hole mobility and conductivity [250–252], that are very low in the pristine material [253, 254]. Typical dopants are 4-tert-butylpyridine (TBP) and bis(trifluoromethane)sulfonimide lithium salt (Li-TFSI) that, unfortunately, cause instability in the device (see sec. 3.1.1).

For inverted planar PSCs, poly(3,4-ethylenedioxythiophene)-poly(styrenesulfonate), also abbreviated as PEDOT:PSS, is the HTL most commonly used [245–247].

A list of other organic and inorganic HTLs employed in PSC can be found in [255].

### ■ Metal electrode

The metal electrodes most commonly used in PSCs are Au, Ag and Al. Au and Ag are generally used as anode in mesoporous and direct planar PSCs, while Al is usually used as cathode in inverted planar PSCs [245, 247, 256]. Gold is more expensive than silver, but PSCs with Au electrode exhibit higher performance and a better stability (see sec. 3.1.1).

In Fig. 3.4 different PSCs are shown following the improvement in time. Early PSCs [21, 257] (2009-2012) had a structure similar to a DSSC (Fig. 3.4(a)):  $m\text{TiO}_2$  was used as ETL and a iodine liquid electrolyte as HTL. Since 2012 solid-state HTLs were used to replace the liquid electrolyte, in which the perovskite dissolved easily [257]. Different structure of PSCs were realized: mesoporous PSCs [173, 237] (Fig. 3.4(b)), planar PSCs [168, 258] (Fig. 3.4(d,e)), meso-superstructured solar cells (MSSC) [209, 259] (Fig. 3.4(c)). In the last case, electrons remain in the perovskite layer until they are collected at the FTO electrode due to the high-energy metal oxide conduction band.

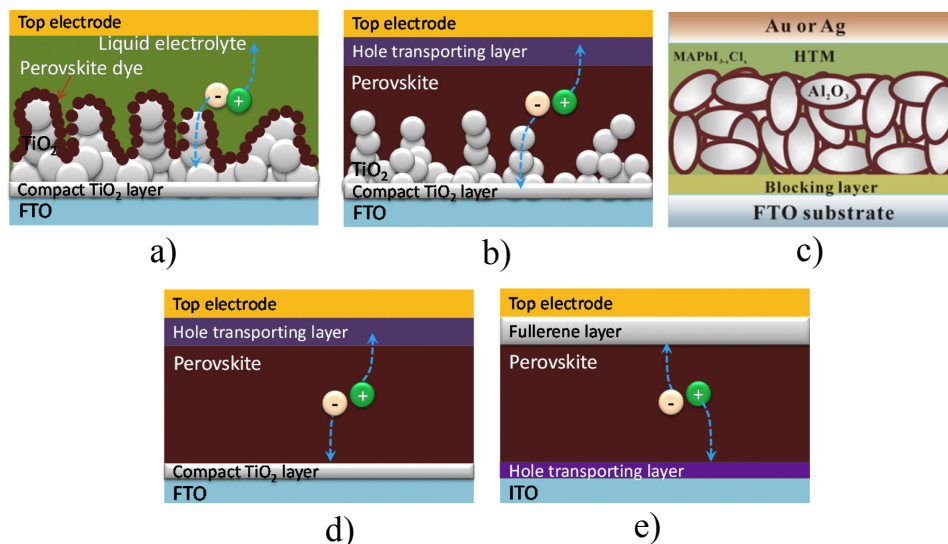


**Figure 3.4:** Different structures of PSCs: a) Perovskite-sensitized solar cell. b) Mesoporous PSC. (c) MSSC. (d) Direct (n-i-p) planar heterojunction solar cell. (e) Inverted (p-i-n) planar heterojunction solar cell. [198, 260]

### 3.1.1 Stability of PSCs

As shown in Fig. 3.5(a), PSCs exhibit a remarkable rise in their PCE, that grew from 3.8% to 22.1% in less than 10 years. Despite the rapid growth in their efficiency, that has values comparable to silicon solar cells, the commercialization of PSCs is still limited by the poor device stability under operation. In Fig. 3.5(b) the improvement in the stability of PSCs from 2009 to date is reported. We can see that the average lifetime of PSCs increased from few hours [21] to one year [261]; however such duration is far from the value of silicon panels, that are usually guaranteed for at least 20 years operation.

The limited lifetime in PSCs is due to several factors: the stability of the perovskite itself and the instability caused by the other components of the cell (transporting layers and electrodes). We already discussed the problem of stability of perovskites in sec. 2.3. In this section we briefly summarize the main factors that cause instability in PSCs devices. Possible strategies that are developed in order to enhance the long-term stability in PSCs are also discussed.

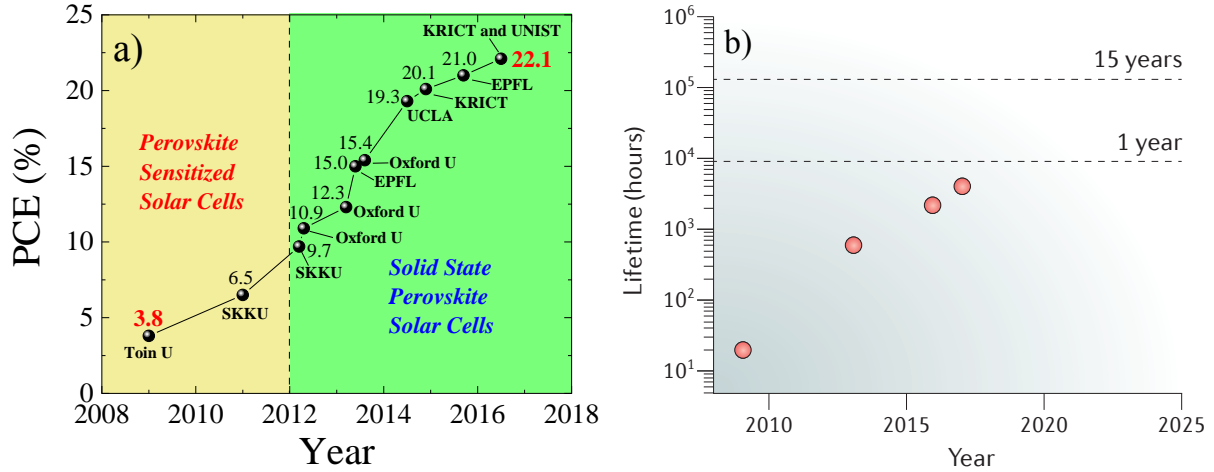


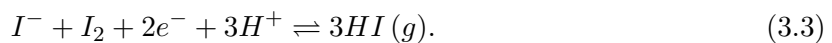
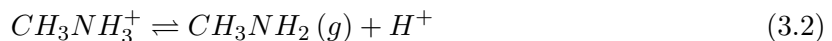
**Figure 3.5:** a) PCE evolution of PSCs from 2009 to date. b) Evolution of the stability of PSCs from 2009 to date [41].

### ETL

■ **TiO<sub>2</sub>** TiO<sub>2</sub> is the ETL most commonly used in PSCs. The instability of PSCs with TiO<sub>2</sub> is mainly due to its sensitive nature to UV light [30, 31].

The stability of PSCs under UV irradiation was investigated for the first time by Snaith and co-workers [30]. Sensitized PSCs with TiO<sub>2</sub> as ETL, stored in N<sub>2</sub> atmosphere, exhibited a rapid drop in photocurrent and PCE if exposed to UV light. The mechanism proposed by Snaith et al. for UV-induced TiO<sub>2</sub> degradation is shown in Fig. 3.6(a). (I) TiO<sub>2</sub> contains many oxygen vacancies (Ti<sup>3+</sup>), especially at the surface of the nanoparticles [262, 263], that act as deep electron-donating sites, placed at about 1 eV below the CB. These electron-donating sites can recombine with molecular oxygen, which is adsorbed at the oxygen vacancy sites. (II) After UV illumination, electron-hole pairs are formed on TiO<sub>2</sub>. Holes in the valence band can recombine with the electrons at the oxygen adsorption site, desorbing the oxygen. Thus, free electrons remain in the conduction band and an unfilled vacancy site at the TiO<sub>2</sub> surface. (III) These deep electronic sites can further trap the photo-generated electrons from sensitizer (perovskite). (IV) Since Spiro-OMeTAD is usually p-doped when is used as HTL [173, 253, 258], there are excess holes which can recombine with the immobile trapped electrons left behind from the excitation, leading to a reduction of the collected charges.

Moreover, also MAPI active layer degrades under UV irradiation in PSCs with mTiO<sub>2</sub> as ETL [31]. Perovskite decomposition under UV light exposure occurs at the TiO<sub>2</sub>/perovskite interface because of the photocatalytic action of TiO<sub>2</sub>. The decomposition of MAPI is driven by electron extraction from a iodide anion into TiO<sub>2</sub> (Fig. 3.6(b)). The possible decomposition process at the interface between TiO<sub>2</sub> and MAPI is summarized by the following reactions [31]:



Since MAPI is composed by MA, Pb<sup>2+</sup> and I<sup>-</sup> ions, TiO<sub>2</sub> can extract electrons from I<sup>-</sup> and deconstructs the perovskite, leading to the formation of I<sub>2</sub> (reaction 3.1). The electrons extracted can return back on the TiO<sub>2</sub> surface to reduce I<sub>2</sub>: consequently, reaction 3.3 can take place



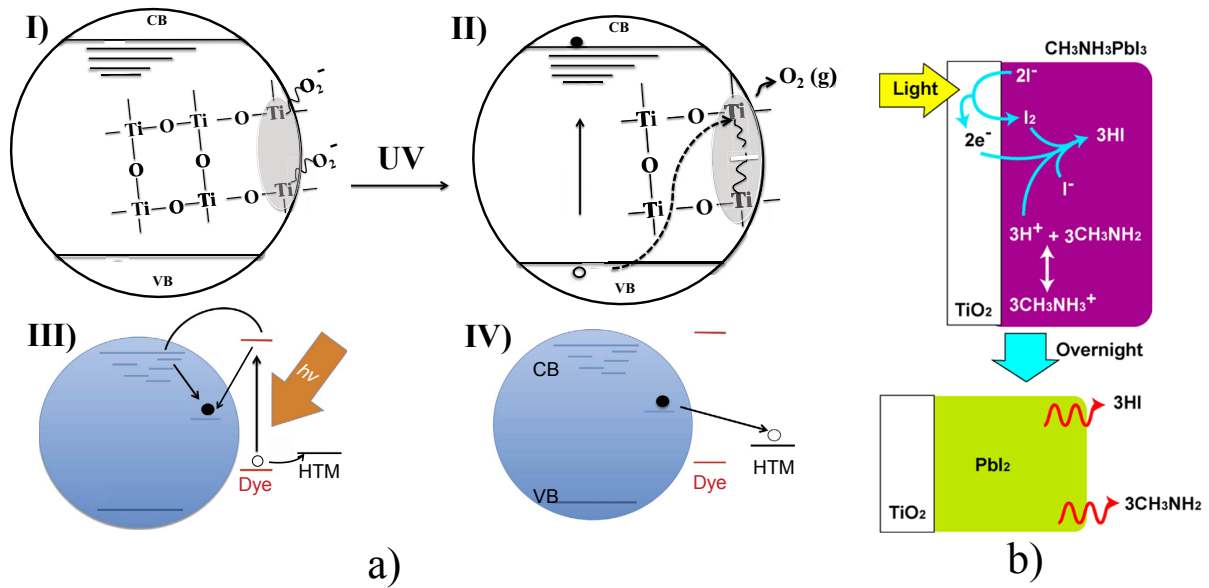


**Figure 3.6:** a) Proposed mechanism for UV degradation in mTiO<sub>2</sub> based sensitized PSCs. In this figure the label “Dye” refers to perovskite [30, 264]. b) Light induced degradation of mTiO<sub>2</sub>/MAPI PSC [31].

releasing HI. Loosing H<sup>+</sup>, the reaction 3.2 can take place and provokes the decomposition of MA into methylamine (CH<sub>3</sub>NH<sub>2</sub>). Finally, methylamine and HI evaporate due to their low boiling point, leaving PbI<sub>2</sub> behind.

In order to prevent the electron extraction from iodine at the TiO<sub>2</sub>/perovskite interface (reaction 3.1), Ito et al. [31] inserted Sb<sub>2</sub>S<sub>3</sub> as blocking layer between TiO<sub>2</sub> and MAPI. This insertion improved the stability of the PSC against light illumination and also the PCE.

■ **PCBM** PCBM can absorb oxygen or water in ambient air [265], leading to the degradation of PCBM itself or of the perovskite layer. Moreover, PCBM layer cannot form a continuous film at the surface of the perovskite film, leading to a rapid chemical reaction between the metal electrode and the perovskite and/or the exposure of perovskite to the ambient environment [266].

### HTL

■ **Spiro-OMeTAD** Spiro-OMeTAD, which is the HTL most commonly used in PSC with direct configuration, is generally p-doped with TBP and/or Li-TFSI in order to increase the hole mobility and conductivity [253]. However, the use of these additives can reduce the stability of the device.

Li-TFSI is generally dissolved in acetonitrile [32, 168, 173, 258], that can corrode the perovskite. Moreover, Qi et al. [32] demonstrated that Li-TFSI can migrate to the top surface of the Spiro-OMeTAD film when the device is exposed to air, leading to a decrease in the photovoltaic performance.

The diffusion of dopants upon air exposure is facilitated by the presence of small-size pinholes that are usually present in Spiro-OMeTAD films, with diameters in the range of 100 nm - 20 μm (see Fig. 3.7(a)). These pinholes form channels across the Spiro-OMeTAD film that facilitate the inward diffusion of O<sub>2</sub> and H<sub>2</sub>O gas molecules present in air, leading to detrimental effect on the perovskite layer. In addition, these pinholes can facilitate the outward diffusion of compounds with high vapor pressure resulting from the decomposition of MAPI (for example MAI and HI).

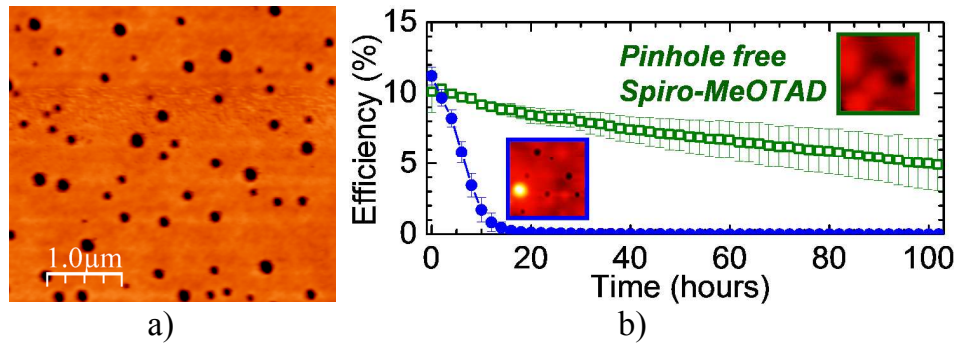


**Figure 3.7:** a) Atomic force microscopy (AFM) topography maps of Spiro-OMeTAD films [32]. b) PCE temporal evolution for PSCs composed by Spiro-OMeTAD HTL with (blue curve) and without pinholes (green curve), under operation in air with controlled RH ( $\sim 42\%$ ) [267].

To solve this problem, pinhole free Spiro-OMeTAD films were realized by changing the synthesis technique [267,268], with a remarkable increase in stability (Fig. 3.7(b)).

■ **PEDOT:PSS** PEDOT:PSS, the HTL most commonly used in inverted PSCs, causes instability in PSCs due to its acidic and hygroscopic nature [269,270]. In particular, ITO/PEDOT:PSS interface is unstable, especially in ambient conditions [270]. Indeed PEDOT:PSS can easily adsorb water molecules in air, that can corrode ITO electrode and/or decompose the perovskite absorbing layer.

### Electrodes

The metal electrodes most commonly used in PSCs for charge collection are Au, Ag and Al (in inverted structure). Ag electrodes, that are cheaper with respect to Au ones, can be corroded in presence of MAPI [33]. The degradation process of Ag electrodes in PSCs is shown in Fig. 3.8. As previously said,  $H_2O$  can diffuse through the pinholes present in the Spiro-OMeTAD layer and reach the perovskite film, leading to its decomposition into MAI,  $PbI_2$  and HI. These iodine compounds containing volatile species can migrate from the MAPI layer to the top surface of the Spiro-OMeTAD film and reach the Ag electrode by surface diffusion. Finally, these iodides containing volatile species react with Ag to form AgI, corroding the electrode. AgI formation

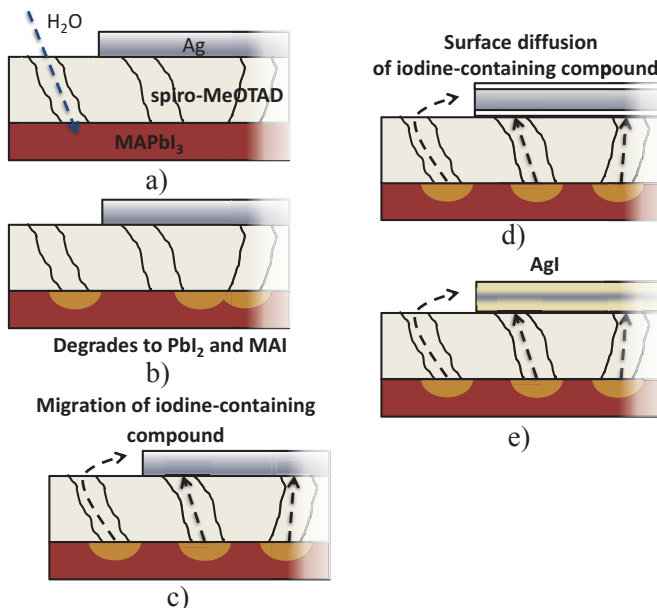


**Figure 3.8:** Schematic illustration of the degradation process of Ag electrodes [33]: a)  $H_2O$  in air diffuse through pinholes in the Spiro-OMeTAD layer. b) Decomposition of MAPI leads to the formation of iodine containing volatile compound. c) Migration of the iodine containing volatile compound from the MAPI layer to the top surface of the Spiro-OMeTAD. d) Surface diffusion of the iodine containing volatile compound, corroding the electrode. e) AgI formation.

was confirmed by XRD spectra in the aged devices [33, 271]. A similar phenomenon was also observed for Al-contacted devices [272].

Another factor of instability related to the electrodes is the migration of metal ions in PSCs. Domansky et al. [273] demonstrated that, heating the device at about 75 °C, Au ions evaporate from the electrode and diffuse across the Spiro-OMeTAD, reaching the perovskite layer. Au atoms inside the perovskite can create deep trap states, which enhance the non-radiative recombination, or produce shunts across the device, leading to a reduction of the photovoltaic performances.

### Hysteresis in PSCs

Another factor of instability in PSCs is the hysteresis in the current density-voltage (J-V) curves, that are found to be dependent on the voltage scan direction (forward or reverse scan) and on the scan rate. Therefore, the photovoltaic parameters are not uniquely determined. Hysteresis is also observed in DSSC, organic solar cell and Si solar cells when the voltage scan is too fast and is explained by capacitive effect in the device. Typically, in the reverse scan (from  $V_{OC}$  to  $J_{SC}$ ) higher current is measured than in the forward scan. Therefore, in presence of hysteresis, the reverse scan and forward scan tend to overestimate and underestimate, respectively, the efficiency of the PSCs.

In PSCs the hysteresis is strongly dependent of the device structure [238]. Snaith et al. [238] showed that planar PSCs and MSSCs presented large hysteresis than mesoporous PSCs. Moreover hysteresis in mesoporous PSCs increased passing from thick to thin  $mTiO_2$  [169, 238]. They also demonstrated that the hysteresis in these solar cells predominantly arises from the interface properties between the perovskite absorber and the transporting layers. In addition, the hysteresis in PSCs depends strongly on the scan speed of the bias voltage [238, 274].

The origin of hysteresis in PSCs is still debated and several mechanism have been proposed, as shown in Fig. 3.9):

- internal electric field associated with the polarization of perovskite ferroelectric domains under external applied bias [276–278].

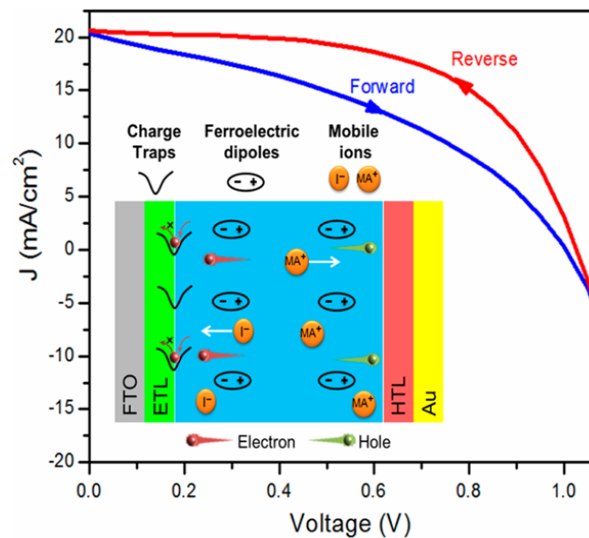


**Figure 3.9:** Example of a J-V curve with hysteresis. In the inset: schematic picture showing the different processes that can lead to hysteresis in a PSCs during J-V measurements [275]

Chen et al. [277] revealed a strong correlation between transient ferroelectric polarization of MAPI induced by a reverse external bias in the dark (pooling) and the hysteresis enhancement in photovoltaic characteristics, whose extent changes considerably with the device architecture. In particular, the effect of the internal polarization on the photo-current is less relevant in mesoporous PSCs since electrons are captured by  $\text{TiO}_2$  surface before their movement is controlled by the ferroelectric dipoles.

- the presence of trap states at the interfaces.

Li et al. [279] explained the hysteresis through dynamic charge trapping–detrapping processes. According to this group, hysteresis is caused by two factors: releasing of carriers from shallow traps with changing bias and change in electric field due to deeper trap states.

- migration of the ions in perovskite ( $\text{MA}^+$ ,  $\text{I}^-$ ,  $\text{Pb}^{2+}$ ) under applied voltage [280, 281].

Under applied bias the volatile ions will migrate towards the electron/hole collector interfaces to compensate the electric field in regions close to the electrodes, leading to an accumulation of positive and negative space charges near the interface of each contact. This charge accumulation is equivalent to n and p-doping near the charge collection interfaces, providing a band bending near the contacts.

### Strategies to improve the stability of PSCs

In order to overcome the problem of instability and produce stable PSCs, several approaches have been developed, that include modification of the perovskite composition and/or the charge transporting layers. We already discussed in sec. 2.3.1 how to improve the stability of the absorbing layer changing the composition. Now, we discuss alternative charge transporting layer to improve the stability of PSCs.

■ **ETLs modification:** In order to overcome the UV instability, Snaith et al. [30, 209] replaced  $\text{mTiO}_2$  with an insulating mesoporous  $\text{Al}_2\text{O}_3$  scaffold. These meso-superstructured solar cells (MSSC) showed performance for a period of over 1000 h. Recently,  $\text{SnO}_2$  was also proposed as a promising ETL [136, 241, 242] due to a lower conduction band [241] and an higher electron mobility [282] with respect to  $\text{TiO}_2$ . PSCs fabricated using  $\text{SnO}_2$  as ETL showed a faster electron extraction [218, 241, 242] and an higher stability [136, 241] with respect to  $\text{TiO}_2$ -based PSCs.

■ **HTLs modification:** Since PEDOT:PSS is unstable in ambient air and the conventionally additives used to dope Spiro-OMeTAD (TBP, Li-TFSI) have negative effect on the stability of perovskite, alternative inorganic and organic HTLs have been explored to improve the stability of PSCs [260].

In PSCs with direct configuration, copper iodide ( $\text{CuI}$ ) [283, 284] and copper thiocyanate ( $\text{CuSCN}$ ) [285, 286] were employed as inorganic HTL to replace Spiro-OMeTAD. PSCs with  $\text{CuI}$  as HTL showed a better stability under illumination [284] and less hysteresis [283] with respect to the device with Spiro-OMeTAD. Devices with  $\text{CuSCN}$  showed a better thermal stability [286] with respect to PSC with Spiro-OMeTAD as HTL.

In inverted PSCs, the most successful results in terms of device stability was obtained by using nickel oxide ( $\text{NiO}_x$ ), that, compared to other inorganic HTLs, is cheaper and easy to

synthesize. By replacing PEDOT:PSS with  $\text{NiO}_x$  [165, 266, 287] a significant enhancement in stability was achieved.

Finally, another material that was recently introduced in PSCs is graphene. We discuss in the following section the improvement in the device performance and stability that were reached by using graphene in PSCs.

### 3.1.2 Graphene in perovskites solar cell

Graphene, an atomically thin layer of carbon atoms stacked in regular two-dimensional (2D) hexagonal lattice, attracted great interest for optoelectronic applications and for energy conversion [288] thanks to its exceptional electronic, optical and mechanical properties. Several unique properties make it attractive: high charge carrier mobility ( $2 \text{ m}^2 \text{ V}^{-1} \text{ s}^{-1}$  [289]), high Young's modulus (1.0 TPa [290]), high thermal conductivity ( $5000 \text{ W m}^{-1} \text{ K}^{-1}$  at room temperature for a single layer [291]) and high optical transmittance [292]. Moreover, its work function (WF), equals to 4.2 eV for pure graphene [293], can be tuned by chemical modification (oxidation, doping) [293–295]. In Tab. 3.1 the WF of pure graphene and graphene related materials (GRMs) are reported.

**Table 3.1:** WF of graphene and GRMs. Variations from the values of this table are reported in the literature.

	WF (eV)	Ref.
Graphene	4.2	[293]
Graphene oxide (GO)	4.95	[296]
Reduced GO (RGO)	4.4–6.7	[297]
Lithium-neutralized GO (GO-Li)	4.3	[295]

The easy tunability of the WF make graphene and GRMs ideal candidates as transporting layers in PSCs, where the band alignment is fundamental to obtain efficient electrons and holes collection. As a matter of fact, graphene and GRMs were recently integrated in PSCs as transporting layers [180, 298, 299], dopants in transporting layers [53, 296, 300–302], or as interlayers between perovskite and transporting layers [53, 296, 303], with the aim of improving the PCE and the long term stability of the device.

#### Graphene-based HTL

GO is generally employed in PSCs as HTL [180] or as interlayer between perovskite and HTL [296, 304] due to its high WF ( $\sim 5 \text{ eV}$ ). GO-based PSC exhibits better photovoltaic performance with respect to cells with the conventional HTLs; in addition, the morphology of MAPI film is improved when it is grown onto GO substrate (see Fig. 3.10(a)).

However, perovskite degradation is faster in GO-based PSCs [296] since GO contains oxygen species (see Fig. 3.10(b)). An improvement of the device stability was obtained by using RGO as HTL [298, 299] instead of GO. The better stability of devices with RGO was associated with the inherent passivation ability of RGO against oxygen and moisture: thus the decomposition of MAPI film is lower [299].

#### Graphene-based ETL

Doping  $\text{mTiO}_2$  with graphene is an effective way to improve the stability and the performance of PSCs [296, 300–302]. Wang et al. [302] introduced graphene flakes into  $\text{mTiO}_2$  ( $\text{G+mTiO}_2$ ),

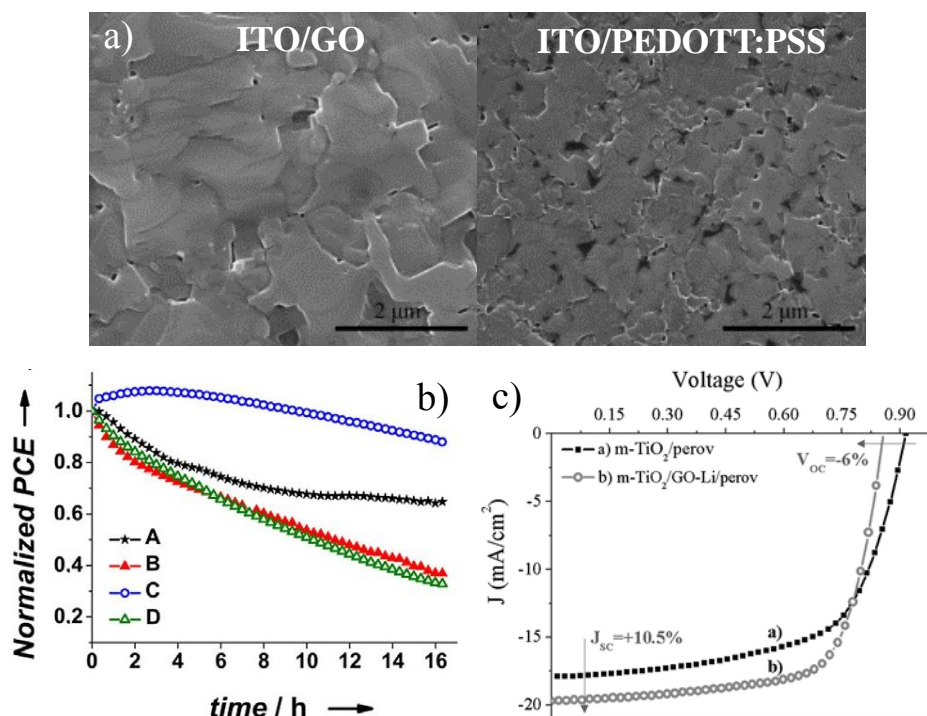


**Figure 3.10:** a) SEM images of perovskite films grown on ITO/GO (left) and ITO/PEDOT:PSS (right). Perovskites grown onto GO exhibited a high surface coverage [180]. b) Normalized PCE evolution versus time for the following devices: (A) Reference (FTO/cTiO<sub>2</sub>/mTiO<sub>2</sub>+G/perovskite/GO/Spiro-OMeTAD/Au), (B) G+mTiO<sub>2</sub> instead of mTiO<sub>2</sub>, (C) GO interlayer between perovskite and Spiro-OMeTAD, (D) mTiO<sub>2</sub>+G instead of mTiO<sub>2</sub>, GO interlayer between perovskite and Spiro-OMeTAD [296]. c) J-V curves under 1 SUN illumination for the devices with mTiO<sub>2</sub> and mTiO<sub>2</sub> plus GO-Li as ETL [303].

increasing the PCE from 10 % to 15.6 %. The PCE enhancement was attributed to a reduction of the energy barrier height at the ETL/FTO interface, because graphene has a WF between that of FTO and the TiO<sub>2</sub> conduction band. Moreover, a better long-term stability under illumination in PSCs with G+mTiO<sub>2</sub> was demonstrated by Agresti et al. [296] (Fig. 3.10(b)). Alternatively, Han et al. used RGO to dope mTiO<sub>2</sub> [301], obtaining again better photovoltaic performance.

Finally, also GO doped with atoms that reduce its WF can be used as ETL. In particular, the substitution of H atoms in the carboxyl groups of GO with Li atoms leads to a reduction of GO WF from 5 eV to ~4.3 eV [295]. Moreover, Li treatment has a beneficial role in the passivation of the surface traps and in the improvement of the electron injection [300, 305].

Since GO-Li WF matches with the TiO<sub>2</sub> conduction band, Aldo di Carlo group's [303] recently introduced GO-Li as interlayer between perovskite and mTiO<sub>2</sub> ETL. A remarkable improvement in PCE was observed in case of mTiO<sub>2</sub> plus GO-Li as ETL, mainly ascribed to an higher fill factor (FF) and an increase of the short circuit current density (J<sub>sc</sub>) (Fig. 3.10(c)). Moreover, the device with mTiO<sub>2</sub>/GO-Li as ETL showed a better long-term stability with respect to the device with only mTiO<sub>2</sub>, because of a passivation of TiO<sub>2</sub> oxygen vacancies, that are the main reaction centers for moisture attack.

To conclude this section, in Tab. 3.2 the structure, performance, the improvement and the drawback of the most representative graphene-based PSCs are listed.

**Table 3.2:** Summary of the most representative graphene-based PSCs: device structures, photovoltaic performances, improvements and drawbacks

Cathode	ETL	Device structure Active Layer	HTL	Anode	PCE (%)	$J_{SC}$ (mA/cm <sup>2</sup> )	$V_{OC}$ (V)	FF (%)	Improvements and drawbacks	Ref.
ZnO/Al	PC <sub>61</sub> BM	MAPbI <sub>3-x</sub> Cl <sub>x</sub>	GO PEDOT:PSS	ITO	12.40 9.26	17.46 15.09	1.00 0.93	71 66	More efficient hole extraction and better crystalline quality of perovskite layer with GO as HTL.	[180]
FTO	cTiO <sub>2</sub>	MAPI	GO/Spiro-OMeTAD Spiro-OMeTAD	Au	14.5 10.0	20.0 18.5	1.03 0.93	72 64	GO improves the contact between perovskite and Spiro-OMeTAD and retards the radiative recombination at the TiO <sub>2</sub> interface.	[304]
Ag/BCP	PC <sub>61</sub> BM	MAPI	RGO PEDOT:PSS	ITO	9.95 8.8	14.81 13.65	0.95 0.92	71.13 69.97	Better charge transfer, long-term stability and perovskite crystalline quality with RGO as HTL.	[299]
FTO	G+mTiO <sub>2</sub> /Al <sub>2</sub> O <sub>3</sub> mTiO <sub>2</sub> /Al <sub>2</sub> O <sub>3</sub>	MAPbI <sub>3-x</sub> Cl <sub>x</sub>	Spiro-OMeTAD	Au	15.6 10.0	21.9 17.7	1.04 1.00	73 61	PCE enhancement with G+mTiO <sub>2</sub> as ETL.	[302]
FTO	cTiO <sub>2</sub> /RGO+mTiO <sub>2</sub> cTiO <sub>2</sub> /mTiO <sub>2</sub>	MAPI	Spiro-OMeTAD	Ag	14.5 11.5	22.0 19.6	0.93 0.86	70.7 66.8	Better charge collection and reduced interfacial resistance doping mTiO <sub>2</sub> with RGO.	[301]
FTO	cTiO <sub>2</sub> /G+mTiO <sub>2</sub> cTiO <sub>2</sub> /mTiO <sub>2</sub>	MAPI	GO/Spiro-OMeTAD GO/Spiro-OMeTAD	Au	18.19 14.11	22.48 20.92	1.08 1.05	75.12 64.10	Better electron extraction and long-term stability in case of G+mTiO <sub>2</sub> ETL. Faster perovskite degradation in presence of GO.	[296]
FTO	cTiO <sub>2</sub> /G+mTiO <sub>2</sub>	MAPI	Spiro-OMeTAD	Au	15.34	20.93	1.03	71.08		
FTO	cTiO <sub>2</sub> /mTiO <sub>2</sub> <sup>[a]</sup>	MAPI	Spiro-OMeTAD	Au	18.89	22.07	1.097	78		
FTO	cTiO <sub>2</sub> /mTiO <sub>2</sub> <sup>[a]</sup> +RGO	MAPI	Spiro-OMeTAD	Au	19.54	21.984	1.11	80	Faster electron extraction when RGO is added in mTiO <sub>2</sub> . RGO gets worse the crystalline quality when is added in perovskite or Spiro-OMeTAD.	[300]
FTO	cTiO <sub>2</sub> /mTiO <sub>2</sub> <sup>[a]</sup>	MAPI	Spiro-OMeTAD	Au	17.8	21.853	1.104	73.8		
FTO	cTiO <sub>2</sub> /mTiO <sub>2</sub> <sup>[a]</sup>	MAPI	RGO+Spiro-OMeTAD	Au	18.76	21.455	1.108	78.9		
FTO	cTiO <sub>2</sub> /mTiO <sub>2</sub> /GO-Li cTiO <sub>2</sub> /mTiO <sub>2</sub>	MAPI	Spiro-OMeTAD	Au	11.8 10.3	19.61 17.7	0.859 0.915	70.3 65.4	Better electron extraction and long-term stability adding GO-Li interlayer.	[303]
FTO	cTiO <sub>2</sub> /mTiO <sub>2</sub>	MAPI	Spiro-OMeTAD	Au	11.6	112.8 <sup>[b]</sup>	8.72	59.4		
FTO	cTiO <sub>2</sub> /mTiO <sub>2</sub> /GO-Li cTiO <sub>2</sub> /G+mTiO <sub>2</sub>	MAPI	Spiro-OMeTAD	Au	11.9 12.5	118.0 <sup>[b]</sup> 121.6 <sup>[b]</sup>	8.23 8.46	62.4 61.4	Better long-term stability in case of G+mTiO <sub>2</sub> as ETL. Higher $J_{SC}$ when graphene-based ETLs are used.	[53]
FTO	cTiO <sub>2</sub> /G+mTiO <sub>2</sub> /GO-Li	MAPI	Spiro-OMeTAD	Au	12.6	114.8 <sup>[b]</sup>	8.57	64.6		

BCP = Bathocuproine

Notes: <sup>[a]</sup> mTiO<sub>2</sub> treated with Li before the deposition of perovskite layer.<sup>[b]</sup> Current (mA) extracted from large area devices (50 cm<sup>2</sup> of active area).



## 3.2 Applications beyond photovoltaics

In this section we discuss the possible application of perovskite materials for light emission (LED and laser).

### 3.2.1 Perovskite LEDs

Electroluminescence (EL) properties in perovskite materials were studied well before their development for photovoltaic absorber. An early work of Saito and coworker [306] in 1994 demonstrated electroluminescence from a 2D layered perovskite  $(C_6H_5C_2H_4NH_3)_2PbI_4$ , but only at liquid-nitrogen temperature. Since this seminal work, only few papers concerning light emission from perovskites were reported until 2014, when the first room-temperature perovskite LED (PeLED) was demonstrated [307]. In this work, hybrid  $MAPbI_3$ ,  $MAPbBr_2I$  and  $MAPbBr_3$  perovskites were used as emitting layers for near-infrared, red and green PeLEDs, respectively: the external quantum efficiency (EQE) ranged from 0.1 to 0.4 %.

A typical PeLED (Fig. 3.11(a)) consists of a front transparent electrode, an ETL (HTL), a perovskite emitter, an HTL (ETL) and a back electrode. Under forward bias, charge carriers are injected into the perovskite emitter where recombine radiatively, emitting photons (see Fig. 3.11(b)). We can see that the structure of a PeLED is similar to a PSC (Fig. 3.2(a)), but the role of the charge transporting layers (ETL and HTL) in the two cases is different: in a PeLED the transporting layers must enable the transport of electrons and holes inside the perovskite layer, where recombine radiatively, whereas in a PSC carriers must be separated in order to generate a photo-current. Therefore, also in a PeLED the choice of the transporting layers with the correct band alignment is crucial to the device efficiency. For an efficient PeLED, an ETL with a deep valence-band (to block holes) and an HTL with a low electron-affinity (to block electrons) is preferred.

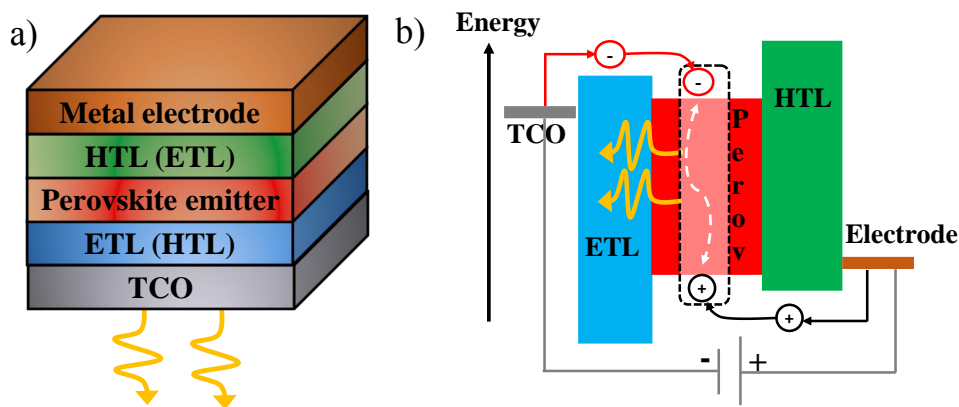


**Figure 3.11:** a) Schematic structure of a PeLED. b) General operation of a PeLED.

Early PeLEDs reported by Tan et al. employed the basic structure of the PSCs [307]: the perovskite active layer ( $MAPbX_3$ ) was sandwiched between  $mTiO_2$  (ETL) and Spiro-OMeTAD (HTL). Subsequently, modification of the transporting layer and the improvement of the quality of the active layer led to an increase of the EQE. In only one year of research, the EQE of  $MAPbBr_3$  PeLEDs passed from 0.1 % [307] to 8.53 % [308]; the rise in the EQE was much faster with respect to the rise of the EQE in organic LEDs (OLEDs) or QD LEDs (QLEDs). [54]. However, the EQE of PeLEDs remains below the efficiency (>20%) demonstrated for

OLEDs and QLEDs operating in the visible [62,63]. To achieve 8.53 % of EQE, Cho et al. [308] synthesised MAPbBr<sub>3</sub> films with small grain size ( $\sim 100$  nm) by using NCs pinning instead of the conventional spin-coating. Indeed, small grains can spatially limit the diffusion length of excitons or carriers, and, therefore, increase the radiative recombination.

Concerning all-inorganic CsPbBr<sub>3</sub> perovskites, the first PeLED was reported by Song et al. [309] in 2015: the EQE was of merely 0.12 %. In CsPbBr<sub>3</sub> PeLEDs, the surface ligands plays a fundamental role for the performances of the device. Although a large number of ligands is necessary to provide sufficient surface passivation, excessive ligands can form an insulating layer because the ligands used during the synthesis of CsPbX<sub>3</sub> NCs usually have a very poor electrical conductivity; therefore, they block the charge injection and transport in the emitter. Chiba et al. [59] developed an effective washing process to remove excess ligands from the CsPbBr<sub>3</sub> NCs surfaces; PeLED based on these washed NCs exhibits an EQE of 8.73 %, that is the highest reported EQE for CsPbBr<sub>3</sub> NCs PeLEDs. High efficiency was also obtained for red CsPbI<sub>3</sub> PeLED (14.1 % [60]). Instead, all-inorganic blue PeLEDs, that are obtained using CsPbCl<sub>3</sub> or mixed CsPbBr<sub>3-x</sub>Cl<sub>x</sub> NCs, exhibit efficiency less than 2 % and poor stability. The low efficiency of blue PeLEDs is due to the low radiative efficiency of chloride-containing perovskite NCs and to the tendency of Cl:Br mixed halide perovskites to show segregate phase (Cl-rich and Br-rich phases) for the migration of the halogen ions under illumination and voltage bias [310,311].

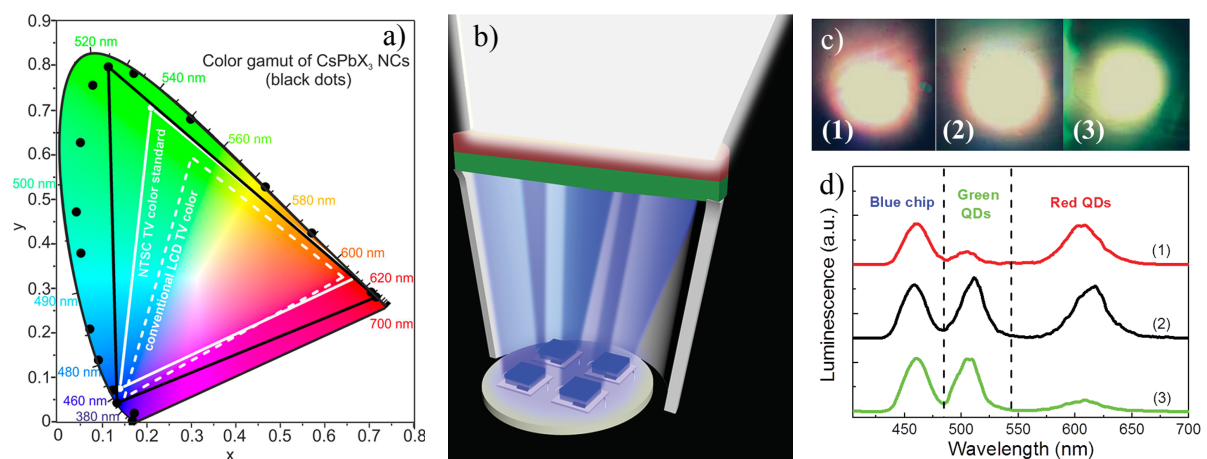


**Figure 3.12:** a) Emission from CsPbX<sub>3</sub> NCs (black data points) plotted on CIE chromaticity coordinates and compared to most common colour standards: conventional LCD TV (dashed white triangle) and National Television System Committee (NTSC) TV (solid white triangle) [18]. b) Scheme of a white LED device combining blue LED chips with CsPbX<sub>3</sub> NCs/PMMA composites [56]. c) Optical images of three typical white LED devices exhibiting (1) red-white, (2) white, and (3) green-white light, respectively [56]. d) EL spectrum of the three LED devices corresponding to the optical images in (c). The EL spectra were measured with an operating voltage of 2.6 V and a current of 8 mA [56].

Apart from LEDs, halide perovskite NCs are promising candidate also as light converters in back-light display applications to replace the common rare-earth-activated phosphors. Indeed, due to the narrow emission and the continuous spectral tunability in the whole visible range (see sec. 1.3.2), CsPbX<sub>3</sub> perovskite NCs show a wide colour gamut, that covers a greater area ( $> 140$  %) than the National Television System Committee (NTSC) colour standard [18] (Fig. 3.12(a)). In a phosphor converted white LED, phosphors absorb the light emitted by a blue chip (typically GaN or InGaN semiconductors) and re-emit this light across the visible spectrum. CsPbX<sub>3</sub> can be used to replace the phosphors to finely tune the emission spectrum, but cannot be coated directly onto the blue chip due to their poor moisture stability and the

anion-exchange reaction [312], that is detrimental for the white-light emission.

For this reasons, CsPbX<sub>3</sub> NCs used for back-light applications are usually embedded in a polymeric matrix (for example Poly(methyl methacrylate), PMMA) [56] or in porous templates [313]. In Fig. 3.12(b) an example of white LEDs obtained combining blue LED chips with green and red perovskite NCs/PMMA composites is reported. These devices showed red-white, white, and green-white light (see Fig. 3.12(c,d). Moreover, the correlated colour temperature (CCT) of these devices can be tuned (2500–11500 K) by changing the ratio of green- and red-emitting perovskite NCs.

### 3.2.2 Lasing in perovskites

Stimulated emission in perovskite films were firstly observed by Kondo et al. [314] in 2005. However, CsPbBr<sub>3</sub> films exhibited a poor crystalline quality and the threshold was very high ( $\sim 100 \text{ kW cm}^{-2}$  at room temperature). In 2014, Xing et al. [315] demonstrated low-threshold amplified spontaneous emission (ASE) in MAPbX<sub>3</sub> perovskite films using a 150 fs pump pulse with a repetition rate of 1 kHz; the reported threshold was of about  $\sim 12 \mu\text{J cm}^{-2}$  at room temperature. At the same time, Deschler et al. [316] first demonstrated room temperature lasing from trihalide perovskite (MAPbCl<sub>x</sub>I<sub>3-x</sub>) in a vertical surface-emitting cavity with the perovskite as active medium. One year later, two groups reported low-threshold ASE and lasing from CsPbBr<sub>3</sub> NCs [64, 151]; in addition, the stimulated emission showed an excellent stability upon uninterrupted laser irradiation [151].

Since the first demonstration of ASE and lasing from lead halide perovskites, room temperature perovskite lasers have been realized with thin films or nanostructures, using different cavities, as shown in Fig. 3.13: perovskite single-crystal Fabry-Pérot cavity [66, 69], whispering-gallery-mode (WGM) cavity [67, 68], vertical surface-emitting laser (VCSEL) [70]. Perovskite NWRs and NPs intrinsically form Fabry-Pérot cavity, delimited by the crystal surface [66, 69]. Instead, polygonal NPs and perovskite-coated spheres naturally form WGM cavities, that provide total internal reflection of light around the resonator [67, 68]. Moreover, halide perovskites can be also embedded between multilayer dielectric Bragg reflectors (DBRs) to form vertical surface-emitting lasers (VCSELs) [70] or integrated in photonic templates [317].

In Tab. 3.3 the most representative results of ASE and lasing from MAPI and CsPbBr<sub>3</sub> perovskites at room temperature are reported. We can see that the threshold values ( $\approx \mu\text{J cm}^{-2}$ ) are comparable to other solution-processed materials, such as chalcogenide quantum dots (CQDS) [318], under similar excitation condition. However, all the results reported in Tab. 3.3 refer to ASE/lasing from lead halide perovskite under pulsed excitation, a condition well away from real

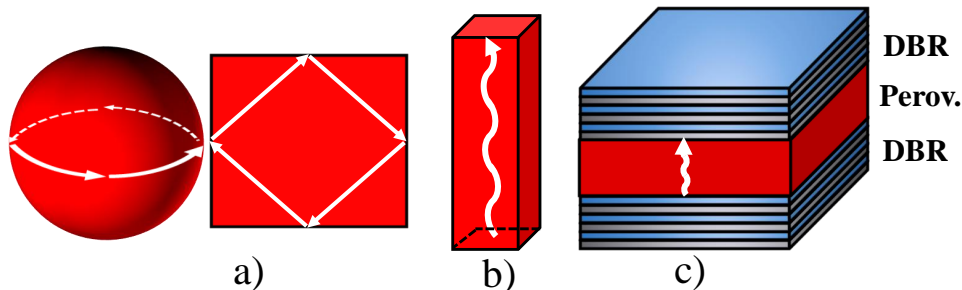


**Figure 3.13:** Different perovskite cavities: a) Spherical (left) and planar (right) WGM cavities. b) Perovskite single-crystal Fabry-Pérot cavity c) VCSEL.

laser devices, that operate under by continuous-wave (CW) optically pumping. Very recently (2018), an unpublished work of Li et al. [71] report, for the first time, lasing action in a surface emitting distributed feedback (DFB) MAPI perovskite resonator on Si substrate at room temperature under CW optical pumping, with a power threshold density of  $13 \text{ W cm}^{-2}$ . This work represents a key step toward the realization of perovskite laser diodes. Room temperature CW lasing was also demonstrated in  $\text{CsPbBr}_3$  perovskites [319], but with a very high threshold ( $\sim 10 \text{ kW cm}^{-2}$ ).

**Table 3.3:** Selected representative results of ASE/lasing from MAPI and  $\text{CsPbBr}_3$  perovskites at room temperature under pulsed excitation.

Emission layer	Morphology	Wavelength (nm)	Pump source $\lambda_{exc}, t_{pulse}, f$	Threshold ( $\mu\text{J cm}^{-2}$ )	Process	Cavity	Ref.
MAPI	thin film	$\approx 780$	530 nm, 4 ns, 10 Hz	7.6	ASE	–	[65]
MAPI	NWRs	$\approx 787$	402 nm, 150 fs, 250 kHz	0.2	lasing	Fabry Péro	[66]
MAPI	NPs	$\approx 776\text{-}784$	400 nm, 150 fs, 1 kHz	37	lasing	Planar WGM	[67]
MAPI	NPs <sup>(a)</sup>	$\approx 785\text{-}795$	400 nm, 120 fs, 76 MHz	11	lasing	WGM (array)	[317]
$\text{CsPbBr}_3$	NCs film	$\approx 535$	400 nm, 100 fs, 1 kHz	2	ASE	–	[320]
$\text{CsPbBr}_3$	NWRs	$\approx 530$	355 nm, 150 fs, 100 kHz	3	lasing	Fabry Péro	[69]
$\text{CsPbBr}_3$	NPs	$\approx 535\text{-}540$	400 nm, 50 fs, 1 kHz	2	lasing	Planar WGM	[68]
$\text{CsPbBr}_3$	NCs film	$\approx 510$	400 nm, 100 fs, 1 kHz	29	lasing	VCSEL	[70]

<sup>(a)</sup> NPs were grown on an array of hexagonal boron nitride buffer layer.

## §4§ Experimental techniques and setup

The study of the optical properties of MAPI and CsPbBr<sub>3</sub> perovskites presented in the following chapters was performed by using photoluminescence (PL) spectroscopy. In this chapter we firstly discuss the principle of this technique, underlying the physical information that can be obtained and then we describe the experimental setups used to carry out the different measurements.

### 4.1 Photoluminescence

PL spectroscopy is an experimental technique extensively used to investigate the optical properties of semiconductors. This technique consists in exciting the material with photons having an energy equals or greater than the semiconductor band gap ( $E_g$ ) and to measure the emitted light, that arises from the radiative recombination, i.e. emitted photons, of photo-excited carriers.

If the excitation is non-resonant ( $E > E_g$ ), carriers are excited with an excess energy respect to the minimum (maximum) of the conduction (valence) band. These non equilibrium carriers typically relax towards bottom of the band before recombining, losing their energy through inelastic scattering processes. The carriers relaxation process can be more or less described by four regimes [321], that occur in different time scales. Firstly, we have the *coherent regime* (duration  $< \text{ps}$ ), characterized by a well-defined phase relationship between the excited carriers and the electromagnetic field that created the excitation. Carrier-carrier scattering is the main responsible of the dephasing, that occurs on a very fast time scale (sub-pico second), leading to the *non-thermal regime*, where the carrier distribution is non-thermal, i.e. it can not be described by a temperature. The non-thermal regime, which takes place on a picosecond time scale, is characterized by carrier-carrier scattering processes and by electron-optical phonon scattering, that bring the non-thermal distribution to a hot thermal distribution (*hot-carrier regime*). In the *hot-carrier regime* (duration  $10 \div 100 \text{ ps}$ ) the carriers are thermalized, but the temperature is higher than the lattice temperature and may be different for the various carriers (electrons, holes, excitons). During this regime, the carriers reach the lattice temperature mainly losing energy through scattering processes with acoustic phonons. At the end of the *hot-carrier regime* all carriers are in thermal equilibrium with the lattice, but there is an excess of electrons and holes compared to the thermodynamic equilibrium. For this reason, in the *isothermal regime* (duration  $> 100 \text{ ps}$ ) these excess electron-hole pairs or excitons recombine and return the semiconductor to the thermodynamic equilibrium. It has to be stressed that there is no clear separation between the different regimes that also occur on a time scale shorter or longer than previously discussed.

#### 4.1.1 Recombination processes

The recombination of charge carriers can be either radiative or non-radiative. Non radiative recombination processes are generally due to the presence of defects that act as capture centres for the carriers and do not lead to photon emission. On the contrary, the radiative recombination processes lead to the emission of photons, giving rise the PL signal. The most important radiative recombination processes in a direct band gap semiconductor are the following:

- recombination of electron-hole pairs. If the recombination occurs between electron-hole in the ground state, the photon energy is equal to the semiconductor band gap  $E_g$ ;
- recombination of free excitons (see sec.1.3.2). In this case the emitted photon energy is

$$h\nu = E_g - E_x, \quad (4.1)$$

where  $E_x$  is the exciton binding energy;

- recombination of bound excitons, that are localized excitons where one of the two carriers is bound to an impurity (donor or acceptor). In this process the emitted photon energy is lower with respect to the recombination of a free exciton:

$$h\nu = E_g - E_x - E_b, \quad (4.2)$$

where  $E_b$  is the exciton binding energy to the impurity.

- recombination of bound carriers;
- phonon replicas of the various types of recombination listed above, that are due to radiative recombination of carriers assisted by the emission of one or more longitudinal-optical (LO) phonons to enable the conservation of the crystal momentum. These emissions are at lower energies with respect to the main recombination and are equally spaced by an amount equals to the LO phonon energy ( $\hbar\omega_{LO}$ ). Therefore, the energy of the  $n$ -th phonon replica ( $E_{nLO}$ ) is given by

$$E_{nLO} = E_0 - n\hbar\omega_{LO}, \quad (4.3)$$

where  $E_0$  is the energy of the main recombination and  $n$  is the number of phonons emitted in the process.

## 4.2 Experimental setups

Now we describe the different experimental setups used to study the optical properties of the perovskite samples. We performed time-integrated photoluminescence (TI-PL) and time-resolved photoluminescence (TR-PL) experiments, varying several conditions (excitation energy, excitation power, sample temperature, polarization). In all measurements the excitation source was a laser, whose beam was focused to the sample by a lens or an objective. In the first case (macro-PL experiments, see sec.4.2.1) the excitation spot was of the order of  $\sim 100$  micron diameter, while in the second case (micro-PL experiments, see sec.4.2.2) the spot was of  $\sim 1$  micron diameter.

Concerning the TR-PL measurements, we used two different approaches:

- time-correlated single photon counting technique (TCSPC), described in sec. 4.2.4, to measure the temporal evolution of the PL signal up to  $\sim 12$  ns after the excitation. The time-resolution of this technique with our setup is of about 60 ps;
- a streak camera, described in sec.4.2.5, that provides a time resolution up to few ps. This detector allows to measure the evolution of the PL signal in the first ns after the excitation

and to extract information also on the early dynamics (relaxation processes), discussed in the previous section.

### 4.2.1 Macro-PL

A scheme of the setup used to perform macro-PL experiments is shown in Fig. 4.1. The excitation source is provided by a continuous wave (CW) or a pulsed laser with an energy equals or greater than the band gap energy  $E_g$  of the investigated sample ( $E_g \sim 1.5 \div 1.7$  eV for MAPI,  $E_g \sim 2.3$  eV for CsPbBr<sub>3</sub>). In case of a laser source with an energy  $E < E_g$ , the beam is frequency-doubled with non-linear crystals. A list of the different laser sources used for TI and TR macro-PL experiments is shown in Tab. 4.1.

**Table 4.1:** List of the laser source used for TI and TR macro-PL experiments.

Laser	Operating Mode	Wavelength (nm)	Notes
Diode laser MLL-III-405	CW	405	
Thorlabs CPS520	CW	515	
Thorlabs CPS532	CW	532	
Dye Laser (Rhodamine 6G)	3 ps pulse; rep. rate 76 MHz	590-620	The laser is optically pumped by a Coherent Antares Nd:YAG laser, whose beam is frequency-doubled with a non-linear lithium triborate (LBO) crystal.
Spectra Physics Ti:Sapphire	1.2 ps pulse; rep. rate 81.3 MHz	700-850	The laser is optically pumped by the second harmonic of a CW Nd:YAG laser.
Frequency doubled Coherent Antares Nd:YAG	100 ps pulse; rep. rate 76 MHz	532	

The laser beam is focused by a lens on the sample, placed in a closed-cycle cold-finger helium cryostat, whose temperature can be varied from 10 K to 300 K. The emitted light from the sample is collimated and then focused on the entrance slit of a spectrometer (*Acton Spectra Pro 2500i*), that has a focus length of 50 cm.

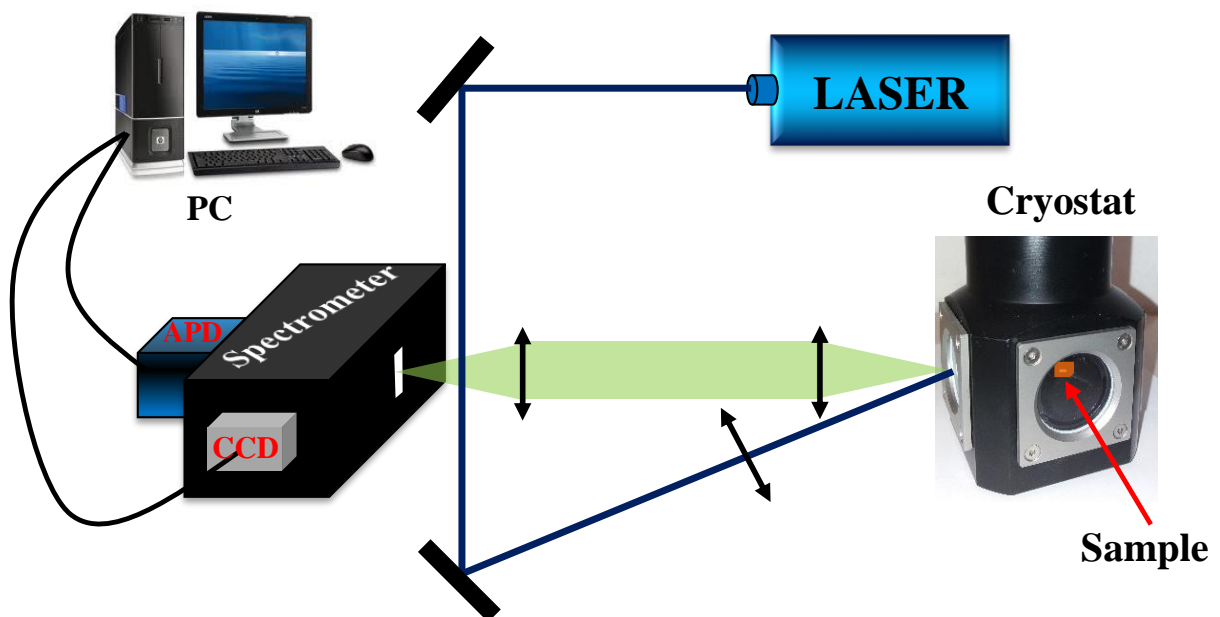


**Figure 4.1:** Scheme of the experimental setup used for macro-PL measurements.



The spectrally dispersed light is detected in two different ways:

- with an avalanche photodiode (APD) *ID Quantique ID100-20* having an active area of  $20\ \mu\text{m}$ , placed at the exit slit of the spectrometer;
- with a charge coupled detector (CCD) *Andor DU420-BU*, composed by a matrix of  $1024 \times 256$  pixels, placed at the flat field exit of the spectrometer. The dimension of each pixel is  $26\ \mu\text{m}$ .

The spectral resolution of our macro-PL setup is of about  $1\ \text{meV}$ .

#### 4.2.2 Micro-PL

In macro-PL setup, the laser beam is focused by a long focal length lens, thus the sample is excited with a spot of the order of  $100\ \mu\text{m}$  diameter. As a consequence, the measured PL signal is the average emission from a large area of the sample. On the contrary, micro-PL setup enables us to excite the sample with a spot of only few microns, allowing us to investigate the emission properties of single micro-structures.

A scheme of the micro-PL setup is shown in Fig.4.2. The excitation source is a mode-locked femtosecond Ti:Sapphire laser (*Spectra Physics Tsunami*), pumped with a frequency doubled CW Nd-YAG laser (*Millennia, Spectra Physics*). This laser emits pulses that have a duration of  $\sim 200\ \text{fs}$ , at a  $81.3\ \text{MHz}$  repetition rate. The emission wavelength is tunable in the range  $700\text{--}850\ \text{nm}$ . To obtain an energy greater than the band gap of our samples the beam is frequency-doubled by a non-linear Beta Borate (BBO) crystal. In addition, the sample can be illuminated also with a white light; the reflected light is detected by a camera to acquire the image of the sample.

In this apparatus we use a confocal geometry: the focalization of the laser and the collection of the PL is obtained by an infinity corrected *Mitutoyo* objective (magnification  $100\times$ , numerical

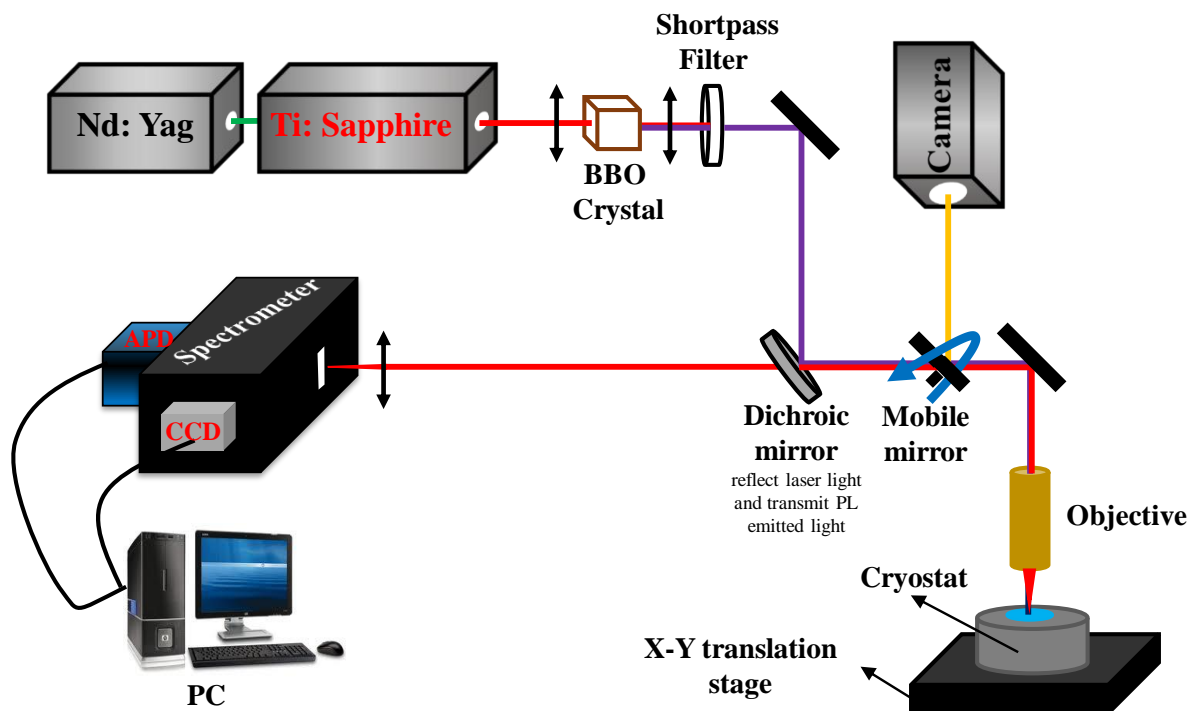


Figure 4.2: Scheme of the experimental setup used for micro-PL measurements.

aperture  $NA = 0.7$ ). The sample is kept in a low-vibration continuous cold-finger flow He cryostat, which is mounted on a *Physik Instrumente* X-Y translation stage for scanning the sample surface. The piezoelectric translation stage enable us to moved the sample with a step of about 100 nm; this allow us to acquire spatially resolved PL maps by moving the laser spot in different points of the sample and acquiring the PL spectrum in each point.

The collected PL is then focused on the entrance slit of an *Acton SP2300i* spectrometer (focal length 30 cm) and detected with a CCD or an APD, as for macro-PL experiment. In this case we use a Si CCD *Acton Pixis 100F*, composed by a matrix of  $1340 \times 100$  pixels, and an *ID quantique ID100-MMF50* APD, with an active area of  $50 \mu\text{m}$ . The spectral resolution is of about 1 meV.

### 4.2.3 Polarization resolved measurements

In order to investigate the origin of the superlinear emission in MAPI perovskites (see sec. 6.4) we also performed micro-PL polarization resolved measurements.

In this kind of measurements before the entrance slit of the spectrometer an half-wave plate is positioned, to rotate the polarization, in combination with a polariser, to select the polarization. We acquire the PL spectrum of the sample as a function of the polarization angle. The principle of this measure is shown in Fig. 4.3. Suppose that  $\theta$  is the polarization angle of the emitted light with respect to the  $x$  axis and that  $\alpha$  is the angle between the optical wave plate's axis and the  $x$  axis. Since an half-wave plate rotates the polarization of an angle that is twice the angle between the input polarization and the optical wave plate's axis, the polarization is rotated of an angle  $2(\alpha - \theta)$  with respect the initial direction. Thus the polarization angle of the light after the half-wave plate is  $2\alpha - \theta$  with respect to the  $x$  axis. We can note that, if the half-wave plate is rotated of an angle  $\alpha$ , the polarization angle is rotated of an amount  $2\alpha$ .

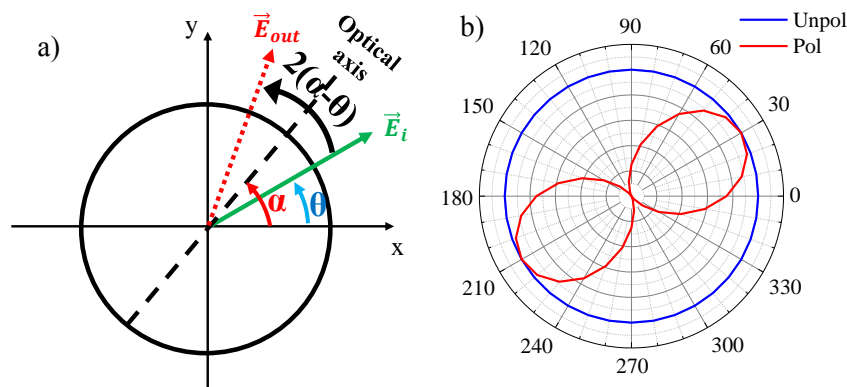


**Figure 4.3:** a) Operating principle of an half-wave plate.  $\vec{E}_i$  and  $\vec{E}_{out}$  are the polarization of the emitted light before and after the half-wave plate, respectively. b) Polar diagram of an unpolarized (blue curve) and of a polarized (red curve) signal. The polarization angle of the red signal is  $30^\circ$  with respect to the  $x$  axis.

Now we consider the polarizer. According to the Malus'law, if the polarizer is aligned along the  $x$  axis, the light intensity after the polarizer is given by

$$I(\alpha) = I_0 \cos^2(2\alpha - \theta), \quad (4.4)$$

where  $I_0$  is the initial intensity. If  $2\alpha = \theta$  we have the maximum intensity. To understand if the emission is polarized or not, we plot the polar diagram, where the intensity is reported

as a function of the polarization angle (Fig. 4.3(b)). If the signal is unpolarized we obtain a circumference (the intensity is constant), otherwise we obtain a curve that is “stretched” along the polarization direction.

#### 4.2.4 Time correlated single photon counting

In this section we describe the time-correlated single photon counting (TCSPC) technique, that is extensively used in several fields besides spectroscopy to measure the temporal evolution of a signal. We use this technique in macro-PL and in micro-PL experiments. The TCSPC technique consists in the periodic excitation of the sample with a periodic pulse having a high repetition rate and in the measurement of the time difference between the first detected photon and the excitation pulse. Repeating the measure over multiple cycles of excitation and emission one can reconstruct the temporal distribution of the emitted photons, as long as the single-photon emission regime condition is satisfied. This technique is based to two assumption:

- the physical event that produces the photon emission is the same for each excitation pulse;
- the probability to detect one photon for each event is much less than one ( $\sim 10^{-3} \div 10^{-4}$ ).

The second hypotheses is fundamental to reconstruct the temporal distribution of the emitted photons and is satisfied only in single-photon detection regime. To maintain a photo-counting regime the average count rate must be at least 100 times below the laser repetition rate. For example, if we use a Ti:Sapphire laser (repetition rate 81.3 MHz), the count rate of the detector (APD) should be less than  $\sim 8 \cdot 10^4$  counts for second.

The setup used for TCSPC measurements is shown in Fig. 4.4. The first photon emitted from the sample is detected with an APD, that produces an electric signal. The signal of the APD is amplified and discriminated by a constant fraction (CFD) to obtain a logical pulse. On the other hand, a reference signal of the excitation pulse is given by a photodiode or by an electrical signal supplied directly by the laser. These pulses are passed together into a time-to-amplitude converter (TAC), that produces a voltage signal proportional to the time difference between these two signals. Finally, the output voltage of the TAC is passed into an analogue-to-digital converter (ADC) and is analysed by a multichannel analyser (MCA), that reconstructs the time histogram. It is worth noting that the *START* signal corresponds to the first emitted

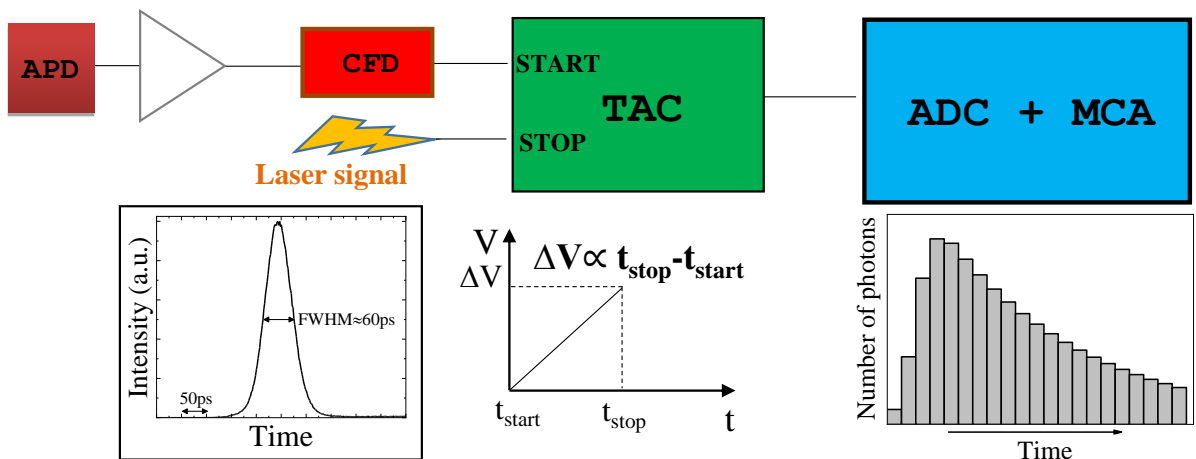


**Figure 4.4:** Experimental setup for TCSPC measurements. Inset: example of a laser temporal profile (Dye laser). The temporal response for TCSPC apparatus is estimated as the FWHM of this curve.

photon, while the *STOP* signal to the laser pulse. The reason of this “reverse configuration” is that, as seen before, this technique reproduces correctly the PL temporal profile only if the probability of detecting one photon for pulse is much less than one. As a consequence, by using the “reverse configuration”, TAC produces a voltage only when a photon is detected. In our setup the temporal resolution of this experimental apparatus is of about  $\sim 60$  ps, as shown in the inset of Fig. 4.4, where an example of a laser temporal profile is reported.

If carriers recombine in a temporal scale that is comparable or higher than the period between two pulses, PL decay signal does not exhaust completely in one period. As a consequence, a pedestal is formed before PL rise due to carriers that recombine at longer time than the repetition period. The pedestal can be seen as an estimate of the stationary population in the radiative states and help us to understand the charge recombination dynamics on CsPbBr<sub>3</sub> NCs in presence of surface states (see Chap. 7).

### 4.2.5 Streak camera

To obtain a better time resolution with respect to the TCSPC technique we used a streak camera (*Hamamatsu C5680*) in macro TR-PL experiments, that allow us to acquire simultaneously the spectral and the temporal evolution of the PL signal. The streak camera is placed at the flat field exit of the spectrometer, as well as the CCD, and the sample is excited with a Ti:Sapphire laser (see Tab. 4.1).

The operating principle of a streak camera, that can be defined an “optical oscilloscope”, is shown in Fig. 4.5. Photons emitted from the sample are spectrally dispersed by the spectrome-

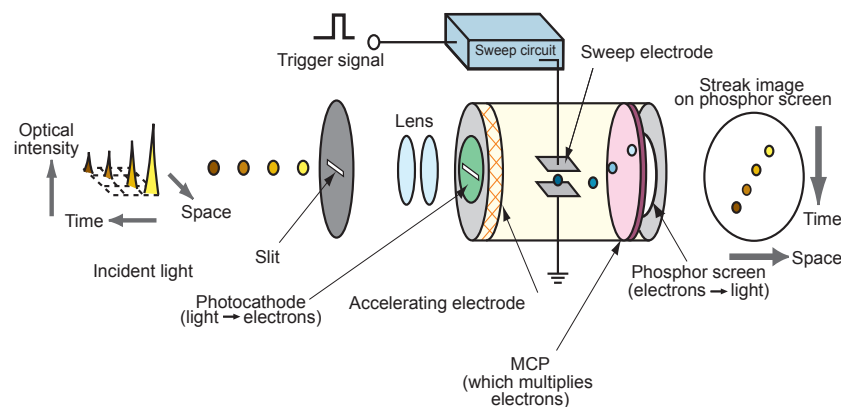


**Figure 4.5:** Operating principle of a streak camera.

ter and reach the entrance slit of the streak camera in different horizontal positions, depending on their energy. A photocathode converts photons into photoelectrons, that are accelerated towards two horizontal sweep electrodes, where an oscillating voltage is applied. This voltage is synchronous (in frequency and phase) with the excitation laser. As a consequence, photoelectrons generated at different times are deflected in different vertical positions from top to bottom. Subsequently, the deflected photoelectrons are multiplied by a micro-channel plate (MCP) intensifier and then reach the phosphor screen, where they are converted back into light. This light is finally detected by a CCD camera, composed by 768 x 572 pixels. A two dimensional image is generated, where the energy/wavelength is in the horizontal direction, while the time

in the vertical direction (from top to bottom).

Our streak camera presents four temporal scales, that correspond to different deflection velocities of the sweep electrodes. Moreover, the streak camera can be also used in *focus* mode: in this case a time integrated PL spectra is acquired, without a temporal information. The temporal resolution of the streak camera depends to the temporal scale used during the measurement, as shown in Tab. 4.2.

**Table 4.2:** Temporal dispersion, temporal resolution and the factors that limit the resolution for the 4 temporal scales of the streak camera used in TR-PL experiments. The resolution is evaluated as the FWHM of the laser temporal profile.

Temporal Scale	Dispersion (ps/px)	Resolution (ps)	Limiting factors
1	0.26	5	Asynchronism between the detector and the excitation source.
2	1.42	15	Image spatial dimension.
3	2.44	25	Image spatial dimension.
4	3.7	40	Image spatial dimension.

# §5§ Graphene-based ETL: a step-up for an efficient carrier collection

As discussed in sec. 3.1.2, graphene and GRMs have a positive impact in PSCs, both in the device performance than in the long-term stability. In this context, we carried out a collaboration with Prof. Aldo di Carlo group's of the Centre for Hybrid and Organic Solar Energy (CHOSE) of University of Rome Tor Vergata in order to better understand why the use of graphene-based ETL in MAPI PSCs improve the performance of the device. We obtained a strict correlation between the morphology of MAPI film, electron collection efficiency and the PCE.

## 5.1 Description of the samples

Four photoelectrodes are prepared by Aldo di Carlo's group of the CHOSE using different combination of mesoporous ETL: mesoporous  $\text{TiO}_2$  ( $\text{mTiO}_2$ ), graphene-doped  $\text{mTiO}_2$  ( $\text{G+mTiO}_2$ ),  $\text{mTiO}_2$  plus lithium-neutralized graphene oxide (GO-Li) interlayer,  $\text{G+mTiO}_2$  plus GO-Li interlayer. The different samples are shown in Fig. 5.1 and listed in Tab. 5.1. For clear comparison a sample of MAPI film on FTO glass without ETL (reference sample) was also investigated.

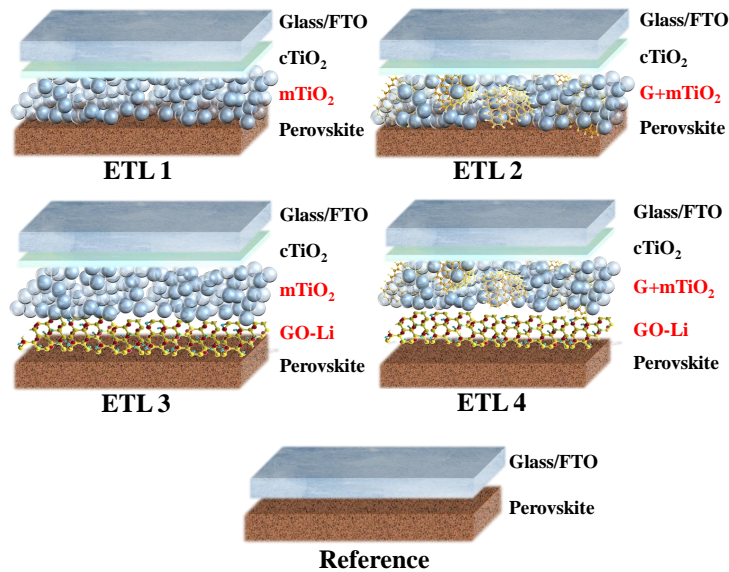


**Figure 5.1:** Structure of the investigated samples. The mesoporous ETLs are indicated in red.

Solar cell photoelectrodes were prepared on FTO conductive glass. The substrates were cleaned in an ultrasonic bath, using three sequential steps: detergent with de-ionized water, acetone and 2-Propanol (10 min for each step). FTO was then covered by a compact layer of

**Table 5.1:** List of the investigated samples and description of their corresponding ETLs.

Sample	ETL
Reference	No ETL
ETL 1	$\text{mTiO}_2$
ETL 2	$\text{G+mTiO}_2$
ETL 3	$\text{mTiO}_2$ plus GO-Li
ETL 4	$\text{G+mTiO}_2$ plus GO-Li

TiO<sub>2</sub> (cTiO<sub>2</sub>), deposited by spray pyrolysis deposition at 450 °C. The final thickness of the cTiO<sub>2</sub> layer was of about 50 nm.

The mTiO<sub>2</sub> layer was obtained starting by an ethanol solution of 18NR-T titania paste dissolved in pure ethanol (1:5 by weight), stirred overnight, and eventually doped with graphene by adding sonicated graphene ink (1% in vol.), prepared as reported in Ref. [296]. Both standard mTiO<sub>2</sub> and G+mTiO<sub>2</sub> dispersions were deposited by spin-coating onto the cTiO<sub>2</sub> surface.

The GO-Li interlayer was realized by spin coating (2000 rpm for 10 s) 200  $\mu$ L of GO-Li dispersion in ethanol/H<sub>2</sub>O (3:1), prepared as reported in Ref. [303], on sintered mTiO<sub>2</sub> (or G+mTiO<sub>2</sub>). After the deposition, the substrates were annealed at 110 °C for 10 min.

The photoelectrodes were completed by depositing the perovskite active layer in dry conditions (relative humidity less than 30%) by a double-step method: a lead iodide solution (PbI<sub>2</sub> in DMF, heated at 70 °C) was spin coated at 6000 rpm for 10 s on heated substrates (50 °C), which were then dipped into a MAI in anhydrous 2-Propanol solution for 15 min. Finally, the samples were heated at 80 °C for 20 min in air. The MAPI absorbing layer has a typical thickness of 350 nm. Since the ETL presents a mesoporous regions of about 200 nm the perovskite nanocrystals penetrate in this layer.

It is worth noting that all the samples prepared for PL measurements are simple photoelectrodes, lacking of the HTL and the bottom contact: this allows us to focus only on the electron collection and transport.

## 5.2 PL at room temperature

In this section we present macro-PL measurements at room temperature ( $T = 300$  K), that allow us to extract the electron collection efficiency for the different ETLs. The photoelectrodes were excited with the Dye laser (see Tab. 4.1), with an excitation energy of 2.06 eV and an average intensity  $I_0 = 10$  W/cm<sup>2</sup>. PL measurements were carried out exciting the samples either on the perovskite film side (side A) or the FTO side (side B). The two excitation conditions are remarkably different. Indeed, because MAPI absorption length ( $1/\alpha$ ) at about 2 eV is roughly 150 nm [7] (see Fig. 1.9(b)) and the thickness of MAPI film was of about 350 nm, by exciting from side A we probed only the perovskite overlayer and no effect related to the presence of ETL was detected. On the contrary, taking into account that FTO and TiO<sub>2</sub> have a negligible absorption, exciting from side B we probed the MAPI layer embedded into the ETL.

PL spectra at room temperature (Fig. 5.2) show a single band, centered of about 1.6 eV, for all the samples and irrespective of the excitation side: no spectral difference are observed from the different samples. This band corresponds to the radiative emission from the tetragonal phase of MAPI, as usually observed at room temperature [103, 105, 106]. However, as shown in Fig. 5.2(c), a significant reduction of the PL intensity is observed exciting from side B in presence of ETL, that can be ascribed to a carriers removal from MAPI layer towards the ETL.

On the contrary, PL decays depend on the excitation side, as shown in Fig. 5.3. By exciting from side A (Fig. 5.3(a)) PL decays are identical for all samples: no effect related to the presence of ETL is detected, since the excitation is provided only to the perovskite overlayer (not embedded in the ETL). In contrast, there is a significant difference in the PL decays by exciting from side B depending on the sample, as shown in Fig. 5.3(b): faster decays are observed in



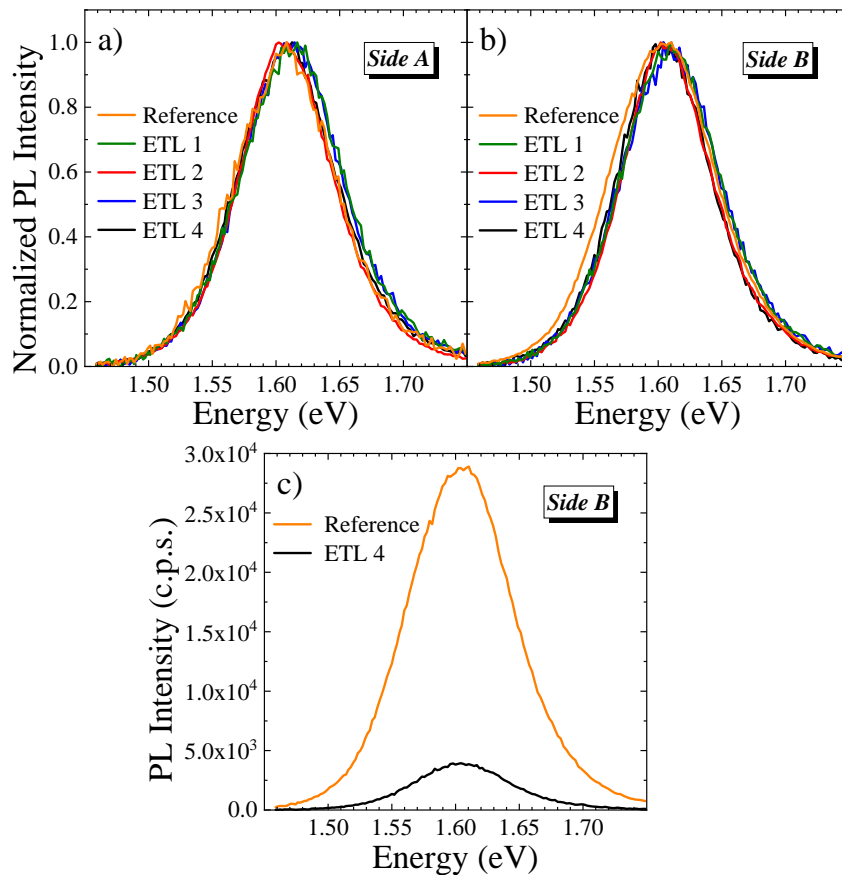


**Figure 5.2:** PL spectra at room temperature, after ps excitation at 2.06 eV with an average intensity of 10 W/cm<sup>2</sup>. a) Normalized PL spectra from side A. b) Normalized PL spectra from side B. c) Comparison between the PL spectra of the reference sample and of the ETL 4, exciting from side B.

presence of ETL, especially when graphene and/or GO-Li are used. It is worth noting that the PL decay of the reference sample excited from side B is slower with respect to the decays of side A. This can be attributed to non-radiative states at the surface of the uncovered perovskite film (side A).

To extract information about the efficiency in the carrier injection from perovskite to ETL, we first fitted the decays of Fig. 5.3(b) with a double exponential [322], taking into account the laser pulse repetition period [323]. We used the following fitting function  $I(t)$

$$I(t) = f(t) + g(t) \quad (5.1)$$

where  $f(t)$  is the original double exponential and  $g(t)$  the correction term due to the intrinsic periodic nature of TCSCP measurements [323]:

$$f(t) = \theta(t - t_0)[Ce^{-(t-t_0)/\tau_1} + (1 - C)e^{-(t-t_0)/\tau_2}] \quad (5.2)$$

$$g(t) = C \frac{e^{-(t-t_0)/\tau_1}}{e^{T/\tau_1} - 1} + (1 - C) \frac{e^{-(t-t_0)/\tau_2}}{e^{T/\tau_2} - 1}. \quad (5.3)$$

In the previous equations  $\theta(t)$  is the Heaviside step function,  $\tau_1$  and  $\tau_2$  are the decay time constants,  $T$  is the laser pulse repetition period (13.15 ns),  $C$  is the contribution of  $\tau_1$  exponential to the fit and  $t_0$  is a constant, which accounts for a time translation. An example of fit according to the Eqn. 5.1 is shown in the inset of Fig. 5.3(b) and the results obtained by this fitting procedure are reported in Tab. 5.2. Inserting graphene-based ETLs in the samples reduces  $\tau_1$

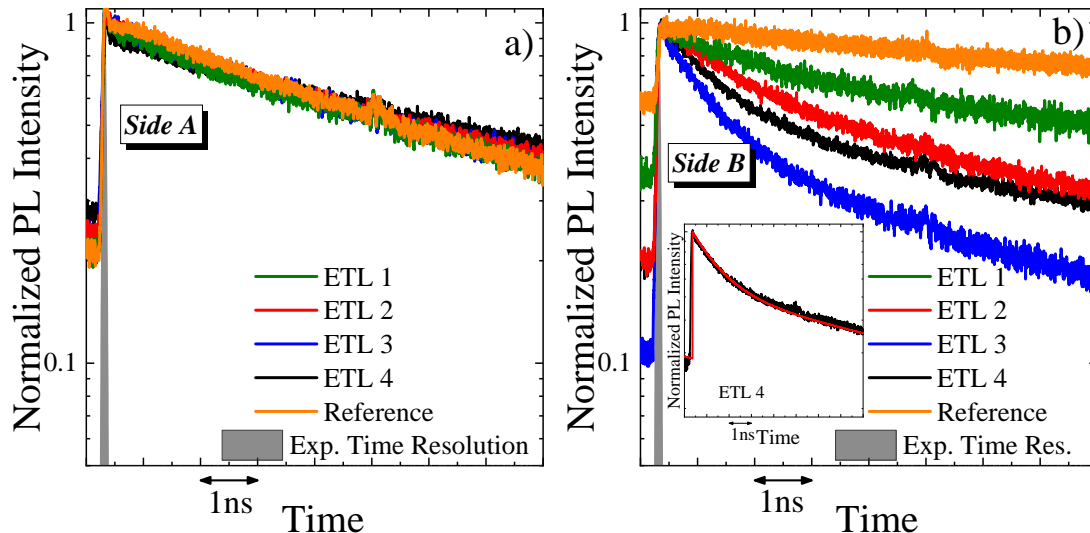


**Figure 5.3:** PL decays (at the PL peak energy) at room temperature, after ps excitation at 2.06 eV with an average intensity of  $10 \text{ W/cm}^2$ . a) From side A. b) From side B. Inset: Example of fit for the PL decay of ETL 4 according to Eqn. 5.1.

from 25 ns to 15 ns, while the reduction of  $\tau_2$  depends on the ETL. In the literature [322], the longer decay constant ( $\tau_1$ ) is ascribed to the radiative recombination in MAPI, while the shorter decay constant can be attributed to the carrier removal from MAPI layer towards the ETL. Thus, faster decays mean a better carrier injection from perovskite towards ETL.

To get rid the local inhomogeneities of the samples, which can give rise a variation of the TR-PL intensity, and considering that the PL time evolution does not depend on the detection spot, we evaluated the time-integrated PL intensity ( $I_{\text{PL}}$ ) from the PL decay and then we estimated the radiative efficiency ( $\eta$ ) since

$$I_{\text{PL}} = \eta P, \quad (5.4)$$

where  $P$  is the pump intensity, equals to  $10 \text{ W/cm}^2$  for all the TR-PL measurements. Assuming an unitary radiative efficiency for the reference sample (MAPI without ETL), we evaluated the change in  $\eta$  for the different ETLs (see Tab. 5.2). Lower  $\eta$  is obtained in case of ETLs 2, 3 and 4: thus the insertion of graphene and/or GO-Li interlayer improves the electron capture from perovskite to ETL by a factor between two and three with respect to the  $\text{mTiO}_2$  ETL. We want to remark that this result does not necessarily imply an increase of the  $J_{\text{SC}}$  of the PSC of the same amount. Indeed hole collection by the HTL [324] and non-radiative recombination in the ETL have to be taken into account. However, as shown in sec. 5.6, a significant increase of  $J_{\text{SC}}$  is measured for complete cell when ETL 4 is used.

Although room temperature PL measurements bring evidence of a better electron collection

**Table 5.2:** Results of the fits of data of Fig. 5.3(b).

Sample	$\tau_1$ ( $\pm 1$ ns)	$\tau_2$ ( $\pm 0.10$ ns)	$C$ ( $\pm 0.03$ )	$\eta$ ( $\pm 0.03$ )
Reference	25	–	1.00	1.00
ETL 1	25	2.05	0.43	0.48
ETL 2	15	1.99	0.36	0.27
ETL 3	15	1.24	0.20	0.16
ETL 4	15	1.30	0.34	0.24

in graphene-based ETLs, they did not provide any information about the crystalline quality of MAPI film embedded in the different ETLs. For this reason, we performed also PL measurements as a function of temperature, excitation wavelength and excitation power.

### 5.3 PL measurements at low temperature

In Fig. 5.4 PL spectra at low temperature ( $T = 11$  K) for the different photoelectrodes are reported. By exciting from side A (Fig. 5.4(a)) there are not spectral differences between the emission of the samples also at low temperature. Indeed, as discussed in the previous section, the emission exciting from side A comes mostly from the MAPI film and no effect related to the presence of the ETL is detected. PL spectra of Fig. 5.4(a) show two peaks, as usually reported for temperatures below 150 K in MAPI perovskites [105,106]. The high energy band, centered at about 1.65 eV, is attributed to the orthorhombic phase of MAPI. But the major contribution to the spectra comes from the low energy band, centred at about 1.55 eV. As discussed in sec. 1.3.2, this emission band is likely due to the sum of two contributions:

- the radiative recombination arising from the residual tetragonal phase at 1.56 eV. In fact tetragonal inclusions in the orthorhombic phase of MAPI at low temperature can remain [156, 157];
- the radiative recombination from localized states below 1.52 eV, that are identified with radiative traps [108, 116, 158] or, recently, to methylammonium-disordered domains in the orthorhombic phase of MAPI [103].

On the contrary, the excitation from side B (Fig. 5.4(b)) reveals the effect of the ETL. First of all, we observe a smaller contribution of the orthorhombic phase for all the samples with respect to the excitation from side A. Moreover, in the case of GO-Li plus G+mTiO<sub>2</sub> as ETL (ETL 4), we detect a strong reduction of the radiative traps at 1.52 eV and the dominance of the emission from the tetragonal phase at 1.56 eV. Such results suggest that an incomplete phase transition occurs for the perovskite wrapped into the mesoporous ETL layer. In particular, in the case of ETL 4, where the PL lineshape shows a negligible low energy tail and a smaller linewidth with respect to the other samples, we can argue that the crystallization of the MAPI film is very good. The better crystalline quality of MAPI film in case of ETL 4 is confirmed by SEM images

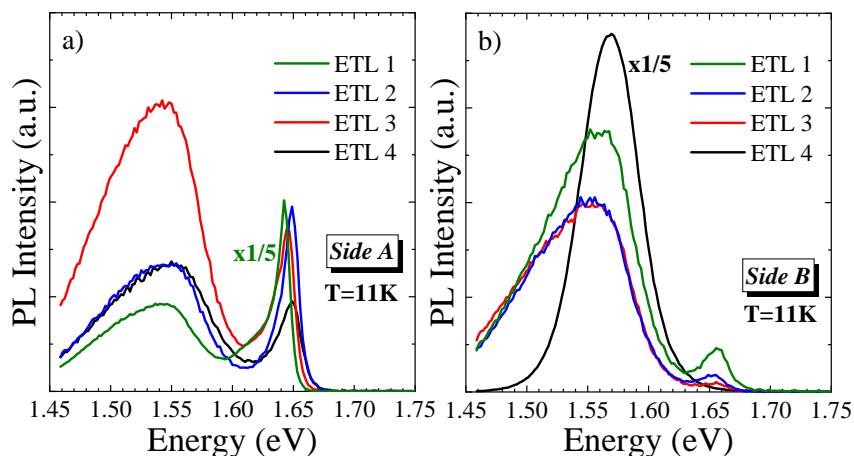


**Figure 5.4:** TI-PL spectra at 11 K for the various samples after excitation at 2.06 eV with an average intensity of 10 W/cm<sup>2</sup> from side A (a) and from side B (b).

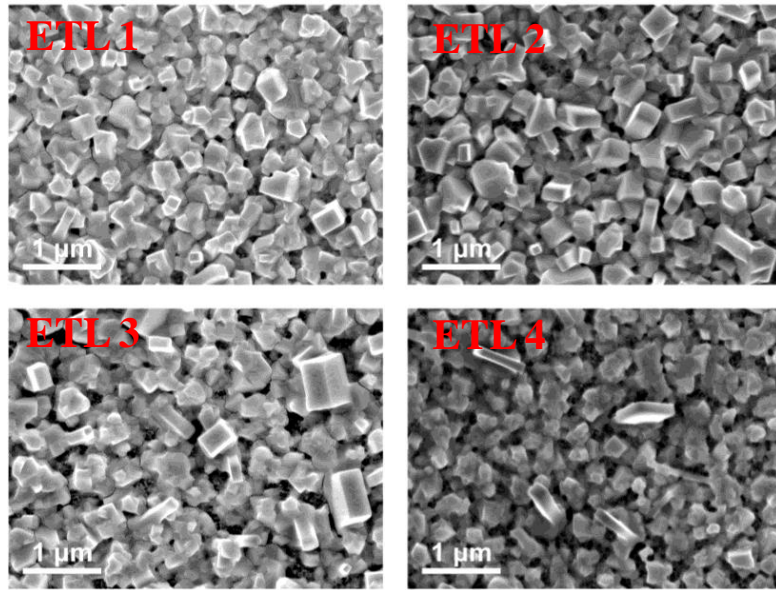


**Figure 5.5:** SEM images of the perovskite surface of the different samples.

(Fig. 5.5) of the perovskite surface: crystal size and shape regularity seems to be enhanced by both the addition of graphene in the mTiO<sub>2</sub> layer and the interposition of GO-Li interlayer.

A further evidence proving the good quality of MAPI layer in ETL 4 comes from power dependent measurements at low temperature (Fig. 5.6). Decreasing the excitation intensity by one order of magnitude, the emission from side B in ETL 4 changes completely, showing a spectrum (blue curve) similar to the side A (red curve), with the dominant contribution of the traps and a small signal from the orthorhombic phase. This is explained by the fact that, lowering the power density, only the trap energy levels close to the band gap tail are filled. In addition, the PL spectrum of the ETL 4, obtained by exciting from side B with an intensity of  $I_0/10$ , is very similar to the spectra of the ETLs 1, 2 and 3 by exciting from side B with an higher intensity  $I_0$  (Fig. 5.4(c)). This means that the trap density in the mesoporous region of MAPI in ETL 4 is lower, of about one order of magnitude, with respect to the other samples. Moreover, in case of ETL 4 excited from side B we observe a single band, that correspond to the tetragonal phase emission. This suggest that the interaction between graphene and MAPI inhibits the phase transition from tetragonal to orthorhombic, probably due to the mechanical

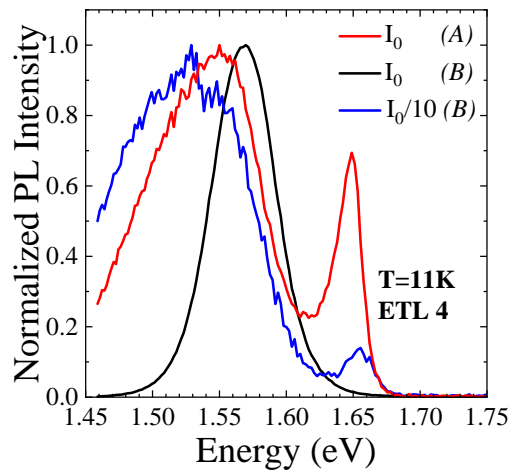


**Figure 5.6:** Normalized PL spectra of ETL4 at 11 K, for different average excitation intensities and excitation sides (in brackets).

stress of perovskite lattice induced by graphene [325, 326]. This hypothesis is confirmed by temperature dependent measurements, reported in the following section.

## 5.4 Temperature dependent PL measurements

In Fig. 5.7(a) we report the emission spectra of ETL 4 exciting from side A, varying the sample temperature from 10 to 300 K. As already shown in the previous section, at low temperature we observe two bands, one at 1.65 eV, corresponding to the orthorhombic phase, and one at about 1.55 eV, corresponding to the sum of the emission from optically active trap states and from a residual tetragonal phase. As expected in MAPI perovskites [103, 105, 116, 117], increasing the temperature, the orthorhombic phase emission shifts at higher energy (see Fig. 5.8(a)), showing a monotonic increase of its FWHM (see Fig. 5.8(b)), and it disappears above 150 K, where the phase transition of MAPI from orthorhombic to tetragonal phase occurs [79].

By increasing the temperature, the low energy band shows instead an S shape both in the peak emission energy (see Fig. 5.8(a)) and its FWHM (see Fig. 5.8(b)). Moreover, the spectrally integrated PL intensity has an enhancement around 150 K, as shown in Fig. 5.8(c). These trends are commonly observed in MAPI in presence of phase transition from orthorhombic to tetragonal phase, with the concurrent lower contribution of the radiative traps [103, 108]. Above 150 K the PL spectrum has only one peak, arising from the tetragonal phase emission, which continues to monotonically blue shift increasing the temperature.

The FWHM of the PL bands as a function of temperature can be fitted taking into account the temperature-independent inhomogeneous broadening and the interaction between carriers and acoustic and longitudinal optical (LO) phonons [103, 117], using the following equation:

$$\Gamma(T) = \Gamma_0 + \gamma_{ac}T + \frac{\gamma_{LO}}{e^{E_{LO}/k_B T} - 1}, \quad (5.5)$$

where  $\Gamma_0$  is the inhomogeneous broadening,  $\gamma_{ac}$  and  $\gamma_{LO}$  are the acoustic and LO phonon-carrier coupling strengths, respectively, and  $E_{LO}$  is the LO phonon energy. We fitted the FWHM data extracted from the PL spectra of Fig. 5.7(a) (excitation from side A), considering the orthorhombic phase from 10 K to 150 K and the tetragonal phase from 150 K up to room temperature. The solid line in Fig. 5.8(b) shows the best fitting curve and the corresponding fitting parameters are

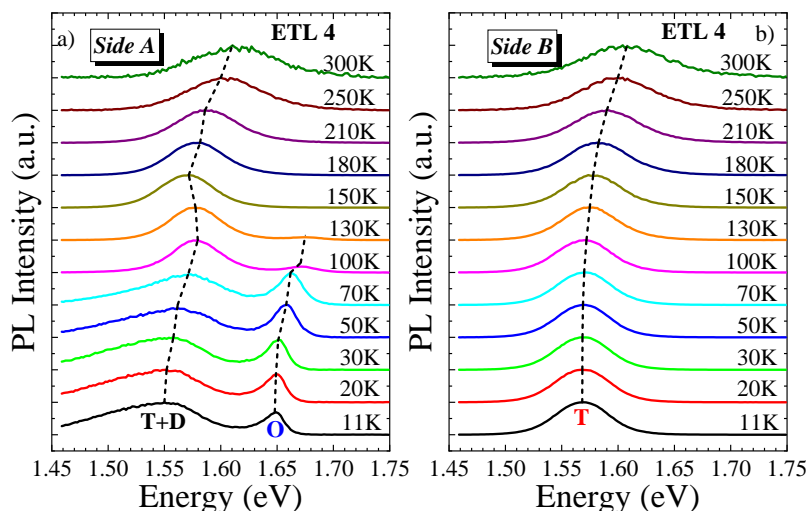


**Figure 5.7:** Temperature-dependent measurement on ETL 4 by exciting with photon energy of 2.06 eV with an average intensity of 10 W/cm<sup>2</sup>. The labels D, T and O stand for defects (trap states), tetragonal and orthorhombic, respectively. a) PL spectra from 10 to 300 K after excitation on side A. b) PL spectra from 10 to 300 K after excitation on side B.

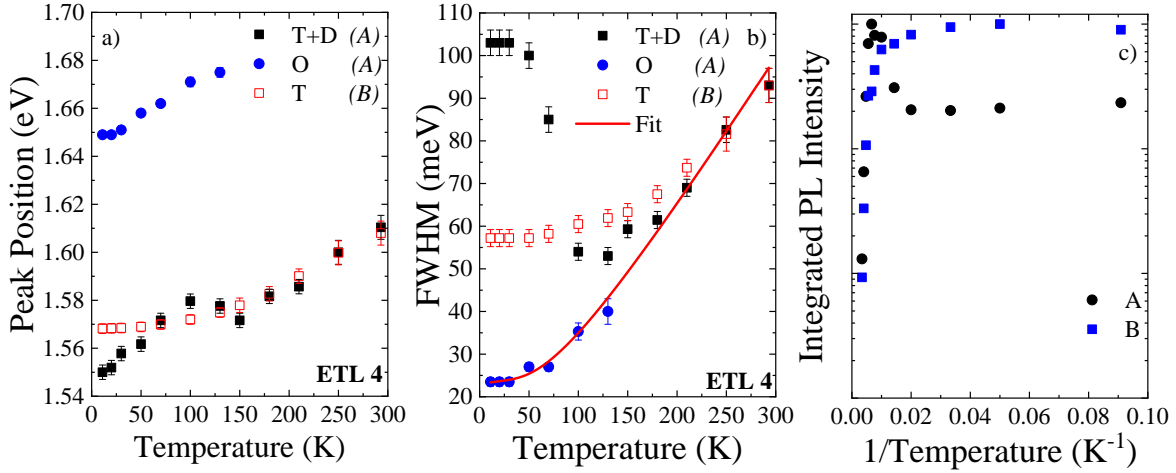


**Figure 5.8:** Analysis of the temperature-dependent measurement performed on ETL 4 (Fig. 5.7). a) Position of the PL peaks of the spectra in Fig. 5.7 as a function of temperature. The excitation side is indicated in brackets. b) FWHM of the PL peaks of Fig. 5.7 as a function of temperature. The excitation side is indicated in brackets. Red solid line shows the fitting of FWHM through Eqn. 5.5. c) Spectrally integrated PL intensity as a function of temperature for ETL 4 after excitation from side A and B.

reported in Tab. 5.3: these values well agree with data in the literature [103, 117]. It is worth noting that we fit the FWHM evolution of orthorhombic and tetragonal phase together with a single function: thus the acoustic and optical phonons causing the PL line broadening have very similar energies for the two phases.

**Table 5.3:** Results of the fit of the temperature FWHM evolution (Fig. 5.7(b)) according to Eqn. 5.5.

$\Gamma_0$	$(23 \pm 1) \text{ meV}$
$\gamma_{ac}$	$(30 \pm 5) \mu\text{eV/K}$
$\gamma_{LO}$	$(75 \pm 5) \text{ meV}$
$E_{LO}$	$(19 \pm 1) \text{ meV}$

Apart from different relative weights of the emission bands, a very similar trend with temperature, as shown in Fig. 5.7(a) for ETL 4, is found for ETL 1, 2 and 3 for both the excitation sides. On the contrary, relevant differences are observed in case of ETL 4 exciting from side B (Fig. 5.7(b)). By increasing the temperature, the PL spectrum shows a single band, corresponding to the tetragonal phase, with a monotonic increase of the emission energy and FWHM. Moreover, no PL enhancement is observed. These trends indicate that the MAPI film embedded in the mesoporous ETL side is frozen in the tetragonal phase even down to 10 K.

## 5.5 PL measurements versus excitation energy

To confirm that the crystalline nature of MAPI film changes when it is in contact with the ETL, in particular in presence of G+mTiO<sub>2</sub> plus GO-Li, we probed ETL 4 along the thickness by varying the excitation photon energies, i.e. the absorption length. We spanned the range from 1.73 to 3.1 eV, where FTO and cTiO<sub>2</sub> have a low and nearly constant absorption. PL spectra at low temperature as a function of excitation energy are reported in Fig. 5.9. Let us focus on side B. At high photon energy excitation, 3.1 eV (blue curve) and 2.06 eV (orange curve), MAPI is excited for a few tens of nanometers close to the ETL and, as already observed above, the spectra show only the tetragonal phase, although the only stable phase of MAPI below 150 K is the orthorhombic one. Decreasing the excitation photon energy down to 1.73 eV, the absorption



coefficient of MAPI decreases (see Fig. 1.9(a)) and therefore the sample is excited more uniformly in depth. In this case the PL spectrum (red curve) shows an increase of the contribution of the orthorhombic phase and, if compared with a spectrum from side A (excitation of 2.06 eV), shows exactly the same contribution from the radiative traps and the tetragonal phase. Therefore, it is the interaction between MAPI and ETL that inhibits the phase transition at low temperature and improves the crystalline quality of MAPI active layer.

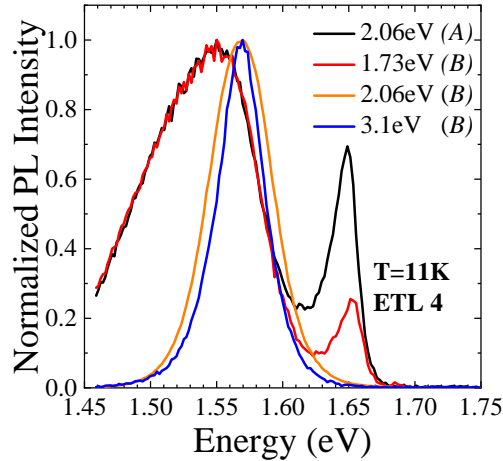


**Figure 5.9:** Normalized PL spectra of ETL4 at  $T=11$  K for different excitation photon energies and excitation sides (in brackets).

## 5.6 J-V characterization

Through macro-PL measurements we demonstrated a substantial improvement of the active layer morphology in  $G+m\text{TiO}_2$  plus GO-Li ETL (ETL 4) with an efficient carrier capture from the ETL. These results are supported by an enhancement in the performance for the complete device, obtained by adding Spiro-OMeTAD as HTL and Au as bottom contact.

Indeed  $J$ - $V$  characterization (Fig. 5.10) performed by Aldo di Carlo's group shows a remarkable increase in the PCE for ETL 4, which is mainly ascribed to an improved  $J_{sc}$  (see Tab. 5.4).

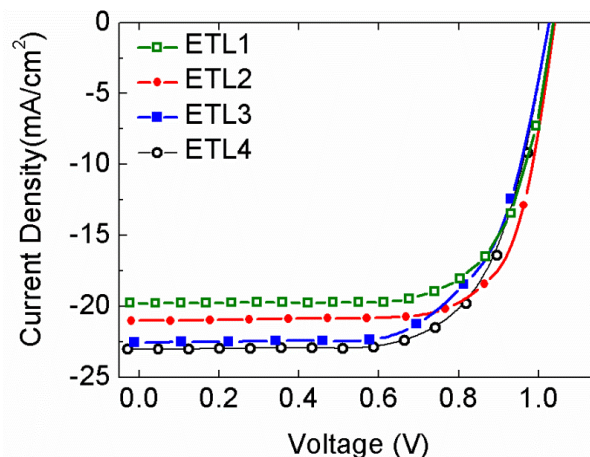


**Figure 5.10:**  $J$ - $V$  characteristics of tested devices employing different ETLs under 1 SUN illumination.

The higher  $J_{sc}$  stems from an improved electron charge transfer from perovskite to graphene-based ETL. We exclude that the increase of the  $J_{sc}$  of the solar cells with graphene-based ETLs is due to an increase of the absorption in the active layer, because the absorbance spectra are



very similar for all the photoelectrodes.

**Table 5.4:** Electrical parameters of the tested devices extracted by the J-V characteristics of Fig. 5.10:  $V_{OC}$  = open circuit voltage,  $J_{SC}$  = short circuit current density, FF = fill factor, PCE = photovoltaic conversion efficiency.

Device	$V_{OC}$ (V)	$J_{SC}$ ( $\text{mA cm}^{-2}$ )	FF (%)	PCE (%)
ETL 1	1.038	-19.74	71.4	14.6
ETL 2	1.041	-20.99	73.2	16.0
ETL 3	1.029	-22.51	65.5	15.2
ETL 4	1.031	-22.85	68.9	16.2

## §6§ Superlinear emission in MAPI perovskites

In this chapter we discuss the physical origin of the superlinear emission in MAPI perovskites with different morphology. All samples were provided us by the Dr. Alexander Weber Bargioni's group of the Molecular Foundry National Laboratory of Berkeley. We performed micro-PL measurements at low temperature ( $T = 10\text{ K}$ ) as a function of the excitation power (sec. 6.2), spatial PL maps (sec. 6.3) and polarization resolved measurements (sec. 6.4), that allowed us to correlate the features of the superlinear emission to the sample morphology.

### 6.1 Description of the samples

MAPI bare film (BF) and microwires (MWRs) were grown on quartz substrates.

MAPI film was synthesized with a double-step deposition method (see sec. 2.1). Instead MAPI MWRs were realized with the dissolution-recrystallization method (see sec. 2.1), following the procedure reported in Ref. [66]. A lead acetate ( $\text{PbAc}_2$ ) film was prepared by drop-casting a solution ( $100\text{ mg ml}^{-1}$ ) of lead acetate trihydrate ( $\text{PbAc}_2 \cdot 3\text{H}_2\text{O}$ ) /DMSO on a quartz substrate treated with oxygen plasma, that was then annealed at  $60^\circ\text{C}$  on a hot plate for 30 min to evaporate the solvent. The  $\text{PbAc}_2$  film was then immersed in 2 ml of MAI/IPA solution (concentration  $30\text{ mg ml}^{-1}$ ) at room temperature for  $\sim 24\text{ h}$  in a nitrogen glove box to grow the MWRs. After the reaction, the sample was rinsed with IPA to remove the residual salt on the film, and then dried under a stream of nitrogen flow.

In Fig. 6.1 typical SNOM maps with the height profile for the BF and for a single MWR are reported. We can see that in the BF the spatial scale of the roughness is of tens of nm, while the MWR shows an homogeneous thickness.

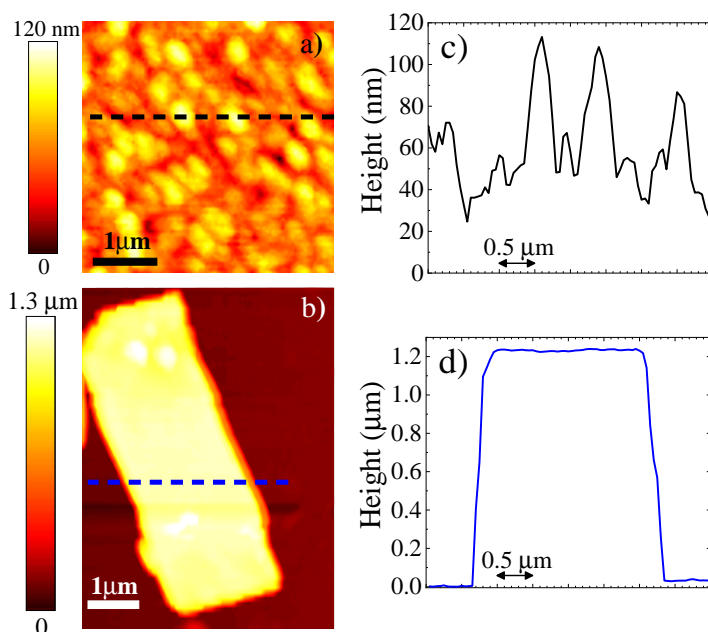


**Figure 6.1:** On the left: SNOM topography maps for the BF (a) and of a MWR (b). On the right: Height profile for the BF (c) and the MWR (d) along the lines indicated in a) and b), respectively.

## 6.2 Power dependent PL measurements

In this section we present the power dependent micro-PL measurements at 10K under pulsed excitation at 3.1 eV exciting with the II harmonic of the Ti:Sapphire laser. In Fig. 6.2, typical micro-PL spectra at 10K for the BF and the MWR at low excitation density are reported. PL spectra of Fig. 6.2 show two emission bands for both samples: the high emission band corresponds to the radiative recombination from the orthorhombic phase of MAPI, while the low energy band arises from recombination of residual tetragonal inclusions in the orthorhombic phase [105,106,156,157]. The relative weight of the two bands changes depending on the selected region of the samples.

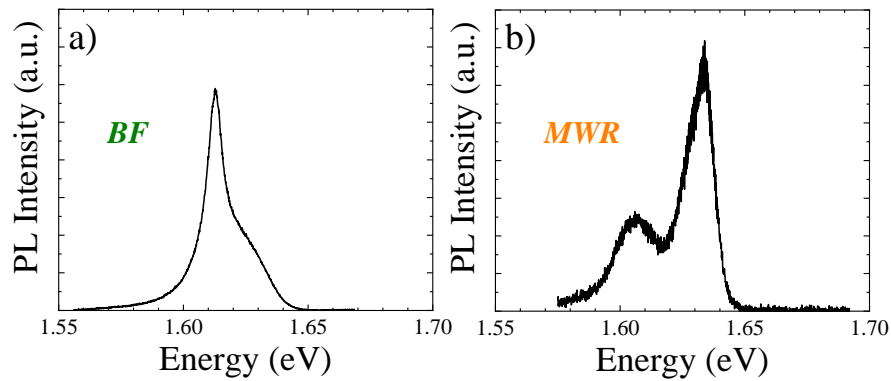


**Figure 6.2:** PL spectra at 10K for the BF (a) and of a MWR (b) under pulsed excitation at 3.1eV, with a excitation density of  $780 \mu\text{J cm}^{-2}$  and  $38 \mu\text{J cm}^{-2}$ , respectively.

Increasing the excitation power (Fig. 6.3(a-b)), PL spectra change in different ways depending on the sample morphology: in the disordered film there is the appearance of multimodal emission (Fig. 6.3(a)), while the MWRs show a spectral narrowing (Fig. 6.3(b)) with the growth of one or few modes depending on the micro-structure. In addition, we observed a superlinear increase of the PL intensity for both the samples when the excitation density exceeds  $\sim 3.5 \text{ mJ cm}^{-2}$  for the BF and  $\sim 70 \mu\text{J cm}^{-2}$  in the MWR. It is worth noting that the superlinear regime occurs at higher density (of about two order of magnitude) in the disordered structure. In Fig. 6.3(c-d) the power dependence of the PL intensity for the BF and the MWR are reported. We separated the contribution of the narrow peak(s) (superlinear emission, SE) from the behaviour of the broad PL band (spontaneous emission, SPE). We found a slightly sublinear trend ( $I \propto P^\alpha$ ,  $\alpha < 1$ ) for the SPE, while a superlinear trend is observed for the narrow peak(s) followed by a saturation.

A further signature of the SE comes from the temporal evolution of the PL signal, as shown in Fig. 6.3(e), where the PL decay of the SE and SPE signals for the MWR are reported: a faster decay occurs in case of SE. In particular, it clearly appears that the SE occurs only in the first few tens of ps and the longer decay time comes from the residual SPE signal. A similar trend was observed for the BF.

## 6.3 Spatial PL maps

In order to investigate the homogeneity of the emission in both the samples we performed spatial resolved PL maps. In the bare film the SE is quite homogeneous, with differences in the PL spectra concerning the pseudo-mode distribution. On the contrary, for the microwire,

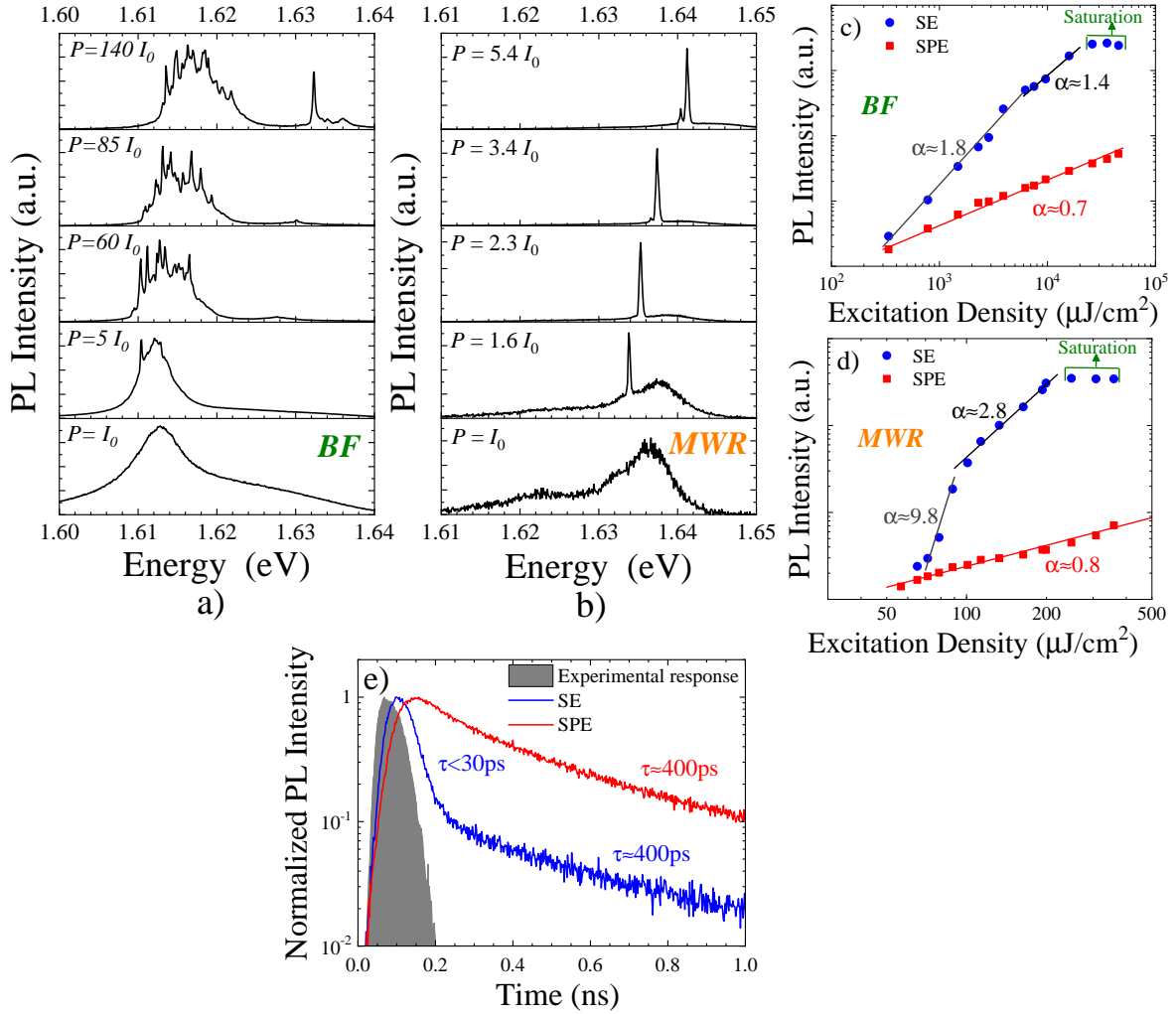


**Figure 6.3: Power dependent micro-PL measurements.** a) PL spectra as a function of the excitation power for the BF.  $I_0$  corresponds to an excitation density of  $780 \mu\text{J cm}^{-2}$  b) PL spectra as a function of the excitation power for the MWR.  $I_0$  correspond to an excitation density of  $38 \mu\text{J cm}^{-2}$ . c) PL intensity as a function of the excitation density for the BF. d) PL intensity as a function of the excitation density for the MWR. e) PL decay for the SE and SPE signal for the MWR after excitation with 0.2 ps pulse.

PL emission under high excitation condition is strongly dependent on the position, as shown in Fig. 6.4(b). In Fig. 6.4(c-d) we report micro-PL spectra collected in two different points of the MWR at the same excitation density ( $197 \mu\text{J cm}^{-2}$ ): the spectra of point A shows a narrow peak, while the spectra of point B is similar to the spectra in low density regime (see Fig. 6.2(b)).

The distribution of the SPE and SE emission in the MWR are remarkably different, as shown in Fig. 6.4(a) and Fig. 6.4(b), where the integrated micro-PL maps for the two emissions are reported. These maps were obtained by integrating PL maps in a narrow spectral region (2 meV), centered at the peak of Fig. 6.4(c) (for the SE) and far from it (for the SPE). These maps bring evidence that, in the MWR, SE comes from specific regions of the samples, whereas the SPE is more uniformly distributed in the MWR. For the BF, differences in the spectra are observed concerning the pseudo-mode distribution and the onset value of the superlinear emission. In the MWR sample the SE comes from hot spots in the sample (region A) as shown in Fig. 6.4(b), while the SPE corresponds to the broad pedestal, more easily observed in Fig. 6.4(d) where the signal is collected from region B.

Quite puzzling is presently the origin of the hot spots which possibly are related to dif-

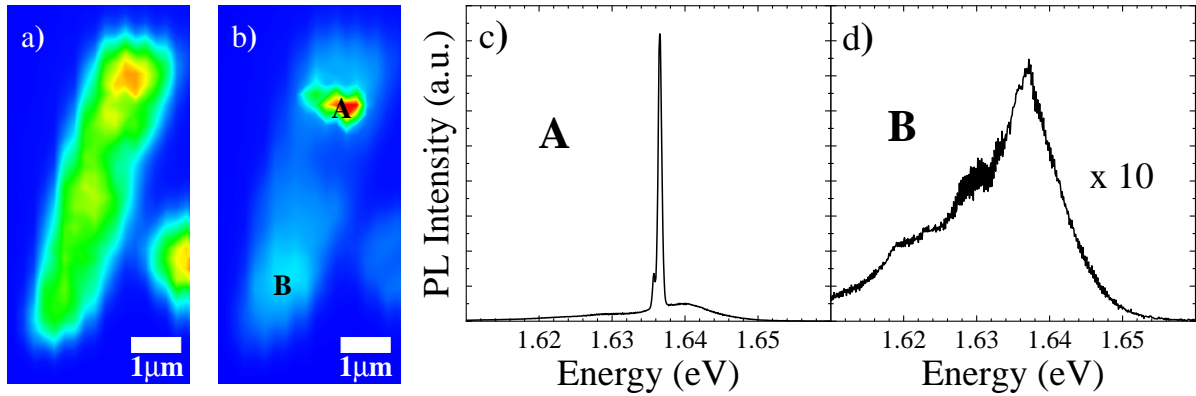


**Figure 6.4:** a) Integrated PL map of the SPE (from 1.639 to 1.645 eV). b) Integrated PL map of the SE (from 1.635 to 1.637 eV). c) PL spectra from point A. d) PL spectra from point B.

fusion/localization centers: in fact diffusion will be of help in the PL signal extraction given our experimental setup where illumination/detection occurs in the direction orthogonal to the sample plane, but exciton localization will provide a favourable condition for light amplification. Since we do not have any evidence of significant inhomogeneity in the spectrum and intensity of the SPE, it is unlikely that hot spots are related to the presence of localized non-radiative centers. Indeed they will play a role also in the low excitation regime.

## 6.4 Polarization resolved measurements

In order to clarify the origin of the SE we performed polarization-resolved measurements, shown in Fig. 6.5. The polar diagram, i.e. the PL intensity as a function of the polarization angle, for the BF (Fig. 6.5(a)) does not show any difference between the low and high excitation regime: the emission turns out to be unpolarized in both cases at fixed energies in the spectrum; in particular we analysed the polarization at the energies where narrow peaks appear at higher excitation density. On the contrary, a strong polarization ( $\sim 80\%$ ) is detected for the SE in the MWR sample, whereas the SPE is unpolarized (Fig. 6.5(b)). Moreover, a cross-polarization is observed in case of two modes and the polarization axis are strongly correlated with the geometry of the micro-crystal (see Fig. 6.5(c-d)).

We performed also TR-PL measurements as a function of the polarization in the MWR sample (Fig. 6.6). In Fig. 6.6(a), PL spectra, under high excitation density ( $200 \mu\text{J cm}^{-2}$ ), at the maximum/minimum polarization angles together with an image of the selected MWR are reported. Also in this case, the polarization direction is correlated to the geometry of the micro-crystal. In Fig. 6.6(b) PL decay at the PL energy peak of Fig. 6.6(a) are reported: a strong dependence to the polarization angle is found. When the PL intensity is maximum, PL decay have a fast decay rate followed by a slow decay rate due to the residual SPE signal, as already observed in Fig. 6.3(e). On the contrary, by choosing the orthogonal polarization ( $176^\circ$ ), we observe only the slow decay rate. In low density condition, no differences between the PL decays are observed by varying the polarization angle.

## 6.5 Conclusions

The experimental results discussed in this chapter allowed us to distinguish the nature of the SE in the BF and in the micro-structures. The lack of polarization and the multimodal features

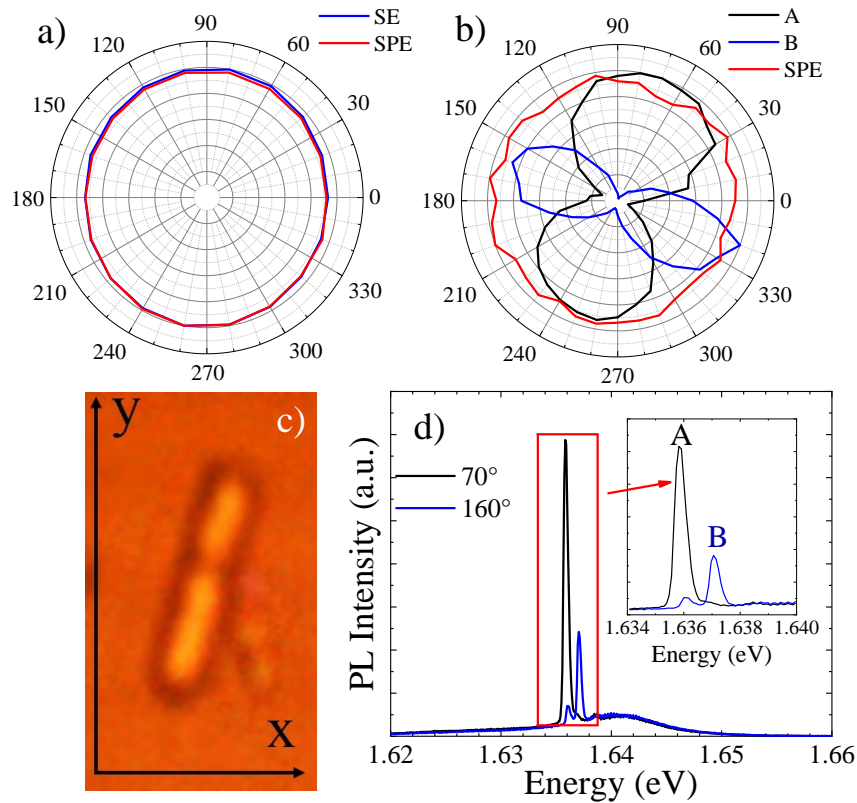


**Figure 6.5:** a) Polar diagram of the polarization of SE and SPE for the BF. b) Polar diagram of the polarization of SPE and A,B modes for the MWR. c) Image of the MWR analyzed. The polariser at  $0^\circ$  is aligned along the x axis. d) PL spectra of the MWR in the superlinear regime at two different polarization angles. In the inset there is a zoom of the two modes A and B.

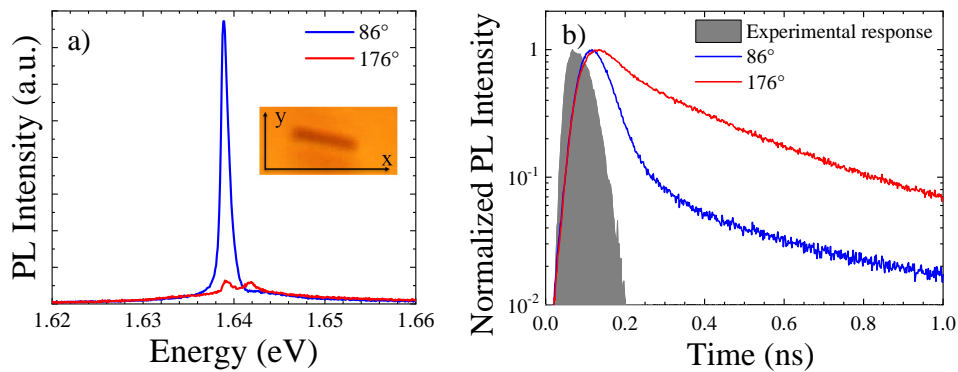


**Figure 6.6:** a) PL spectra in the superlinear regime at two different polarization angles for the MWR shown in the inset. b) PL decays (at the PL energy peak) at the two different polarization angles.

of the emission suggest that the SE in disordered films comes from an amplified spontaneous emission (ASE), as commonly observed in random lasers [327]: each pseudo-mode corresponds to a specific path of the emitted photon. On the contrary, the strong polarization of the PL signal in MWRs can be seen as a true lasing, where the microcrystal acts as an optical cavity, delimited by the crystal surface. The effectiveness of the cavity in the MWR shows up in the reduced threshold for the superlinear signal with respect to the BF.

## §7§ Surface states in CsPbBr<sub>3</sub> nanocrystals

In a semiconductor, the surface represents a break in the periodic crystal potential and thus it introduces new localized states, which in some sense behave like defect states. Surface states significantly affect the photoexcited carriers dynamics since they usually act as non-radiative recombination centres, which can efficiently capture carriers. Eventually, these trapped carriers can be released by thermal activation. The contribution of these surface states is particularly important in semiconductor NCs and QDs due to the larger surface-to-volume ratio.

In this chapter, we discuss experimental results about the carrier recombination dynamics in a thin nanocrystalline film of CsPbBr<sub>3</sub>, showing the relevant role of the surface states. This work was done in collaboration with Dr. Stefano Caporali's group at the Department of Industrial Engineering and the Department of Chemistry of the University of Florence, that prepared the sample. First of all, we describe the investigated sample (sec. 7.1), then we present macro-PL measurements (TI and TR) at low temperature (sec. 7.2) and finally the PL measurements as a function of temperature (sec. 7.3).

### 7.1 Description of the sample

The investigated sample was a nanocrystalline film of CsPbBr<sub>3</sub>, deposited by drop-casting on a glass substrate.

CsPbBr<sub>3</sub> NCs solution was prepared with the hot injection method (see sec. 2.2), following the synthesis protocol of Protesescu et al. [18]. Caesium carbonate (Cs<sub>2</sub>CO<sub>3</sub>, 0.1 g) was loaded into 100 mL two-neck flask along with octadecene (ODE, 30 mL) and oleic acid (OA, 2.5 mL), dried for 1 h at 120 °C, and then heated under N<sub>2</sub> flux to 150 °C until all Cs<sub>2</sub>CO<sub>3</sub> reacted with OA. ODE (5 mL) and PbBr<sub>2</sub> (0.069 g) were loaded into 25 mL two-neck flask and dried under vacuum for 1 h at 120 °C. Dried oleylamine (OLA, 0.5 ml) and dried OA (0.5 mL) were injected at 120 °C under N<sub>2</sub> flux. After complete solubilization of a PbBr<sub>2</sub> salt, the temperature was raised to 150 °C for tuning the NCs size. Cs-oleate solution (0.4 mL in ODE, prepared as described above) was pre-heated to 100 °C and then quickly injected. The obtained suspension was centrifuged and the supernatant removed. Then, the precipitate was washed with toluene and re-centrifuged another time. The new precipitate was dispersed in toluene forming long-term colloidal stable dispersion and deposited by drop-cast on a glass substrate. Finally, CsPbBr<sub>3</sub> was covered by a metallic deposition of Pd/Au of about 10 nm to avoid the interaction with the environment. Dr. Stefano Caporali's chemistry group performed XRD analysis, which indicates only small traces of spurious phases (CsBr and PbBr<sub>2</sub>), while the CsPbBr<sub>3</sub> orthorhombic phase dominates.

In Fig. 7.1 an optical microscope image of the drop-cast CsPbBr<sub>3</sub> film is shown before the gold deposition. We can see that the sample is composed by NCs of different size, even though it was not possible to estimate the size distribution of NCs.



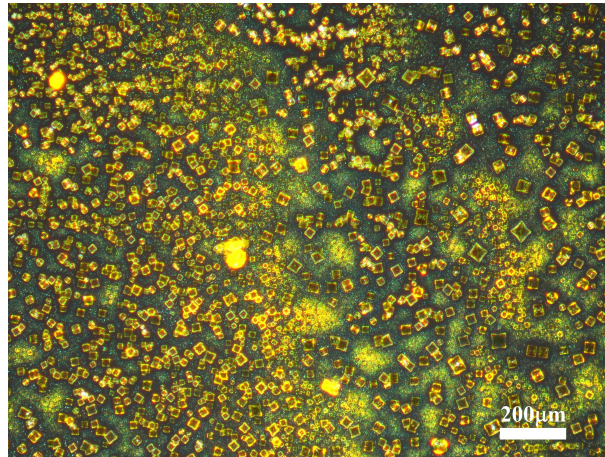


Figure 7.1: Optical microscope image of a CsPbBr<sub>3</sub> drop-casting film.

## 7.2 PL measurements at low temperature

In Fig. 7.2(a) typical PL spectra at low temperature ( $T = 11$  K) of different regions of the sample (laser spot  $\approx 100$   $\mu\text{m}$  diameter) under CW excitation at 3.06 eV are reported: multiple bands are observed. We can see that the relative weight of each band changes when the excitation spot is moved on the sample over an area of a few  $\text{mm}^2$  due to the intrinsic inhomogeneity of the drop-cast deposition. In addition, the FWHM of each band is of about 20 meV, indicating the good quality of the sample [328]. Power dependent measurements show a linear dependence of the spectrally integrated PL intensity of each band on the excitation intensity (see Fig. 7.2(c)), indicating that the radiative recombination arises from excitons [329], in agreement with previous reports [330, 331].

In order to identify the origin of the various bands we compare (Fig. 7.2(b)) the PL spectra of this sample (DC) with the PL spectra of a long ( $> 500$   $\mu\text{m}$ ) CsPbBr<sub>3</sub> bulk crystal (CR). The PL bands are all at higher energies with respect to the bulk emission, and, therefore, given the morphology of this sample, we can assume that these bands originate from quantum confinement of excitons in CsPbBr<sub>3</sub> NCs [107, 120, 189, 190].

To estimate the NCs size we modelled our NCs as cubic QDs (3D confinement) surrounded by an infinite potential barrier for the carriers. The size  $L$  is thus obtained through the following

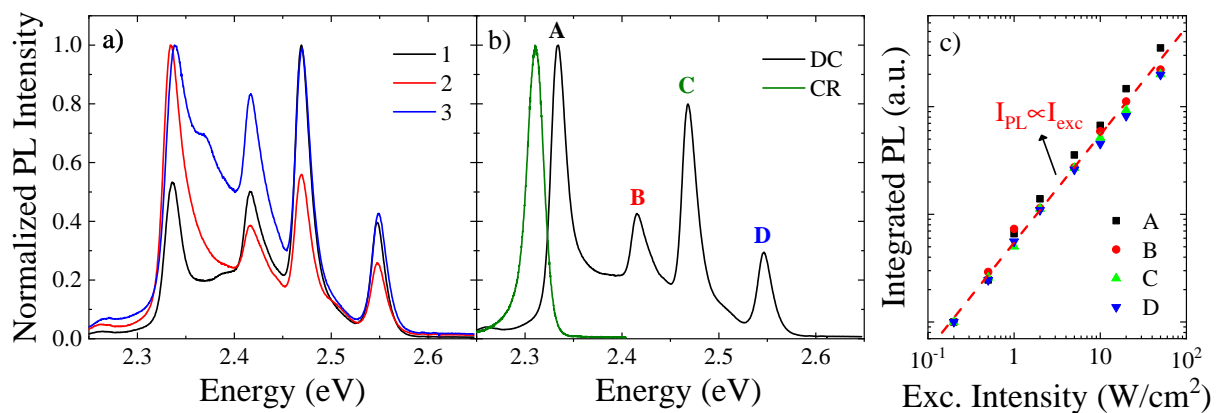


Figure 7.2: a) Normalized PL spectra at  $T = 11$  K in different regions of the sample (1, 2, 3) after CW excitation at 3.06 eV with an excitation intensity of about  $10 \text{ W cm}^{-2}$ . b) Comparison between a normalized PL spectra of the sample (DC) and a normalized PL spectra of a bulk CsPbBr<sub>3</sub> crystal (CR). c) Integrated PL intensity as a function of the excitation intensity for each PL band of the DC sample.

relation:

$$L = \sqrt{\frac{3\pi^2\hbar^2}{2\mu^*E_{conf}}}, E_{conf} = E_{em} - E_{CR} + E_x \quad (7.1)$$

where  $\mu^*$  is the reduced effective mass and  $E_{conf}$  the confinement energy, obtained from the difference between the emission energy ( $E_{em}$ ) of the PL bands and that of the bulk crystal ( $E_{CR}$ ), plus the exciton binding energy ( $E_x = 40$  meV for CsPbBr<sub>3</sub> [18]). By using the Eqn. 7.1 we estimate NCs size of 16, 10, 9.0 and 7.5 nm for the bands A, B, C and D, respectively. It is not clear the reason for which we see this specific tail distribution of nanocrystals. Unfortunately, we did not have any high resolution images of the sample to obtain the size distribution of the NCs in this sample.

In order to study the recombination dynamics in this sample, we also performed TR-PL measurements under ps excitation at 3.35 eV with the frequency-doubled Ti:Sapphire laser, using the TCSPC technique to detect the signal. In Fig. 7.3(a) PL decays at 11 K for the different PL bands are reported. We can note that PL decays at the peak energy of each band cannot be reproduced by a single exponential, as usually observed in CsPbBr<sub>3</sub> NCs with a distribution of traps; the slow decay component is related to the trap dynamics [155]. Moreover, there is a clear slowing down of the PL time evolution when the energy decreases. In other words, the PL dynamics is faster for the smaller NCs.

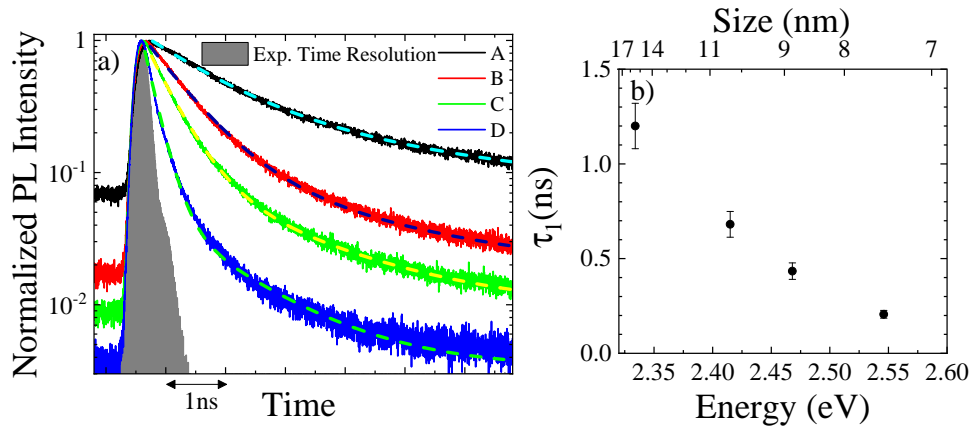


**Figure 7.3:** a) PL decays at  $T = 11$  K, at the PL peak energy of the different bands of Fig. 7.2(b), after ps excitation at 3.35 eV. The dashed lines are fits of the experimental data according to Eqn. 5.1. b) Fast decay component  $\tau_1$  as a function of the emission energy extracted from the PL decay of Fig. 7.3(b).

To obtain the spontaneous emission rate we fitted the decay curves of Fig. 7.3(a) with a two exponential function (dashed lines of Fig. 7.3(a)), taking into account the laser pulse repetition rate (see Eqn. 5.1). The fast time constant ( $\tau_1$ ) changes with the NCs size, while the slower component is of about 5 ns for all emission bands and its weight is more important for the larger NCs. In Fig. 7.3(b) the radiative lifetime ( $\tau_1$ ) is reported as a function of the emission energy:  $\tau_1$  decreases increasing the emission energy and a clear non linear trend is evident.

In the strong confinement regime, that occur when the NCs dimension is lower than the carrier's Bohr radius (7.5 nm for CsPbBr<sub>3</sub> [18]), the spontaneous emission rate  $\Gamma = 1/\tau_1$  is expected to linearly vary with QDs' size only because emission energy is changing [332], being the matrix element constant. In our case, the expected variation of  $\tau_1$  is much smaller than the experimental observation in Fig. 7.3(b). A PL time evolution very similar to the one here reported has been already observed in colloidal QDs (CQDs) [333] and can be explained in terms

of the thermal population of exciton dark states [332,334], i.e. states with low optical transition probability, or invoking the contribution of surface state population [335]. We point out that dark states are always in thermal equilibrium with the radiative states, while this is not true for surface states, given the presence of the potential barrier due to the surface. Therefore in presence of only dark states the PL decay should be monoexponential [332]. As a consequence, since in our case the PL decay (Fig. 7.2(a)) is multiexponential, it is reasonable to assume the change of  $\tau_1$  mainly comes from the presence of surface trap states.

## 7.3 PL measurements as a function of temperature

The population in the dark or surface states usually acts as a reservoir for the radiative states and a significant slowing down of the PL time evolution is found increasing the temperature [333–335]. For this reason, to further investigate the carrier recombination dynamics in this nanocrystalline sample, we also performed temperature dependent PL measurements.

In Fig. 7.4(a) PL spectra as a function of temperature are reported. These PL spectra show, with increasing temperature, a broadening of the emission and a blue shift (Fig. 7.4(b)) for all the bands, typical of perovskite materials. Contrary to what observed in MAPI perovskites, no anomalous behaviour in the emission energy (Fig. 7.4(b)) and in the spectrally integrated PL intensity (Fig. 7.4(e)) is observed, because no phase transition occur for CsPbBr<sub>3</sub> perovskite in this range of temperatures (see Tab. 1.2). It is worth noting that the ratio between the PL peak intensities changes with temperature: this indicates a lack of transfer of population between the different NCs, confirming that the PL comes from states of different structures. In addition, also the spectral broadening and the blue shift are different for the various bands, with an higher

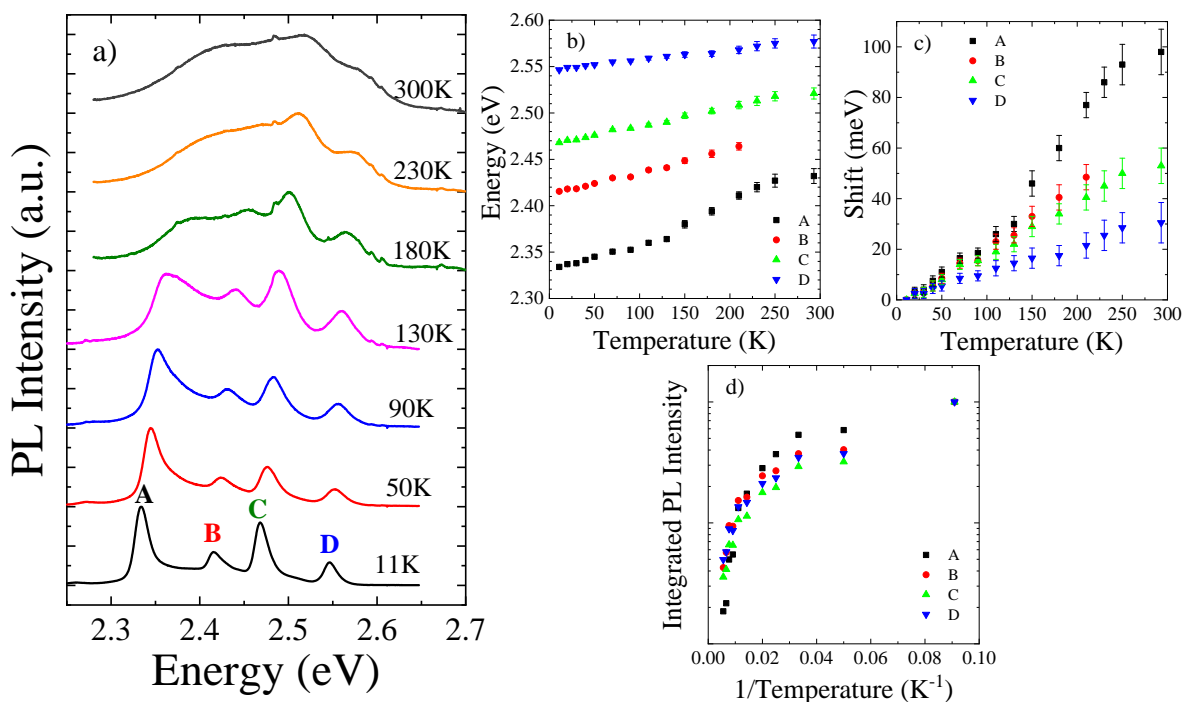


**Figure 7.4:** Temperature dependent PL measurements on the DC sample under CW excitation at 3.06 eV with an average intensity of 10 W/cm<sup>2</sup>. a) PL spectra versus temperature. b) Position of the PL peak of the various bands as a function of temperature. c) Shift of the position of the PL peak with respect to the value at 11 K for the different bands as a function of temperature. d) Integrated PL intensity as a function of temperature for the different bands.

blue shift for the low energy bands (Fig. 7.4(c)).

Concerning the recombination dynamics, an overall slowing down of the PL decays is observed for each emission band raising the temperature from 10 K to 300 K (Fig. 7.5) and, as a consequence, the pedestal P, observed before the PL rise, increases with respect to the PL intensity at the peak decay. In particular, this effect is more relevant for the high energy emission bands (C, D). As discussed in sec. 4.2.4, this pedestal is due to the periodic nature of the excitation/detection and arises from carriers that recombine at longer time than the repetition period between two following pulses (in this case 12.3 ns). The growth of this pedestal with temperature indicates an increment of the stationary population in the radiative states ( $N_{t=\infty}$ ) with respect to the initial value ( $N_{t=0}$ ) since  $P \propto N_{t=\infty}/N_{t=0}$ . This result is not in contrast with the decrease of the spectrally integrated PL with the increase of temperature observed in Fig. 7.4(d), since this reduction originates from a reduced number of photogenerated carriers into the radiative states. The slowing down of the PL dynamics can be explained assuming a thermally activated transfer of population from the non-radiative states, where carriers are easily trapped but do not recombine, back to radiative states. This transfer process becomes more effective increasing the temperature.

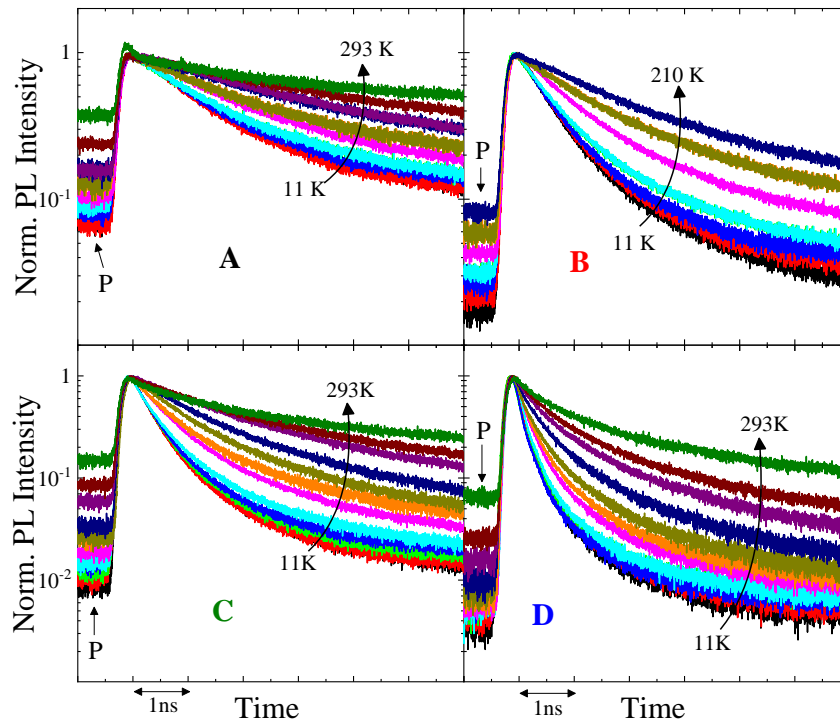


**Figure 7.5:** PL decays as a function of temperature for the four PL bands.

Given the morphology of the sample, the origin of these non-radiative states, acting as a sink for the radiative states, can be attributed to the NCs surface. Their role is expected to be more relevant for the smaller crystals due to an increase of the ratio between the surface states and the volume states. In order to reproduce the growth of the pedestal P with the temperature  $T$  (Fig. 7.6), we assumed that the transfer of population from the surface states back to the radiative states occurs through a mechanism similar to the thermionic emission [94]. We fitted

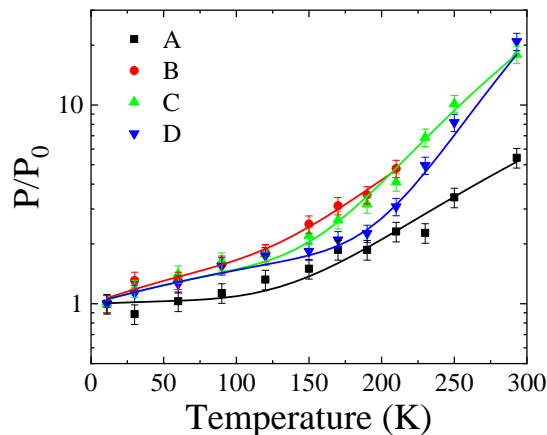


**Figure 7.6:** Temperature dependence of the pedestal  $P$ , normalized to the value at 11 K ( $P_0$ ), for each band. Continuous lines are the fits according to the Eqn. 7.2.

the dependence of pedestal  $P$  on the temperature  $T$  according to the following equation:

$$P(T) = \alpha T + \beta T^2 e^{-E_B/k_B T}, \quad (7.2)$$

where the first term accounts for a phonon activated process, while the second term accounts for a thermally activated transfer of carriers from the surface states back to the radiative states with an energy barrier  $E_B$ . In Eqn. 7.2  $\alpha$  and  $\beta$  are two constants. The fitting results are shown in Tab. 7.1. We can see that, passing from band D to A, the energy barrier  $E_B$  reduces from 120 meV to 33 meV and that the parameter  $\beta$  decreases of about two order of magnitude. Instead,  $\alpha$  is of the same order of magnitude for the different bands. These results confirm that the thermally activated transfer process from the surface states back to the radiative states is more relevant for the smaller crystals (higher  $\beta$  value). Moreover, an higher energy barriers is found for the smaller NCs due to their higher emission energies. Finally, these results also indicate that at room temperature a thermal equilibrium between the surface and the bulk radiative states is possible only for the larger crystals.

**Table 7.1:** Results of the fits of the pedestal evolution (Fig. 7.6) according to Eqn. 7.2.

Band	$\alpha$ ( $10^{-3} \text{ K}^{-1}$ )	$\beta$ ( $10^{-3} \text{ K}^{-2}$ )	$E_B$ (meV)
A	$5.0 \pm 0.2$	$0.18 \pm 0.02$	$33 \pm 3$
B	$6.1 \pm 0.2$	$0.48 \pm 0.05$	$39 \pm 4$
C	$4.8 \pm 0.2$	$2.6 \pm 0.3$	$67 \pm 7$
D	$4.8 \pm 0.2$	$25 \pm 3$	$120 \pm 10$

## §8§ Cooling dynamics in CsPbBr<sub>3</sub> perovskites

In this chapter we will discuss the relaxation and thermalization process in CsPbBr<sub>3</sub> single crystal (CR) and spin-coated (SC) film to bring evidence of the thermalization conditions and provide quantitative information of the characteristic time-scale of this process. Moreover, we will discuss TR-PL measurements in presence of an additional CW bias (resonant and non-resonant): results will show a significant non-linearity in the emission.

### 8.1 Description of the samples

Two different CsPbBr<sub>3</sub> samples were prepared by Dr. Stefano Caporali's group: a single CR and a SC thin film deposited on a glass substrate. In both cases, CsPbBr<sub>3</sub> solution was prepared dissolving equal molar quantity of the precursors (CsPb and PbBr<sub>2</sub>) in DMSO. The solution was stirred overnight to obtain a clear liquid.

The deposition of the film onto the glass substrate was done using a spin-coater system. The substrate was covered with 20  $\mu$ L of CsPbBr<sub>3</sub> solution and spinning for 10 s at 500 rpm and 5000 rpm, respectively<sup>1</sup>, to obtain a uniform distribution of the liquid. The substrate was then transferred on a hot-plate set at 120 °C to dry and anneal the perovskite film. After 10 min on the hot plate the perovskite film was done. Instead, CsPbBr<sub>3</sub> single crystals were grew by using the AVC method discussed in sec. 2.2. In this case, methanol was used as antisolvent.

In Fig. 8.1 two SEM images of the two samples are reported. We can see that the dimension of the single CR is of about 700  $\mu$ m and that the SC film is composed by micro-crystals with lateral dimension between 100 nm and few microns. Moreover, the SNOM image of the SC film shows that the micro-crystals have a thickness that ranges from 40 nm to several hundred of nm.

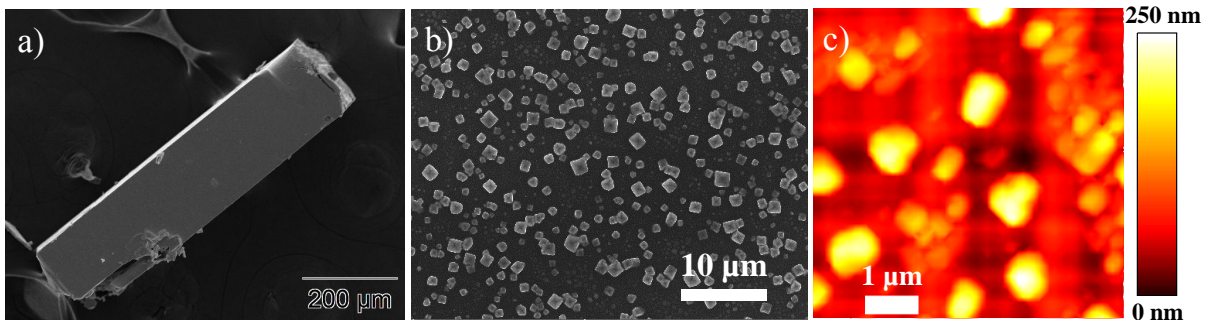


**Figure 8.1:** a) SEM image of the single-crystal. b) SEM image of the SC film c) SNOM topography map of the SC film.

### 8.2 Main PL features

Before discussing the thermalization dynamics, we briefly present the main PL features of the two samples.

<sup>1</sup>To reach the angular velocity the substrate was accelerated at 100 rpm s<sup>-1</sup> and 1000 rpm<sup>-1</sup> in the first and second step, respectively.



### 8.2.1 Single-crystal

In Fig. 8.2(a) a typical low-temperature PL spectrum of the CsPbBr<sub>3</sub> CR under CW excitation at 3.06 eV is reported. The PL spectrum shows two bands, whose relative weight changes exciting different points of the sample; the PL intensity of the low energy band is anyway higher with respect to the high energy band. In the literature [97,147,336], the high energy band ( $\sim 2.32$  eV) is ascribed to the free exciton (FE) emission, while the low energy band ( $\sim 2.29$  eV) is attributed to recombination from a bound exciton (BE) or to a phonon replica of the FE.

In this sample, we attribute the low energy band to a BE emission for the following reasons:

- the recombination dynamics of the low energy band is slower with respect to the FE emission (see sec. 8.3). Instead, phonon replicas have the same dynamics of the main radiative exciton recombination lines (or zero phonon lines (ZPL)), since it derives by the recombination of the same population [337,338];
- the low energy band has an higher intensity with respect to the FE emission, whereas the intensity of the phonon replicas is usually smaller with respect to the ZPL [337,338].
- the PL quenching of the low-energy emission increasing temperature is more relevant respect to the FE band.

In Fig. 8.2(b) low-temperature PL spectra in logarithmic scale of the CR under non resonant and resonant excitation are compared. Both spectra show exponential tails of the emission in the low (Urbach tail) and high energy sides, denoting in the last case a thermalization condition. Exponential fit of the low-energy tail gives an Urbach energy of about 20 meV in both cases.

In thermal condition, the slope of the high energy tail is correlated to the carriers temperature ( $T_C$ ) since

$$I_{PL}(E) \propto DOS(E)e^{-E/k_B T_C}, \quad (8.1)$$

where DOS is the density of states of the system. We can see that the slope of the thermal tail is different in the two cases, greater under resonant excitation, indicating a colder carrier distribution. Through an exponential fit of the tail we obtained a carrier temperature of about 15 K in the resonant case and of about 45 K in the non-resonant case: in the last case the carrier

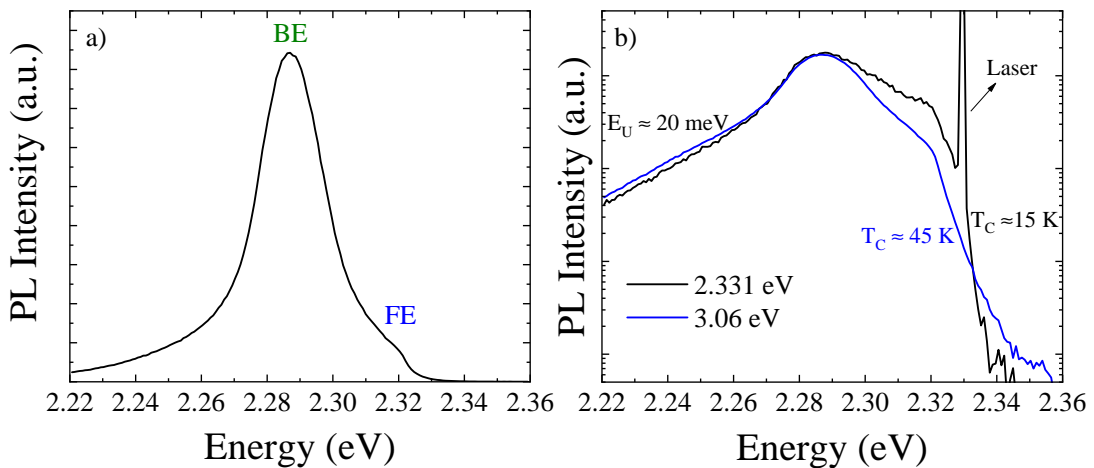


**Figure 8.2:** a) PL spectrum at 10 K of the CR under CW excitation at 3.06 eV. b) Comparison between low-temperature PL spectra of the CR under resonant and non-resonant excitation.



temperature is much higher than the lattice temperature (10 K). We will discuss in sec. 8.3 the thermalization under non-resonant excitation.

### 8.2.2 Spin-coated film

In Fig. 8.3(a) typical low-temperature macro-PL spectra under non-resonant excitation in different points of the SC film are reported: we can see different PL bands, ranging from 2.31 eV to 2.39 eV. Given the dimensions of our NCs (lateral dimensions > 100 nm, thickness > 40 nm), we exclude that the PL shift observed in macro-PL spectra of Fig. 8.3(a) is due to quantum confinement effects. The possible explanations of this PL shift can be the following:

- biaxial lattice strain, that produces a local variation of the band gap [339];
- photon emission and reabsorption processes [340,341].

SNOM measurements at room temperature exciting the SC film at 3.06 eV bring evidence that the PL emission peak is correlated to the micro-crystals thickness, as shown in Fig. 8.3(d). The spectral shift of Fig. 8.3(d) can be ascribed to a photon emission and reabsorption process, already observed in lead halide perovskites [340,341]. Indeed the absorption length of CsPbBr<sub>3</sub> perovskites at 3 eV is below 100 nm [10], that is smaller than the micro-crystals height. Therefore, only a small region of the micro-crystals is excited and emits photons. The high energy side of the PL emitted light can be reabsorbed by the interior regions of the micro-crystals, and, as a consequence, the measured PL spectra is red-shifted. This process is more important increasing

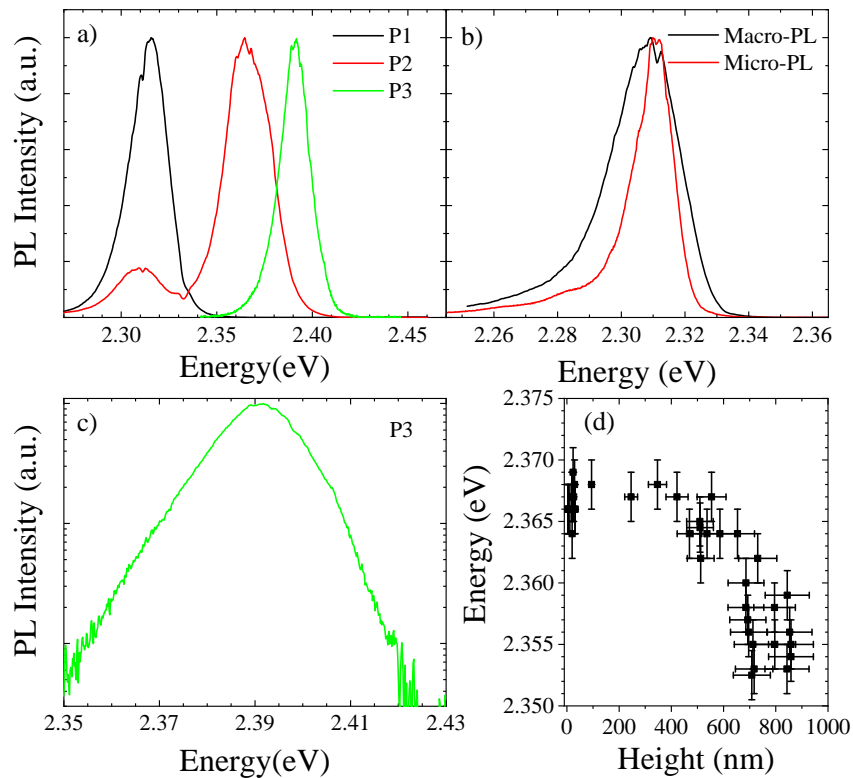


**Figure 8.3:** a) PL spectra at 10 K in different points of the SC film under excitation at 3.35 eV. Inset: PL spectrum of point 3 in logarithmic scale that shows a thermalization condition. b) Comparison between low-temperature macro- and micro-PL spectra of the SC film. c) Macro-PL spectrum of point 3 in logarithmic scale that shows a thermalization condition. d) Peak emission energy of the room temperature SNOM PL spectra of the SC film as a function of the micro-crystals height (thickness).

the micro-crystals height: so thicker the region the more red-shifted is the emission.

However, we can note that the PL shift of Fig. 8.3(d) ( $\sim 15$  meV) is much smaller than the variation observed in macro-PL spectra of Fig. 8.3(a) ( $\sim 80$  meV). For this reasons, we retain that the major contribution of the PL energy variation of Fig. 8.3(a) comes from biaxial lattice strain. As a matter of fact, band gap variation greater than 100 meV was calculated by Grote et al. [339] in CsPbI<sub>3</sub> perovskites with a biaxial strain of about  $\pm 3\%$  in the lattice parameters. In particular, with a tensile biaxial strain of  $\sim 3\%$  the band gap increases of about 60 meV: this variation is of the same order of magnitude than the variation observed in Fig. 8.3(a).

In Fig. 8.3(b), a low-temperature macro-PL spectrum is compared with a micro-PL spectrum (single micro-crystal), that shows a smaller linewidth due to a different inhomogeneous broadening. On the contrary, at room temperature the spectral broadening of the macro- and micro-PL spectra is similar ( $\sim 70$  meV) since the homogeneous broadening dominates due to the electron-phonon interaction. We can note that the FWHM of the low-temperature micro-PL spectrum of Fig. 8.3(b) is of about 14 meV, that is high for a single micro-crystal: this inhomogeneous broadening, that is similar to the spectral shift of Fig. 8.3(d), probably comes from thickness variation in the single micro-crystal.

In Fig. 8.3(c) the PL spectra of the high energy band (2.39 eV) is reported in logarithmic scale: also in this case the PL spectra show a high energy thermal tail with a slope that corresponds to a carrier temperature of about 50 K, similar to the single CR.

## 8.3 Thermalization

As discussed in sec. 4.1, the excess energy of the carriers after non-resonant excitation is lost through scattering with phonons. During this process, the carriers cooling proceeds until a thermal equilibrium with the lattice is reached. In order to investigate the relaxation and thermalization processes in CsPbBr<sub>3</sub>, we performed low temperature TR-PL measurements exciting the samples with the II harmonic of a Ti:Sapphire laser at about 3.35 eV, using the streak camera to detect the PL signal (see sec. 4.2.5). In all measurements the average excitation intensity was about  $6 \text{ W cm}^{-2}$ .

### 8.3.1 Single-crystal

In Fig. 8.4 the PL images in two different time scale (1, 2) at 10 K for the single crystal are reported, while in Fig. 8.5(a-c) the corresponding TR-PL spectra, obtained as horizontal cuts of the PL images, are shown.

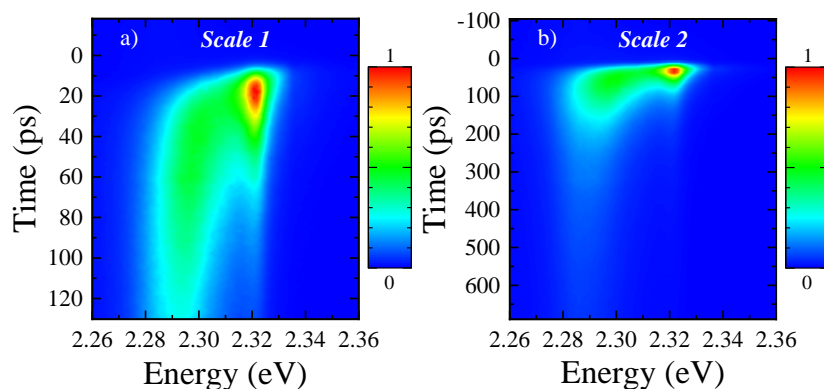


**Figure 8.4:** PL images at 10 K of the CR in scale 1 (a) and 2 (b) after ps excitation at 3.35 eV.

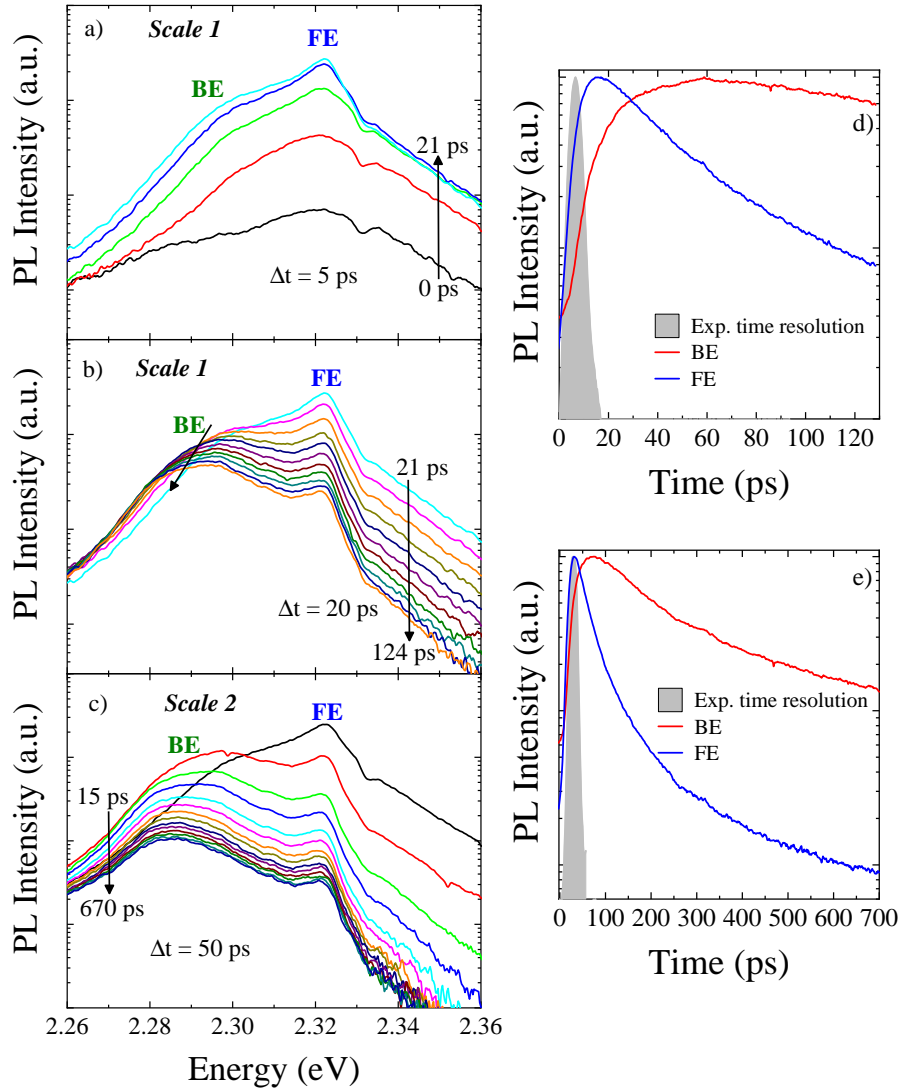


**Figure 8.5:** TR measurements at 10K of the CR under ps excitation at 3.35 eV: a) TR spectra from 21 ps to 124 ps with a step of 20 ps. b) TR spectra from 15 ps to 670 ps with a step of 50 ps. All TR spectra were obtained from horizontal cuts of the PL images with a width of 10 pixels, that correspond to a temporal window of 2.6 ps and 14.2 ps in scale 1 and 2, respectively. d-e) PL decays, at the peak energy of the TI-PL spectra, for the BE and FE emissions in scale 1 (d) and in scale 2 (e). The experimental time resolution is also reported.

From the TR-PL spectra we can see that the PL intensity of the FE emission increases in the first 20 ps and then decreases, while the rise of the BE emission is slower. In the first 40 ps after the excitation pulse the emission of the FE is prevalent, while at longer times the PL comes mostly from the BE band. This trend is clearly shown in the PL decay of the two emissions, as reported in Fig. 8.5(d-e): the FE shows a rise of the PL signal of  $\sim 10$  ps, slightly longer than the temporal resolution in scale 1 (see Tab. 4.2), while the rise of the BE emission is of about 40 ps. Moreover, a longer decay is detected for the BE emission. The energy position of the FE emission remains almost constant, with a small red shift ( $\sim 2$  meV) in the first 100 ps, indicating exciton localization, while the energy shift of BE emission is more relevant (15 meV); the BE emission approaches the value of the TI spectra (2.29 eV) after  $\sim 300$  ps (see Fig. 8.6(a)).

Moreover, the PL spectra of Fig. 8.5(a-c) show an exponential tail in the high energy side, indicating a thermalization condition. The slope of the exponential tail increases with time as a consequence of the cooling of charge carriers. It is worth noting that after 50 ps two exponentials

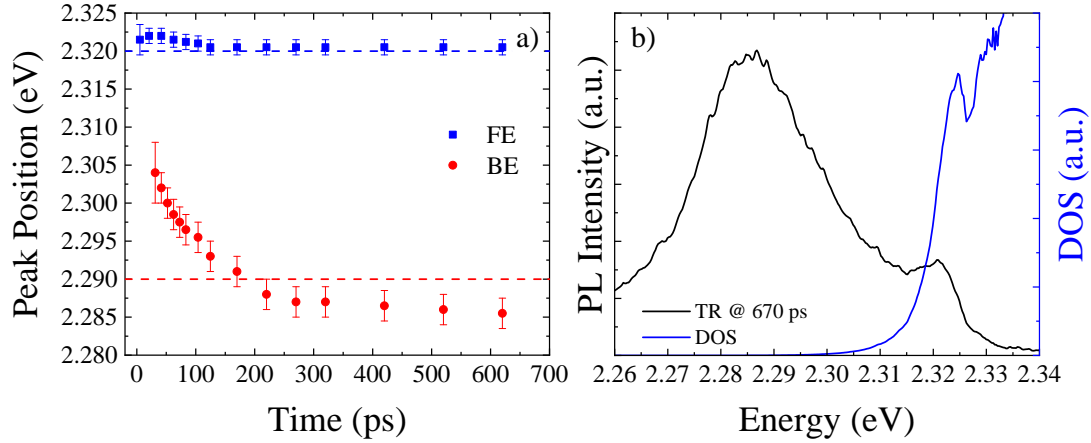


**Figure 8.6:** a) Peak positions of the FE and BE emission as a function of time extracted from the TR-PL spectra of Fig. 8.5(a-c). Dashed lines are the positions of the two emissions in the TI spectra. b) Comparison between the TR spectra of the single CR at 670 ps and the DOS obtained from this spectra using the Eqn. 8.3.

occur in the high energy side of the TR spectra. These two exponentials are not related to two population thermalized at different temperatures, but they come from the DOS of the system.

In fact, if we assume that the PL arises from a thermal distribution, from Eqn. 8.1 we have that

$$I_{PL}(E, t) \propto DOS(E)e^{-E/k_B T_{eff}(t)}, \quad (8.2)$$

where  $T_{eff}(t)$  is the effective carrier temperature at the time  $t$ . In order to evaluate the DOS and extract the carriers temperature we proceed in the following way. In sec. 8.2.1 we showed that, under non resonant-excitation, the carrier temperature in stationary condition ( $T_S$ ) for the CR is about 45 K, that is larger than the lattice temperature. Assuming that at longer time (670 ps) the carriers are thermalized at the temperature  $T_S$

$$DOS(E) \propto I_{PL}(E, t^* = 670 \text{ ps})e^{E/k_B T_S}. \quad (8.3)$$

Therefore, the DOS can be obtained dividing the TR spectra at 670 ps for the Boltzmann factor  $e^{-E/k_B T_S}$ . In Fig. 8.6(b) the DOS obtained with the Eqn. 8.3 is compared with the TR spectra at 670 ps; we can see a peak due to the FE resonance, that is blue shifted ( $\sim 4$  meV) with respect to the FE peak in the corresponding PL spectrum.

We can divide each TR spectrum for the DOS, obtaining

$$\beta(E, t) \equiv \frac{I_{PL}(E, t)}{DOS(E)} \propto e^{-E/k_B T_{eff}(t)}. \quad (8.4)$$

In Fig. 8.7(a-b) the quantity  $\beta$  at early ( $< 30$  ps) and long delays is reported. We can see that in the first 20 ps the curves are not exponential, indicating an incomplete thermalization condition. Instead, for  $t > 30$  ps the curves are nice exponentials, with an increase of the slope ( $1/k_B T_{eff}(t)$ ) with time, that indicates a reduction of  $T_{eff}$ . Through exponential fits of the curves of Fig. 8.7(a-b) we estimated the temperature  $T_{eff}$  for each delay: the results are reported in Fig. 8.7(c).  $T_{eff}$  reduces from 60 K to 47 K in the first 200 ps and then stays almost constant; an exponential fit of the data gives an initial carriers cooling rate of 50 ps. It is worth noting that the lattice temperature is not reached; therefore a bottleneck in the thermalization is evidenced. A slowing

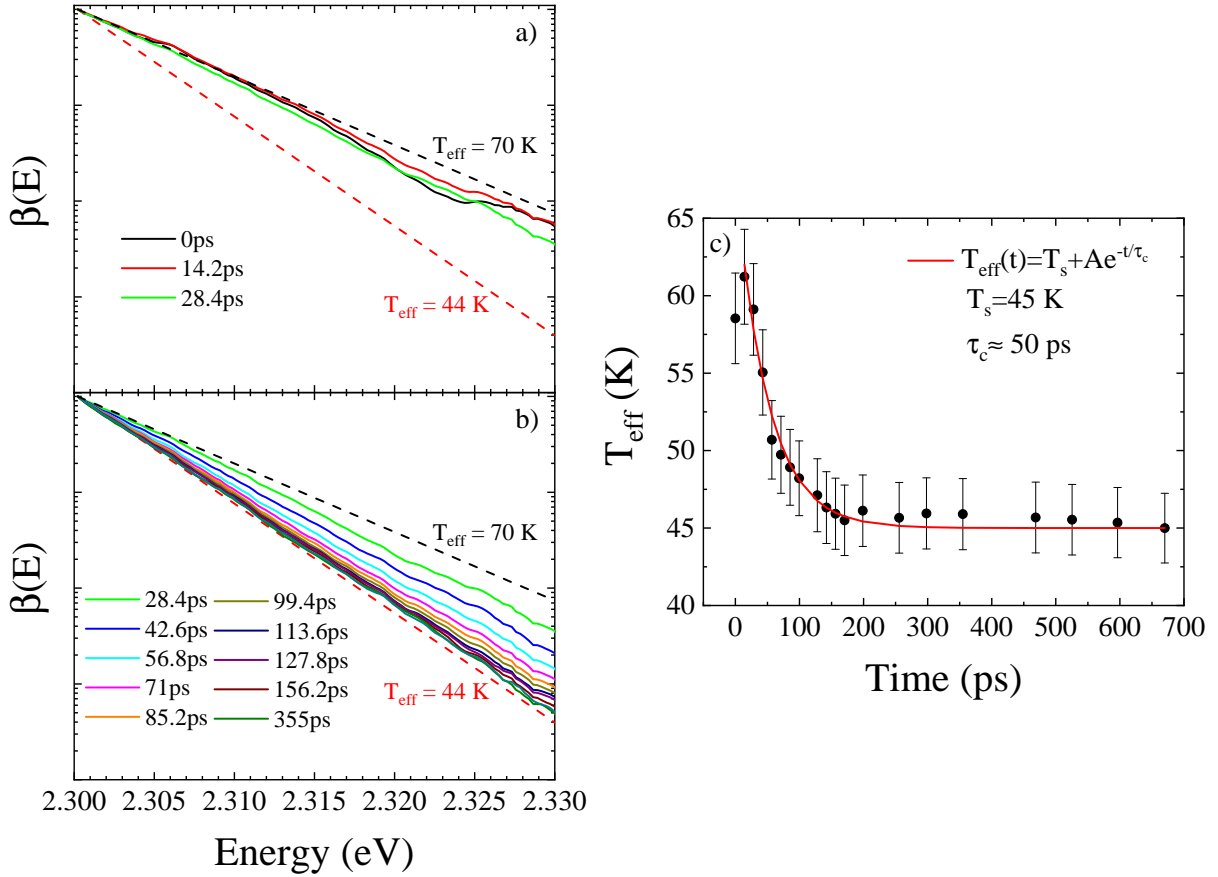


**Figure 8.7:** a-b) Parameter  $\beta(E)$  as a function of time, normalized at the value at 2.3 eV for a clear comparison. Dashed lines represent the parameter  $\beta$  in case of a  $T_{eff}$  of 70 K and 44 K. c)  $T_{eff}$  as a function of time for the CR obtained by an exponential fit of  $\beta$ . The continuous line is an exponential fit of data to estimate the carrier cooling rate.

down of the carrier cooling was also observed by Yang et al. [342] in lead-halide perovskites and it was attributed to the reabsorption of the low-energy emitted phonons, that produces an heating of the carriers. Thermalization bottleneck could be also originated from efficient Auger processes [343], but given the Auger coefficient in this material ( $10^{-29} \text{ cm}^6 \text{ s}^{-1}$  [153]) and our experimental excitation density ( $10^{16} \text{ cm}^{-3}$ ) Auger scattering can be considered negligible.

### 8.3.2 Spin-coated film

Concerning the thermalization of the SC film, we will discuss the TR measurements performed on the high energy band at 2.39 eV. Similar results are obtained for the low energy bands.

In Fig. 8.8(a-c) the PL image in scale 1 and the corresponding TR-PL spectra at 10 K for the SC film are reported. Also in this case, PL spectra show a thermal tail with a progressive increase of the slope with time due to the cooling of carriers. Moreover, the PL peak energy red shifts of about 4 meV in the first 50 ps, reaching the value of the TI spectra (2.39 eV). From the TR spectra we extracted the effective carrier temperature through an exponential fit of the high energy tail: the results are shown in Fig. 8.8(d). We can see an initial fast cooling, that is faster than in the CR (Fig. 8.7(c)), and that there is also in this case a bottleneck in the thermalization. In Fig. 8.9(a) the DOS extracted from the TR-PL spectrum at 130 ps through Eqn. 8.1 ( $T_C = 56$  K) is reported: a step-like DOS is obtained, similar to a two-dimensional (2D) system.

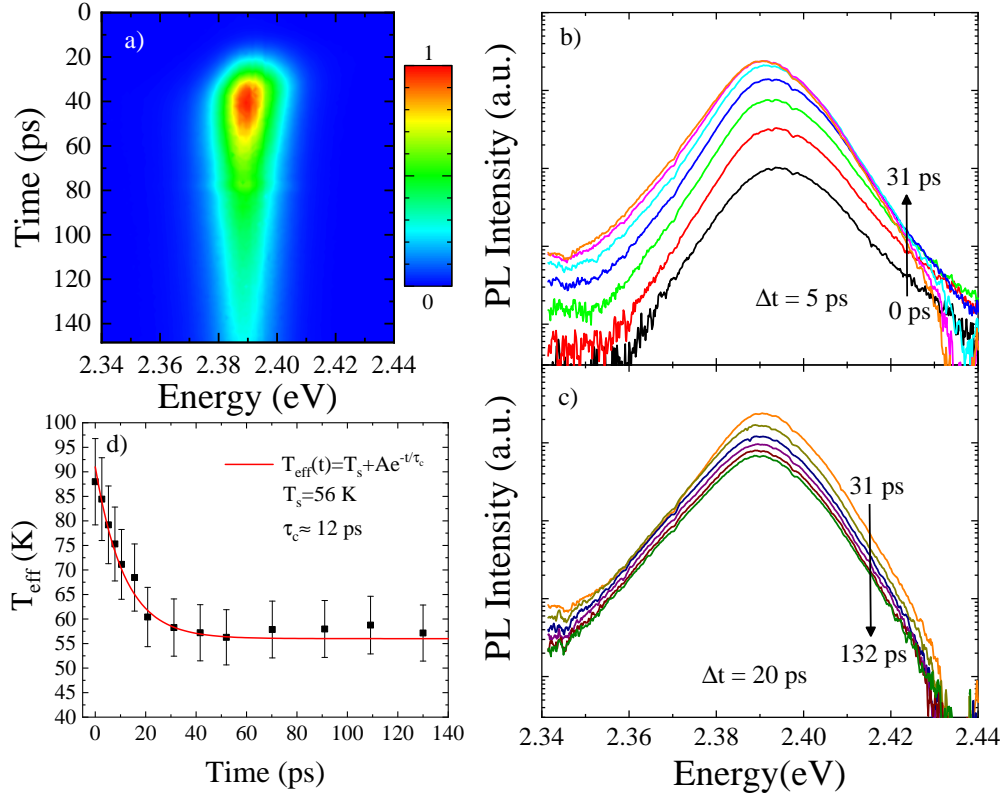


**Figure 8.8:** TR measurements at 10 K of the SC film under ps excitation at 3.35 eV: a) PL image. b) TR spectra from 0 ps to 31 ps with a step of 5 ps. c) TR spectra from 31 ps to 132 ps with a step of 20 ps. d)  $T_{eff}$  for the SC film as a function of time.  $T_{eff}$  was obtained with an exponential fit of the high energy thermal tail of the TR spectra. The continuous line is an exponential fit of data to estimate the carriers cooling.

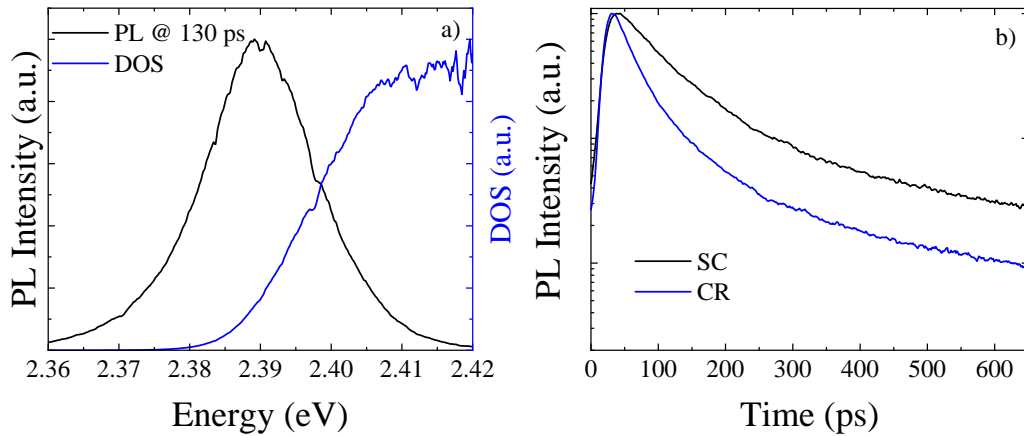


**Figure 8.9:** a) Comparison between the TR spectra at 130 ps of the SC film and the DOS obtained from this spectra using the Eqn. 8.1. b) Comparison between the PL decay of the FE emission in the CR and in the SC film.

To conclude this paragraph, we compare in Fig. 8.9(b) the PL decays of the FE emission in the CR and in the SC film: a faster decay is found in the single crystal due to the exciton localization. Moreover, the longer decay component in the SC film comes from the contribution of the surface states population, as discussed in Chap. 7.

## 8.4 Measurements with CW bias

As previously shown both in the single crystal and in the SC film, the PL measurements reveal a significant contribution from localized/bound states. In order to better understand the

recombination dynamics in CsPbBr<sub>3</sub> we performed TR-PL measurements exciting the samples with the Ti:Sapphire laser plus an additional CW bias. The aim of this measure was to bring evidence of possible non-linearity in the emission related to the saturation of localized states and the population of free states. The same intensity ( $6 \text{ W cm}^{-2}$ ) was chosen for both the CW and pulsed laser beams.

Our experiment is quite similar to transient absorption (TA) spectroscopy, in which the sample is excited with two sources: a pulsed laser (pump) and a weak laser beam (probe), delayed of a time  $\tau$  with respect to the pump. The transmitted probe signal is detected. The TA provides the change of absorption of the probe in presence of the pump, as a function of  $\tau$ . However, whereas the TA spectroscopy measures the change in the absorption spectra, in our case we measure how the temporal/spectral evolution of the PL signal changes in presence of the CW bias, so the change is related to the absorption and population of the radiative states.

As CW bias, we used resonant and non-resonant laser sources:

- as non-resonant bias we used a CW 405 nm laser;
- as resonant bias we used a CW 532 nm laser in case of single CR (resonant with the FE emission) and a 515 nm laser for the SC sample (resonant with the band at 2.39 eV).

For each set of measurements, we acquired three images with the streak camera, exciting the sample in the same point with the pulsed laser ( $I_P$ ), the CW bias ( $I_B$ ) and both of them ( $I_{P+B}$ ), respectively. In absence of non-linear effects, the image  $I_{P+B}$  should be equals to the sum of the images  $I_P$  and  $I_B$ . For this reason, to bring evidence the presence of non-linearity, we extracted the difference image

$$I_D(E, t) = I_{P+B}(E, t) - I_{SUM}(E, t), \quad (8.5)$$

where  $I_{SUM}(E, t) = I_B(E, t) + I_P(E, t)$ ,  $t$  is the time and  $E$  is the energy. If the difference  $I_D(E, t)$  is positive, there is a superlinear increase of the PL intensity, if  $I_D(E, t)$  is negative, there is a saturation of the PL intensity produced by the CW bias. In Fig. 8.10 the difference images  $I_D$  under non-resonant and resonant bias for the single crystal are reported. From these images we can extract TR difference spectra at different delays ( $I_D(E)$ ). Results are shown in

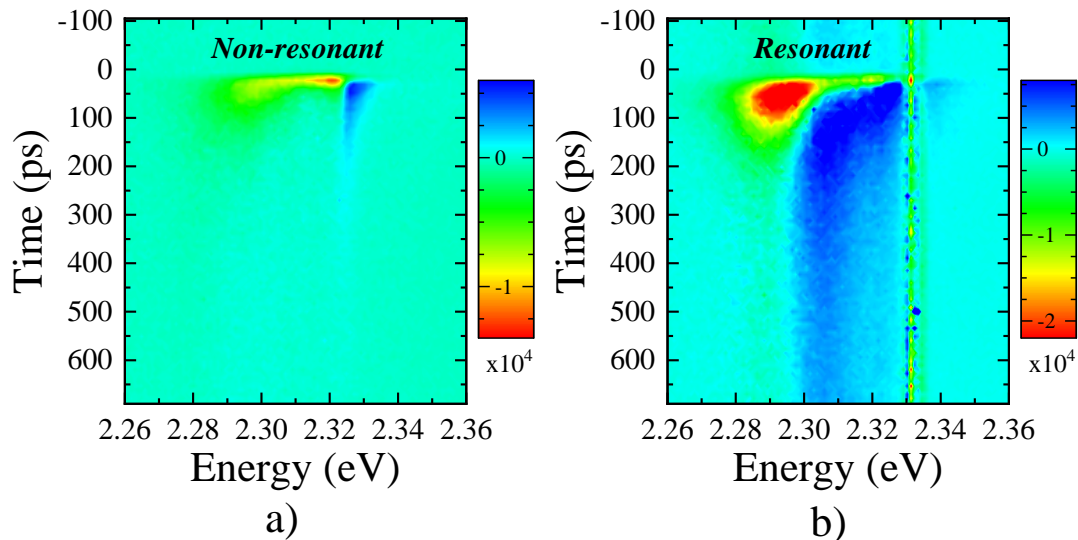


**Figure 8.10:** Difference images for the CR under non-resonant (a) and resonant (b) bias.



Fig. 8.10. We can see that non-linearities are present in the emission, both in resonant than

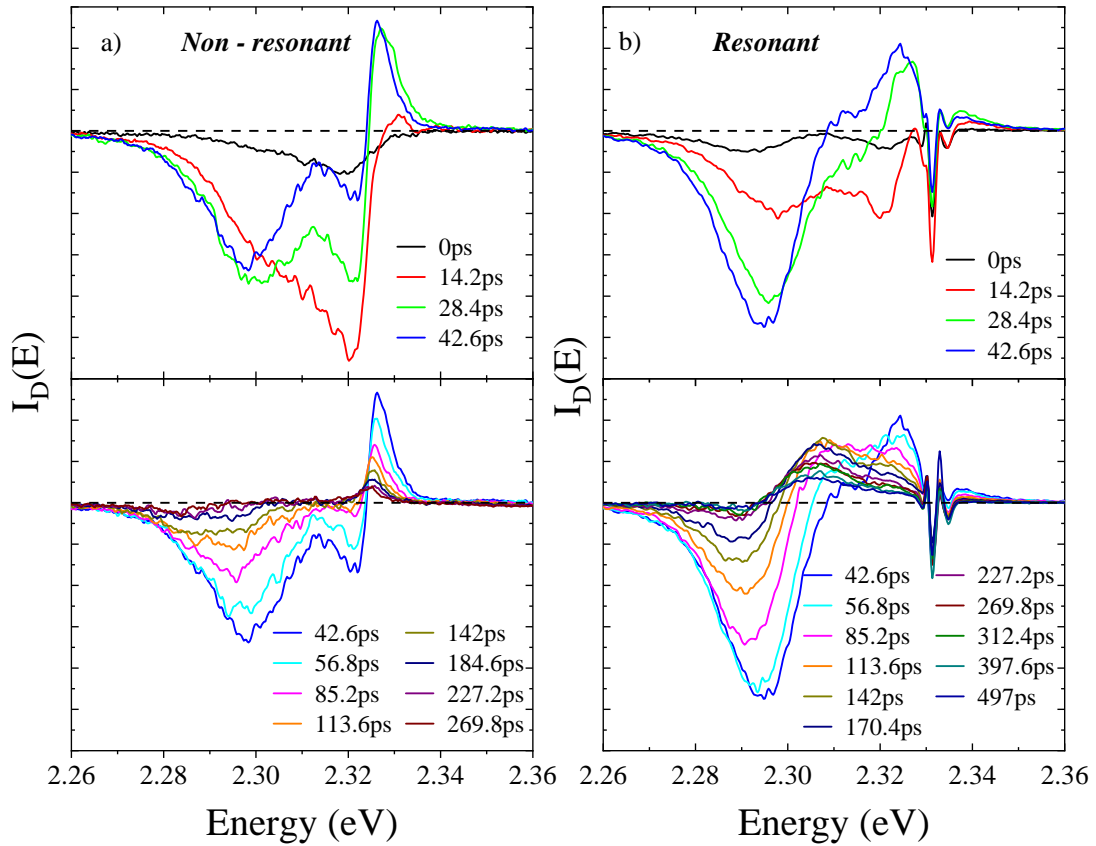


**Figure 8.11:** Difference spectra for the CR, extracted from the images of Fig. 8.10, under non-resonant (a) and resonant (b) bias as a function of time.

in non-resonant case. The recovery time from these non-linearity is greater than 100 ps and much longer in the resonant case for the superlinearity. Applying a non-resonant bias, there is saturation of the bound states ( $< 2.3$  eV) and of the localized states and a superlinear increase of the FE population. In the resonant case, the trend is similar to the non-resonant case, but with a major contribution of the superlinear increase of the FE population and a longer recovery time. Furthermore, we can note a non-linear behaviour under resonant excitation around the laser line, possibly indicating a bleaching of the Resonant Rayleigh Scattering.

To provide an estimate of the non-linear ( $NL$ ) contribution, we spectrally integrated ( $A_{\pm}(t)$ ) the positive (+) or negative (-) part of the difference spectra divided by  $A_{SUM}(t)$ , which is the spectrally integrated PL intensity of the  $TR_{SUM}(t) = TR_B(t) + TR_P(t)$  spectra, where  $TR_{B(P)}(t)$  are the TR spectra with the pulsed laser (P) and the CW bias (B), respectively. In formulas,

$$NL_{\pm}(t) = \frac{A_{\pm}(t)}{A_{SUM}(t)} \quad (8.6)$$

$$A_{SUM}(t) = \int TR_{SUM}(E, t) dE. \quad (8.7)$$

In Fig. 8.12(a,b) the  $NL$  (in %) for the resonant and non-resonant case is reported. In the non-resonant case, the superlinear contribution ( $NL_+$ ) is  $\lesssim 1\%$ , while the negative part ( $NL_-$ ) is of about 4% at short time ( $< 30$  ps) and then decreases, approaching zero in a time scale of about 200 ps. In the resonant case, both the contributions have an initial rise, slower for  $NL_+$ , and

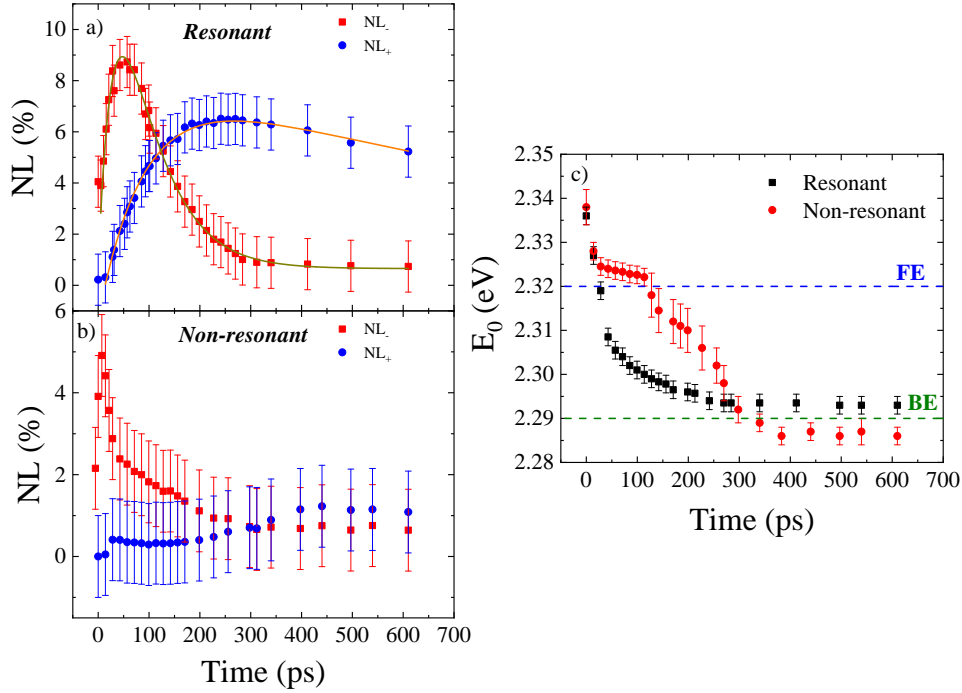


**Figure 8.12:** a-b) Non-linearity for the CR under resonant (a) and non-resonant (b) bias as a function of time. Continuous lines are fits according to the Eqn. 8.8. c) Zero crossing energy ( $E_0$ ) for the CR as a function of time, extracted by the difference spectra of Fig. 8.11. Dashed lines indicate the position of the FE and BE emission in the TI spectra.

the recovery from the superlinearity is much longer than the non-resonant case. In particular,  $NL_+$  remains about 5% after 600 ps.

To estimate the time scale of the non-linearity processes we fit the curve of Fig. 8.12(a) with a double exponential

$$NL(t) = A(e^{-t/\tau_2} - e^{-t/\tau_1}), \quad (8.8)$$

where  $\tau_2$  and  $\tau_1$  the recovery time and the rise time, respectively. Example of fits are shown for the resonant case in Fig. 8.12(a) and the results are shown in Tab. 8.1. We can see that, in the resonant case, the rise time of the superlinear contribution equals the recovery time from the saturation. This suggests that the increase of population of the FE states comes from a transfer of population from the localized/bound states. Instead, in the non-resonant case the rise time is below 10 ps and two decay constants are necessary to fit the recovery from the bleaching: the fast decay constant is of about 20 ps, while the slow decay constant is of about 120 ps.

**Table 8.1:** Results of the fits of the non-linearity of Fig. 8.12(a-b) in the CR according to Eqn. 8.8. The labels “fast” and “slow” refer to the two decay constants.

Excitation	Non-linearity	$\tau_1$ (ps)	$\tau_2$ (ps)
Resonant	$NL_-$	$40 \pm 10$	$70 \pm 20$
	$NL_+$	$80 \pm 20$	$(1.4 \pm 0.2) \cdot 10^3$
Non-resonant	$NL_-$		$20 \pm 10$ (fast)
			$120 \pm 20$ (slow)

Another important parameter in the difference spectra is the zero crossing energy ( $E_0$ ), that marks the transition between the two non-linear regimes (superlinear and saturation). In Fig. 8.12(c) the energy  $E_0$  as a function of time in the CR, extracted from the difference spectra,

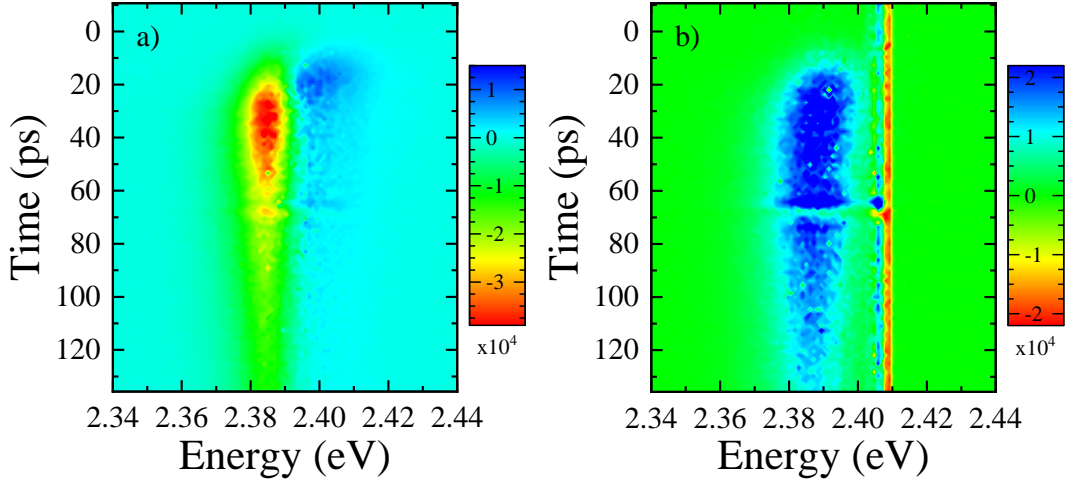


**Figure 8.13:** Difference images for the SC film under non-resonant (a) and resonant (b) bias.

is reported for the resonant and non-resonant case. We can see that  $E_0$  red shifts with time and reaches the value of the BE emission (2.29 eV) after  $\sim 300$  ps. The shift of the zero crossing energy is related to a different recovery of the non-linearity between the high and low energy part of the PL spectrum.

In the SC film, different non-linear behaviours are found under resonant and non-resonant excitation, as shown in Fig. 8.13, where the difference images for the high energy band are reported. Under resonant excitation, if we exclude the spectral region near the laser line, there is only a superlinear increase of the PL intensity. The NL reaches a maximum of  $\sim 14\%$  after 70 ps and a full recovery of the non-linearity occurs at 300 ps (see Fig. 8.14(b)). Fitting the curve of Fig. 8.14(b) with the Eqn. 8.8 we obtain a rise time  $\tau_1$  of  $\sim 60$  ps and a recovery time  $\tau_2$  of  $\sim 80$  ps for the SC film. Therefore, population of the free states and the recovery from the superlinearity in the resonant case is faster in the SC film than in the single crystal. Similar results are obtained for the low energy bands.

Instead, under non-resonant excitation (Fig. 8.13(b)), as well as in the single CR, there is a saturation of the low energy states (localized states) and a superlinear increase of the free states. Concerning the superlinearity (not shown), the contribution is below 2% (irrespective of the excitation power), as for the SC (see Fig. 8.12(b)). Instead, as shown in Fig. 8.14(a), there

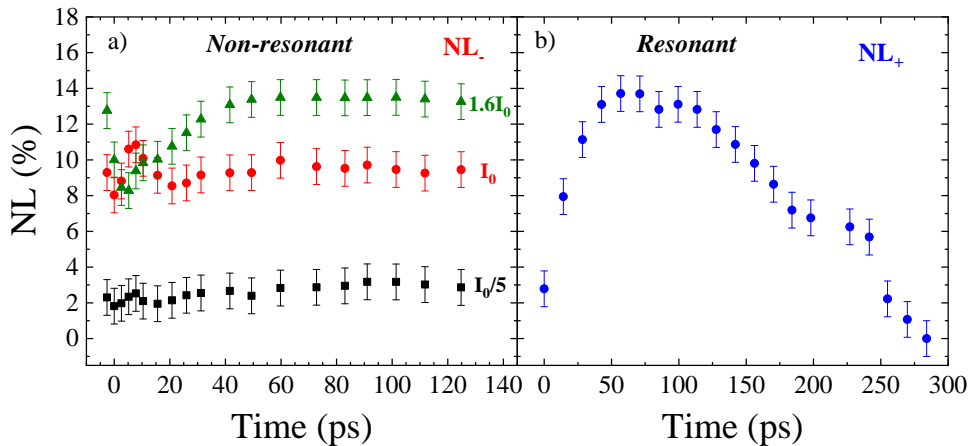


**Figure 8.14:** a)  $NL_-$  for the SC film under non-resonant bias at different excitation intensity.  $I_0$  corresponds to an intensity of  $6 \text{ W cm}^{-2}$ . b)  $NL_+$  for the SC film under resonant excitation at  $I_0$ .

is not a full recovery of NL<sub>-</sub> between a pulse and the following. The lack of full recovery of the bleaching, that becomes much important increasing the power of the CW bias, suggests that long-living defect states rule the non-linear dynamics. Given the morphology of the SC film, that is composed by micro-crystals, we suppose that this behaviour is related to the presence of surface states. To conclude, we report in Fig. 8.15 the zero crossing energy as a function of time for the SC film under non-resonant excitation. A red shift of  $E_0$  ( $\sim 8$  meV) is observed in the first 100 ps, irrespective of the power of the CW bias. We can see that this shift is smaller if compared with the single crystal (Fig. 8.12(c)).

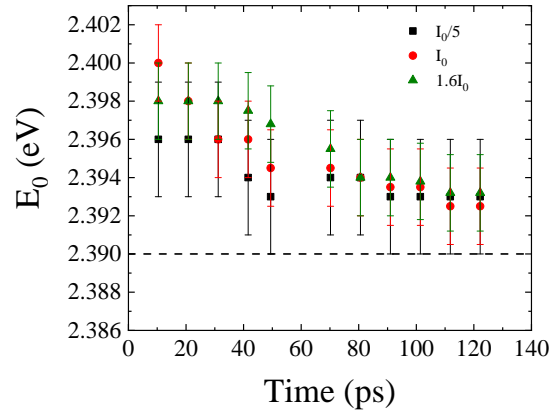


**Figure 8.15:** Zero crossing energy ( $E_0$ ) for the SC film as a function of time. Dashed line indicates the peak of the PL emission in the TI spectra.

## §9§ Conclusions and perspectives

In this work we presented an experimental study of the optical properties of MAPI and CsPbBr<sub>3</sub> perovskites by means of high resolution PL spectroscopy, with the aim of providing a knowledge of the physical processes that rule the emission properties in these materials.

MAPI, with a band gap of 1.6 eV at room temperature, is extensively used as absorbing layer in a new generation of low-cost solar cells. In this kind of solar cells, the transporting layers, that separately collect photo-generated charge carriers, play a fundamental role. For this reason, we investigated the recombination dynamics in MAPI PSCs with different mesoporous ETLs. By using photoelectrodes instead of complete cells we provide quantitative information on the electron collection efficiency varying the ETL. Firstly, the observation of faster PL decays at room temperature exciting from the FTO side when graphene-based ETL are used accounted for a better carrier removal from MAPI layer toward the ETL so demonstrating that the use of graphene based ETL improves the electron collection respect to the conventional mTiO<sub>2</sub> ETL. Moreover, we showed that the choice of the ETL also influences the morphology of MAPI film. In case of G+mTiO<sub>2</sub> plus GO-Li as ETL, PL spectra as a function of temperature, power density and excitation energy indicated a better crystalline quality, with a lower density of traps, of the MAPI film embedded in the mesoporous layer and that the interaction between MAPI and ETL inhibits the phase transition from the tetragonal to the orthorhombic phase.

MAPI is also studied for near-infrared light-emitting sources. In this context, we correlated the physical origin of the superlinear emission (SE) in MAPI perovskites with the sample morphology (single micro-crystals or disordered films). In case of disordered films, the emission under high excitation density ( $> 3 \text{ mJ/cm}^2$ ) is characterized by a multimodal emission and it is not polarized, suggesting that the SE in disordered films comes from an amplified spontaneous emission (ASE). On the contrary, the SE in the MWR, that occurs at lower excitation density ( $> 70 \text{ } \mu\text{J/cm}^2$ ) is characterized by few narrow modes (FWHM  $< 1 \text{ meV}$ ) and a strong polarization is observed ( $\sim 80\%$ ). Moreover, the polarization axis is strongly correlated to the geometry of the microcrystal. Therefore, the SE in MAPI MWRs can be seen as a true lasing, where the microcrystal acts as an optical cavity, delimited by the crystal surfaces.

Concerning CsPbBr<sub>3</sub> perovskites, that are mainly investigated for the realization of efficient green light sources, we studied different aspects of the radiative emission (recombination dynamics, relaxation processes) in thin films and single crystals. In nanocrystalline films, we showed the significant role of the carrier trapping in surface states on the carrier recombination dynamics in CsPbBr<sub>3</sub> NCs. Increasing temperature from 10 K to 300 K a significant slowdown of the recombination dynamics was observed, more relevant for the high energy PL bands, that correspond to the emission from smaller NCs. This slowdown of the recombination dynamics was interpreted as the consequence of a transfer of population from non-radiative states, where carriers are easily trapped but do not recombine, back to the radiative states. In fact, given the morphology of the NCs, the origin of the non-radiative states acting as a sink for the radiative

states can be ascribed to the NCs surface and their role is expected to be more relevant for smaller NCs, since the ratio between the volume and surface density of states scaled with the crystal size.

Finally, in this thesis we discussed the relaxation and thermalization process in CsPbBr<sub>3</sub> single crystals and spin-coated films. High resolution low temperature TR-PL measurements bring evidence of a thermalized carrier distribution, as marked by the presence of an exponential tail in the high energy side of the TR-PL spectra. However, there is a bottleneck in the thermalization under non-resonant excitation: the carriers temperature remains higher than the lattice temperature. This bottleneck can be attributed to the reabsorption of the low-energy emitted phonons during the relaxation, that produces an heating of the carriers. We point out that the thermalization bottleneck could be also originated from efficient Auger processes, but given the Auger coefficient in CsPbBr<sub>3</sub> ( $10^{-29} \text{ cm}^6 \text{ s}^{-1}$ ) and our experimental excitation density ( $10^{16} \text{ cm}^{-3}$ ) Auger scattering can be considered negligible.

Moreover, non-linearities in the emission are observed when an additional CW bias is applied together with the pulsed laser. The bleaching of the emission is attributed to the saturation of the localized/bound states, whereas the superlinearity to the population of the free states. In the single crystal, under non-resonant excitation the superlinearity is below 1 %, while a significant bleaching of the emission occurs in the first 200 ps. Instead, under resonant-excitation a transfer of population from the localized/bound states to the free states is evidenced. For the spin-coated film, under resonant excitation there is only a superlinear increase of the PL intensity, with a faster recovery time than in the case of single crystal. Moreover, under non-resonant excitation, there is not a full recovery of the bleaching between an excitation pulse and the following, that is more relevant increasing the power of the CW bias. This suggest that long-living defect states rule the non-linear dynamics. Given the morphology of the spin-coated film, that is composed by micro-crystals, we suppose that this behaviour is related to the presence of surface states.

In this thesis we investigated several fundamental aspects of the emission properties in perovskites, correlated to the different applications of these materials. For MAPI, we focused on the carrier recombination dynamics in PSCs, demonstrating that the use of graphene-based ETL improves the electron collection efficiency and the morphology of the active layer, leading to better photovoltaic performance. Moreover, we provided a correlation between the physical origin of the stimulated emission and the morphology of the material. For CsPbBr<sub>3</sub>, we investigated the recombination dynamics and the relaxation process in thin films and single crystals, showing the contribution of surface states, localized states and free states. However, several aspects require further investigation. Firstly, we point out that CsPbBr<sub>3</sub> samples studied in this thesis are nanocrystalline films, that show significant inhomogeneities in structural and optical properties. With the aim to obtain a device, an improvement of the synthesis technique is therefore necessary since an homogeneous film with well-defined thickness is preferable. In addition, despite a remarkable improvement in the stability was obtained by using all-inorganic perovskites, the high sensitivity to environmental conditions and the low operating stability of PeLEDs must be solved before using them in industry. Finally, also the toxicity problem of perovskites due to the presence of lead is another serious problem that must be resolved. Alternative metal cations

( $\text{Sn}^{2+}$ ,  $\text{Ge}^{2+}$ ) were recently investigated as substitute of lead, but Pb-free perovskite devices exhibit worse performance compared to lead halide counterparts.

Therefore, we believe that much fundamental research in different fields (material science, physics, chemistry etc.) is required to really take advantage of the extraordinary properties of perovskites.



## List of abbreviations

<b>ASE</b>	<i>Amplified spontaneous emission</i>
<b>CW</b>	<i>Continuous wave</i>
<b>DMSO</b>	<i>Dimethyl sulfoxide</i>
<b>DOS</b>	<i>Density of states</i>
<b><math>E_g</math></b>	<i>Band gap</i>
<b>EQE</b>	<i>External quantum efficiency</i>
<b>ETL</b>	<i>Electron transporting layer</i>
<b>FF</b>	<i>Fill factor</i>
<b>FWHM</b>	<i>Full width half maximum</i>
<b>GO-Li</b>	<i>Lithium-neutralized graphene oxide</i>
<b>HTL</b>	<i>Hole transporting layer</i>
<b><math>J_{SC}</math></b>	<i>Short circuit current density</i>
<b>MAPI</b>	<i>Methylammonium lead iodide (<math>CH_3NH_3PbI_3</math>)</i>
<b>mTiO<sub>2</sub></b>	<i>Mesoporous titanium oxide</i>
<b>MWR</b>	<i>Microwire</i>
<b>NC</b>	<i>Nanocrystal</i>
<b>PCE</b>	<i>Photovoltaic conversion efficiency</i>
<b>PeLED</b>	<i>Perovskite LED</i>
<b>PL</b>	<i>Photoluminescence</i>
<b>PLQY</b>	<i>Photoluminescence quantum yield</i>
<b>PSC</b>	<i>Perovskite solar cell</i>
<b>QD</b>	<i>Quantum dot</i>
<b>SEM</b>	<i>Scanning electron microscopy</i>
<b>SNOM</b>	<i>Near-field scanning optical microscopy</i>
<b>SUN</b>	<i>1 SUN = 1 kW/m<sup>2</sup></i>
<b>TCSPC</b>	<i>Time correlated single photon counting</i>
<b>TI</b>	<i>Time integrated</i>
<b>TR</b>	<i>Time resolved</i>
<b>XRD</b>	<i>X-ray diffraction</i>
<b><math>V_{OC}</math></b>	<i>Open-circuit voltage</i>

## List of publications

- BICCARI, F., GABELLONI, F., FRANCONI, C., LA CHINA, F., CASELLI, N., INTONTI, F., GURIOLI, M., LEE, J., LEBLEBICI, S., WEBER-BARGIONI, A. AND VINATTIERI, A., “Superlinear emission in bare perovskite: amplified spontaneous emission in disordered film versus single crystal lasing”, *Mater. Today: Proc.* **4**, S12–S18 (2017), [doi: 10.1016/j.matpr.2017.05.005](https://doi.org/10.1016/j.matpr.2017.05.005).
- BICCARI, F., GABELLONI, F., BURZI, E., GURIOLI, M., PESCELELLI, S., AGRESTI, A., DEL RIO CASTILLO, A. E., ANSALDO, A., KYMAKIS, E., BONACCORSO, F., DI CARLO, A. AND VINATTIERI, A., “Graphene-based electron transport layers in perovskite solar cells: a step-up for an efficient carrier collection”, *Adv. Energy Mater.* **7**(22), 1701349 (2017), [doi: 10.1002/aenm.201701349](https://doi.org/10.1002/aenm.201701349).
- GABELLONI, F., BICCARI, F., ANDREOTTI, G., BALESTRI, D., CHECCUCCI, S., MILANESI, A., CALISI, N., CAPORALI, S. AND VINATTIERI, A., “Recombination dynamics in CsPbBr<sub>3</sub> nanocrystals: role of surface states”, *Opt. Mater. Express* **7**(12), 4367–4373 (2017), [doi: 10.1364/ome.7.004367](https://doi.org/10.1364/ome.7.004367).

## Partecipation to conferences

- “Near-field optical spectroscopy of CsPbBr<sub>3</sub> microstructures” (Poster), *OSA Advanced Photonic Congress*, 2–5 July 2018, Zürich.
- “Anomalous increase of the photoluminescence decay time with the temperature in CsPbBr<sub>3</sub> nanocrystals: role of the thermally activated transfer from the surface states” (Poster), *nanoGe September Meeting 17*, 7–8 September 2017, Barcelona.
- “Exciton recombination kinetics in high quality CsPbBr<sub>3</sub> thin films” (Poster), *The International Conference on Perovskite Thin Film Photovoltaics (ABXPV17)*, 27–28 February 2017, Valencia.
- “Probing graphene-based electron transport layer in perovskite solar cells by photoluminescence spectroscopy” (Poster), *The International Conference on Perovskite Thin Film Photovoltaics (ABXPV17)*, 27–28 February 2017, Valencia.

## References

- [1] “Enerdata - Global energy statistical yearbook 2018”, <https://yearbook.enerdata.net/total-energy/world-consumption-statistics.html>.
- [2] “BP - Statistical review of world energy 2018”, <https://www.bp.com/en/global/corporate/energy-economics/statistical-review-of-world-energy.html>.
- [3] MANSER, J. S., CHRISTIANS, J. A. AND KAMAT, P. V., “Intriguing optoelectronic properties of metal halide perovskites”, *Chem. Rev.* **116**(21), 12956–13008 (2016), [doi: 10.1021/acs.chemrev.6b00136](https://doi.org/10.1021/acs.chemrev.6b00136).
- [4] CHEN, Q., MARCO, N. D., YANG, Y. M., SONG, T.-B., CHEN, C.-C., ZHAO, H., HONG, Z., ZHOU, H. AND YANG, Y., “Under the spotlight: the organic-inorganic hybrid halide perovskite for optoelectronic applications”, *Nano Today* **10**(3), 355–396 (2015), [doi: 10.1016/j.nantod.2015.04.009](https://doi.org/10.1016/j.nantod.2015.04.009).
- [5] XIAO, Z., YUAN, Y., WANG, Q., SHAO, Y., BAI, Y., DENG, Y., DONG, Q., HU, M., BI, C. AND HUANG, J., “Thin-film semiconductor perspective of organometal trihalide perovskite materials for high-efficiency solar cells”, *Mater. Sci. Eng. R* **101**, 1–38 (2016), [doi: 10.1016/j.mser.2015.12.002](https://doi.org/10.1016/j.mser.2015.12.002).
- [6] WOLF, S. D., HOLOVSKY, J., MOON, S.-J., LÖPER, P., NIESEN, B., LEDINSKY, M., HAUG, F.-J., YUM, J.-H. AND BALLIF, C., “Organometallic halide perovskites: sharp optical absorption edge and its relation to photovoltaic performance”, *J. Phys. Chem. Lett.* **5**, 1035–1039 (2014), [doi: 10.1021/jz500279b](https://doi.org/10.1021/jz500279b).
- [7] LÖPER, P., STUCKELBERGER, M., NIESEN, B., WERNER, J., FILIPIČ, M., MOON, S.-J., YUM, J.-H., TOPIČ, M., WOLF, S. D. AND BALLIF, C., “Complex refractive index spectra of CH<sub>3</sub>NH<sub>3</sub>PbI<sub>3</sub> perovskite thin films determined by spectroscopic ellipsometry and spectrophotometry”, *J. Phys. Chem. Lett.* **6**, 66–71 (2015), [doi: 10.1021/jz502471h](https://doi.org/10.1021/jz502471h).
- [8] YIN, W.-J., SHI, T. AND YAN, Y., “Unique properties of halide perovskites as possible origins of the superior solar cell performance”, *Adv. Mater.* **26**(27), 4653–4658 (2014), [doi: 10.1002/adma.201306281](https://doi.org/10.1002/adma.201306281).
- [9] DONG, Q., FANG, Y., SHAO, Y., MULLIGAN, P., QIU, J., CAO, L. AND HUANG, J., “Electron-hole diffusion lengths > 175 μm in solution-grown CH<sub>3</sub>NH<sub>3</sub>PbI<sub>3</sub> single crystals”, *Science* **347**(6225), 967–970 (2015), [doi: 10.1126/science.aaa5760](https://doi.org/10.1126/science.aaa5760).
- [10] SONG, J., CUI, Q., LI, J., XU, J., WANG, Y., XU, L., XUE, J., DONG, Y., TIAN, T., SUN, H. AND ZENG, H., “Ultralarge all-inorganic perovskite bulk single crystal for high-performance visible-infrared dual-modal photodetectors”, *Adv. Opt. Mater.* **5**(12), 1700157 (2017), [doi: 10.1002/adom.201700157](https://doi.org/10.1002/adom.201700157).

- [11] STRANKS, S. D., EPERON, G. E., GRANCINI, G., MENELAOU, C., ALCOCKER, M. J. P., LEIJTENS, T., HERZ, L. M., PETROZZA, A. AND SNAITH, H. J., “Electron-hole diffusion lengths exceeding 1 micrometer in an organometal trihalide perovskite absorber”, *Science* **342**(6156), 341–344 (2013), doi: [10.1126/science.1243982](https://doi.org/10.1126/science.1243982).
- [12] YETTAPU, G. R., TALUKDAR, D., SARKAR, S., SWARNKAR, A., NAG, A., GHOSH, P. AND MANDAL, P., “Terahertz conductivity within colloidal CsPbBr<sub>3</sub> perovskite nanocrystals: remarkably high carrier mobilities and large diffusion lengths”, *Nano Lett.* **16**(8), 4838–4848 (2016), doi: [10.1021/acs.nanolett.6b01168](https://doi.org/10.1021/acs.nanolett.6b01168).
- [13] GIORGI, G., FUJISAWA, J.-I., SEGAWA, H. AND YAMASHITA, K., “Small photocarrier effective masses featuring ambipolar transport in methylammonium lead iodide perovskite: a density functional analysis”, *J. Phys. Chem. Lett.* **4**(24), 4213–4216 (2013), doi: [10.1021/jz4023865](https://doi.org/10.1021/jz4023865).
- [14] MIYATA, A., MITIOGLU, A., PLOCHOCKA, P., PORTUGALL, O., WANG, J. T.-W., STRANKS, S. D., SNAITH, H. J. AND NICHOLAS, R. J., “Direct measurement of the exciton binding energy and effective masses for charge carriers in organic-inorganic trihalide perovskites”, *Nat. Phys.* **11**(7), 582–587 (2015), doi: [10.1038/nphys3357](https://doi.org/10.1038/nphys3357).
- [15] SHI, D., ADINOLFI, V., COMIN, R., YUAN, M., ALAROUSU, E., BUIN, A., CHEN, Y., HOOGLAND, S., ROTHENBERGER, A., KATSIEV, K., LOSOVYJ, Y., ZHANG, X., DOWBEN, P. A., MOHAMMED, O. F., SARGENT, E. H. AND BAKR, O. M., “Low trap-state density and long carrier diffusion in organolead trihalide perovskite single crystals”, *Science* **347**(6221), 519–522 (2015), doi: [10.1126/science.aaa2725](https://doi.org/10.1126/science.aaa2725).
- [16] YIN, W.-J., SHI, T. AND YAN, Y., “Superior photovoltaic properties of lead halide perovskites: insights from first-principles theory”, *J. Phys. Chem. C* **119**(10), 5253–5264 (2015), doi: [10.1021/jp512077m](https://doi.org/10.1021/jp512077m).
- [17] KANG, J. AND WANG, L.-W., “High defect tolerance in lead halide perovskite CsPbBr<sub>3</sub>”, *J. Phys. Chem. Lett.* **8**, 489–493 (2017), doi: [10.1021/acs.jpcclett.6b02800](https://doi.org/10.1021/acs.jpcclett.6b02800).
- [18] PROTESESCU, L., YAKUNIN, S., BODNARCHUK, M. I., KRIEG, F., CAPUTO, R., HENDON, C. H., YANG, R. X., WALSH, A. AND KOVALENKO, M. V., “Nanocrystals of cesium lead halide perovskites (CsPbX<sub>3</sub>, X = Cl, Br, and I): novel optoelectronic materials showing bright emission with wide color gamut”, *Nano Lett.* **15**, 3692–3696 (2015), doi: [10.1021/nl5048779](https://doi.org/10.1021/nl5048779).
- [19] GREEN, M. A. AND HO-BAILLIE, A., “Perovskite solar cells: The birth of a new era in photovoltaics”, *ACS Energy Letters* **2**(4), 822–830 (2017), doi: [10.1021/acsenerylett.7b00137](https://doi.org/10.1021/acsenerylett.7b00137).
- [20] POLMAN, A., KNIGHT, M., GARNETT, E. C., EHRLER, B. AND SINKE, W. C., “Photovoltaic materials: present efficiencies and future challenges”, *Science* **352**(6283), aad4424 (2016), doi: [10.1126/science.aad4424](https://doi.org/10.1126/science.aad4424).

- [21] KOJIMA, A., TESHIMA, K., SHIRAI, Y. AND MIYASAKA, T., “Organometal halide perovskites as visible-light sensitizers for photovoltaic cells”, *J. Am. Chem. Soc.* **131**(17), 6050–6051 (2009), doi: [10.1021/ja809598r](https://doi.org/10.1021/ja809598r).
- [22] YANG, W. S., PARK, B.-W., JUNG, E. H., JEON, N. J., KIM, Y. C., LEE, D. U., SHIN, S. S., SEO, J., KIM, E. K., NOH, J. H. AND SEOK, S. I., “Iodide management in formamidinium-lead-halide-based perovskite layers for efficient solar cells”, *Science* **356**(6345), 1376–1379 (2017), doi: [10.1126/science.aan2301](https://doi.org/10.1126/science.aan2301).
- [23] “NREL best research-cell efficiency chart”, <https://www.nrel.gov/pv/assets/images/efficiency-chart.png>.
- [24] ASGHAR, M., ZHANG, J., WANG, H. AND LUND, P., “Device stability of perovskite solar cells - A review”, *Renewable Sustainable Energy Rev.* **77**, 131–146 (2017), doi: [10.1016/j.rser.2017.04.003](https://doi.org/10.1016/j.rser.2017.04.003).
- [25] LEGUY, A. M. A., HU, Y., CAMPOY-QUILES, M., ALONSO, M. I., WEBER, O. J., AZARHOOSH, P., VAN SCHILFGAARDE, M., WELLER, M. T., BEIN, T., NELSON, J., DOCAMPO, P. AND BARNES, P. R. F., “Reversible hydration of  $\text{CH}_3\text{NH}_3\text{PbI}_3$  in films, single crystals, and solar cells”, *Chem. Mater.* **27**(9), 3397–3407 (2015), doi: [10.1021/acs.chemmater.5b00660](https://doi.org/10.1021/acs.chemmater.5b00660).
- [26] CHRISTIANS, J. A., HERRERA, P. A. M. AND KAMAT, P. V., “Transformation of the excited state and photovoltaic efficiency of  $\text{CH}_3\text{NH}_3\text{PbI}_3$  perovskite upon controlled exposure to humidified air”, *J. Am. Chem. Soc.* **137**(4), 1530–1538 (2015), doi: [10.1021/ja511132a](https://doi.org/10.1021/ja511132a).
- [27] MISRA, R. K., AHARON, S., LI, B., MOGILYANSKY, D., VISOLY-FISHER, I., ETGAR, L. AND KATZ, E. A., “Temperature- and component-dependent degradation of perovskite photovoltaic materials under concentrated sunlight”, *J. Phys. Chem. Lett.* **6**, 326–330 (2015), doi: [10.1021/jz502642b](https://doi.org/10.1021/jz502642b).
- [28] ABDELMAGEED, G., JEWELL, L., HELLIER, K., SEYMOUR, L., LUO, B., BRIDGES, F., ZHANG, J. Z. AND CARTER, S., “Mechanisms for light induced degradation in  $\text{MAPbI}_3$  perovskite thin films and solar cells”, *Appl. Phys. Lett.* **109**, 233905 (2016), doi: [10.1063/1.4967840](https://doi.org/10.1063/1.4967840).
- [29] DUALEH, A., TÉTREAU, N., MOEHL, T., GAO, P., NAZEERUDDIN, M. K. AND GRÄTZEL, M., “Effect of annealing temperature on film morphology of organic-inorganic hybrid perovskite solid-state solar cells”, *Adv. Funct. Mater.* **24**, 3250–3258 (2014), doi: [10.1002/adfm.201304022](https://doi.org/10.1002/adfm.201304022).
- [30] LEIJTENS, T., EPERON, G. E., PATHAK, S., ABATE, A., LEE, M. M. AND SNAITH, H. J., “Overcoming ultraviolet light instability of sensitized  $\text{TiO}_2$  with meso-structured organometal tri-halide perovskite solar cells”, *Nat. Commun.* **4**, 2885 (2013), doi: [10.1038/ncomms3885](https://doi.org/10.1038/ncomms3885).

- [31] ITO, S., TANAKA, S., MANABE, K. AND NISHINO, H., “Effects of surface blocking layer of  $\text{Sb}_2\text{S}_3$  on nanocrystalline  $\text{TiO}_2$  for  $\text{CH}_3\text{NH}_3\text{PbI}_3$  perovskite solar cells”, *J. Phys. Chem. C* **118**, 16995–17000 (2014), doi: [10.1021/jp500449z](https://doi.org/10.1021/jp500449z).
- [32] HAWASH, Z., ONO, L. K., RAGA, S. R., LEE, M. V. AND QI, Y., “Air-exposure induced dopant redistribution and energy level shifts in spin-coated Spiro-MeOTAD films”, *Chem. Mater.* **27**, 562–569 (2015), doi: [10.1021/cm504022q](https://doi.org/10.1021/cm504022q).
- [33] KATO, Y., ONO, L. K., LEE, M. V., WANG, S., RAGA, S. R. AND QI, Y., “Silver iodide formation in methyl ammonium lead iodide perovskite solar cells with silver top electrodes”, *Adv. Mater. Interfaces* **2**, 1500195 (2015), doi: [10.1002/admi.201500195](https://doi.org/10.1002/admi.201500195).
- [34] BEAL, R. E., SLOTCAVAGE, D. J., LEIJTENS, T., BOWRING, A. R., BELISLE, R. A., NGUYEN, W. H., BURKHARD, G. F., HOKE, E. T. AND MCGEHEE, M. D., “Cesium lead halide perovskites with improved stability for tandem solar cells”, *J. Phys. Chem. Lett.* **7**, 746–751 (2016), doi: [10.1021/acs.jpcllett.6b00002](https://doi.org/10.1021/acs.jpcllett.6b00002).
- [35] KULBAK, M., GUPTA, S., KEDEM, N., LEVINE, I., BENDIKOV, T., HODES, G. AND CAHEN, D., “Cesium enhances long-term stability of lead bromide perovskite-based solar cells”, *J. Phys. Chem. Lett.* **7**, 167–172 (2016), doi: [10.1021/acs.jpcllett.5b02597](https://doi.org/10.1021/acs.jpcllett.5b02597).
- [36] CHO, H., KIM, J. S., KIM, Y.-H. AND LEE, T.-W., “Influence of A-site cation on the thermal stability of metal halide perovskite polycrystalline films”, *Journal of Information Display* **19**(1), 53–60 (2018), doi: [10.1080/15980316.2018.1424652](https://doi.org/10.1080/15980316.2018.1424652).
- [37] EPERON, G. E., STRANKS, S. D., MENELAOU, C., JOHNSTON, M. B., HERZ, L. M. AND SNAITH, H. J., “Formamidinium lead trihalide: a broadly tunable perovskite for efficient planar heterojunction solar cells”, *Energy Environ. Sci.* **7**, 982–988 (2014), doi: [10.1039/c3ee43822h](https://doi.org/10.1039/c3ee43822h).
- [38] LEE, J.-W., KIM, D.-H., KIM, H.-S., SEO, S.-W., CHO, S. M. AND PARK, N.-G., “Formamidinium and cesium hybridization for photo- and moisture-stable perovskite solar cell”, *Adv. Energy Mater.* **5**, 1501310 (2015), doi: [10.1002/aenm.201501310](https://doi.org/10.1002/aenm.201501310).
- [39] PELLET, N., GAO, P., GREGORI, G., YANG, T.-Y., NAZEERUDDIN, M. K., MAIER, J. AND GRÄTZEL, M., “Mixed-organic-cation perovskite photovoltaics for enhanced solar-light harvesting”, *Angew. Chem. Int. Ed.* **53**, 3151–3157 (2014), doi: [10.1002/anie.201309361](https://doi.org/10.1002/anie.201309361).
- [40] NOH, J. H., IM, S. H., HEO, J. H., MANDAL, T. N. AND SEOK, S. I., “Chemical management for colorful, efficient, and stable inorganic–organic hybrid nanostructured solar cells”, *Nano Lett.* **13**, 1764–1769 (2013), doi: [10.1021/nl400349b](https://doi.org/10.1021/nl400349b).
- [41] LI, Z., KLEIN, T. R., KIM, D. H., YANG, M., BERRY, J. J., VAN HEST, M. F. A. M. AND ZHU, K., “Scalable fabrication of perovskite solar cells”, *Nature Reviews Materials* **3**(4), 18017 (2018), doi: [10.1038/natrevmats.2018.17](https://doi.org/10.1038/natrevmats.2018.17).

- [42] ZHANG, Q., HAO, F., LI, J., ZHOU, Y., WEI, Y. AND LIN, H., “Perovskite solar cells: must lead be replaced - and can it be done?”, *Sci. Technol. Adv. Mater.* **19**(1), 425–442 (2018), doi: [10.1080/14686996.2018.1460176](https://doi.org/10.1080/14686996.2018.1460176).
- [43] OGOMI, Y., MORITA, A., TSUKAMOTO, S., SAITHO, T., FUJIKAWA, N., SHEN, Q., TOYODA, T., YOSHINO, K., PANDEY, S. S., MA, T. AND HAYASE, S., “CH<sub>3</sub>NH<sub>3</sub>Sn<sub>x</sub>Pb<sub>(1-x)</sub>I<sub>3</sub> perovskite solar cells covering up to 1060 nm”, *J. Phys. Chem. Lett.* **5**(6), 1004–1011 (2014), doi: [10.1021/jz5002117](https://doi.org/10.1021/jz5002117).
- [44] SHOCKLEY, W. AND QUEISSER, H. J., “Detailed balance limit of efficiency of p-n junction solar cells”, *J. Appl. Phys.* **32**(3), 510–519 (1961), doi: [10.1063/1.1736034](https://doi.org/10.1063/1.1736034).
- [45] TAKAHASHI, Y., OBARA, R., LIN, Z.-Z., TAKAHASHI, Y., NAITO, T., INABE, T., ISHIBASHI, S. AND TERAOKA, K., “Charge-transport in tin-iodide perovskite CH<sub>3</sub>NH<sub>3</sub>SnI<sub>3</sub>: origin of high conductivity”, *Dalton Trans.* **40**(20), 5563 (2011), doi: [10.1039/c0dt01601b](https://doi.org/10.1039/c0dt01601b).
- [46] NOEL, N. K., STRANKS, S. D., ABATE, A., WEHRENFENNIG, C., GUARNERA, S., HAGHIGHIRAD, A.-A., SADHANALA, A., EPERON, G. E., PATHAK, S. K., JOHNSTON, M. B., PETROZZA, A., HERZ, L. M. AND SNAITH, H. J., “Lead-free organic-inorganic tin halide perovskites for photovoltaic applications”, *Energy Environ. Sci.* **7**(9), 3061–3068 (2014), doi: [10.1039/c4ee01076k](https://doi.org/10.1039/c4ee01076k).
- [47] IEFANOVA, A., ADHIKARI, N., DUBEY, A., KHATIWADA, D. AND QIAO, Q., “Lead free CH<sub>3</sub>NH<sub>3</sub>SnI<sub>3</sub> perovskite thin-film with p-type semiconducting nature and metal-like conductivity”, *AIP Advances* **6**(8), 085312 (2016), doi: [10.1063/1.4961463](https://doi.org/10.1063/1.4961463).
- [48] XIAO, M., GU, S., ZHU, P., TANG, M., ZHU, W., LIN, R., CHEN, C., XU, W., YU, T. AND ZHU, J., “Tin-based perovskite with improved coverage and crystallinity through tin-fluoride-assisted heterogeneous nucleation”, *Adv. Opt. Mater.* **6**(1), 1700615 (2017), doi: [10.1002/adom.201700615](https://doi.org/10.1002/adom.201700615).
- [49] SONG, T.-B., YOKOYAMA, T., ARAMAKI, S. AND KANATZIDIS, M. G., “Performance enhancement of lead-free tin-based perovskite solar cells with reducing atmosphere-assisted dispersible additive”, *ACS Energy Letters* **2**(4), 897–903 (2017), doi: [10.1021/acseenergylett.7b00171](https://doi.org/10.1021/acseenergylett.7b00171).
- [50] KIM, Y. Y., PARK, E. Y., YANG, T.-Y., NOH, J. H., SHIN, T. J., JEON, N. J. AND SEO, J., “Fast two-step deposition of perovskite via mediator extraction treatment for large-area, high-performance perovskite solar cells”, *J. Mater. Chem. A* **6**(26), 12447–12454 (2018), doi: [10.1039/c8ta02868k](https://doi.org/10.1039/c8ta02868k).
- [51] CHEN, H., YE, F., TANG, W., HE, J., YIN, M., WANG, Y., XIE, F., BI, E., YANG, X., GRÄTZEL, M. AND HAN, L., “A solvent- and vacuum-free route to large-area perovskite films for efficient solar modules”, *Nature* (2017), doi: [10.1038/nature23877](https://doi.org/10.1038/nature23877).
- [52] CALABRÒ, E., MATTEOCCHI, F., PALMA, A. L., VESCE, L., TAHERI, B., CARLINI, L., PIS, I., NAPPINI, S., DAGAR, J., BATTOCCHIO, C., BROWN, T. M. AND CARLO,



- A. D., “Low temperature, solution-processed perovskite solar cells and modules with an aperture area efficiency of 11%”, *Sol. Energy Mater. Sol. Cells* **185**, 136–144 (2018), doi: [10.1016/j.solmat.2018.05.001](https://doi.org/10.1016/j.solmat.2018.05.001).
- [53] AGRESTI, A., PESCE TELLI, S., PALMA, A. L., CASTILLO, A. E. D. R., KONIOS, D., KAKAVELAKIS, G., RAZZA, S., CINÀ, L., KYMAKIS, E., BONACCORSO, F. AND CARLO, A. D., “Graphene interface engineering for perovskite solar modules: 12.6% power conversion efficiency over 50 cm<sup>2</sup> active area”, *ACS Energy Letters* **2**, 279–287 (2017), doi: [10.1021/acseenergylett.6b00672](https://doi.org/10.1021/acseenergylett.6b00672).
- [54] KIM, Y.-H., CHO, H. AND LEE, T.-W., “Metal halide perovskite light emitters”, *PNAS* **113**(42), 11694–11702 (2016), doi: [10.1073/pnas.1607471113](https://doi.org/10.1073/pnas.1607471113).
- [55] VELDHUIS, S. A., BOIX, P. P., YANTARA, N., LI, M., SUM, T. C., MATHEWS, N. AND MHAISALKAR, S. G., “Perovskite materials for light-emitting diodes and lasers”, *Adv. Mater.* **28**(32), 6804–6834 (2016), doi: [10.1002/adma.201600669](https://doi.org/10.1002/adma.201600669).
- [56] LI, X., WU, Y., ZHANG, S., CAI, B., GU, Y., SONG, J. AND ZENG, H., “CsPbX<sub>3</sub> quantum dots for lighting and displays: room-temperature synthesis, photoluminescence superiorities, underlying origins and white light-emitting diodes”, *Adv. Funct. Mater.* **26**(15), 2435–2445 (2016), doi: [10.1002/adfm.201600109](https://doi.org/10.1002/adfm.201600109).
- [57] WEI, S., YANG, Y., KANG, X., WANG, L., HUANG, L. AND PAN, D., “Room-temperature and gram-scale synthesis of CsPbX<sub>3</sub> (X = Cl, Br, I) perovskite nanocrystals with 50–85% photoluminescence quantum yields”, *Chem. Commun.* **52**(45), 7265–7268 (2016), doi: [10.1039/c6cc01500j](https://doi.org/10.1039/c6cc01500j).
- [58] SWARNKAR, A., CHULLIYIL, R., RAVI, V. K., IRFANULLAH, M., CHOWDHURY, A. AND NAG, A., “Colloidal CsPbBr<sub>3</sub> perovskite nanocrystals: luminescence beyond traditional quantum dots”, *Angew. Chem. Int. Ed.* **54**(51), 15424–15428 (2015), doi: [10.1002/anie.201508276](https://doi.org/10.1002/anie.201508276).
- [59] CHIBA, T., HOSHI, K., PU, Y.-J., TAKEDA, Y., HAYASHI, Y., OHISA, S., KAWATA, S. AND KIDO, J., “High-efficiency perovskite quantum-dot light-emitting devices by effective washing process and interfacial energy level alignment”, *ACS Appl. Mater. Interfaces* **9**(21), 18054–18060 (2017), doi: [10.1021/acsmi.7b03382](https://doi.org/10.1021/acsmi.7b03382).
- [60] LI, G., HUANG, J., ZHU, H., LI, Y., TANG, J.-X. AND JIANG, Y., “Surface ligand engineering for near-unity quantum yield inorganic halide perovskite QDs and high-performance QLEDs”, *Chem. Mater.* **30**(17), 6099–6107 (2018), doi: [10.1021/acs.chemmater.8b02544](https://doi.org/10.1021/acs.chemmater.8b02544).
- [61] PAN, J., QUAN, L. N., ZHAO, Y., PENG, W., MURALI, B., SARMAH, S. P., YUAN, M., SINATRA, L., ALYAMI, N. M., LIU, J., YASSITEPE, E., YANG, Z., VOZNYI, O., COMIN, R., HEDHILI, M. N., MOHAMMED, O. F., LU, Z. H., KIM, D. H., SARGENT, E. H. AND BAKR, O. M., “Highly efficient perovskite-quantum-dot light-emitting diodes by surface engineering”, *Adv. Mater.* **28**(39), 8718–8725 (2016), doi: [10.1002/adma.201600784](https://doi.org/10.1002/adma.201600784).

- [62] DAI, X., ZHANG, Z., JIN, Y., NIU, Y., CAO, H., LIANG, X., CHEN, L., WANG, J. AND PENG, X., “Solution-processed, high-performance light-emitting diodes based on quantum dots”, *Nature* **515**(7525), 96–99 (2014), [doi: 10.1038/nature13829](https://doi.org/10.1038/nature13829).
- [63] AIZAWA, N., PU, Y.-J., WATANABE, M., CHIBA, T., IDETA, K., TOYOTA, N., IGARASHI, M., SUZURI, Y., SASABE, H. AND KIDO, J., “Solution-processed multilayer small-molecule light-emitting devices with high-efficiency white-light emission”, *Nat. Commun.* **5**(1) (2014), [doi: 10.1038/ncomms6756](https://doi.org/10.1038/ncomms6756).
- [64] YAKUNIN, S., PROTESESCU, L., KRIEG, F., BODNARCHUK, M. I., NEDELCU, G., HUMER, M., LUCA, G. D., FIEBIG, M., HEISS, W. AND KOVALENKO, M. V., “Low-threshold amplified spontaneous emission and lasing from colloidal nanocrystals of caesium lead halide perovskites”, *Nat. Commun.* **6**(1) (2015), [doi: 10.1038/ncomms9056](https://doi.org/10.1038/ncomms9056).
- [65] STRANKS, S. D., WOOD, S. M., WOJCIECHOWSKI, K., DESCHLER, F., SALIBA, M., KHANDELWAL, H., PATEL, J. B., ELSTON, S. J., HERZ, L. M., JOHNSTON, M. B., SCHENNING, A. P. H. J., DEBIJE, M. G., RIEDE, M. K., MORRIS, S. M. AND SNAITH, H. J., “Enhanced amplified spontaneous emission in perovskites using a flexible cholesteric liquid crystal reflector”, *Nano Lett.* **15**(8), 4935–4941 (2015), [doi: 10.1021/acs.nanolett.5b00678](https://doi.org/10.1021/acs.nanolett.5b00678).
- [66] ZHU, H., FU, Y., MENG, F., WU, X., GONG, Z., DING, Q., GUSTAFSSON, M. V., TRINH, M. T., JIN, S. AND ZHU, X.-Y., “Lead halide perovskite nanowire lasers with low lasing thresholds and high quality factors”, *Nat. Mater.* **14**(6), 636–642 (2015), [doi: 10.1038/nmat4271](https://doi.org/10.1038/nmat4271).
- [67] ZHANG, Q., HA, S. T., LIU, X., SUM, T. C. AND XIONG, Q., “Room-temperature near-infrared high-Q perovskite whispering-gallery planar nanolasers”, *Nano Lett.* **14**(10), 5995–6001 (2014), [doi: 10.1021/nl503057g](https://doi.org/10.1021/nl503057g).
- [68] ZHANG, Q., SU, R., LIU, X., XING, J., SUM, T. C. AND XIONG, Q., “High-quality whispering-gallery-mode lasing from cesium lead halide perovskite nanoplatelets”, *Adv. Funct. Mater.* **26**(34), 6238–6245 (2016), [doi: 10.1002/adfm.201601690](https://doi.org/10.1002/adfm.201601690).
- [69] PARK, K., LEE, J. W., KIM, J. D., HAN, N. S., JANG, D. M., JEONG, S., PARK, J. AND SONG, J. K., “Light-matter interactions in cesium lead halide perovskite nanowire lasers”, *J. Phys. Chem. Lett.* **7**(18), 3703–3710 (2016), [doi: 10.1021/acs.jpcllett.6b01821](https://doi.org/10.1021/acs.jpcllett.6b01821).
- [70] WANG, Y., LI, X., NALLA, V., ZENG, H. AND SUN, H., “Solution-processed low threshold vertical cavity surface emitting lasers from all-inorganic perovskite nanocrystals”, *Adv. Funct. Mater.* **27**(13), 1605088 (2017), [doi: 10.1002/adfm.201605088](https://doi.org/10.1002/adfm.201605088).
- [71] LI, Z., MOON, J., GHARAJEH, A., HAROLDSON, R., HAWKINS, R., HU, W., ZAKHIDOV, A. AND GU, Q., “Room-temperature continuous-wave operation of organometal halide perovskite lasers”, (2018), <https://arxiv.org/abs/1805.01092v2>.

- [72] ROSE, G., *De novis quibusdam fossilibus quae in montibus Uraliis inveniuntur*, Berlin (1839).
- [73] GOLDSCHMIDT, V. M., “Krystallbau und chemische zusammensetzung”, *Ber. Dtsch. Chem.* **60**(5), 1263–1296 (1927), doi: [10.1002/cber.19270600550](https://doi.org/10.1002/cber.19270600550).
- [74] LI, C., LU, X., DING, W., FENG, L., GAO, Y. AND GUO, Z., “Formability of ABX<sub>3</sub> (X= F, Cl, Br, I) halide perovskites”, *Acta Crystallogr. Sect. B* **64**(6), 702–707 (2008), doi: [10.1107/s0108768108032734](https://doi.org/10.1107/s0108768108032734).
- [75] KIESLICH, G., SUN, S. AND CHEETHAM, A. K., “Solid-state principles applied to organic-inorganic perovskites: new tricks for an old dog”, *Chem. Sci.* **5**(12), 4712–4715 (2014), doi: [10.1039/c4sc02211d](https://doi.org/10.1039/c4sc02211d).
- [76] KIESLICH, G., SUN, S. AND CHEETHAM, A. K., “An extended tolerance factor approach for organic-inorganic perovskites”, *Chemical Science* **6**(6), 3430–3433 (2015), doi: [10.1039/c5sc00961h](https://doi.org/10.1039/c5sc00961h).
- [77] ALLAN, N. L., DAYER, M. J., KULP, D. T. AND MACKRODT, W. C., “Atomistic lattice simulations of the ternary fluorides AMF<sub>3</sub> (A = Li, Na, K, Rb, Cs; M = Mg, Ca, Sr, Ba)”, *J. Mater. Chem.* **1**(6), 1035 (1991), doi: [10.1039/jm9910101035](https://doi.org/10.1039/jm9910101035).
- [78] YOUNG, J. AND RONDINELLI, J. M., “Octahedral rotation preferences in perovskite iodides and bromides”, *J. Phys. Chem. Lett.* **7**(5), 918–922 (2016), doi: [10.1021/acs.jpcllett.6b00094](https://doi.org/10.1021/acs.jpcllett.6b00094).
- [79] POGLITSCH, A. AND WEBER, D., “Dynamic disorder in methylammoniumtrihalogenoplumbates (II) observed by millimeter-wave spectroscopy”, *J. Chem. Phys.* **87**(11), 6373 (1987), doi: [10.1063/1.453467](https://doi.org/10.1063/1.453467).
- [80] HIROTSU, S., HARADA, J., IIZUMI, M. AND GESI, K., “Structural phase transitions in CsPbBr<sub>3</sub>”, *J. Phys. Soc. Jpn.* **37**(5), 1393–1398 (1974), doi: [10.1143/jpsj.37.1393](https://doi.org/10.1143/jpsj.37.1393).
- [81] FUJII, Y., HOSHINO, S., YAMADA, Y. AND SHIRANE, G., “Neutron-scattering study on phase transitions of CsPbCl<sub>3</sub>”, *Phys. Rev. B* **9**(10), 4549–4559 (1974), doi: [10.1103/physrevb.9.4549](https://doi.org/10.1103/physrevb.9.4549).
- [82] TROTS, D. AND MYAGKOTA, S., “High-temperature structural evolution of caesium and rubidium triiodoplumbates”, *J. Phys. Chem. Solids* **69**(10), 2520–2526 (2008), doi: [10.1016/j.jpcs.2008.05.007](https://doi.org/10.1016/j.jpcs.2008.05.007).
- [83] UMARI, P., MOSCONI, E. AND DE ANGELIS, F., “Relativistic GW calculations on CH<sub>3</sub>NH<sub>3</sub>PbI<sub>3</sub> and CH<sub>3</sub>NH<sub>3</sub>SnI<sub>3</sub> perovskites for solar cell applications.”, *Sci. Rep.* **4**, 4467 (2014), doi: [10.1038/srep04467](https://doi.org/10.1038/srep04467).
- [84] MURTAZA, G. AND AHMAD, I., “First principle study of the structural and optoelectronic properties of cubic perovskites CsPbM<sub>3</sub> (M=Cl, Br, I)”, *Physica B* **406**, 3222–3229 (2011), doi: [10.1016/j.physb.2011.05.028](https://doi.org/10.1016/j.physb.2011.05.028).

- [85] MOSCONI, E., UMARI, P. AND ANGELIS, F. D., “Electronic and optical properties of MAPbX<sub>3</sub> perovskites (X = I, Br, Cl): a unified DFT and GW theoretical analysis”, *Phys. Chem. Chem. Phys.* **18**, 27158–27164 (2016), doi: [10.1039/c6cp03969c](https://doi.org/10.1039/c6cp03969c).
- [86] ZHU, X., SU, H., MARCUS, R. A. AND MICHEL-BEYERLE, M. E., “Computed and experimental absorption spectra of the perovskite CH<sub>3</sub>NH<sub>3</sub>PbI<sub>3</sub>”, *J. Phys. Chem. Lett.* **5**, 3061–3065 (2014), doi: [10.1021/jz501174e](https://doi.org/10.1021/jz501174e).
- [87] UMEBAYASHI, T., ASAI, K., KONDO, T. AND NAKAO, A., “Electronic structures of lead iodide based low-dimensional crystals”, *Phys. Rev. B* **67**, 155405 (2003), doi: [10.1103/physrevb.67.155405](https://doi.org/10.1103/physrevb.67.155405).
- [88] BRIVIO, F., WALKER, A. B. AND WALSH, A., “Structural and electronic properties of hybrid perovskites for high-efficiency thin-film photovoltaics from first-principles”, *APL Mater.* **1**, 042111 (2013), doi: [10.1063/1.4824147](https://doi.org/10.1063/1.4824147).
- [89] BRANDT, R. E., STEVANOVIĆ, V., GINLEY, D. S. AND BUONASSISI, T., “Identifying defect-tolerant semiconductors with high minority-carrier lifetimes: beyond hybrid lead halide perovskites”, *MRS Commun.* **5**(2), 265–275 (2015), doi: [10.1557/mrc.2015.26](https://doi.org/10.1557/mrc.2015.26).
- [90] RAVI, V. K., MARKAD, G. B. AND NAG, A., “Band edge energies and excitonic transition probabilities of colloidal CsPbX<sub>3</sub> (X = Cl, Br, I) perovskite nanocrystals”, *ACS Energy Lett.* **1**(4), 665–671 (2016), doi: [10.1021/acsenerylett.6b00337](https://doi.org/10.1021/acsenerylett.6b00337).
- [91] BRIVIO, F., BUTLER, K. T., WALSH, A. AND VAN SCHILFGAARDE, M., “Relativistic quasiparticle self-consistent electronic structure of hybrid halide perovskite photovoltaic absorbers”, **89**, 155204 (2014), doi: [10.1103/PhysRevB.89.155204](https://doi.org/10.1103/PhysRevB.89.155204).
- [92] WANG, Y. AND SUN, H., “All-inorganic metal halide perovskite nanostructures: from photophysics to light-emitting applications”, *Small Methods* **2**(1), 1700252 (2017), doi: [10.1002/smt.201700252](https://doi.org/10.1002/smt.201700252).
- [93] TAO, S. X., CAO, X. AND BOBBERT, P. A., “Accurate and efficient band gap predictions of metal halide perovskites using the DFT-1/2 method: GW accuracy with DFT expense”, *Sci. Rep.* **7**(1) (2017), doi: [10.1038/s41598-017-14435-4](https://doi.org/10.1038/s41598-017-14435-4).
- [94] GRUNDMANN, M., *Physics of semiconductors*, Springer (2006).
- [95] LEGUY, A. M. A., AZARHOOSH, P., ALONSO, M. I., CAMPOY-QUILES, M., WEBER, O. J., YAO, J., BRYANT, D., WELLER, M. T., NELSON, J., WALSH, A., VAN SCHILFGAARDE, M. AND BARNES, P. R. F., “Experimental and theoretical optical properties of methylammonium lead halide perovskites”, *Nanoscale* **8**(12), 6317–6327 (2016), doi: [10.1039/c5nr05435d](https://doi.org/10.1039/c5nr05435d).
- [96] STOUMPOS, C. C., MALLIAKAS, C. D., PETERS, J. A., LIU, Z., SEBASTIAN, M., IM, J., CHASAPIS, T. C., WIBOWO, A. C., CHUNG, D. Y., FREEMAN, A. J., WESSELS, B. W. AND KANATZIDIS, M. G., “Crystal growth of the perovskite semiconductor CsPbBr<sub>3</sub>: a new material for high-energy radiation detection”, *Cryst. Growth Des.* **13**(7), 2722–2727 (2013), doi: [10.1021/cg400645t](https://doi.org/10.1021/cg400645t).

- [97] SEBASTIAN, M., PETERS, J. A., STOUMPOS, C. C., IM, J., KOSTINA, S. S., LIU, Z., KANATZIDIS, M. G., FREEMAN, A. J. AND WESSELS, B. W., “Excitonic emissions and above-band-gap luminescence in the single-crystal perovskite semiconductors CsPbBr<sub>3</sub> and CsPbCl<sub>3</sub>”, *Phys. Rev. B* **92**, 235210 (2015), doi: [10.1103/physrevb.92.235210](https://doi.org/10.1103/physrevb.92.235210).
- [98] HAO, F., STOUMPOS, C. C., CHANG, R. P. H. AND KANATZIDIS, M. G., “Anomalous band gap behavior in mixed Sn and Pb perovskites enables broadening of absorption spectrum in solar cells”, *J. Am. Chem. Soc.* **136**(22), 8094–8099 (2014), doi: [10.1021/ja5033259](https://doi.org/10.1021/ja5033259).
- [99] STOUMPOS, C. C., MALLIAKAS, C. D. AND KANATZIDIS, M. G., “Semiconducting tin and lead iodide perovskites with organic cations: phase transitions, high mobilities, and near-infrared photoluminescent properties”, *Inorg. Chem.* **52**, 9019–9038 (2013), doi: [10.1021/ic401215x](https://doi.org/10.1021/ic401215x).
- [100] AMAT, A., MOSCONI, E., RONCA, E., QUARTI, C., UMARI, P., NAZEERUDDIN, M. K., GRÄTZEL, M. AND DE ANGELIS, F., “Cation-induced band-gap tuning in organohalide perovskites: interplay of spin-orbit coupling and octahedra tilting”, *Nano Lett.* **14**(6), 3608–3616 (2014), doi: [10.1021/nl5012992](https://doi.org/10.1021/nl5012992).
- [101] MELONI, S., PALERMO, G., ASHARI-ASTANI, N., GRÄTZEL, M. AND ROTH LISBERGER, U., “Valence and conduction band tuning in halide perovskites for solar cell applications”, *J. Mater. Chem. A* **4**(41), 15997–16002 (2016), doi: [10.1039/c6ta04949d](https://doi.org/10.1039/c6ta04949d).
- [102] WELLER, M. T., WEBER, O. J., FROST, J. M. AND WALSH, A., “Cubic perovskite structure of black formamidinium lead iodide,  $\alpha$ -HC(NH<sub>2</sub>)<sub>2</sub>PbI<sub>3</sub>, at 298 K”, *J. Phys. Chem. Lett.* **6**(16), 3209–3212 (2015), doi: [10.1021/acs.jpcllett.5b01432](https://doi.org/10.1021/acs.jpcllett.5b01432).
- [103] DAR, M. I., JACOPIN, G., MELONI, S., MATTONI, A., ARORA, N., BOZIKI, A., ZAKEERUDDIN, S. M., ROTH LISBERGER, U. AND TZEL, M. G., “Origin of unusual bandgap shift and dual emission in organic-inorganic lead halide perovskites”, *Sci. Adv.* **2**(10), e1601156–e1601156 (2016), doi: [10.1126/sciadv.1601156](https://doi.org/10.1126/sciadv.1601156).
- [104] SINGH, S., LI, C., PANZER, F., NARASIMHAN, K. L., GRAESER, A., GUJAR, T. P., KÖHLER, A., THELAKKAT, M., HUETTNER, S. AND KABRA, D., “Effect of thermal and structural disorder on the electronic structure of hybrid perovskite semiconductor CH<sub>3</sub>NH<sub>3</sub>PbI<sub>3</sub>”, *J. Phys. Chem. Lett.* **7**(15), 3014–3021 (2016), doi: [10.1021/acs.jpcllett.6b01207](https://doi.org/10.1021/acs.jpcllett.6b01207).
- [105] KONG, W., YE, Z., QI, Z., ZHANG, B., WANG, M., RAHIMI-IMAN, A. AND WU, H., “Characterization of an abnormal photoluminescence behavior upon crystal-phase transition of perovskite CH<sub>3</sub>NH<sub>3</sub>PbI<sub>3</sub>”, *Phys. Chem. Chem. Phys.* **17**, 16405–16411 (2015), doi: [10.1039/c5cp02605a](https://doi.org/10.1039/c5cp02605a).
- [106] MILOT, R. L., EPERON, G. E., SNAITH, H. J., JOHNSTON, M. B. AND HERZ, L. M., “Temperature-dependent charge-carrier dynamics in CH<sub>3</sub>NH<sub>3</sub>PbI<sub>3</sub> perovskite thin films”, *Adv. Funct. Mater.* **25**(39), 6218–6227 (2015), doi: [10.1002/adfm.201502340](https://doi.org/10.1002/adfm.201502340).

- [107] LI, J., YUAN, X., JING, P., LI, J., WEI, M., HUA, J., ZHAO, J. AND TIAN, L., “Temperature-dependent photoluminescence of inorganic perovskite nanocrystal films”, *RSC Adv.* **6**(82), 78311–78316 (2016), doi: [10.1039/c6ra17008k](https://doi.org/10.1039/c6ra17008k).
- [108] DOBROVOLSKY, A., MERDASA, A., UNGER, E. L., YARTSEV, A. AND SCHEBLYKIN, I. G., “Defect-induced local variation of crystal phase transition temperature in metal-halide perovskites”, *Nat. Commun.* **8** (2017), doi: [10.1038/s41467-017-00058-w](https://doi.org/10.1038/s41467-017-00058-w).
- [109] WEI, K., XU, Z., CHEN, R., ZHENG, X., CHENG, X. AND JIANG, T., “Temperature-dependent excitonic photoluminescence excited by two-photon absorption in perovskite CsPbBr<sub>3</sub> quantum dots”, *Opt. Lett.* **41**(16), 3821 (2016), doi: [10.1364/ol.41.003821](https://doi.org/10.1364/ol.41.003821).
- [110] VARSHNI, Y. P., “Temperature dependence of the energy gap in semiconductors”, *Physica* **34**, 149–154 (1967), doi: [10.1016/0031-8914\(67\)90062-6](https://doi.org/10.1016/0031-8914(67)90062-6).
- [111] OLGUIN, D., CARDONA, M. AND CANTARERO, A., “Electron-phonon effects on the direct band gap in semiconductors: LCAO calculations”, *Solid State Commun.* **122**(11), 575–589 (2002), doi: [10.1016/s0038-1098\(02\)00225-9](https://doi.org/10.1016/s0038-1098(02)00225-9).
- [112] LAUTENSCHLAGER, P., ALLEN, P. B. AND CARDONA, M., “Temperature dependence of band gaps in Si and Ge”, *Phys. Rev. B* **31**(4), 2163–2171 (1985), doi: [10.1103/physrevb.31.2163](https://doi.org/10.1103/physrevb.31.2163).
- [113] CODY, G. D., TIEDJE, T., ABELES, B., BROOKS, B. AND GOLDSTEIN, Y., “Disorder and the optical-absorption edge of hydrogenated amorphous silicon”, *Phys. Rev. Lett.* **47**(20), 1480–1483 (1981), doi: [10.1103/physrevlett.47.1480](https://doi.org/10.1103/physrevlett.47.1480).
- [114] SOMA, T., SATOH, J. AND MATSUO, H., “Thermal expansion coefficient of GaAs and InP”, *Solid State Commun.* **42**(12), 889–892 (1982), doi: [10.1016/0038-1098\(82\)90233-2](https://doi.org/10.1016/0038-1098(82)90233-2).
- [115] YU, C., CHEN, Z., WANG, J. J., PFENNINGER, W., VOCKIC, N., KENNEY, J. T. AND SHUM, K., “Temperature dependence of the band gap of perovskite semiconductor compound CsSnI<sub>3</sub>”, *J. Appl. Phys.* **110**(6), 063526 (2011), doi: [10.1063/1.3638699](https://doi.org/10.1063/1.3638699).
- [116] FANG, H.-H., RAISSA, R., ABDU-AGUYE, M., ADJOKATSE, S., BLAKE, G. R., EVEN, J. AND LOI, M. A., “Photophysics of organic-inorganic hybrid lead iodide perovskite single crystals”, *Adv. Funct. Mater.* **25**(16), 2378–2385 (2015), doi: [10.1002/adfm.201404421](https://doi.org/10.1002/adfm.201404421).
- [117] WRIGHT, A. D., VERDI, C., MILOT, R. L., EPERON, G. E., PÉREZ-OSORIO, M. A., SNAITH, H. J., GIUSTINO, F., JOHNSTON, M. B. AND HERZ, L. M., “Electron-phonon coupling in hybrid lead halide perovskites”, *Nat. Commun.* **7**, 11755 (2016), doi: [10.1038/ncomms11755](https://doi.org/10.1038/ncomms11755).
- [118] AKKERMAN, Q. A., MOTTI, S. G., KANDADA, A. R. S., MOSCONI, E., D’INNOCENZO, V., BERTONI, G., MARRAS, S., KAMINO, B. A., MIRANDA, L., ANGELIS, F. D., PETROZZA, A., PRATO, M. AND MANNA, L., “Solution synthesis approach to colloidal cesium lead halide perovskite nanoplatelets with monolayer-level thickness control”, *J. Am. Chem. Soc.* **138**(3), 1010–1016 (2016), doi: [10.1021/jacs.5b12124](https://doi.org/10.1021/jacs.5b12124).



- [119] BEKENSTEIN, Y., KOSCHER, B. A., EATON, S. W., YANG, P. AND ALIVISATOS, A. P., “Highly luminescent colloidal nanoplates of perovskite cesium lead halide and their oriented assemblies”, *J. Am. Chem. Soc.* **137**(51), 16008–16011 (2015), [doi: 10.1021/jacs.5b11199](https://doi.org/10.1021/jacs.5b11199).
- [120] BUTKUS, J., VASHISHTHA, P., CHEN, K., GALLAHER, J. K., PRASAD, S. K. K., METIN, D. Z., LAUFERSKY, G., GASTON, N., HALPERT, J. E. AND HODGKISS, J. M., “The evolution of quantum confinement in CsPbBr<sub>3</sub> perovskite nanocrystals”, *Chem. Mater.* **29**(8), 3644–3652 (2017), [doi: 10.1021/acs.chemmater.7b00478](https://doi.org/10.1021/acs.chemmater.7b00478).
- [121] HE, H., TANG, B. AND MA, Y., “Controlled synthesis of quantum confined CsPbBr<sub>3</sub> perovskite nanocrystals under ambient conditions”, *Nanotechnology* **29**(5), 055601 (2018), [doi: 10.1088/1361-6528/aa9c08](https://doi.org/10.1088/1361-6528/aa9c08).
- [122] IMRAN, M., STASIO, F. D., DANG, Z., CANALE, C., KHAN, A. H., SHAMSI, J., BRESCIA, R., PRATO, M. AND MANNA, L., “Colloidal synthesis of strongly fluorescent CsPbBr<sub>3</sub> nanowires with width tunable down to the quantum confinement regime”, *Chem. Mater.* **28**(18), 6450–6454 (2016), [doi: 10.1021/acs.chemmater.6b03081](https://doi.org/10.1021/acs.chemmater.6b03081).
- [123] WANG, Y., LI, X., SREEJITH, S., CAO, F., WANG, Z., STUPARU, M. C., ZENG, H. AND SUN, H., “Photon driven transformation of cesium lead halide perovskites from few-monolayer nanoplatelets to bulk phase”, *Adv. Mater.* **28**(48), 10637–10643 (2016), [doi: 10.1002/adma.201604110](https://doi.org/10.1002/adma.201604110).
- [124] YUAN, X., HOU, X., LI, J., QU, C., ZHANG, W., ZHAO, J. AND LI, H., “Thermal degradation of luminescence in inorganic perovskite CsPbBr<sub>3</sub> nanocrystals”, *Phys. Chem. Chem. Phys.* **19**(13), 8934–8940 (2017), [doi: 10.1039/c6cp08824d](https://doi.org/10.1039/c6cp08824d).
- [125] XING, G., MATHEWS, N., SUN, S., LIM, S. S., LAM, Y. M., GRATZEL, M., MHAISALKAR, S. AND SUM, T. C., “Long-range balanced electron- and hole-transport lengths in organic-inorganic CH<sub>3</sub>NH<sub>3</sub>PbI<sub>3</sub>”, *Science* **342**(6156), 344–347 (2013), [doi: 10.1126/science.1243167](https://doi.org/10.1126/science.1243167).
- [126] STEWART, R. J., GRIECO, C., LARSEN, A. V., DOUCETTE, G. S. AND ASBURY, J. B., “Molecular origins of defects in organohalide perovskites and their influence on charge carrier dynamics”, *J. Phys. Chem. C* **120**(23), 12392–12402 (2016), [doi: 10.1021/acs.jpcc.6b03472](https://doi.org/10.1021/acs.jpcc.6b03472).
- [127] GUO, Z., MANSER, J. S., WAN, Y., KAMAT, P. V. AND HUANG, L., “Spatial and temporal imaging of long-range charge transport in perovskite thin films by ultrafast microscopy”, *Nat. Commun.* **6**(1) (2015), [doi: 10.1038/ncomms8471](https://doi.org/10.1038/ncomms8471).
- [128] LA-O VORAKIAT, C. L., SALIM, T., KADRO, J., KHUC, M.-T., HASELSBERGER, R., CHENG, L., XIA, H., GURZADYAN, G. G., SU, H., LAM, Y. M., MARCUS, R. A., MICHEL-BEYERLE, M.-E. AND CHIA, E. E. M., “Elucidating the role of disorder and free-carrier recombination kinetics in CH<sub>3</sub>NH<sub>3</sub>PbI<sub>3</sub> perovskite films”, *Nat. Commun.* **6**(1) (2015), [doi: 10.1038/ncomms8903](https://doi.org/10.1038/ncomms8903).



- [129] WEHRENFENNIG, C., EPERON, G. E., JOHNSTON, M. B., SNAITH, H. J. AND HERZ, L. M., “High charge carrier mobilities and lifetimes in organolead trihalide perovskites”, *Adv. Mater.* **26**(10), 1584–1589 (2013), doi: [10.1002/adma.201305172](https://doi.org/10.1002/adma.201305172).
- [130] PONSECA, C. S., SAVENIJE, T. J., ABDELLAH, M., ZHENG, K., YARTSEV, A., PASCHER, T., HARLANG, T., CHABERA, P., PULLERITS, T., STEPANOV, A., WOLF, J.-P. AND SUNDSTRÖM, V., “Organometal halide perovskite solar cell materials rationalized: Ultrafast charge generation, high and microsecond-long balanced mobilities, and slow recombination”, *J. Am. Chem. Soc.* **136**(14), 5189–5192 (2014), doi: [10.1021/ja412583t](https://doi.org/10.1021/ja412583t).
- [131] KARAKUS, M., JENSEN, S. A., D’ANGELO, F., TURCHINOVICH, D., BONN, M. AND CÁNOVAS, E., “Phonon-electron scattering limits free charge mobility in methylammonium lead iodide perovskites”, *J. Phys. Chem. Lett.* **6**(24), 4991–4996 (2015), doi: [10.1021/acs.jpcllett.5b02485](https://doi.org/10.1021/acs.jpcllett.5b02485).
- [132] OGA, H., SAEKI, A., OGOMI, Y., HAYASE, S. AND SEKI, S., “Improved understanding of the electronic and energetic landscapes of perovskite solar cells: high local charge carrier mobility, reduced recombination, and extremely shallow traps”, *J. Am. Chem. Soc.* **136**(39), 13818–13825 (2014), doi: [10.1021/ja506936f](https://doi.org/10.1021/ja506936f).
- [133] SAIDAMINOV, M. I., ABDELHADY, A. L., MURALI, B., ALAROUSU, E., BURLAKOV, V. M., PENG, W., DURSUN, I., WANG, L., HE, Y., MACULAN, G., GORIELY, A., WU, T., MOHAMMED, O. F. AND BAKR, O. M., “High-quality bulk hybrid perovskite single crystals within minutes by inverse temperature crystallization”, *Nat. Commun.* **6**(1) (2015), doi: [10.1038/ncomms8586](https://doi.org/10.1038/ncomms8586).
- [134] ZHANG, H., LIU, X., DONG, J., YU, H., ZHOU, C., ZHANG, B., XU, Y. AND JIE, W., “Centimeter-sized inorganic lead halide perovskite CsPbBr<sub>3</sub> crystals grown by an improved solution method”, *Cryst. Growth Des.* **17**(12), 6426–6431 (2017), doi: [10.1021/acs.cgd.7b01086](https://doi.org/10.1021/acs.cgd.7b01086).
- [135] SAIDAMINOV, M. I., HAQUE, M. A., ALMUTLAQ, J., SARMAH, S., MIAO, X.-H., BEGUM, R., ZHUMEKENOV, A. A., DURSUN, I., CHO, N., MURALI, B., MOHAMMED, O. F., WU, T. AND BAKR, O. M., “Inorganic lead halide perovskite single crystals: phase-selective low-temperature growth, carrier transport properties, and self-powered photodetection”, *Adv. Opt. Mater.* **5**(2), 1600704 (2016), doi: [10.1002/adom.201600704](https://doi.org/10.1002/adom.201600704).
- [136] SONG, J., ZHENG, E., BIAN, J., WANG, X.-F., TIAN, W., SANEHIRA, Y. AND MIYASAKA, T., “Low-temperature SnO<sub>2</sub>-based electron selective contact for efficient and stable perovskite solar cells”, *J. Mater. Chem. A* **3**(20), 10837–10844 (2015), doi: [10.1039/c5ta01207d](https://doi.org/10.1039/c5ta01207d).
- [137] “Ioffe semiconductors database”, <http://www.ioffe.ru/SVA/NSM/Semicond/>.
- [138] URBACH, F., “The long-wavelength edge of photographic sensitivity and of the electronic absorption of solids”, *Phys. Rev.* **92**(5), 1324–1324 (1953), doi: [10.1103/physrev.92.1324](https://doi.org/10.1103/physrev.92.1324).

- [139] YAMADA, Y., NAKAMURA, T., ENDO, M., WAKAMIYA, A. AND KANEMITSU, Y., “Photoelectronic responses in solution-processed perovskite  $\text{CH}_3\text{NH}_3\text{PbI}_3$  solar cells studied by photoluminescence and photoabsorption spectroscopy”, *IEEE J. Photovolt.* **5**(1), 401–405 (2015), doi: [10.1109/jphotov.2014.2364115](https://doi.org/10.1109/jphotov.2014.2364115).
- [140] SESTU, N., CADELANO, M., SARRITZU, V., CHEN, F., MARONGIU, D., PIRAS, R., MAINAS, M., QUOCHI, F., SABA, M., MURA, A. AND BONGIOVANNI, G., “Absorption f-sum rule for the exciton binding energy in methylammonium lead halide perovskites”, *J. Phys. Chem. Lett.* **6**(22), 4566–4572 (2015), doi: [10.1021/acs.jpcllett.5b02099](https://doi.org/10.1021/acs.jpcllett.5b02099).
- [141] SABA, M., CADELANO, M., MARONGIU, D., CHEN, F., SARRITZU, V., SESTU, N., FIGUS, C., ARESTI, M., PIRAS, R., LEHMANN, A. G., CANNAS, C., MUSINU, A., QUOCHI, F., MURA, A. AND BONGIOVANNI, G., “Correlated electron-hole plasma in organometal perovskites”, *Nat. Commun.* **5**, 5049 (2014), doi: [10.1038/ncomms6049](https://doi.org/10.1038/ncomms6049).
- [142] EVEN, J., PEDESSEAU, L. AND KATAN, C., “Analysis of multivalley and multibandgap absorption and enhancement of free carriers related to exciton screening in hybrid perovskites”, *J. Phys. Chem. C* **118**(22), 11566–11572 (2014), doi: [10.1021/jp503337a](https://doi.org/10.1021/jp503337a).
- [143] ISHIHARA, T., “Optical properties of PbI-based perovskite structures”, *J. Lumin.* **60-61**, 269–274 (1994), doi: [10.1016/0022-2313\(94\)90145-7](https://doi.org/10.1016/0022-2313(94)90145-7).
- [144] SUN, S., SALIM, T., MATHEWS, N., DUCHAMP, M., BOOTHROYD, C., XING, G., SUM, T. C. AND LAM, Y. M., “The origin of high efficiency in low-temperature solution-processable bilayer organometal halide hybrid solar cells”, *Energy Environ. Sci.* **7**(1), 399–407 (2014), doi: [10.1039/c3ee43161d](https://doi.org/10.1039/c3ee43161d).
- [145] LIN, Q., ARMIN, A., NAGIRI, R. C. R., BURN, P. L. AND MEREDITH, P., “Electro-optics of perovskite solar cells”, *Nat. Photonics* **9**(2), 106–112 (2014), doi: [10.1038/nphoton.2014.284](https://doi.org/10.1038/nphoton.2014.284).
- [146] YANG, Y., OSTROWSKI, D. P., FRANCE, R. M., ZHU, K., VAN DE LAGEMAAT, J., LUTHER, J. M. AND BEARD, M. C., “Observation of a hot-phonon bottleneck in lead-iodide perovskites”, *Nat. Photonics* **10**(1), 53–59 (2015), doi: [10.1038/nphoton.2015.213](https://doi.org/10.1038/nphoton.2015.213).
- [147] FRÖHLICH, D., HEIDRICH, K., KÜNZEL, H., TRENDEL, G. AND TREUSCH, J., “Cesium-trihalogen-plumbates a new class of ionic semiconductors”, *J. Lumin.* **18-19**, 385–388 (1979), doi: [10.1016/0022-2313\(79\)90146-7](https://doi.org/10.1016/0022-2313(79)90146-7).
- [148] CADELANO, M., SABA, M., SESTU, N., SARRITZU, V., MARONGIU, D., CHEN, F., PIRAS, R., QUOCHI, F., MURA, A. AND BONGIOVANNI, G., “Photoexcitations and emission processes in organometal trihalide perovskites”, in “Perovskite Materials - Synthesis, Characterisation, Properties, and Applications”, InTech (2016), doi: [10.5772/61282](https://doi.org/10.5772/61282).
- [149] HIRASAWA, M., ISHIHARA, T., GOTO, T., UCHIDA, K. AND MIURA, N., “Magnetoabsorption of the lowest exciton in perovskite-type compound  $\text{CH}_3\text{NH}_3\text{PbI}_3$ ”, *Physica B* **201**, 427–430 (1994), doi: [10.1016/0921-4526\(94\)91130-4](https://doi.org/10.1016/0921-4526(94)91130-4).

- [150] ONODA-YAMAMURO, N., MATSUO, T. AND SUGA, H., “Dielectric study of  $\text{CH}_3\text{NH}_3\text{PbX}_3$  ( $X = \text{Cl}, \text{Br}, \text{I}$ )”, *J. Phys. Chem. Solids* **53**(7), 935–939 (1992), doi: [10.1016/0022-3697\(92\)90121-s](https://doi.org/10.1016/0022-3697(92)90121-s).
- [151] WANG, Y., LI, X., SONG, J., XIAO, L., ZENG, H. AND SUN, H., “All-inorganic colloidal perovskite quantum dots: a new class of lasing materials with favorable characteristics”, *Adv. Mater.* **27**(44), 7101–7108 (2015), doi: [10.1002/adma.201503573](https://doi.org/10.1002/adma.201503573).
- [152] WEI, K., ZHENG, X., CHENG, X., SHEN, C. AND JIANG, T., “Observation of ultrafast exciton-exciton annihilation in  $\text{CsPbBr}_3$  quantum dots”, *Adv. Opt. Mater.* **4**(12), 1993–1997 (2016), doi: [10.1002/adom.201600352](https://doi.org/10.1002/adom.201600352).
- [153] EPERON, G. E., JEDLICKA, E. AND GINGER, D. S., “Biexciton auger recombination differs in hybrid and inorganic halide perovskite quantum dots”, *J. Phys. Chem. Lett.* **9**(1), 104–109 (2017), doi: [10.1021/acs.jpcllett.7b02805](https://doi.org/10.1021/acs.jpcllett.7b02805).
- [154] DRAGUTA, S., THAKUR, S., MOROZOV, Y. V., WANG, Y., MANSER, J. S., KAMAT, P. V. AND KUNO, M., “Spatially non-uniform trap state densities in solution-processed hybrid perovskite thin films”, *J. Phys. Chem. Lett.* **7**(4), 715–721 (2016), doi: [10.1021/acs.jpcllett.5b02888](https://doi.org/10.1021/acs.jpcllett.5b02888).
- [155] KOSCHER, B. A., SWABECK, J. K., BRONSTEIN, N. D. AND ALIVISATOS, A. P., “Essentially trap-free  $\text{CsPbBr}_3$  colloidal nanocrystals by postsynthetic thiocyanate surface treatment”, *J. Am. Chem. Soc.* **139**(19), 6566–6569 (2017), doi: [10.1021/jacs.7b02817](https://doi.org/10.1021/jacs.7b02817).
- [156] WEHRENFENNIG, C., LIU, M., SNAITH, H. J., JOHNSTON, M. B. AND HERZ, L. M., “Charge carrier recombination channels in the low-temperature phase of organic-inorganic lead halide perovskite thin films”, *APL Mater.* **2**, 081513 (2014), doi: [10.1063/1.4891595](https://doi.org/10.1063/1.4891595).
- [157] PHUONG, L. Q., YAMADA, Y., NAGAI, M., MARUYAMA, N., WAKAMIYA, A. AND KANEMITSU, Y., “Free carriers versus excitons in  $\text{CH}_3\text{NH}_3\text{PbI}_3$  perovskite thin films at low temperatures: charge transfer from the orthorhombic phase to the tetragonal phase”, *J. Phys. Chem. Lett.* **7**, 2316–2321 (2016), doi: [10.1021/acs.jpcllett.6b00781](https://doi.org/10.1021/acs.jpcllett.6b00781).
- [158] WU, X., TRINH, M. T., NIESNER, D., ZHU, H., NORMAN, Z., OWEN, J. S., YAFFE, O., KUDISCH, B. J. AND ZHU, X.-Y., “Trap states in lead iodide perovskites”, *J. Am. Chem. Soc.* **137**(5), 2089–2096 (2015), doi: [10.1021/ja512833n](https://doi.org/10.1021/ja512833n).
- [159] QUARTI, C., MOSCONI, E., BALL, J. M., D'INNOCENZO, V., TAO, C., PATHAK, S., SNAITH, H. J., PETROZZA, A. AND ANGELIS, F. D., “Structural and optical properties of methylammonium lead iodide across the tetragonal to cubic phase transition: implications for perovskite solar cells”, *Energy Environ. Sci.* **9**(1), 155–163 (2016), doi: [10.1039/c5ee02925b](https://doi.org/10.1039/c5ee02925b).
- [160] ZHANG, H., QIAO, X., SHEN, Y., MOEHL, T., ZAKEERUDDIN, S. M., GRÄTZEL, M. AND WANG, M., “Photovoltaic behaviour of lead methylammonium triiodide per-

- ovskite solar cells down to 80 K”, *J. Mater. Chem. A* **3**(22), 11762–11767 (2015), [doi: 10.1039/c5ta02206a](https://doi.org/10.1039/c5ta02206a).
- [161] STASIO, F. D., CHRISTODOULOU, S., HUO, N. AND KONSTANTATOS, G., “Near-unity photoluminescence quantum yield in CsPbBr<sub>3</sub> nanocrystal solid-state films via postsynthesis treatment with lead bromide”, *Chem. Mater.* **29**(18), 7663–7667 (2017), [doi: 10.1021/acs.chemmater.7b02834](https://doi.org/10.1021/acs.chemmater.7b02834).
- [162] FU, M., TAMARAT, P., HUANG, H., EVEN, J., ROGACH, A. L. AND LOUNIS, B., “Neutral and charged exciton fine structure in single lead halide perovskite nanocrystals revealed by magneto-optical spectroscopy”, *Nano Lett.* **17**(5), 2895–2901 (2017), [doi: 10.1021/acs.nanolett.7b00064](https://doi.org/10.1021/acs.nanolett.7b00064).
- [163] RAMADE, J., ANDRIAMBARIARIJAONA, L. M., STEINMETZ, V., GOUBET, N., LEGRAND, L., BARISIEN, T., BERNARDOT, F., TESTELIN, C., LHUILLIER, E., BRAMATI, A. AND CHAMARRO, M., “Fine structure of excitons and electron-hole exchange energy in polymorphic CsPbBr<sub>3</sub> single nanocrystals”, *Nanoscale* **10**(14), 6393–6401 (2018), [doi: 10.1039/c7nr09334a](https://doi.org/10.1039/c7nr09334a).
- [164] BECKER, M. A., VAXENBURG, R., NEDELCO, G., SERCEL, P. C., SHABAEV, A., MEHL, M. J., MICHPOULOS, J. G., LAMBRAKOS, S. G., BERNSTEIN, N., LYONS, J. L., STÖFERLE, T., MAHRT, R. F., KOVALENKO, M. V., NORRIS, D. J., RAINÒ, G. AND EFROS, A. L., “Bright triplet excitons in caesium lead halide perovskites”, *Nature* **553**(7687), 189–193 (2018), [doi: 10.1038/nature25147](https://doi.org/10.1038/nature25147).
- [165] KIM, J., LEE, S.-H., LEE, J. H. AND HONG, K.-H., “The role of intrinsic defects in methylammonium lead iodide perovskite”, *J. Phys. Chem. Lett.* **5**(8), 1312–1317 (2014), [doi: 10.1021/jz500370k](https://doi.org/10.1021/jz500370k).
- [166] KOVALENKO, M. V., PROTESESCU, L. AND BODNARCHUK, M. I., “Properties and potential optoelectronic applications of lead halide perovskite nanocrystals”, *Science* **358**(6364), 745–750 (2017), [doi: 10.1126/science.aam7093](https://doi.org/10.1126/science.aam7093).
- [167] HARUYAMA, J., SODEYAMA, K., HAN, L. AND TATEYAMA, Y., “Termination dependence of tetragonal CH<sub>3</sub>NH<sub>3</sub>PbI<sub>3</sub> surfaces for perovskite solar cells”, *J. Phys. Chem. Lett.* **5**(16), 2903–2909 (2014), [doi: 10.1021/jz501510v](https://doi.org/10.1021/jz501510v).
- [168] LIU, M., JOHNSTON, M. B. AND SNAITH, H. J., “Efficient planar heterojunction perovskite solar cells by vapour deposition”, *Nature* **501**, 395 (2013), [doi: 10.1038/nature12509](https://doi.org/10.1038/nature12509).
- [169] CHEN, C.-W., KANG, H.-W., HSIAO, S.-Y., YANG, P.-F., CHIANG, K.-M. AND LIN, H.-W., “Efficient and uniform planar-type perovskite solar cells by simple sequential vacuum deposition”, *Adv. Mater.* **26**(38), 6647–6652 (2014), [doi: 10.1002/adma.201402461](https://doi.org/10.1002/adma.201402461).
- [170] LI, Y., COOPER, J. K., BUONSANTI, R., GIANNINI, C., LIU, Y., TOMA, F. M. AND SHARP, I. D., “Fabrication of planar heterojunction perovskite solar cells by

- controlled low-pressure vapor annealing”, *J. Phys. Chem. Lett.* **6**(3), 493–499 (2015), doi: [10.1021/jz502720a](https://doi.org/10.1021/jz502720a).
- [171] CHEN, Q., ZHOU, H., HONG, Z., LUO, S., DUAN, H.-S., WANG, H.-H., LIU, Y., LI, G. AND YANG, Y., “Planar heterojunction perovskite solar cells via vapor-assisted solution process”, *J. Am. Chem. Soc.* **136**(2), 622–625 (2013), doi: [10.1021/ja411509g](https://doi.org/10.1021/ja411509g).
- [172] IM, J.-H., KIM, H.-S. AND PARK, N.-G., “Morphology-photovoltaic property correlation in perovskite solar cells: one-step versus two-step deposition of  $\text{CH}_3\text{NH}_3\text{PbI}_3$ ”, *APL Mater.* **2**(8), 081510 (2014), doi: [10.1063/1.4891275](https://doi.org/10.1063/1.4891275).
- [173] BURSCHKA, J., PELLET, N., MOON, S.-J., HUMPHRY-BAKER, R., GAO, P., NAZEERUDDIN, M. K. AND GRÄTZEL, M., “Sequential deposition as a route to high-performance perovskite-sensitized solar cells”, *Nature* **499**, 316–319 (2013), doi: [10.1038/nature12340](https://doi.org/10.1038/nature12340).
- [174] XIAO, M., HUANG, F., HUANG, W., DKHISSI, Y., ZHU, Y., ETHERIDGE, J., GRAY-WEALE, A., BACH, U., CHENG, Y.-B. AND SPICCIA, L., “A fast deposition-crystallization procedure for highly efficient lead iodide perovskite thin-film solar cells”, *Angew. Chem.* **126**(37), 10056–10061 (2014), doi: [10.1002/ange.201405334](https://doi.org/10.1002/ange.201405334).
- [175] ZHANG, W., SALIBA, M., MOORE, D. T., PATHAK, S. K., HÖRANTNER, M. T., STERGIPOPOULOS, T., STRANKS, S. D., EPERON, G. E., ALEXANDER-WEBBER, J. A., ABATE, A., SADHANALA, A., YAO, S., CHEN, Y., FRIEND, R. H., ESTROFF, L. A., WIESNER, U. AND SNAITH, H. J., “Ultrasoft organic-inorganic perovskite thin-film formation and crystallization for efficient planar heterojunction solar cells”, *Nat. Commun.* **6**(1) (2015), doi: [10.1038/ncomms7142](https://doi.org/10.1038/ncomms7142).
- [176] WANG, F., YU, H., XU, H. AND ZHAO, N., “ $\text{HPbI}_3$ : a new precursor compound for highly efficient solution-processed perovskite solar cells”, *Adv. Funct. Mater.* **25**(7), 1120–1126 (2015), doi: [10.1002/adfm.201404007](https://doi.org/10.1002/adfm.201404007).
- [177] ZHAO, Y. AND ZHU, K., “ $\text{CH}_3\text{NH}_3\text{Cl}$ -assisted one-step solution growth of  $\text{CH}_3\text{NH}_3\text{PbI}_3$ : structure, charge-carrier dynamics, and photovoltaic properties of perovskite solar cells”, *J. Phys. Chem. C* **118**(18), 9412–9418 (2014), doi: [10.1021/jp502696w](https://doi.org/10.1021/jp502696w).
- [178] MILLER, E. M., ZHAO, Y., MERCADO, C. C., SAHA, S. K., LUTHER, J. M., ZHU, K., STEVANOVIĆ, V., PERKINS, C. L. AND VAN DE LAGEMAAT, J., “Substrate-controlled band positions in  $\text{CH}_3\text{NH}_3\text{PbI}_3$  perovskite films”, *Phys. Chem. Chem. Phys.* **16**(40), 22122–22130 (2014), doi: [10.1039/c4cp03533j](https://doi.org/10.1039/c4cp03533j).
- [179] CLIMENT-PASCUAL, E., HAMES, B. C., MORENO-RAMÍREZ, J. S., ÁLVAREZ, A. L., JUAREZ-PEREZ, E. J., MAS-MARZA, E., MORA-SERÓ, I., DE ANDRÉS, A. AND COYA, C., “Influence of the substrate on the bulk properties of hybrid lead halide perovskite films”, *J. Mater. Chem. A* **4**(46), 18153–18163 (2016), doi: [10.1039/c6ta08695k](https://doi.org/10.1039/c6ta08695k).
- [180] WU, Z., BAI, S., XIANG, J., YUAN, Z., YANG, Y., CUI, W., GAO, X., LIU, Z., JIN, Y. AND SUN, B., “Efficient planar heterojunction perovskite solar cells

- employing graphene oxide as hole conductor”, *Nanoscale* **6**(18), 10505–10510 (2014), [doi: 10.1039/c4nr03181d](https://doi.org/10.1039/c4nr03181d).
- [181] BI, C., WANG, Q., SHAO, Y., YUAN, Y., XIAO, Z. AND HUANG, J., “Non-wetting surface-driven high-aspect-ratio crystalline grain growth for efficient hybrid perovskite solar cells”, *Nat. Commun.* **6**(1) (2015), [doi: 10.1038/ncomms8747](https://doi.org/10.1038/ncomms8747).
- [182] OLTHOF, S. AND MEERHOLZ, K., “Substrate-dependent electronic structure and film formation of MAPbI<sub>3</sub> perovskites”, *Sci. Rep.* **7**(1) (2017), [doi: 10.1038/srep40267](https://doi.org/10.1038/srep40267).
- [183] YANG, S., ZHENG, Y. C., HOU, Y., CHEN, X., CHEN, Y., WANG, Y., ZHAO, H. AND YANG, H. G., “Formation mechanism of freestanding CH<sub>3</sub>NH<sub>3</sub>PbI<sub>3</sub> functional crystals: in situ transformation vs dissolution-crystallization”, *Chem. Mater.* **26**(23), 6705–6710 (2014), [doi: 10.1021/cm5028817](https://doi.org/10.1021/cm5028817).
- [184] FU, Y., MENG, F., ROWLEY, M. B., THOMPSON, B. J., SHEARER, M. J., MA, D., HAMERS, R. J., WRIGHT, J. C. AND JIN, S., “Solution growth of single crystal methylammonium lead halide perovskite nanostructures for optoelectronic and photovoltaic applications”, *J. Am. Chem. Soc.* **137**(17), 5810–5818 (2015), [doi: 10.1021/jacs.5b02651](https://doi.org/10.1021/jacs.5b02651).
- [185] YANTARA, N., BHAUMIK, S., YAN, F., SABBA, D., DEWI, H. A., MATHEWS, N., BOIX, P. P., DEMIR, H. V. AND MHAISALKAR, S., “Inorganic halide perovskites for efficient light-emitting diodes”, *J. Phys. Chem. Lett.* **6**(21), 4360–4364 (2015), [doi: 10.1021/acs.jpcllett.5b02011](https://doi.org/10.1021/acs.jpcllett.5b02011).
- [186] YONG, Z.-J., ZHOU, Y., MA, J.-P., CHEN, Y.-M., YANG, J.-Y., SONG, Y.-L., WANG, J. AND SUN, H.-T., “Controlling crystallization of all-inorganic perovskite films for ultralow-threshold amplification spontaneous emission”, *ACS Appl. Mater. Interfaces* **9**(38), 32920–32929 (2017), [doi: 10.1021/acsami.7b10863](https://doi.org/10.1021/acsami.7b10863).
- [187] KULBAK, M., CAHEN, D. AND HODES, G., “How important is the organic part of lead halide perovskite photovoltaic cells? Efficient CsPbBr<sub>3</sub> cells”, *J. Phys. Chem. Lett.* **6**(13), 2452–2456 (2015), [doi: 10.1021/acs.jpcllett.5b00968](https://doi.org/10.1021/acs.jpcllett.5b00968).
- [188] LIU, D., HU, Z., HU, W., WANGYANG, P., YU, K., WEN, M., ZU, Z., LIU, J., WANG, M., CHEN, W., ZHOU, M., TANG, X. AND ZANG, Z., “Two-step method for preparing all-inorganic CsPbBr<sub>3</sub> perovskite film and its photoelectric detection application”, *Mater. Lett.* **186**, 243–246 (2017), [doi: 10.1016/j.matlet.2016.10.015](https://doi.org/10.1016/j.matlet.2016.10.015).
- [189] PAN, A., HE, B., FAN, X., LIU, Z., URBAN, J. J., ALIVISATOS, A. P., HE, L. AND LIU, Y., “Insight into the ligand-mediated synthesis of colloidal CsPbBr<sub>3</sub> perovskite nanocrystals: the role of organic acid, base, and cesium precursors”, *ACS Nano* **10**(8), 7943–7954 (2016), [doi: 10.1021/acs.nano.6b03863](https://doi.org/10.1021/acs.nano.6b03863).
- [190] SHAMSI, J., DANG, Z., BIANCHINI, P., CANALE, C., STASIO, F. D., BRESCIA, R., PRATO, M. AND MANNA, L., “Colloidal synthesis of quantum confined single crystal CsPbBr<sub>3</sub> nanosheets with lateral size control up to the micrometer range”, *J. Am. Chem. Soc.* **138**(23), 7240–7243 (2016), [doi: 10.1021/jacs.6b03166](https://doi.org/10.1021/jacs.6b03166).



- [191] ROO, J. D., IBÁÑEZ, M., GEIREGAT, P., NEDELCO, G., WALRAVENS, W., MAES, J., MARTINS, J. C., DRIESSCHE, I. V., KOVALENKO, M. V. AND HENS, Z., “Highly dynamic ligand binding and light absorption coefficient of cesium lead bromide perovskite nanocrystals”, *ACS Nano* **10**(2), 2071–2081 (2016), doi: [10.1021/acsnano.5b06295](https://doi.org/10.1021/acsnano.5b06295).
- [192] SUN, S., YUAN, D., XU, Y., WANG, A. AND DENG, Z., “Ligand-mediated synthesis of shape-controlled cesium lead halide perovskite nanocrystals *via* re-precipitation process at room-temperature”, *ACS Nano* **10**(3), 3648–3657 (2016), doi: [10.1021/acsnano.5b08193](https://doi.org/10.1021/acsnano.5b08193).
- [193] KOBAYASHI, M., OMATA, K., SUGIMOTO, S., TAMAGAWA, Y., KUROIWA, T., ASADA, H., TAKEUCHI, H. AND KONDO, S., “Scintillation characteristics of CsPbCl<sub>3</sub> single crystals”, *Nucl. Instrum. Methods Phys. Res., Sect. A* **592**(3), 369–373 (2008), doi: [10.1016/j.nima.2008.04.079](https://doi.org/10.1016/j.nima.2008.04.079).
- [194] RAKITA, Y., KEDEM, N., GUPTA, S., SADHANALA, A., KALCHENKO, V., BÖHM, M. L., KULBAK, M., FRIEND, R. H., CAHEN, D. AND HODES, G., “Low-temperature solution-grown CsPbBr<sub>3</sub> single crystals and their characterization”, *Cryst. Growth Des.* **16**(10), 5717–5725 (2016), doi: [10.1021/acs.cgd.6b00764](https://doi.org/10.1021/acs.cgd.6b00764).
- [195] KADRO, J. M., NONOMURA, K., GACHET, D., GRÄTZEL, M. AND HAGFELDT, A., “Facile route to freestanding CH<sub>3</sub>NH<sub>3</sub>PbI<sub>3</sub> crystals using inverse solubility”, *Sci. Rep.* **5**(1) (2015), doi: [10.1038/srep11654](https://doi.org/10.1038/srep11654).
- [196] MACULAN, G., SHEIKH, A. D., ABDELHADY, A. L., SAIDAMINOV, M. I., HAQUE, M. A., MURALI, B., ALAROUSU, E., MOHAMMED, O. F., WU, T. AND BAKR, O. M., “CH<sub>3</sub>NH<sub>3</sub>PbCl<sub>3</sub> single crystals: Inverse temperature crystallization and visible-blind UV-photodetector”, *J. Phys. Chem. Lett.* **6**(19), 3781–3786 (2015), doi: [10.1021/acs.jpcllett.5b01666](https://doi.org/10.1021/acs.jpcllett.5b01666).
- [197] DIRIN, D. N., CHERNIUKH, I., YAKUNIN, S., SHYNKARENKO, Y. AND KOVALENKO, M. V., “Solution-grown CsPbBr<sub>3</sub> perovskite single crystals for photon detection”, *Chem. Mater.* **28**(23), 8470–8474 (2016), doi: [10.1021/acs.chemmater.6b04298](https://doi.org/10.1021/acs.chemmater.6b04298).
- [198] TIEP, N. H., KU, Z. AND FAN, H. J., “Recent advances in improving the stability of perovskite solar cells”, *Adv. Energy Mater.* **6**, 1501420 (2016), doi: [10.1002/aenm.201501420](https://doi.org/10.1002/aenm.201501420).
- [199] SHAHBAZI, M. AND WANG, H., “Progress in research on the stability of organometal perovskite solar cells”, *Solar Energy* **123**, 74–87 (2016), doi: [10.1016/j.solener.2015.11.008](https://doi.org/10.1016/j.solener.2015.11.008).
- [200] SUPASAI, T., RUJISAMPHAN, N., ULLRICH, K., CHEMSEDDINE, A. AND DITTRICH, T., “Formation of a passivating CH<sub>3</sub>NH<sub>3</sub>PbI<sub>3</sub>/PbI<sub>2</sub> interface during moderate heating of CH<sub>3</sub>NH<sub>3</sub>PbI<sub>3</sub> layers”, *Appl. Phys. Lett.* **103**, 183906 (2013), doi: [10.1063/1.4826116](https://doi.org/10.1063/1.4826116).



- [201] AHARON, S., DYMSHITS, A., ROTEM, A. AND ETGAR, L., “Temperature dependence of hole conductor free formamidinium lead iodide perovskite based solar cells”, *J. Mater. Chem. A* **3**, 9171–9178 (2014), doi: [10.1039/c4ta05149a](https://doi.org/10.1039/c4ta05149a).
- [202] ARISTIDOU, N., SANCHEZ-MOLINA, I., CHOTCHUANGCHUTCHAVAL, T., BROWN, M., MARTINEZ, L., RATH, T. AND HAQUE, S. A., “The role of oxygen in the degradation of methylammonium lead trihalide perovskite photoactive layers”, *Angew. Chem. Int. Ed.* **54**(28), 8208–8212 (2015), doi: [10.1002/ange.201503153](https://doi.org/10.1002/ange.201503153).
- [203] LEE, S.-W., KIM, S., BAE, S., CHO, K., CHUNG, T., MUNDT, L. E., LEE, S., PARK, S., PARK, H., SCHUBERT, M. C., GLUNZ, S. W., KO, Y., JUN, Y., KANG, Y., LEE, H.-S. AND KIM, D., “UV degradation and recovery of perovskite solar cells”, *Sci. Rep.* **6**(38150), 38150 (2016), doi: [10.1038/srep38150](https://doi.org/10.1038/srep38150).
- [204] TANG, X., BRANDL, M., MAY, B., LEVCHUK, I., HOU, Y., RICHTER, M., CHEN, H., CHEN, S., KAHMANN, S., OSVET, A., MAIER, F., STEINRÜCK, H.-P., HOCK, R., MATT, G. J. AND BRABEC, C. J., “Photoinduced degradation of methylammonium lead triiodide perovskite semiconductors”, *J. Mater. Chem. A* **4**, 15896–15903 (2016), doi: [10.1039/c6ta06497c](https://doi.org/10.1039/c6ta06497c).
- [205] RAJAMANICKAM, N., KUMARI, S., VENDRA, V. K., LAVERY, B. W., SPURGEON, J., DRUFFEL, T. AND SUNKARA, M. K., “Stable and durable  $\text{CH}_3\text{NH}_3\text{PbI}_3$  perovskite solar cells at ambient conditions”, *Nanotechnology* **27**, 235404 (2016), doi: [10.1088/0957-4484/27/23/235404](https://doi.org/10.1088/0957-4484/27/23/235404).
- [206] MERDASA, A., BAG, M., TIAN, Y., KÄLLMAN, E., DOBROVOLSKY, A. AND SCHEBLYKIN, I. G., “Super-resolution luminescence microspectroscopy reveals the mechanism of photoinduced degradation in  $\text{CH}_3\text{NH}_3\text{PbI}_3$  perovskite nanocrystals”, *J. Phys. Chem. C* **120**, 10711–10719 (2016), doi: [10.1021/acs.jpcc.6b03512](https://doi.org/10.1021/acs.jpcc.6b03512).
- [207] GIBBS, H. D., “The boiling-points of ammonia, methyl amine, methyl chloride and sulphur dioxide.”, *J. Am. Chem. Soc.* **27**, 851–865 (1905), doi: [10.1021/ja01985a003](https://doi.org/10.1021/ja01985a003).
- [208] SONG, J., HU, W., WANG, X.-F., CHEN, G., TIAN, W. AND MIYASAKA, T., “ $\text{HC}(\text{NH}_2)_2\text{PbI}_3$  as a thermally stable absorber for efficient ZnO-based perovskite solar cells”, *J. Mater. Chem. A* **4**(21), 8435–8443 (2016), doi: [10.1039/c6ta01074a](https://doi.org/10.1039/c6ta01074a).
- [209] LEE, M. M., TEUSCHER, J., MIYASAKA, T., MURAKAMI, T. N. AND SNAITH, H. J., “Efficient hybrid solar cells based on meso-superstructured organometal halide perovskites”, *Science* **338**, 643–647 (2012), doi: [10.1126/science.1228604](https://doi.org/10.1126/science.1228604).
- [210] PARK, N.-G., GRÄTZEL, M. AND MIYASAKA, T., *Organic-inorganic halide perovskite photovoltaics*, Springer International Publishing (2016).
- [211] SMECCA, E., NUMATA, Y., DERETZIS, I., PELLEGRINO, G., BONINELLI, S., MIYASAKA, T., MAGNA, A. L. AND ALBERTI, A., “Stability of solution-processed  $\text{MAPbI}_3$  and  $\text{FAPbI}_3$  layers”, *Phys. Chem. Chem. Phys.* **18**, 13413–13422 (2016), doi: [10.1039/c6cp00721j](https://doi.org/10.1039/c6cp00721j).

- [212] HUANG, S., LI, Z., WANG, B., ZHU, N., ZHANG, C., KONG, L., ZHANG, Q., SHAN, A. AND LI, L., “Morphology evolution and degradation of CsPbBr<sub>3</sub> nanocrystals under blue light-emitting diode illumination”, *ACS Appl. Mater. Interfaces* **9**(8), 7249–7258 (2017), doi: [10.1021/acsami.6b14423](https://doi.org/10.1021/acsami.6b14423).
- [213] LOIUDICE, A., SARIS, S., OVEISI, E., ALEXANDER, D. T. L. AND BUON-SANTI, R., “CsPbBr<sub>3</sub> QD/AlO<sub>x</sub> inorganic nanocomposites with exceptional stability in water, light, and heat”, *Angew. Chem. Int. Ed.* **56**(36), 10696–10701 (2017), doi: [10.1002/anie.201703703](https://doi.org/10.1002/anie.201703703).
- [214] JING, Q., ZHANG, M., HUANG, X., REN, X., WANG, P. AND LU, Z., “Surface passivation of mixed-halide perovskite CsPb(Br<sub>x</sub>I<sub>1-x</sub>)<sub>3</sub> nanocrystals by selective etching for improved stability”, *Nanoscale* **9**(22), 7391–7396 (2017), doi: [10.1039/c7nr01287j](https://doi.org/10.1039/c7nr01287j).
- [215] WOO, J. Y., KIM, Y., BAE, J., KIM, T. G., KIM, J. W., LEE, D. C. AND JEONG, S., “Highly stable cesium lead halide perovskite nanocrystals through in situ lead halide inorganic passivation”, *Chem. Mater.* **29**(17), 7088–7092 (2017), doi: [10.1021/acs.chemmater.7b02669](https://doi.org/10.1021/acs.chemmater.7b02669).
- [216] KIM, Y., YASSITEPE, E., VOZNYI, O., COMIN, R., WALTERS, G., GONG, X., KAN-JANABOOS, P., NOGUEIRA, A. F. AND SARGENT, E. H., “Efficient luminescence from perovskite quantum dot solids”, *ACS Appl. Mater. Interfaces* **7**(45), 25007–25013 (2015), doi: [10.1021/acsami.5b09084](https://doi.org/10.1021/acsami.5b09084).
- [217] PALAZON, F., STASIO, F. D., LAUCIELLO, S., KRAHNE, R., PRATO, M. AND MANNA, L., “Evolution of CsPbBr<sub>3</sub> nanocrystals upon post-synthesis annealing under an inert atmosphere”, *J. Mater. Chem. C* **4**(39), 9179–9182 (2016), doi: [10.1039/c6tc03342c](https://doi.org/10.1039/c6tc03342c).
- [218] JIANG, Q., ZHANG, L., WANG, H., YANG, X., MENG, J., LIU, H., YIN, Z., WU, J., ZHANG, X. AND YOU, J., “Enhanced electron extraction using SnO<sub>2</sub> for high-efficiency planar-structure HC(NH<sub>2</sub>)<sub>2</sub>PbI<sub>3</sub>-based perovskite solar cells”, *Nature Energy* **2**, 16177 (2016), doi: [10.1038/nenergy.2016.177](https://doi.org/10.1038/nenergy.2016.177).
- [219] SUN, H., LI, Z., KONG, L., WANG, B., ZHANG, C., YUAN, Q., HUANG, S., LIU, Y. AND LI, L., “Enhancing the stability of CsPbBr<sub>3</sub> nanocrystals by sequential surface adsorption of S<sup>2-</sup> and metal ions”, *Chem. Commun.* **54**(67), 9345–9348 (2018), doi: [10.1039/c8cc04171g](https://doi.org/10.1039/c8cc04171g).
- [220] LI, Z., KONG, L., HUANG, S. AND LI, L., “Highly luminescent and ultrastable CsPbBr<sub>3</sub> perovskite quantum dots incorporated into a silica/alumina monolith”, *Angew. Chem. Int. Ed.* **56**(28), 8134–8138 (2017), doi: [10.1002/anie.201703264](https://doi.org/10.1002/anie.201703264).
- [221] LI, Z.-J., HOFMAN, E., LI, J., DAVIS, A. H., TUNG, C.-H., WU, L.-Z. AND ZHENG, W., “Photoelectrochemically active and environmentally stable CsPbBr<sub>3</sub>/TiO<sub>2</sub> core/shell nanocrystals”, *Adv. Funct. Mater.* **28**(1), 1704288 (2018), doi: [10.1002/adfm.201704288](https://doi.org/10.1002/adfm.201704288).
- [222] STAEBLER, D. L., CRANDALL, R. S. AND WILLIAMS, R., “Stability of n-i-p amorphous silicon solar cells”, *Appl. Phys. Lett.* **39**(9), 733–735 (1981), doi: [10.1063/1.92865](https://doi.org/10.1063/1.92865).

- [223] YOSHIKAWA, K., KAWASAKI, H., YOSHIDA, W., IRIE, T., KONISHI, K., NAKANO, K., UTO, T., ADACHI, D., KANEMATSU, M., UZU, H. AND YAMAMOTO, K., “Silicon heterojunction solar cell with interdigitated back contacts for a photoconversion efficiency over 26 %”, *Nature Energy* **2**(5), 17032 (2017), doi: [10.1038/nenergy.2017.32](https://doi.org/10.1038/nenergy.2017.32).
- [224] LEE, T. D. AND EBONG, A. U., “A review of thin film solar cell technologies and challenges”, *Renewable Sustainable Energy Rev.* **70**, 1286–1297 (2016), doi: [10.1016/j.rser.2016.12.028](https://doi.org/10.1016/j.rser.2016.12.028).
- [225] O'REGAN, B. AND GRÄTZEL, M., “A low-cost, high-efficiency solar cell based on dye-sensitized colloidal TiO<sub>2</sub> films”, *Nature* **353**(6346), 737–740 (1991), doi: [10.1038/353737a0](https://doi.org/10.1038/353737a0).
- [226] YEH, N. AND YEH, P., “Organic solar cells: their developments and potentials”, *Renewable Sustainable Energy Rev.* **21**, 421–431 (2013), doi: [10.1016/j.rser.2012.12.046](https://doi.org/10.1016/j.rser.2012.12.046).
- [227] KAMAT, P. V., “Quantum dot solar cells. Semiconductor nanocrystals as light harvesters”, *J. Phys. Chem. C* **112**(48), 18737–18753 (2008), doi: [10.1021/jp806791s](https://doi.org/10.1021/jp806791s).
- [228] TRESS, W., MARINOVA, N., INGANÄS, O., NAZEERUDDIN, M. K., ZAKEERUDDIN, S. M. AND GRAETZEL, M., “Predicting the open-circuit voltage of CH<sub>3</sub>NH<sub>3</sub>PbI<sub>3</sub> perovskite solar cells using electroluminescence and photovoltaic quantum efficiency spectra: the role of radiative and non-radiative recombination”, *Adv. Energy Mater.* **5**(3), 1400812 (2014), doi: [10.1002/aenm.201400812](https://doi.org/10.1002/aenm.201400812).
- [229] TRESS, W., “Perovskite solar cells on the way to their radiative efficiency limit - Insights into a success story of high open-circuit voltage and low recombination”, *Adv. Energy Mater.* **7**(14), 1602358 (2017), doi: [10.1002/aenm.201602358](https://doi.org/10.1002/aenm.201602358).
- [230] RÜHLE, S., “Tabulated values of the Shockley-Queisser limit for single junction solar cells”, *Solar Energy* **130**, 139–147 (2016), doi: [10.1016/j.solener.2016.02.015](https://doi.org/10.1016/j.solener.2016.02.015).
- [231] WU, Y., YANG, X., CHEN, H., ZHANG, K., QIN, C., LIU, J., PENG, W., ISLAM, A., BI, E., YE, F., YIN, M., ZHANG, P. AND HAN, L., “Highly compact TiO<sub>2</sub> layer for efficient hole-blocking in perovskite solar cells”, *Appl. Phys Express* **7**(5), 052301 (2014), doi: [10.7567/apex.7.052301](https://doi.org/10.7567/apex.7.052301).
- [232] ONO, L. K., LEYDEN, M. R., WANG, S. AND QI, Y., “Organometal halide perovskite thin films and solar cells by vapor deposition”, *J. Mater. Chem. A* **4**(18), 6693–6713 (2016), doi: [10.1039/c5ta08963h](https://doi.org/10.1039/c5ta08963h).
- [233] CHEN, W.-Y., DENG, L.-L., DAI, S.-M., WANG, X., TIAN, C.-B., ZHAN, X.-X., XIE, S.-Y., HUANG, R.-B. AND ZHENG, L.-S., “Low-cost solution-processed copper iodide as an alternative to PEDOT:PSS hole transport layer for efficient and stable inverted planar heterojunction perovskite solar cells”, *J. Mater. Chem. A* **3**(38), 19353–19359 (2015), doi: [10.1039/c5ta05286f](https://doi.org/10.1039/c5ta05286f).

- [234] ELANGOVA, E. AND RAMAMURTHI, K., “A study on low cost-high conducting fluorine and antimony-doped tin oxide thin films”, *Appl. Surf. Sci.* **249**(1-4), 183–196 (2005), doi: [10.1016/j.apsusc.2004.11.074](https://doi.org/10.1016/j.apsusc.2004.11.074).
- [235] KARASAWA, T. AND MIYATA, Y., “Electrical and optical properties of indium tin oxide thin films deposited on unheated substrates by d.c. reactive sputtering”, *Thin Solid Films* **223**(1), 135–139 (1993), doi: [10.1016/0040-6090\(93\)90737-a](https://doi.org/10.1016/0040-6090(93)90737-a).
- [236] NANTO, H., MINAMI, T., ORITO, S. AND TAKATA, S., “Electrical and optical properties of indium tin oxide thin films prepared on low-temperature substrates by RF magnetron sputtering under an applied external magnetic field”, *J. Appl. Phys.* **63**(8), 2711–2716 (1988), doi: [10.1063/1.340964](https://doi.org/10.1063/1.340964).
- [237] KIM, H.-S., LEE, C.-R., IM, J.-H., LEE, K.-B., MOEHL, T., MARCHIORO, A., MOON, S.-J., HUMPHRY-BAKER, R., YUM, J.-H., MOSER, J. E., GRÄTZEL, M. AND PARK, N.-G., “Lead iodide perovskite sensitized all-solid-state submicron thin film mesoscopic solar cell with efficiency exceeding 9%”, *Sci. Rep.* **2**(1), 591 (2012), doi: [10.1038/srep00591](https://doi.org/10.1038/srep00591).
- [238] SNAITH, H. J., ABATE, A., BALL, J. M., EPERON, G. E., LEIJTENS, T., NOEL, N. K., STRANKS, S. D., WANG, J. T.-W., WOJCIECHOWSKI, K. AND ZHANG, W., “Anomalous hysteresis in perovskite solar cells”, *J. Phys. Chem. Lett.* **5**(9), 1511–1515 (2014), doi: [10.1021/jz500113x](https://doi.org/10.1021/jz500113x).
- [239] LIU, D. AND KELLY, T. L., “Perovskite solar cells with a planar heterojunction structure prepared using room-temperature solution processing techniques”, *Nat. Photonics* **8**, 133 (2013), doi: [10.1038/nphoton.2013.342](https://doi.org/10.1038/nphoton.2013.342).
- [240] SON, D.-Y., IM, J.-H., KIM, H.-S. AND PARK, N.-G., “11% efficient perovskite solar cell based on ZnO nanorods: an effective charge collection system”, *J. Phys. Chem. C* **118**, 16567–16573 (2014), doi: [10.1021/jp412407j](https://doi.org/10.1021/jp412407j).
- [241] BAENA, J. P. C., STEIER, L., TRESS, W., SALIBA, M., NEUTZNER, S., MATSUI, T., GIORDANO, F., JACOBSSON, T. J., KANDADA, A. R. S., ZAKEERUDDIN, S. M., PETROZZA, A., ABATE, A., NAZEERUDDIN, M. K., GRÄTZEL, M. AND HAGFELDT, A., “Highly efficient planar perovskite solar cells through band alignment engineering”, *Energy Environ. Sci.* **8**, 2928–2934 (2015), doi: [10.1039/c5ee02608c](https://doi.org/10.1039/c5ee02608c).
- [242] DONG, Q., SHI, Y., WANG, K., LI, Y., WANG, S., ZHANG, H., XING, Y., DU, Y., BAI, X. AND MA, T., “Insight into perovskite solar cells based on SnO<sub>2</sub> compact electron-selective layer”, *J. Phys. Chem. C* **119**(19), 10212–10217 (2015), doi: [10.1021/acs.jpcc.5b00541](https://doi.org/10.1021/acs.jpcc.5b00541).
- [243] KE, W., FANG, G., LIU, Q., XIONG, L., QIN, P., TAO, H., WANG, J., LEI, H., LI, B., WAN, J., YANG, G. AND YAN, Y., “Low-temperature solution-processed tin oxide as an alternative electron transporting layer for efficient perovskite solar cells”, *J. Am. Chem. Soc.* **137**(21), 6730–6733 (2015), doi: [10.1021/jacs.5b01994](https://doi.org/10.1021/jacs.5b01994).

- [244] TIWANA, P., DOCAMPO, P., JOHNSTON, M. B., SNAITH, H. J. AND HERZ, L. M., “Electron mobility and injection dynamics in mesoporous ZnO, SnO<sub>2</sub>, and TiO<sub>2</sub> films used in Dye-Sensitized Solar Cells”, *ACS Nano* **5**(6), 5158–5166 (2011), doi: [10.1021/nm201243y](https://doi.org/10.1021/nm201243y).
- [245] YOU, J., HONG, Z., YANG, Y. M., CHEN, Q., CAI, M., SONG, T.-B., CHEN, C.-C., LU, S., LIU, Y., ZHOU, H. AND YANG, Y., “Low-temperature solution-processed perovskite solar cells with high efficiency and flexibility”, *ACS Nano* **8**(2), 1674–1680 (2014), doi: [10.1021/nn406020d](https://doi.org/10.1021/nn406020d).
- [246] SHAO, Y., XIAO, Z., BI, C., YUAN, Y. AND HUANG, J., “Origin and elimination of photocurrent hysteresis by fullerene passivation in CH<sub>3</sub>NH<sub>3</sub>PbI<sub>3</sub> planar heterojunction solar cells”, *Nat. Commun.* **5**, 5784 (2014), doi: [10.1038/ncomms6784](https://doi.org/10.1038/ncomms6784).
- [247] MENG, L., YOU, J., GUO, T.-F. AND YANG, Y., “Recent advances in the inverted planar structure of perovskite solar cells”, *Acc. Chem. Res.* **49**(1), 155–165 (2015), doi: [10.1021/acs.accounts.5b00404](https://doi.org/10.1021/acs.accounts.5b00404).
- [248] BI, D., YI, C., LUO, J., DÉCOPPET, J.-D., ZHANG, F., ZAKEERUDDIN, S. M., LI, X., HAGFELDT, A. AND GRÄTZEL, M., “Polymer-templated nucleation and crystal growth of perovskite films for solar cells with efficiency greater than 21%”, *Nature Energy* **1**(10) (2016), doi: [10.1038/nenergy.2016.142](https://doi.org/10.1038/nenergy.2016.142).
- [249] BACH, U., LUPO, D., COMTE, P., MOSER, J. E., WEISSÖRTEL, F., SALBECK, J., SPREITZER, H. AND GRÄTZEL, M., “Solid-state dye-sensitized mesoporous TiO<sub>2</sub> solar cells with high photon-to-electron conversion efficiencies”, *Nature* **395**, 583–585 (1998), doi: [10.1038/26936](https://doi.org/10.1038/26936).
- [250] SNAITH, H. J. AND GRÄTZEL, M., “Enhanced charge mobility in a molecular hole transporter via addition of redox inactive ionic dopant: implication to dye-sensitized solar cells”, *Appl. Phys. Lett.* **89**(26), 262114 (2006), doi: [10.1063/1.2424552](https://doi.org/10.1063/1.2424552).
- [251] KRÜGER, J., PLASS, R., CEVEY, L., PICCIRELLI, M., GRÄTZEL, M. AND BACH, U., “High efficiency solid-state photovoltaic device due to inhibition of interface charge recombination”, *Appl. Phys. Lett.* **79**(13), 2085–2087 (2001), doi: [10.1063/1.1406148](https://doi.org/10.1063/1.1406148).
- [252] JUAREZ-PEREZ, E. J., LEYDEN, M. R., WANG, S., ONO, L. K., HAWASH, Z. AND QI, Y., “Role of the dopants on the morphological and transport properties of Spiro-MeOTAD hole transport layer”, *Chem. Mater.* **28**(16), 5702–5709 (2016), doi: [10.1021/acs.chemmater.6b01777](https://doi.org/10.1021/acs.chemmater.6b01777).
- [253] LEIJTENS, T., LIM, J., TEUSCHER, J., PARK, T. AND SNAITH, H. J., “Charge density dependent mobility of organic hole-transporters and mesoporous TiO<sub>2</sub> determined by transient mobility spectroscopy: implications to dye-sensitized and organic solar cells”, *Adv. Mater.* **25**, 3227–3233 (2013), doi: [10.1002/adma.201300947](https://doi.org/10.1002/adma.201300947).
- [254] GANESAN, P., FU, K., GAO, P., RAABE, I., SCHENK, K., SCOPELLITI, R., LUO, J., WONG, L. H., GRÄTZEL, M. AND NAZEERUDDIN, M. K., “A simple spiro-type hole

- transporting material for efficient perovskite solar cells”, *Energy Environ. Sci.* **8**(7), 1986–1991 (2015), doi: [10.1039/c4ee03773a](https://doi.org/10.1039/c4ee03773a).
- [255] VIVO, P., SALUNKE, J. K. AND PRIIMAGI, A., “Hole-transporting materials for printable perovskite solar cells”, *Materials* **10**(9), 1087 (2017), doi: [10.3390/ma10091087](https://doi.org/10.3390/ma10091087).
- [256] JENG, J.-Y., CHIANG, Y.-F., LEE, M.-H., PENG, S.-R., GUO, T.-F., CHEN, P. AND WEN, T.-C., “CH<sub>3</sub>NH<sub>3</sub>PbI<sub>3</sub> perovskite/fullerene planar-heterojunction hybrid solar cells”, *Adv. Mater.* **25**(27), 3727–3732 (2013), doi: [10.1002/adma.201301327](https://doi.org/10.1002/adma.201301327).
- [257] IM, J.-H., LEE, C.-R., LEE, J.-W., PARK, S.-W. AND PARK, N.-G., “6.5% efficient perovskite quantum-dot-sensitized solar cell”, *Nanoscale* **3**(10), 4088–4093 (2011), doi: [10.1039/c1nr10867k](https://doi.org/10.1039/c1nr10867k).
- [258] ZHOU, H., CHEN, Q., LI, G., LUO, S., B. SONG, T., DUAN, H.-S., HONG, Z., YOU, J., LIU, Y. AND YANG, Y., “Interface engineering of highly efficient perovskite solar cells”, *Science* **345**, 542–546 (2014), doi: [10.1126/science.1254050](https://doi.org/10.1126/science.1254050).
- [259] BALL, J. M., LEE, M. M., HEY, A. AND SNAITH, H. J., “Low-temperature processed meso-superstructured to thin-film perovskite solar cells”, *Energy Environ. Sci.* **6**(6), 1739–1743 (2013), doi: [10.1039/c3ee40810h](https://doi.org/10.1039/c3ee40810h).
- [260] XU, T., CHEN, L., GUO, Z. AND MA, T., “Strategic improvement of the long-term stability of perovskite materials and perovskite solar cells”, *Phys. Chem. Chem. Phys.* **18**, 27026–27050 (2016), doi: [10.1039/c6cp04553g](https://doi.org/10.1039/c6cp04553g).
- [261] GRANCINI, G., ROLDÁN-CARMONA, C., ZIMMERMANN, I., MOSCONI, E., LEE, X., MARTINEAU, D., NARBÉY, S., OSWALD, F., ANGELIS, F. D., GRAETZEL, M. AND NAZEERUDDIN, M. K., “One-year stable perovskite solar cells by 2D/3D interface engineering”, *Nat. Commun.* **8**, 15684 (2017), doi: [10.1038/ncomms15684](https://doi.org/10.1038/ncomms15684).
- [262] HENDERSON, M. A., EPLING, W. S., PERKINS, C. L., PEDEN, C. H. F. AND DIEBOLD, U., “Interaction of molecular oxygen with the vacuum-annealed TiO<sub>2</sub>(110) surface: molecular and dissociative channels”, *J. Phys. Chem. B* **103**, 5328–5337 (1999), doi: [10.1021/jp990655q](https://doi.org/10.1021/jp990655q).
- [263] LU, G., LINSEBIGLER, A. AND YATES, J. T., “The adsorption and photodesorption of oxygen on the TiO<sub>2</sub>(110) surface”, *J. Chem. Phys.* **102**, 4657–4662 (1995), doi: [10.1063/1.469513](https://doi.org/10.1063/1.469513).
- [264] PATHAK, S. K., ABATE, A., RUCKDESCHEL, P., ROOSE, B., GÖDEL, K. C., VAYNZOF, Y., SANTHALA, A., WATANABE, S.-I., HOLLMAN, D. J., NOEL, N., SEPE, A., WIESNER, U., FRIEND, R., SNAITH, H. J. AND STEINER, U., “Performance and stability enhancement of dye-sensitized and perovskite solar cells by Al doping of TiO<sub>2</sub>”, *Adv. Funct. Mater.* **24**, 6046–6055 (2015), doi: [10.1002/adfm.201401658](https://doi.org/10.1002/adfm.201401658).
- [265] BAO, Q., LIU, X., BRAUN, S. AND FAHLMAN, M., “Oxygen- and water-based degradation in [6,6]-phenyl-C61-butyric acid methyl ester (PCBM) films”, *Adv. Energy Mater.* **4**, 1301272 (2014), doi: [10.1002/aenm.201301272](https://doi.org/10.1002/aenm.201301272).



- [266] YOU, J., MENG, L., SONG, T.-B., GUO, T.-F., YANG, Y. M., CHANG, W.-H., HONG, Z., CHEN, H., ZHOU, H., CHEN, Q., LIU, Y., MARCO, N. D. AND YANG, Y., “Improved air stability of perovskite solar cells via solution-processed metal oxide transport layers”, *Nat. Nanotechnol.* **11**, 75–81 (2016), doi: [10.1038/nnano.2015.230](https://doi.org/10.1038/nnano.2015.230).
- [267] ONO, L. K., RAGA, S. R., REMEIKI, M., WINCHESTER, A. J., GABE, A. AND QI, Y., “Pinhole-free hole transport layers significantly improve the stability of MAPbI<sub>3</sub>-based perovskite solar cells under operating conditions”, *J. Mater. Chem. A* **3**, 15451–15456 (2015), doi: [10.1039/c5ta03443d](https://doi.org/10.1039/c5ta03443d).
- [268] JUNG, M.-C., RAGA, S. R., ONO, L. K. AND QI, Y., “Substantial improvement of perovskite solar cells stability by pinhole-free hole transport layer with doping engineering”, *Sci. Rep.* **5**, 9863 (2015), doi: [10.1038/srep09863](https://doi.org/10.1038/srep09863).
- [269] KAWANO, K., PACIOS, R., POPLAVSKYY, D., NELSON, J., BRADLEY, D. D. C. AND DURRANT, J. R., “Degradation of organic solar cells due to air exposure”, *Sol. Energy Mater. Sol. Cells* **90**(20), 3520–3530 (2006), doi: [10.1016/j.solmat.2006.06.041](https://doi.org/10.1016/j.solmat.2006.06.041).
- [270] DE JONG, M. P., VAN IJZENDOORN, L. J. AND DE VOIGT, M. J. A., “Stability of the interface between indium-tin-oxide and poly(3,4-ethylenedioxythiophene)/poly(styrenesulfonate) in polymer light-emitting diodes”, *Appl. Phys. Lett.* **77**, 2255–2257 (2000), doi: [10.1063/1.1315344](https://doi.org/10.1063/1.1315344).
- [271] HAN, Y., MEYER, S., DKHISSI, Y., WEBER, K., PRINGLE, J. M., BACH, U., SPICCIA, L. AND CHENG, Y.-B., “Degradation observations of encapsulated planar CH<sub>3</sub>NH<sub>3</sub>PbI<sub>3</sub> perovskite solar cells at high temperatures and humidity”, *J. Mater. Chem. A* **3**(15), 8139–8147 (2015), doi: [10.1039/c5ta00358j](https://doi.org/10.1039/c5ta00358j).
- [272] BACK, H., KIM, G., KIM, J., KONG, J., KIM, T. K., KANG, H., KIM, H., LEE, J., LEE, S. AND LEE, K., “Achieving long-term stable perovskite solar cells via ion neutralization”, *Energy Environ. Sci.* **9**(4), 1258–1263 (2016), doi: [10.1039/c6ee00612d](https://doi.org/10.1039/c6ee00612d).
- [273] DOMANSKI, K., CORREA-BAENA, J.-P., MINE, N., NAZEERUDDIN, M. K., ABATE, A., SALIBA, M., TRESS, W., HAGFELDT, A. AND GRÄTZEL, M., “Not all that glitters is gold: metal-migration-induced degradation in perovskite solar cells”, *ACS Nano* **10**, 6306–6314 (2016), doi: [10.1021/acsnano.6b02613](https://doi.org/10.1021/acsnano.6b02613).
- [274] DUALEH, A., MOEHL, T., TÉTREAULT, N., TEUSCHER, J., GAO, P., NAZEERUDDIN, M. K. AND GRÄTZEL, M., “Impedance spectroscopic analysis of lead iodide perovskite-sensitized solid-state solar cells”, *ACS Nano* **8**(1), 362–373 (2013), doi: [10.1021/nn404323g](https://doi.org/10.1021/nn404323g).
- [275] CHEN, B., YANG, M., PRIYA, S. AND ZHU, K., “Origin of J-V hysteresis in perovskite solar cells”, *J. Phys. Chem. Lett.* **7**(5), 905–917 (2016), doi: [10.1021/acs.jpcllett.6b00215](https://doi.org/10.1021/acs.jpcllett.6b00215).



- [276] WEI, J., ZHAO, Y., LI, H., LI, G., PAN, J., XU, D., ZHAO, Q. AND YU, D., “Hysteresis analysis based on the ferroelectric effect in hybrid perovskite solar cells”, *J. Phys. Chem. Lett.* **5**(21), 3937–3945 (2014), doi: [10.1021/jz502111u](https://doi.org/10.1021/jz502111u).
- [277] CHEN, H.-W., SAKAI, N., IKEGAMI, M. AND MIYASAKA, T., “Emergence of hysteresis and transient ferroelectric response in organo-lead halide perovskite solar cells”, *J. Phys. Chem. Lett.* **6**(1), 164–169 (2014), doi: [10.1021/jz502429u](https://doi.org/10.1021/jz502429u).
- [278] FROST, J. M., BUTLER, K. T. AND WALSH, A., “Molecular ferroelectric contributions to anomalous hysteresis in hybrid perovskite solar cells”, *APL Mater.* **2**(8), 081506 (2014), doi: [10.1063/1.4890246](https://doi.org/10.1063/1.4890246).
- [279] LI, W., DONG, H., DONG, G. AND WANG, L., “Hysteresis mechanism in perovskite photovoltaic devices and its potential application for multi-bit memory devices”, *Org. Electron.* **26**, 208–212 (2015), doi: [10.1016/j.orgel.2015.07.026](https://doi.org/10.1016/j.orgel.2015.07.026).
- [280] ZHANG, Y., LIU, M., EPERON, G. E., LEIJTENS, T. C., McMEEKIN, D., SALIBA, M., ZHANG, W., DE BASTIANI, M., PETROZZA, A., HERZ, L. M., JOHNSTON, M. B., LIN, H. AND SNAITH, H. J., “Charge selective contacts, mobile ions and anomalous hysteresis in organic-inorganic perovskite solar cells”, *Mater. Horiz.* **2**(3), 315–322 (2015), doi: [10.1039/c4mh00238e](https://doi.org/10.1039/c4mh00238e).
- [281] ZHAO, Y., LIANG, C., ZHANG, H., LI, D., TIAN, D., LI, G., JING, X., ZHANG, W., XIAO, W., LIU, Q., ZHANG, F. AND HE, Z., “Anomalously large interface charge in polarity-switchable photovoltaic devices: an indication of mobile ions in organic-inorganic halide perovskites”, *Energy Environ. Sci.* **8**(4), 1256–1260 (2015), doi: [10.1039/c4ee04064c](https://doi.org/10.1039/c4ee04064c).
- [282] GUBBALA, S., CHAKRAPANI, V., KUMAR, V. AND SUNKARA, M. K., “Band-edge engineered hybrid structures for dye-sensitized solar cells based on SnO<sub>2</sub> nanowires”, *Adv. Funct. Mater.* **18**, 2411–2418 (2008), doi: [10.1002/adfm.200800099](https://doi.org/10.1002/adfm.200800099).
- [283] SEPALAGE, G. A., MEYER, S., PASCOE, A., SCULLY, A. D., HUANG, F., BACH, U., CHENG, Y.-B. AND SPICCIA, L., “Copper(I) iodide as hole-conductor in planar perovskite solar cells: Probing the origin of J-V hysteresis”, *Adv. Funct. Mater.* **25**, 5650–5661 (2015), doi: [10.1002/adfm.201502541](https://doi.org/10.1002/adfm.201502541).
- [284] CHRISTIANS, J. A., FUNG, R. C. M. AND KAMAT, P. V., “An inorganic hole conductor for organo-lead halide perovskite solar cells. improved hole conductivity with copper iodide”, *J. Am. Chem. Soc.* **136**, 758–764 (2014), doi: [10.1021/ja411014k](https://doi.org/10.1021/ja411014k).
- [285] QIN, P., TANAKA, S., ITO, S., TETREAU, N., MANABE, K., NISHINO, H., NAZEERUDDIN, M. K. AND GRÄTZEL, M., “Inorganic hole conductor-based lead halide perovskite solar cells with 12.4% conversion efficiency”, *Nat. Commun.* **5** (2014), doi: [10.1038/ncomms4834](https://doi.org/10.1038/ncomms4834).

- [286] JUNG, M., KIM, Y. C., JEON, N. J., YANG, W. S., SEO, J., NOH, J. H. AND IL SEOK, S., “Thermal stability of CuSCN hole conductor-based perovskite solar cells”, *ChemSusChem* **9**, 2592–2596 (2016), doi: [10.1002/cssc.201600957](https://doi.org/10.1002/cssc.201600957).
- [287] ZHANG, H., CHENG, J., LIN, F., HE, H., MAO, J., WONG, K. S., JEN, A. K.-Y. AND CHOY, W. C. H., “Pinhole-free and surface-nanostructured NiO<sub>x</sub> film by room-temperature solution process for high-performance flexible perovskite solar cells with good stability and reproducibility”, *ACS Nano* **10**(1), 1503–1511 (2016), doi: [10.1021/acsnano.5b07043](https://doi.org/10.1021/acsnano.5b07043).
- [288] BONACCORSO, F., COLOMBO, L., YU, G., STOLLER, M., TOZZINI, V., FERRARI, A. C., RUOFF, R. S. AND PELLEGRINI, V., “Graphene, related two-dimensional crystals, and hybrid systems for energy conversion and storage”, *Science* **347**, 1246501 (2015), doi: [10.1126/science.1246501](https://doi.org/10.1126/science.1246501).
- [289] MOROZOV, S. V., NOVOSELOV, K. S., KATSNELSON, M. I., SCHEDIN, F., ELIAS, D. C., JASZCZAK, J. A. AND GEIM, A. K., “Giant intrinsic carrier mobilities in graphene and its bilayer”, *Phys. Rev. Lett.* **100**, 016602 (2008), doi: [10.1103/physrevlett.100.016602](https://doi.org/10.1103/physrevlett.100.016602).
- [290] SAKHAEI-POUR, A., “Elastic properties of single-layered graphene sheet”, *Solid State Commun.* **149**, 91–95 (2009), doi: [10.1016/j.ssc.2008.09.050](https://doi.org/10.1016/j.ssc.2008.09.050).
- [291] GHOSH, S., BAO, W., NIKA, D. L., SUBRINA, S., POKATILOV, E. P., LAU, C. N. AND BALANDIN, A. A., “Dimensional crossover of thermal transport in few-layer graphene”, *Nat. Mater.* **9**(7), 555–558 (2010), doi: [10.1038/nmat2753](https://doi.org/10.1038/nmat2753).
- [292] BAE, S., KIM, H., LEE, Y., XU, X., PARK, J.-S., ZHENG, Y., BALAKRISHNAN, J., LEI, T., RI KIM, H., SONG, Y. I., KIM, Y.-J., KIM, K. S., OZYILMAZ, B., AHN, J.-H., HONG, B. H. AND IJIMA, S., “Roll-to-roll production of 30-inch graphene films for transparent electrodes”, *Nat. Nanotechnol.* **5**(8), 574–578 (2010), doi: [10.1038/nnano.2010.132](https://doi.org/10.1038/nnano.2010.132).
- [293] KWON, K. C., CHOI, K. S. AND KIM, S. Y., “Increased work function in few-layer graphene sheets via metal chloride doping”, *Adv. Funct. Mater.* **22**(22), 4724–4731 (2012), doi: [10.1002/adfm.201200997](https://doi.org/10.1002/adfm.201200997).
- [294] MISHRA, M., JOSHI, R. K., OJHA, S., KANJILAL, D. AND MOHANTY, T., “Role of oxygen in the work function modification at various stages of chemically synthesized graphene”, *J. Phys. Chem. C* **117**, 19746–19750 (2013), doi: [10.1021/jp406712s](https://doi.org/10.1021/jp406712s).
- [295] KAKAVELAKIS, G., KONIOS, D., STRATAKIS, E. AND KYMAKIS, E., “Enhancement of the efficiency and stability of organic photovoltaic devices via the addition of a lithium-neutralized graphene oxide electron-transporting layer”, *Chem. Mater.* **26**, 5988–5993 (2014), doi: [10.1021/cm502826f](https://doi.org/10.1021/cm502826f).
- [296] AGRETI, A., PESCELELLI, S., TAHERI, B., DEL RIO CASTILLO, A. E., CINÀ, L., BONACCORSO, F. AND DI CARLO, A., “Graphene-perovskite solar cells ex-

- ceed 18% efficiency: a stability study”, *ChemSusChem* **9**(18), 2609–2619 (2016), doi: [10.1002/cssc.201600942](https://doi.org/10.1002/cssc.201600942).
- [297] GARG, R., DUTTA, N. K. AND ROY CHOUDHURY, N., “Work function engineering of graphene”, *Nanomaterials* **4**(2), 267–300 (2014), doi: [10.3390/nano4020267](https://doi.org/10.3390/nano4020267).
- [298] PALMA, A. L., CINÀ, L., PESCE TELLI, S., AGRESTI, A., RAGGIO, M., PAOLESSE, R., BONACCORSO, F. AND DI CARLO, A., “Reduced graphene oxide as efficient and stable hole transporting material in mesoscopic perovskite solar cells”, *Nano Energy* **22**(Supplement C), 349–360 (2016), doi: [10.1016/j.nanoen.2016.02.027](https://doi.org/10.1016/j.nanoen.2016.02.027).
- [299] YEO, J.-S., KANG, R., LEE, S., JEON, Y.-J., MYOUNG, N., LEE, C.-L., KIM, D.-Y., YUN, J.-M., SEO, Y.-H., KIM, S.-S. AND NA, S.-I., “Highly efficient and stable planar perovskite solar cells with reduced graphene oxide nanosheets as electrode interlayer”, *Nano Energy* **12**(Supplement C), 96–104 (2015), doi: [10.1016/j.nanoen.2014.12.022](https://doi.org/10.1016/j.nanoen.2014.12.022).
- [300] CHO, K. T., GRANCINI, G., LEE, Y., KONIOS, D., PAEK, S., KYMAKIS, E. AND NAZEERUDDIN, M. K., “Beneficial role of reduced graphene oxide for electron extraction in highly efficient perovskite solar cells”, *ChemSusChem* **9**(21), 3040–3044 (2016), doi: [10.1002/cssc.201601070](https://doi.org/10.1002/cssc.201601070).
- [301] HAN, G. S., SONG, Y. H., JIN, Y. U., LEE, J.-W., PARK, N.-G., KANG, B. K., LEE, J.-K., CHO, I. S., YOON, D. H. AND JUNG, H. S., “Reduced graphene oxide/mesoporous TiO<sub>2</sub> nanocomposite based perovskite solar cells”, *ACS Appl. Mater. Interfaces* **7**, 23521–23526 (2015), doi: [10.1021/acsami.5b06171](https://doi.org/10.1021/acsami.5b06171).
- [302] WANG, J. T.-W., BALL, J. M., BAREA, E. M., ABATE, A., ALEXANDER-WEBBER, J. A., HUANG, J., SALIBA, M., MORA-SERO, I., BISQUERT, J., SNAITH, H. J. AND NICHOLAS, R. J., “Low-temperature processed electron collection layers of graphene/TiO<sub>2</sub> nanocomposites in thin film perovskite solar cells”, *Nano Lett.* **14**(2), 724–730 (2014), doi: [10.1021/nl403997a](https://doi.org/10.1021/nl403997a).
- [303] AGRESTI, A., PESCE TELLI, S., CINÀ, L., KONIOS, D., KAKAVELAKIS, G., KYMAKIS, E. AND DI CARLO, A., “Efficiency and stability enhancement in perovskite solar cells by inserting lithium-neutralized graphene oxide as electron transporting layer”, *Adv. Funct. Mater.* **26**(16), 2686–2694 (2016), doi: [10.1002/adfm.201504949](https://doi.org/10.1002/adfm.201504949).
- [304] LI, W., DONG, H., GUO, X., LI, N., LI, J., NIU, G. AND WANG, L., “Graphene oxide as dual functional interface modifier for improving wettability and retarding recombination in hybrid perovskite solar cells”, *J. Mater. Chem. A* **2**(47), 20105–20111 (2014), doi: [10.1039/c4ta05196c](https://doi.org/10.1039/c4ta05196c).
- [305] GIORDANO, F., ABATE, A., BAENA, J. P. C., SALIBA, M., MATSUI, T., IM, S. H., ZAKEERUDDIN, S. M., NAZEERUDDIN, M. K., HAGFELDT, A. AND GRAETZEL, M., “Enhanced electronic properties in mesoporous TiO<sub>2</sub> via lithium doping for high-efficiency perovskite solar cells”, *Nat. Commun.* **7**, 10379 (2016), doi: [10.1038/ncomms10379](https://doi.org/10.1038/ncomms10379).

- [306] ERA, M., MORIMOTO, S., TSUTSUI, T. AND SAITO, S., “Organic-inorganic heterostructure electroluminescent device using a layered perovskite semiconductor  $(\text{C}_6\text{H}_5\text{C}_2\text{H}_4\text{NH}_3)_2\text{PbI}_4$ ”, *Appl. Phys. Lett.* **65**(6), 676–678 (1994), [doi: 10.1063/1.112265](https://doi.org/10.1063/1.112265).
- [307] TAN, Z.-K., MOGHADDAM, R. S., LAI, M. L., DOCAMPO, P., HIGLER, R., DESCHLER, F., PRICE, M., SADHANALA, A., PAZOS, L. M., CREDGINGTON, D., HANUSCH, F., BEIN, T., SNAITH, H. J. AND FRIEND, R. H., “Bright light-emitting diodes based on organometal halide perovskite”, *Nat. Nanotechnol.* **9**(9), 687–692 (2014), [doi: 10.1038/nnano.2014.149](https://doi.org/10.1038/nnano.2014.149).
- [308] CHO, H., JEONG, S.-H., PARK, M.-H., KIM, Y.-H., WOLF, C., LEE, C.-L., HEO, J. H., SADHANALA, A., MYOUNG, N., YOO, S., IM, S. H., FRIEND, R. H. AND LEE, T.-W., “Overcoming the electroluminescence efficiency limitations of perovskite light-emitting diodes”, *Science* **350**(6265), 1222–1225 (2015), [doi: 10.1126/science.aad1818](https://doi.org/10.1126/science.aad1818).
- [309] SONG, J., LI, J., LI, X., XU, L., DONG, Y. AND ZENG, H., “Quantum dot light-emitting diodes based on inorganic perovskite cesium lead halides ( $\text{CsPbX}_3$ )”, *Adv. Mater.* **27**(44), 7162–7167 (2015), [doi: 10.1002/adma.201502567](https://doi.org/10.1002/adma.201502567).
- [310] DRAGUTA, S., SHARIA, O., YOON, S. J., BRENNAN, M. C., MOROZOV, Y. V., MANSER, J. S., KAMAT, P. V., SCHNEIDER, W. F. AND KUNO, M., “Rationalizing the light-induced phase separation of mixed halide organic-inorganic perovskites”, *Nat. Commun.* **8**(1) (2017), [doi: 10.1038/s41467-017-00284-2](https://doi.org/10.1038/s41467-017-00284-2).
- [311] LI, G., RIVAROLA, F. W. R., DAVIS, N. J. L. K., BAI, S., JELICOE, T. C., DE LA PEÑA, F., HOU, S., DUCATI, C., GAO, F., FRIEND, R. H., GREENHAM, N. C. AND TAN, Z.-K., “Highly efficient perovskite nanocrystal light-emitting diodes enabled by a universal crosslinking method”, *Adv. Mater.* **28**(18), 3528–3534 (2016), [doi: 10.1002/adma.201600064](https://doi.org/10.1002/adma.201600064).
- [312] AKKERMAN, Q. A., D’INNOCENZO, V., ACCORNERO, S., SCARPELLINI, A., PETROZZA, A., PRATO, M. AND MANNA, L., “Tuning the optical properties of cesium lead halide perovskite nanocrystals by anion exchange reactions”, *J. Am. Chem. Soc.* **137**(32), 10276–10281 (2015), [doi: 10.1021/jacs.5b05602](https://doi.org/10.1021/jacs.5b05602).
- [313] WANG, H.-C., LIN, S.-Y., TANG, A.-C., SINGH, B. P., TONG, H.-C., CHEN, C.-Y., LEE, Y.-C., TSAI, T.-L. AND LIU, R.-S., “Mesoporous silica particles integrated with all-inorganic  $\text{CsPbBr}_3$  perovskite quantum-dot nanocomposites (MP-PQDs) with high stability and wide color gamut used for backlight display”, *Angew. Chem. Int. Ed.* **55**(28), 7924–7929 (2016), [doi: 10.1002/anie.201603698](https://doi.org/10.1002/anie.201603698).
- [314] KONDO, S., TAKAHASHI, K., NAKANISHI, T., SAITO, T., ASADA, H. AND NAKAGAWA, H., “High intensity photoluminescence of microcrystalline  $\text{CsPbBr}_3$  films: Evidence for enhanced stimulated emission at room temperature”, *Curr. Appl Phys.* **7**(1), 1–5 (2007), [doi: 10.1016/j.cap.2005.08.001](https://doi.org/10.1016/j.cap.2005.08.001).

- [315] XING, G., MATHEWS, N., LIM, S. S., YANTARA, N., LIU, X., SABBA, D., GRÄTZEL, M., MHAISALKAR, S. AND SUM, T. C., “Low-temperature solution-processed wavelength-tunable perovskites for lasing”, *Nat. Mater.* **13**(5), 476–480 (2014), doi: [10.1038/nmat3911](https://doi.org/10.1038/nmat3911).
- [316] DESCHLER, F., PRICE, M., PATHAK, S., KLINTBERG, L. E., JARAUSCH, D.-D., HIGLER, R., HÜTTNER, S., LEIJTENS, T., STRANKS, S. D., SNAITH, H. J., ATATÜRE, M., PHILLIPS, R. T. AND FRIEND, R. H., “High photoluminescence efficiency and optically pumped lasing in solution-processed mixed halide perovskite semiconductors”, *J. Phys. Chem. Lett.* **5**(8), 1421–1426 (2014), doi: [10.1021/jz5005285](https://doi.org/10.1021/jz5005285).
- [317] LIU, X., NIU, L., WU, C., CONG, C., WANG, H., ZENG, Q., HE, H., FU, Q., FU, W., YU, T., JIN, C., LIU, Z. AND SUM, T. C., “Periodic organic-inorganic halide perovskite microplatelet arrays on silicon substrates for room-temperature lasing”, *Adv. Sci.* **3**(11), 1600137 (2016), doi: [10.1002/advs.201600137](https://doi.org/10.1002/advs.201600137).
- [318] SHE, C., FEDIN, I., DOLZHIKOV, D. S., DEMORTIÈRE, A., SCHALLER, R. D., PELTON, M. AND TALAPIN, D. V., “Low-threshold stimulated emission using colloidal quantum wells”, *Nano Lett.* **14**(5), 2772–2777 (2014), doi: [10.1021/nl500775p](https://doi.org/10.1021/nl500775p).
- [319] EVANS, T. J. S., SCHLAUS, A., FU, Y., ZHONG, X., ATALLAH, T. L., SPENCER, M. S., BRUS, L. E., JIN, S. AND ZHU, X.-Y., “Continuous-wave lasing in cesium lead bromide perovskite nanowires”, *Adv. Opt. Mater.* **6**(2), 1700982 (2017), doi: [10.1002/adom.201700982](https://doi.org/10.1002/adom.201700982).
- [320] KRIEG, F., OCHSENBEIN, S. T., YAKUNIN, S., TEN BRINCK, S., AELLEN, P., SÜESS, A., CLERC, B., GUGGISBERG, D., NAZARENKO, O., SHYNKARENKO, Y., KUMAR, S., SHIH, C.-J., INFANTE, I. AND KOVALENKO, M. V., “Colloidal CsPbX<sub>3</sub> (X = Cl, Br, I) nanocrystals 2.0: Zwitterionic capping ligands for improved durability and stability”, *ACS Energy Lett.* **3**(3), 641–646 (2018), doi: [10.1021/acsenerylett.8b00035](https://doi.org/10.1021/acsenerylett.8b00035).
- [321] SHAH, J., *Ultrafast Spectroscopy of Semiconductors and Semiconductor Nanostructures*, Springer Berlin Heidelberg (1999).
- [322] SON, D.-Y., LEE, J.-W., CHOI, Y. J., JANG, I.-H., LEE, S., YOO, P. J., SHIN, H., AHN, N., CHOI, M., KIM, D. AND PARK, N.-G., “Self-formed grain boundary healing layer for highly efficient CH<sub>3</sub>NH<sub>3</sub>PbI<sub>3</sub> perovskite solar cells”, *Nature Energy* **1**(7), 16081 (2016), doi: [10.1038/nenergy.2016.81](https://doi.org/10.1038/nenergy.2016.81).
- [323] WARREN, S. C., MARGINEANU, A., ALIBHAI, D., KELLY, D. J., TALBOT, C., ALEXANDROV, Y., MUNRO, I., KATAN, M., DUNSBY, C. AND FRENCH, P. M. W., “Rapid global fitting of large fluorescence lifetime imaging microscopy datasets”, *PLoS ONE* **8**(8), e70687 (2013), doi: [10.1371/journal.pone.0070687](https://doi.org/10.1371/journal.pone.0070687).
- [324] PYDZIŃSKA, K., KAROLCZAK, J., KOSTA, I., TENA-ZAERA, R., TODINOVA, A., IDÍGORAS, J., ANTA, J. A. AND ZIÓLEK, M., “Determination of interfacial charge-transfer rate constants in perovskite solar cells”, *ChemSusChem* **9**(13), 1647–1659 (2016), doi: [10.1002/cssc.201600210](https://doi.org/10.1002/cssc.201600210).

- [325] VOLONAKIS, G. AND GIUSTINO, F., “Ferroelectric graphene-perovskite interfaces”, *J. Phys. Chem. Lett.* **6**(13), 2496–2502 (2015), doi: [10.1021/acs.jpcllett.5b01099](https://doi.org/10.1021/acs.jpcllett.5b01099).
- [326] MASUDA, Y., GIORGI, G. AND YAMASHITA, K., “DFT study of anatase-derived TiO<sub>2</sub> nanosheets/graphene hybrid materials”, *Phys. Status Solidi B* **251**(8), 1471–1479 (2014), doi: [10.1002/pssb.201451089](https://doi.org/10.1002/pssb.201451089).
- [327] DHANKER, R., BRIGEMAN, A. N., LARSEN, A. V., STEWART, R. J., ASBURY, J. B. AND GIEBINK, N. C., “Random lasing in organo-lead halide perovskite microcrystal networks”, *Appl. Phys. Lett.* **105**(15), 151112 (2014), doi: [10.1063/1.4898703](https://doi.org/10.1063/1.4898703).
- [328] DIROLL, B. T., ZHOU, H. AND SCHALLER, R. D., “Low-temperature absorption, photoluminescence, and lifetime of CsPbX<sub>3</sub> (X = Cl, Br, I) nanocrystals”, *Adv. Funct. Mater.* **28**(30), 1800945 (2018), doi: [10.1002/adfm.201800945](https://doi.org/10.1002/adfm.201800945).
- [329] DOTTI, N., SARTI, F., BIETTI, S., AZAROV, A., KUZNETSOV, A., BICCARI, F., VINATIERI, A., SANGUINETTI, S., ABBARCHI, M. AND GURIOLI, M., “Germanium-based quantum emitters towards a time-reordering entanglement scheme with degenerate exciton and biexciton states”, *Phys. Rev. B* **91**(20) (2015), doi: [10.1103/physrevb.91.205316](https://doi.org/10.1103/physrevb.91.205316).
- [330] HE, H., YU, Q., LI, H., LI, J., SI, J., JIN, Y., WANG, N., WANG, J., HE, J., WANG, X., ZHANG, Y. AND YE, Z., “Exciton localization in solution-processed organolead trihalide perovskites”, *Nat. Commun.* **7**, 10896 (2016), doi: [10.1038/ncomms10896](https://doi.org/10.1038/ncomms10896).
- [331] LI, J., LUO, L., HUANG, H., MA, C., YE, Z., ZENG, J. AND HE, H., “2D behaviors of excitons in cesium lead halide perovskite nanoplatelets”, *J. Phys. Chem. Lett.* **8**(6), 1161–1168 (2017), doi: [10.1021/acs.jpcllett.7b00017](https://doi.org/10.1021/acs.jpcllett.7b00017).
- [332] VAN DRIEL, A. F., ALLAN, G., DELERUE, C., LODAHL, P., VOS, W. L. AND VANMAEKELBERGH, D., “Frequency-dependent spontaneous emission rate from CdSe and CdTe nanocrystals: influence of dark states”, *Phys. Rev. Lett.* **95**(23) (2005), doi: [10.1103/physrevlett.95.236804](https://doi.org/10.1103/physrevlett.95.236804).
- [333] GONG, K., ZENG, Y. AND KELLEY, D. F., “Extinction coefficients, oscillator strengths, and radiative lifetimes of CdSe, CdTe, and CdTe/CdSe nanocrystals”, *J. Phys. Chem. C* **117**(39), 20268–20279 (2013), doi: [10.1021/jp4065449](https://doi.org/10.1021/jp4065449).
- [334] DE MELLO DONEGÁ, C., BODE, M. AND MEIJERINK, A., “Size- and temperature-dependence of exciton lifetimes in CdSe quantum dots”, *Phys. Rev. B* **74**(8) (2006), doi: [10.1103/physrevb.74.085320](https://doi.org/10.1103/physrevb.74.085320).
- [335] JONES, M., LO, S. S. AND SCHOLLES, G. D., “Signatures of exciton dynamics and carrier trapping in the time-resolved photoluminescence of colloidal CdSe nanocrystals”, *J. Phys. Chem. C* **113**(43), 18632–18642 (2009), doi: [10.1021/jp9078772](https://doi.org/10.1021/jp9078772).
- [336] NITSCH, K., HAMPLOVÁ, V., NIKL, M., POLÁK, K. AND RODOVÁ, M., “Lead bromide and ternary alkali lead bromide single crystals – growth and emission properties”, *Chem. Phys. Lett.* **258**(3-4), 518–522 (1996), doi: [10.1016/0009-2614\(96\)00665-3](https://doi.org/10.1016/0009-2614(96)00665-3).



- [337] CAVIGLI, L., GABRIELI, R., GURIOLI, M., BOGANI, F., FELTIN, E., CARLIN, J.-F., BUTTÉ, R., GRANDJEAN, N. AND VINATTIERI, A., “Probing exciton density of states through phonon-assisted emission in GaN epilayers: A and B exciton contributions”, *Phys. Rev. B* **82**(11) (2010), doi: [10.1103/physrevb.82.115208](https://doi.org/10.1103/physrevb.82.115208).
- [338] VINATTIERI, A., BOGANI, F., CAVIGLI, L., MANZI, D., GURIOLI, M., FELTIN, E., CARLIN, J.-F., MARTIN, D., BUTTÉ, R. AND GRANDJEAN, N., “Large-k exciton dynamics in GaN epilayers: nonthermal and thermal regimes”, *Phys. Rev. B* **87**(7) (2013), doi: [10.1103/physrevb.87.075202](https://doi.org/10.1103/physrevb.87.075202).
- [339] GROTE, C. AND BERGER, R. F., “Strain tuning of tin-halide and lead-halide perovskites: a first-principles atomic and electronic structure study”, *J. Phys. Chem. C* **119**(40), 22832–22837 (2015), doi: [10.1021/acs.jpcc.5b07446](https://doi.org/10.1021/acs.jpcc.5b07446).
- [340] DURSUN, I., ZHENG, Y., GUO, T., BASTIANI, M. D., TUREDI, B., SINATRA, L., HAQUE, M. A., SUN, B., ZHUMEKENOV, A. A., SAIDAMINOV, M. I., DE ARQUER, F. P. G., SARGENT, E. H., WU, T., GARTSTEIN, Y. N., BAKR, O. M., MOHAMMED, O. F. AND MALKO, A. V., “Efficient photon recycling and radiation trapping in cesium lead halide perovskite waveguides”, *ACS Energy Lett.* **3**(7), 1492–1498 (2018), doi: [10.1021/acsenergylett.8b00758](https://doi.org/10.1021/acsenergylett.8b00758).
- [341] YAMADA, T., YAMADA, Y., NAKAIKE, Y., WAKAMIYA, A. AND KANEMITSU, Y., “Photon emission and reabsorption processes in  $\text{CH}_3\text{NH}_3\text{PbBr}_3$  single crystals revealed by time-resolved two-photon-excitation photoluminescence microscopy”, *Phys. Rev. Appl.* **7**(1) (2017), doi: [10.1103/physrevapplied.7.014001](https://doi.org/10.1103/physrevapplied.7.014001).
- [342] YANG, J., WEN, X., XIA, H., SHENG, R., MA, Q., KIM, J., TAPPING, P., HARADA, T., KEE, T. W., HUANG, F., CHENG, Y.-B., GREEN, M., HO-BAILLIE, A., HUANG, S., SHRESTHA, S., PATTERSON, R. AND CONIBEEER, G., “Acoustic-optical phonon up-conversion and hot-phonon bottleneck in lead-halide perovskites”, *Nat. Commun.* **8**, 14120 (2017), doi: [10.1038/ncomms14120](https://doi.org/10.1038/ncomms14120).
- [343] DE JONG, E. M. L. D., YAMASHITA, G., GOMEZ, L., ASHIDA, M., FUJIWARA, Y. AND GREGORKIEWICZ, T., “Multiexciton lifetime in all-inorganic  $\text{CsPbBr}_3$  perovskite nanocrystals”, *J. Phys. Chem. C* **121**(3), 1941–1947 (2017), doi: [10.1021/acs.jpcc.6b10551](https://doi.org/10.1021/acs.jpcc.6b10551).